UNIVERSITY OF SOUTHAMPTON

Faculty of Engineering and Applied Science
Department of Electronics and Computer Science

Flame Hydrolysis Deposition of Photosensitive Silicate Layers Suitable for the Definition of Waveguiding Structures through Direct Ultraviolet Writing

By

Samuel Paul Watts

A thesis submitted for the degree of
Doctor of Philosophy

September 2002

UNIVERSITY OF SOUTHAMPTON

Abstract

FACULTY OF ENGINEERING AND APPLIED SCIENCE
DEPARTMENT OF ELECTRONICS AND COMPUTER SCIENCE

Doctor of philosophy

FLAME HYDROLYSIS DEPOSITION OF PHOTOSENSITIVE SILICATE LAYERS SUITABLE FOR THE DEFINITION OF WAVEGUIDING STRUCTURES THROUGH DIRECT ULTRAVIOLET WRITING

By Samuel Paul Watts

This thesis presents the construction of equipment suitable for the fabrication of doped silicate layers through use of the Flame Hydrolysis Deposition technique. The subsequent optimisation of equipment and deposition processes has seen the realisation of fully dense amorphous silica layers doped with Phosphorus, Boron and Germanium. Accurate control of dopant inclusion has allowed the independent control of processing properties and optical characteristics, while maintaining the tolerances imposed by waveguiding. The Flame Hydrolysis Deposition Technique has been applied to the fabrication of three layer nominally index matched planar waveguiding structures, consisting of low photosensitivity cladding layers and high photosensitivity core layers. Application of the direct UV writing technique to planar structures has been investigated, and the induced physical and optical effects characterised. The additional application of the Deuterium loading process has been used to further enhance photosensitivity and has resulted in the production of channel waveguides with propagation losses of ~0.2dB/cm and relative core refractive indices of the order 1×10^{-2}. The use of a novel UV writing technique has shown the simultaneous definition of waveguiding channels with inherent Bragg grating structures, the characterisation of which has resulted in birefringence as low as $\sim3\times10^{-5}$.

Table of Contents

Acknowledgements

I would like very much to thank my supervisor Dr. Peter Smith for his unwavering support and considerable guidance during the course of my PhD. Dr. Richard Williams has also been invaluable, if it was not for his vast knowledge and experience the Flame Hydrolysis Deposition system would not be what it is today.

The research group as a whole has assisted me greatly both technically and by keeping me on the straight and narrow. In particular, the help offered by Greg Emmerson, who has been involved in almost all aspects of the project, was gratefully received most notably his recent work in bullying the grating writing and characterisation equipment into life. I am indebted to Alexander Fu for his early work on the UV writing equipment, his considerable knowledge directly led to the current state-of-the-art system. Dr. Christos Riziotis and Vassilios Albanis have also contributed to the UV writing and subsequent characterisation of samples for which I am grateful. The help offered by Dr. Corin Gawith has been welcomed, his development of an integrated grating definition process and his selfless dedication to polishing samples has been invaluable. I would like to thank Denis Guilhot and Ian Sparrow for their work in continuing the development of the deposition system, while I was finally getting some data.

I would like to acknowledge the efforts of the technical staff, without whom the equipment which we all rely upon on a daily basis would not run as effectively and reliably.

Thanks must also be given to the Engineering and Physical Science Research Council, who directly funded me during the course of this project.

I am particularly grateful to my friends and family for their backing during the course of my PhD, and for not asking "When are you going to get a proper job?" too often. I would especially like to thank Evanna for her unending support whilst I have been on the emotional roller coaster ride that has been my PhD, and for generally putting up with me.

Sam Watts

1 Introduction

1.1 Background of optics in telecommunication

The field of optical telecommunications first emerged in the 1960s, and the first working networks were installed in the 1970s. The large-scale adoption of optical communication systems began around 1982, when the US government deregulated the telecommunications industry resulting in today's long-haul telecommunications traffic being almost entirely carried on optical fibre systems. The development of the dispersion-shifted fibre, introduced in 1985, marked a further revolution in optical communications. The combination of the attenuation minimum found in the 1550nm window and dispersion compensation, allowed higher data rates to be carried over longer distances. In the early 1990's the erbium fibre amplifier was developed, overcoming the bit rate limitations of electrical systems and allowing non-repeated length to increase ten-fold. The introduction of fibre amplifiers led the way to Wavelength Division Multiplexing (WDM) and suggested that in the near future all optical networks would become possible. The next revolution is likely to come in the form of optical switching and routing, through the use of wavelength selective cross-connects and wavelength add/drop multiplexers. The reduction in overall cost and the increase in bandwidth and speed of systems through the minimisation of optical-electrical-optical conversion continues to drive development.

1.2 Integrated optics

In 1969 S.E. Miller proposed that optical elements could be integrated in one common block of glass, thus forming an integrated optical element. The development of integrated optical systems has lagged behind that of optical fibres. However with the increasing need to process signals optically within optical networks, the integration of optical elements has become increasingly appealing. Optical signal processing is possible through other routes, but with fibre devices only capable of the simplest functionality and bulk devices being expensive, development of integrated optics has thrived. Currently commercial Planar Lightwave Circuits (PLC) are becoming increasingly widely deployed by carriers due to the inherent convenience of on-chip devices.

The majority of the Dense Wavelength Division Mulitipling (DWDM) PLC devices currently used are simple "dumb" fibre multipliers. The use of Arrayed Waveguide Gratings

(AWGs) as multiplexers and demultiplexers have found widespread development as PLC devices. It is clear that high levels of integration will greatly reduce the cost of implementing networks with ever increasing bandwidth.

The further development of PLC devices to include increasingly complex processing capabilities is expected. Devices for add/drop multiplexing, optical switching and more complicated processing are currently under development. An analogy can be drawn between the advances in electronics processing due to the introduction of Integrated Circuits (ICs) and the possible future advances in optical communication due to PLCs. It is important to note the miniaturisation limits for PLC compared to ICs, due to waveguiding structures at telecommunications wavelengths being considerably larger than electrical tracks. However it is expected that similar growth in the field of PLCs can be expected as observed for ICs. The apparent continued growth of the internet and in addition to general globalisation makes it difficult to see an end to the increasing demands for faster, higher capacity systems.

1.3 The aim of the research undertaken

The mission statement for the project undertaken consists of the fabrication of materials and structures, using flame hydrolysis deposition (FHD), suitable for the production of PLC devices in photosensitive silicate glasses. This includes the key points below:

- Construction of deposition equipment and subsequent development of doped silicate layer fabrication techniques through modifying deposition parameter and materials properties.
- Production of a recipe list consisting of compositions with varying concentrations of photosensitive dopant, and independent control of processing characteristics and refractive index.
- Construction of planar waveguiding structures and subsequent application of the direct UV writing technique.
- Characterisation of the UV induced waveguiding structures and associated processes, with respect to materials properties and writing parameters.

1.4 Summary

The following Chapters progressively discuss the work undertaken during the course of this project and encompasses the various aspects that were embarked upon during the fulfilment of the tasks outlined. It should be noted that in general the work presented has been the culmination of various individuals efforts, although the research presented is wholly the authors it would not have been possible to achieve so much without the significant input of others. Chapter 2 discusses the various deposition techniques that are suitable for the fabrication of doped silicate layers, focusing on those that have historically found widespread application. Having concluded that FHD is suitable due to a high degree of flexibility, the specific mechanisms that occur within the FHD process during production of fully dense amorphous layers are treated in detail. Chapter 3 outlines the design, construction and development of the processing equipment, and the considerations that have to be taken into account during the conception and subsequent implementation of both equipment and process in order to produce layers with desired properties. Some of the equipment presented benefited considerably from the efforts of Dr. Richard Williams, Greg Emmerson and Denis Guilhot. Chapter 4 presents the implementation of the fabrication equipment, and elaborates on the specific nature of the FHD process during the production of layers. In particular, the problems that were found and the solutions applied are discussed in detail. The thorough investigation of the various layer production mechanisms ensured that full advantage could be taken from the fabrication technique. Chapter 5 focuses on the optimisation of the FHD process during the production of layers with required optical and processing characteristics. The FHD process is further characterised during this procedure. Chapter 6 treats the application of the direct UV writing process to layered structures constructed from compositions determined in Chapter 5, and details the physical damage that is observed for certain exposure conditions. The development of the UV writing equipment represents an entirely separate projects, therefore the investigation of UV writing would not have been possible without the work of Alexander Fu, Dr. Christos Riziotis and Vassilios Albanis and various others. Chapter 7 investigates the production of channels through use of UV induce refractive index change, and describes the optical characterisation of the waveguides produced, concentrating on the magnitude of UV induced index and propagation properties. Chapter 8 proposes a novel technique for simultaneously defining waveguiding channels with Bragg gratings within the planar geometry, and discusses the optical properties that can be determined via grating characterisation. Again, the efforts

required to implement the novel simultaneous Bragg grating definition technique and subsequent characterisation of the structures would not have been possible without the considerable amount of assistance given by Greg Emmerson and Dr. Corin Gawith. Finally Chapter 9 concludes the work that has been presented and highlights the multitude of possible future work that may stem from it.

2: Fabrication technique, theory and principles

The fabrication of silicate materials suitable for planar waveguides can take place via a number of routes, the selection of a technique that is as flexible as possible and capable of producing Germanosilicate layers of high quality and reproducibility is therefore of paramount importance. This Chapter reviews some of the techniques that are most widely used and have played a considerable part in the prior art within this field of research.

Having discussed the motives for selecting Flame Hydrolysis Deposition, the theory behind the production of amorphous layers using associated processes is treated. A full knowledge of the mechanisms that influence fabrication of layers will ultimately allow a controllable and reproducible process to be developed through tailoring deposition parameters and resulting materials properties, thereby utilising the full potential of Flame Hydrolysis Deposition.

2.1 Review of Deposition Processes suitable for PLC fabrication

The following section critically reviews fabrication techniques that are suitable for the deposition of silicate planar waveguides. The presentation of prior art is included in order to give a view of the suitability of the chosen technique for the task. The review is by no means exhaustive as there are undoubtly many variants on the main techniques that can produce silicate layers. However, those included represent the most widely used and therefore are expected to be the most suitable.

2.1.1 Flame Hydrolysis Deposition

The flame hydrolysis reaction was first utilised in the production of preforms suitable for drawing into optical fibres. The vapour axial deposition (VAD) process employs an Oxygen-Hydrogen flame into which Silicon Tetrachloride ($SiCl_4$) vapour is injected, resulting in the formation of fine silica particles commonly known as "soot". The introduction of further vapours into the flame in addition to $SiCl_4$ allows the incorporation of dopant species within the soot; Germanium Tetrachloride ($GeCl_4$), Phosphorus Oxychloride ($POCl_3$) and Boron Tribromide (BBr_3) are common examples. The close proximity of the flame to a mandrel results in the deposition of the silicate particles, thus forming a layer, showing in figure 2.1a. Subsequent consolidation of the soot layer through exposure to high temperatures results in a fully dense silicate preform suitable for the fibre drawing process.

The application of the flame hydrolysis reaction to deposit soot layers on planar substrates commonly known as Flame Hydrolysis Deposition (FHD), and thus producing planar waveguides rather than the cylindrical waveguides produced by VAD, has become widespread, shown in figure 2.1b. Typical FHD systems borrow burners and glass forming systems directly from VAD, building on a significant amount of prior art regarding weakly doped silicates suitable for waveguiding applications.

The refractive indices of the deposited layers can be accurately controlled through

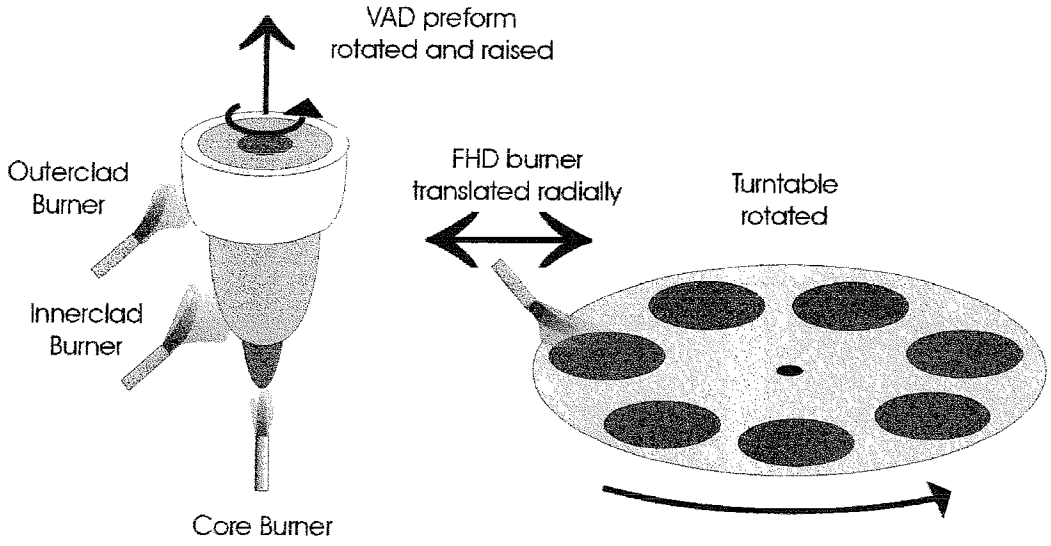

Figure 2.1, a) Schematic of Vapour Axial Deposition process,
b) Schematic of typical Flame Hydrolysis Deposition process

varying the amount and type of dopant used in addition to $SiCl_4$ during the deposition process. The thickness and uniformity of the deposited soot layers are controlled by the vapour supply rate to the burner and the translation of the burner relative to the substrate. FHD has been demonstrated by NTT to produce uniform, fully dense layers with thickness from several microns up to hundreds of microns, with refractive index differences of 0.75% [Kawachi, 1990]. Further compositional variation allows an index difference of up to 1 or 2%, and the production of waveguiding structures with losses as low as 0.05dB/cm for single-mode operation [Sun and Schmidt, 1999].

It has been widely demonstrated that FHD is a suitable fabrication process for forming media appropriate for optically integrated devices in the planar geometry. However, a number of technical considerations impose limitations upon the range of layers that can be produced. Introducing dopant species into the silica matrix not only alters the refractive index, but also modifies the temperature at which densification occurs and the thermal expansion coefficient for the layers. The doping regimes used for layers that are

present within a single structure must therefore be complementary if the structure is to survive the high temperature consolidation process that commonly takes place at 1200-1400°C.

The selection of the substrate material on which the layers are deposited directly affects the processing and subsequent optical nature of the structures produced. The two most commonly used materials are silica and Silicon, both of which have limitations that affect the formation of layers using FHD and subsequent high temperature consolidation. Silicon wafers are widely available due to extensive use in the microelectronics industry, and offer a high purity, high uniformity surface suitable depositions. The possibility of subsequent integration of electro-optic semiconductor type devices on to the same substrate as passive waveguiding components is also attractive [Okamoto, 1998]. However, the considerable thermal expansion mismatch between Silicon and silica results in a degree of stress induced birefringence within the fully dense FHD layers after the consolidation process, although this can be avoided by tailoring layer compositions [Kilian *et al*, 2000]. The relatively low melting point of Silicon compared to silica also imposes a ceiling upon the range of consolidation temperatures that can be used. Silica does not have any of the thermal expansion mismatch problems associated with Silicon and can withstand higher temperatures, however a degree of deformation due to temperatures above the softening point of silica can result in uniformity problems. The production of high uniformity silica wafers to the standard of Silicon wafers is not trivial, and the availability of such substrates is limited due to lack of demand. Both silica and Silicon are used as substrate materials within the field of FHD since one is not considerable more advantageous than the other.

In general, the FHD process affords a reliable and highly flexible method from producing planar waveguiding structures. The high temperature nature of the required consolidation process is the source of the disadvantages associated with FHD. However, the particulate nature of the layer produced affords an extra degree of flexibility that is not available to techniques that deposit fully dense layers. In particular, the large surface area of unconsolidated or partially consolidated layers allows the introduction of additional dopant species either through solution doping or pressurised gas saturation.

2.1.2 PECVD

The generic use of chemical vapour deposition (CVD) involves the dissociation of reagents and subsequent atomic scale growth of compound materials consisting of

components from the original reactant species [Sherman, 1987]. The desired material formed from thermal decomposition and/or reaction of gaseous compounds is deposited onto the surface of the substrate directly from the gas phase as a film [Brodie and Muray, 1982][Jaeger, 1989]. Basic CVD reactors take the form of tube furnaces into which substrates are placed, subsequent introduction of gaseous species results in thermally initiated molecular decomposition and the associated deposition, see figure 2.2a. The modification of pressure within the deposition chamber and the heating regime has led to a number of CVD derivative processes, many of which find widespread use in the microelectronics industry. In particular polysilicon, silicon dioxide and silicon nitride, as well as some refractory metals, are all commonly fabricated using CVD type processes.

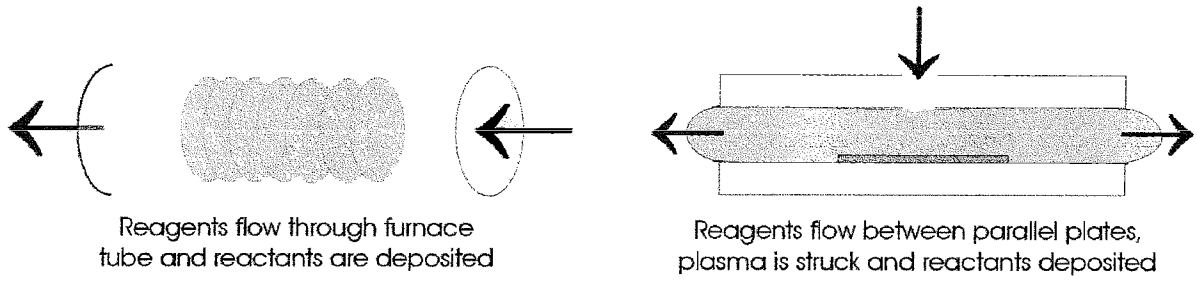

Figure 2.2, a) CVD reactor, b) PECVD reactor

One of the main disadvantages of the CVD processes outlined so far is the requirement of a suitably high temperature to result in reagent dissociation. The use of high temperatures can result in diffusion of dopants within structures that are already present on the substrate and in thermal expansion mismatch between deposited layer and substrate. The use of Plasma Enhanced CVD (PECVD) allows the dissociation of reagent gases by electron impact in a glow discharge plasma and requires only moderate heating (<300°C) of substrates in order for uniform deposition to occur. The parallel plate plasma reactor is a commonly used design and illustrates the operational components of a PECVD system, shown in figure 2.2b. In a parallel plate reactor substrates are placed on an aluminium platen, which is grounded and forms the bottom electrode required to establish a plasma. Heating of the substrates normally takes place via resistance heaters embedded in the bottom platen. The top electrode is another aluminium platen that is brought into close proximity with the substrate surfaces. The reagent gases along with an inert carrier gas flows through the chamber and in-between the platens and application of a radio-frequency (RF) signal to the top electrode establishes a plasma. A further derivative of PECVD allows increased deposition rates and uniformity through using a hollow cathode (HC) as a very effective plasma source [Bardos *et al*, 1997]. The geometry of HC-PECVD systems

promotes oscillations of hot electrons inside the cathode, thereby enhancing ionisation, ion bombardment of the inner walls and other subsequent processes. For a given power, a hollow-cathode plasma source is capable of producing plasma densities one or two orders of magnitude greater than for conventional planar electrodes, with the associated increases in film growth rate.

PECVD has found widespread use in the field of microelectronics and subsequently in the production of planar waveguiding structures. HC-PECVD is particularly attractive for the production of waveguiding structures due to the large relative thickness of waveguiding layers compared to films required in microelectronic devices. A wide range of precursors including gaseous metal hydrides (e.g. Silane), metal halides (e.g. Silicon Tetrachloride) and metalorganics (e.g. Tetraethoxysilane), have been demonstrated to produce silicate layers. The modification of layer properties is achieved through the introduction of dopant species during the deposition process, thus allowing the fabrication of a range of silicates with similar optical properties to those produced by FHD.

The main advantages of PECVD would appear to be the relatively low temperature processing, however it has been observed that a high temperature annealing steps (>1100°C) can be required in order to reduce losses to a suitable level [Hoffmann *et al*, 1997]. The argument that PECVD is a single step low temperature fabrication process is therefore not always valid. However, the extensive prior art of planar thin film deposition associated within PECVD technologies cannot be ignored, and is no doubt a significant advantage to the future production of planar media suitable for optically integrated devices.

2.1.3 Sol-gel

The Sol-gel process is a technique that is employed in the production of a large number of ceramic derived materials, including oxide glasses [Brinker and Scherer, 1990]. The production of materials using the Sol-gel technique involves the formation of a Sol; a colloidal suspension of solid particles in a liquid, which in turn forms a gel; a semi-solid two-component system rich in liquid. Through controlled removal of the solvent from the gel, it is possible to tailor the physical arrangement of the remaining components. There are two main structures that can be produced Xerogels; dried by evaporation causing shrinkage resulting in tightly packed structure with small pore volume, and Aerogels; supercritical drying by evaporation with no shrinkage resulting in open structure with extremely high pore volume.

The production of thin films using the Sol-gel technique is a development of the Xerogel process in which Gelation and evaporation take place simultaneously and result in Xerogel film. Coating of such films on to substrates normally takes place using dip coating or spin coating using a Sol. Xerogel films are then generally processed via an elevated temperature partially for consolidation and partially to remove unwanted organic components, thus resulting in a fully dense and uniform film consisting of the surviving components from the original Sol.

The use of Sol-gel techniques to produce structures for waveguiding application is widely accepted as being cheap and flexible, particularly when it comes to controlling properties such as pore size, pore volume and surface area. However there are considerable complications associated with the production of Sols that form suitably robust gels. The extremely sensitive nature of the Xerogel films with respect to drying conditions also presents a considerable problem, cracking, peeling and lateral shrinkage can all contribute to Xerogels being insufficiently uniform. The resulting Xerogel films also have to be processed at elevated temperature (~500°C), however temperatures are moderate compared to those required for FHD.

Planar waveguide devices have been demonstrated within the silicate materials system using Sol-Gel techniques, with losses as low as 0.3dB/cm [Coudray *et* al, 1996] and refractive indices in the range 1.39-1.65 [Yoshida and Prasad, 1996]. Sol-gel technology offers an interesting alternative route to producing silicate waveguiding structures compared to the better-known "physical deposition" techniques typified by the FHD and PECVD processes.

2.1.4 PVD

Physical vapour deposition (PVD) is a general term for processes that involve the controllable transfer of atoms from a source to a substrate, resulting in the formation of a film [Ohring, 1992]. There are two important routes for PVD production of thin films: Firstly, evaporation characterised by the removal of atoms from the source thermally. Secondly sputtering which involves the removal of atoms from the source through impaction of gaseous ions. Both evaporation and sputtering rely on sufficient energy being supplied to the source for atomisation to occur, the resulting atoms must also have enough energy and be unimpeded in order to allow incidence and condensation upon the substrate. A key part of any PVD process is therefore the vacuum conditions under which deposition

takes place, typically pressures of ~10^{-8} torr are required to produce high quality and purity films.

In the case of evaporation, removal of atoms from the source can take place in a number of ways, purely thermal processes can be employed using resistive elements and crucibles. However, contamination of the deposited film can easily occur through evaporation from components other than the intended source. Such contamination issues can largely be eliminated using focused electron beams as the energy source to induce evaporation. The evaporation of materials suitable for waveguiding applications is not trivial. In general, appropriate inorganic compounds do not evaporate without molecular change; the vapour composition therefore generally varies from that of the source. Oxides in particular dioxides are normally deposited in an O_2 partial pressure, in an attempt to stabilise the stoichiometry of the deposited film.

Sputtering processes can be explained by considering a simplified sputtering system, consisting of a target plate forming the cathode, the substrates being sited on the anode. A driving voltage is then applied between the two parallel plates. The whole system is situated within a vacuum chamber containing the sputtering gas, generally argon which is introduced into the chamber after pump down, typically resulting in a process pressure of 100 mtorr. Different sputtering techniques arise depending on the method employed to sustain the glow discharge or plasma within the chamber and the composition of the plasma. Deposition of oxides suitable for waveguiding applications have taken place using either RF sputtering with a target consisting of the required material, or by reactive sputtering using a pure metallic target in the presence of a reactive gas.

As has been mentioned it is possible to deposit oxide glasses suitable for waveguiding applications using both evaporation and sputtering techniques. Both techniques do suffer from the need for high purity high compositionally uniform sources and targets, since any inhomogeneities are reproduced in the deposited film. Evaporation generally suffers from significant decomposition and dissociation of compounds, making the deposition of doped silica layers problematic. Sputtering on the other hand does not suffer to such a degree, but does still have problems producing compound glasses with strict stoichiometry. The uniform doping of silica glasses can therefore be a problem for both Evaporation and Sputtering processes, often requiring complicated multi-source techniques to produce adequate results.

The use of RF sputtering to produce silicate waveguiding structures has been reported [Tosello *et al*, 2001], however losses of ~1.2dB/cm arising from excessive

particulate contamination where reported. Generally, it is seen that PVD processes suffer from contamination, excessively slow deposition rates or inhomogeneous composition and have therefore not seen widespread adoption within the field of silicate based planar waveguide fabrication.

2.1.5 Thermal Oxidation

Silicon's high affinity for oxygen causes oxide layers to form rapidly when it is exposed to oxygen under ambient conditions. The further growth of this native oxide layer can be promoted until it reaches suitable dimensions for optical waveguiding, i.e. layer of order 5μm. During the process of oxidation, the Si-SiO_2 interface moves into the silicon, since Si is consumed in producing SiO_2. However, the surface of the oxide also moves away from the plane initially represented by the silicon surface. This outward growth occurs due to the volume change associated with the Si-SiO_2 transition. The consumption of the silicon is roughly 44% of the total resulting oxide thickness [Sze, 1988].

The most commonly used thermal oxidation technique for IC production and general microelectronics is high-pressure steam oxidation. This simply involves placing silicon wafers in a furnace at ~800-1000°C containing a wet atmosphere (produced either pyrogenically or through bubbling) at a pressure of up to ~25atm. The use of high pressure and a wet atmosphere greatly improves the rate of oxidation. It is possible to produce microns of oxide in a matter of hours using this process. Although the production of multiple 5-20μm layers that are required for waveguiding structures can take considerably longer.

High-pressure steam oxidation is a process that has been developed on a large scale, and is well understood in the context of thin oxide production in the microelectronics industry. However the long layer growth times and the difficulties associated with incorporating refractive index altering dopants uniformly into oxide layers, limits the usefulness of this technique for producing complete waveguiding structures. It can however be used effectively as part of a composite process, for instance in the bulk production of standard underclad layers suitable for subsequent core/overclad deposition.

The possibility of using thermal oxidation related processes in the formation of waveguiding structures has been highlighted in work investigating the anodisation of Silicon wafers [Haiyan *et al*, 1999]. The formation of a porous layer on the surface of Silicon wafers though electro-chemical anodisation in an electrolytic solution, was found to

promote the growth rate of subsequent thermal oxide layers. Inclusion of dopant species, in particular Phosphorus, in the electrolytic solution during porous layer formation resulted in refractive index modification of the final thermal oxide layer. A refractive index range of 1.283-1.554 was achieved through varying Phosphorus concentration and the thermal oxide growth conditions. A large degree of the refractive index variation is expected to be due to the production non-fully-dense silicate layers. However, the technique does indicate a possible route through which dopants could be incorporated within thermal oxides and subsequently used in waveguiding structures.

2.1.6 Others

Several other techniques are suitable for the fabrication of doped silicate glass layers with a view to forming planar waveguiding structures. New deposition techniques such as laser reactive deposition (LRD), which is similar to FHD but relies of the focus of a laser beam to provide the reaction energy instead of a flame, has been shown to produce low-loss waveguides (Neophotonics Inc.). The advantages touted by advocates of LRD is it flexibility with respect to reaction kinetics, since it is easier to tailor the energy within the focus of laser beam than it is to modify flame temperature. It is the view of this author that a new deposition technique will have to have overwhelming advantages in order to supersede the techniques previously outlined. In particular, FHD and PECVD are so well established and have considerable prior art behind them that is difficult to see current alternative techniques becoming dominant. The only exception is Sol-gel technology, which is significantly different and offers such a different set of possibilities with respect to materials development and novel nano-scale structuring that it maybe a feasible alternative route.

The selection of FHD as the primary means of fabricating doped silicate layers centred on its inherent flexibility and relative ease of implementation. Considerable prior art and experience exists within the Optoelectronics Research Centre with respect to the production of novel silicate materials and structures for used in fibre waveguides. FHD is considered more similar to the fibre fabrication routes employed than any of the other possible planar fabrication routes, and could therefore use much of the knowledge already present within the department. It was also expected that FHD would be a suitable route to apply to the planar geometry many of the novel techniques developed for use in fibre waveguides, due to the similarity of fabrication processes.

2.2 Principles of FHD

The following section describes the mechanisms involved in the FHD process. In particular, the complexities of flame structure and the reactions that take place during soot production. The effect of flame and substrate parameters upon the nature of the soot deposited is also discussed. The thorough understanding of the FHD process greatly aids the experimental application of the technique to the fabrication of planar waveguides.

2.2.1 Reagents and Reactions in the Flame

A flame can be described as a self-sustaining endothermic breakdown of reagents, and exothermic recombination of radicals thus forming reaction products. The thermal breakdown of reagents within a flame leads to the formation of radicals through ionisation processes. At the point of ignition, a flame is therefore a highly reactive environment, in particular a Hydrogen-Oxygen flame can be characterised by the slightly endothermic reactions which lead to chain-branching [Gaydon and Wolfhard, 1970];

$$O + H_2 = OH + H$$
$$H + O_2 = OH + O$$

and the propagation step;

$$OH + H_2 = H_2O + H$$

leading to a rapid build up of an excess population of free atoms and radicals in the reaction zone.

The structure of a flame and the injection of additional reagents into the reaction zone are of critical importance when using a flame as a reaction media. Flames can be classically characterised as; premixed where oxidiser and fuel are in intimate contact prior to intersection with the flame front, or diffusion where fuel and oxidiser only come into contact at the flame front forming a wedge of intermediate combustion products in between oxidiser and fuel. In reality unless a flame is rigorously confined to a single mechanism through careful burner design, then both diffusion and premixed conditions often occur. Typically, burners used within VAD and FHD processes are of "jet" type, and result in premixed flame characteristics close to the gas outlets with the rest of the flame dominated by diffusion.

The thermal gradient experienced by reagents travelling through the flame front is of importance to the reaction processes that occur. The temperature of the gas flowing within a flame relative to the flame front can be split into three regions preheat, reaction, and

afterburning, shown schematically in figure 2.3. The preheat zone is characterised by the region prior to the initiation of exothermic reactions, where temperature increase is purely due to heat transfer against the flow of gas. The reaction zone is classically defined by the flame front, and the propagation and chain-branching reactions previously described with the addition of exothermic recombination reactions. The afterburning zone is characterised by the recombination of excess radicals after the reaction zone, implying that endothermic reactions have ceased. The process of heat transfer within a flame is largely due to convection and conduction within the gas flow, since emission for a H_2/O_2 flame is largely in the UV and is relatively weak.

The theoretical flame temperature for a stoichiometry H_2/O_2 flame is 3083K with

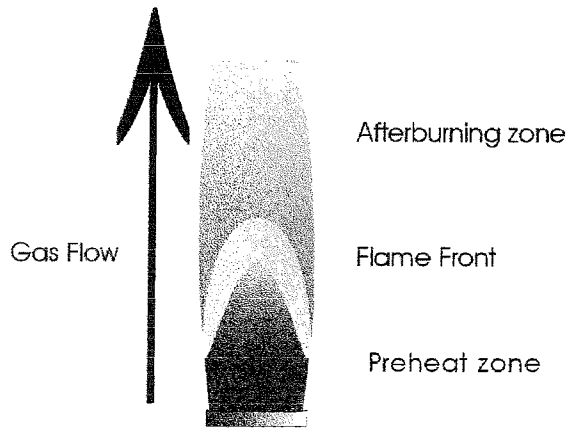

Figure 2.3, schematic showing flame propagation

exhaust gases consisting of 57% H_2O, 5% O_2, 16% H_2, 10% OH, 8% H and 4% O [Strehlow, 1984]. The actually observed flame temperature will be highly dependent upon the specific burner and imposed flame dynamics. Any deviation from stoichiometry or dilution by a non-reactive gas will have the effect of decreasing the flame temperature.

The injection of Halide reagents into the H_2/O_2 flame during the FHD process can result in two possible reaction processes leading to the formation of oxide soot. Oxidation of Halides within the flame can be described by the reaction below;

$$SiCl_4 + O_2 \rightarrow SiO_2 + 2Cl_2$$

Such a reaction is assumed to occur if the temperature within the preheated zone prior to gas flow intersection with the flame front is high enough to cause direct oxidation, and that back-diffusion of H_2O or related species from the flame front is not significant. The hydrolysis of Halides is characterised by the reaction below;

$$SiCl_4 + 2H_2O \rightarrow SiO_2 + HCl$$

This reaction is assumed to occur if the temperature of the preheated zone is not high enough to result in direct oxidation, leading to halides coming into intimate contact with H_2O or related species. The hydrolysis reaction is likely to extend throughout the reaction zone and possibly into the afterburning zone, since diffusion of reactive species is the rate determining mechanism. Experimentally it has been shown that oxidation of halides occurs for flame temperatures above 1200°C [Bautista and Atkins, 1991], below this hydrolysis is the dominant reaction. It was also noted that the occurrence of oxidation is somewhat self-sustaining due to the exothermic nature of the reaction.

2.2.2 Particle Formation, Aggregation and Deposition

The formation of the soot particles within the flame from the oxide vapour resulting from the oxidation/hydrolysis reactions is almost instantaneous due to the large equilibrium constants (k_p) associated with the phase change. A value of k_p less than one indicates that equilibrium tends towards the solid to vapour transition, k_p greater than one indicates that equilibrium tends towards the vapour to solid transition and a k_p of one indicates both phase are equally stable [Atkins, 1992]. The k_p for oxides of Silicon, Boron and Phosphorus are significantly greater than one, Germanium is less high but still forms particles in the flame although a degree of revaporisation may occur depending upon flame temperature. Values

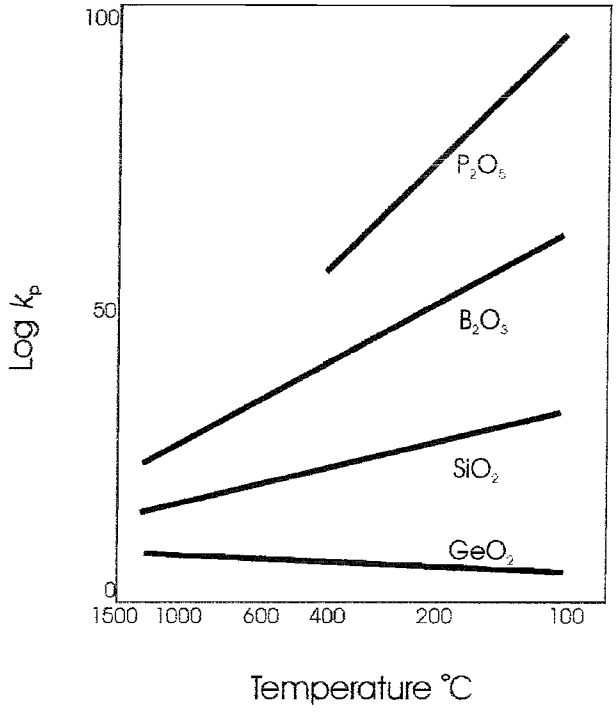

Figure 2.4,Relative equilibrium constants for dopant species [Sakaguchi, 1994a]

of k_p are shown in figure 2.4. The difference in k_p for the various oxides may result in a degree of spatially varying differential particle formation dependent upon the temperature gradient within the flame [Sakaguchi, 1994a]. However, the rate of general particle growth will be dependent upon the oxide vapour concentration gradient within the flame, thus dictating the maximum size that single particles can achieve.

The halt of primary particle growth associated with a decrease in oxide vapour concentration dictates that the subsequent soot particle growth mechanism is dominated by the coalition and aggregation of existing particles [Ulrich and Riehl, 1982]. The rate of aggregate growth is determined by the Brownian collision frequency of the particles within the flame and the relative "stickiness" of the particles. However, for a particle stream with high density is has been found that collision rate exceeds that expected by purely Brownian motion. The rate of growth and maximum achievable size for aggregate particles is primarily dependent upon the molten nature of the particles dictated by the temperature gradient associated with the flame, the composition of the particles and the dwell time of the particles at elevated temperature.

The particle growth mechanisms that take place in the particle stream between particle creation and soot deposition on a substrate can be summaries in the following manner:

1. Condensation of a specific oxide via nucleation from the saturated vapour phase.
2. Growth of a single particle within the vapour rich region of the flame.
3. Aggregation and coalescence of particles in the high temperature vapour poor region.
4. Coagulation of solid particles in the temperature gradient from flame to substrate.

It can therefore be seen that the specific nature of the flame and the composition of the reagent vapour-stream injected into the flame, will have a pronounced effect upon the nature of the particles that are incident with the substrate and therefore the soot that is deposited.

The dominant particle deposition mechanism is widely thought to be thermophoresis; the net force that a suspended particle experiences in the direction of decreasing temperature in a non isothermal medium, the thermophoretic velocity V_t can be expressed as;

$$V_t = -\frac{Kv}{T}\nabla T$$

where T is the temperature, v is the viscosity, and K is an empirically determined constant [Cho *et al*, 1998]. The dominance of thermophorisis as the primary deposition mechanism arises from the soot particles being too small for inertial impaction. However, it is the view of the author that a combination of additional mechanisms is also likely to play a part in soot-substrate adhesion. Regardless of the mechanism responsible for deposition, it is widely observed that when a particle stream impinges upon a substrate soot deposition results.

2.2.3 Effect of Substrate Temperature

The thermophoretic nature of the deposition process dictates that the temperature of the substrate directly affects the rate of deposition. Since a relative decrease in surface temperature enhances thermophoresis by increasing temperature gradients near the substrate surface. However, a theoretical study of thermophoretic transport within FHD [Hsin-Chuan *et al*, 1996] suggests that a maximum deposition efficiency is experienced with a substrate temperature of ~600°C. It should be noted that although substrate temperature directly affects the temperature gradient, the flame also has a considerable effect. The nature of the flame is likely to be highly system specific and therefore greatly affects the temperature for which maximum deposition efficiency occurs.

As has been mentioned in section 2.2.2 Germanium oxide forms particles in the flame, but due to a relatively low k_p the vapour phase may also be present in varying degrees. A critical value for phase equilibrium constant with respect to the nature of particle production occurs at $\log k_p = 3$. For k_p greater than a thousand it is found that amorphous particles form through the mechanism previously outlined, for k_p less than a thousand it is found that the vapour phase is sufficiently stable to allow crystal growth from the saturated vapour [Sakaguchi, 1994b]. The phase equilibrium constant for Germanium oxide can be below one thousand and therefore the crystalline phase is expected to occur either through film growth directly onto the substrate or on soot particles present within the vapour stream, or alternatively as growth of discrete crystallites. It has been seen experimentally [Kawachi *et al*, 1980] that the temperature dependence of the phase equilibrium constant for GeO_2 manifests itself as a substrate temperature dependence upon the phase that is deposited. For substrate temperatures above 500°C a purely amorphous phase is deposited, for

temperatures below 400°C the hexagonal crystalline phase of GeO_2 is present within the soot layer, shown in figure 2.5.

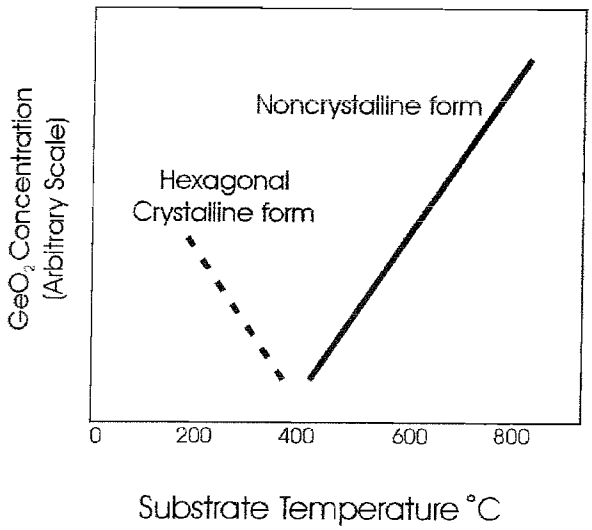

Figure 2.5, Phase dependence on temperature for GeO_2 [Kawachi *et al*, 1980]

The deposition of crystalline B_2O_3 has also been observed [Edahiro *et al*, 1980], with the relative amount of the crystalline form decreasing over the substrate temperature 200-500°C and the amorphous form increasing between 200-800°C. It should be noted that the occurrence of the crystalline form within FHD soots has not been reported else where, this is possibly due to the low melting point of crystalline B_2O_3 (580°C) leading to remelting in the flame and subsequently forming the amorphous phase. The occurrence of crystalline B_2O_3 may therefore be highly system dependent, with the majority of systems producing thermal gradients within the flame that are not conducive to the deposition of crystalline B_2O_3.

It has been shown that theoretically crystalline GeO_2 can be deposited and that experimentally both crystalline B_2O_3 and GeO_2 have been observed within FHD soots. However, it is unlikely that the crystalline form of either dopant will remain within the fully dense layers, since consolidation normally requires heating to greater than 1200°C and the melting point of crystalline GeO_2 and B_2O_3 are 1110°C and 580°C respectively. It must however be assumed that the deposition of crystalline forms may result in significant compositional inhomogeneities when compared to layers that have been fully amorphous at all stages.

2.3 Principles of Consolidation, Sintering and Densification

The theoretical treatment of FHD soot consolidation and the factors that must be considered when the production of fully dense amorphous layers is required, takes place in

the following section. A thorough understanding of the fundamental science behind the mechanisms involved allows the techniques to be practically exploited to the full.

2.3.1 Viscous Sintering

The mechanism through which FHD soot layers become fully dense at elevated temperature is widely accepted as a sintering process. Sintering is a term commonly used to refer to processes involved in the heat treatment of powder compacts at elevated temperature, normally in the range at which appreciable diffusional mass transport occurs. The driving force for sintering is a decrease in the surface free energy of powder compacts, by replacing solid-vapour interfaces with solid-solid interfaces. Thermodynamically sintering is an irreversible process in which a free energy decrease is brought about by a decrease in the surface area [Waldron and Daniell, 1978].

Viscous sintering occurs when there is a sufficient degree of particle softening due to heating, resulting in surface tension pulling particles together therefore decreasing surface area and bringing about a corresponding decrease in free energy. Assuming FHD produces amorphous particles then viscous sintering is the primary mechanism for consolidation. If any crystallites are present, the consolidation temperature must be above the melting point of the crystalline material thus introducing a degree of liquid phase sintering, in which mass transport occurs via liquid flow. However, it is widely accepted that viscous sintering can be considered as the sole densification mechanism during the consolidation of FHD soot layers [Scherer, 1977a].

The process of consolidation via viscous sintering is dependent upon the temperature-viscosity relationship for the material, but also upon the free energy associated with the system. Sintering can be theoretically treated by considering the necking that occurs between two spherical particles during the consolidation process, see figure 2.6. The rate of initial neck growth can be given by;

$$\frac{x}{R} = \left(\frac{3\gamma}{2\eta r}\right)^{1/2} t^{1/2}$$

where γ is a surface tension, η is viscosity and t is time [Rabinovich, 1985]. The time for full coalescence of the particles ($x \approx R_0$) with original radius R_0 is of the magnitude;

$$\tau \approx \frac{h}{\gamma} R_0$$

where $h = R(1-\cos\phi)$. Thus, a material with a lower viscosity at a given temperature will consolidate at a greater rate than a material with a higher viscosity at the same temperature. It should also be noted that smaller particle-size also results in a relative decrease in time required for full coalescence. The increase in surface area associated with smaller particle-size leads to a larger potential reduction in free energy for the system upon full densification, thereby increasing the driving force behind sintering and increasing the relative rate of consolidation.

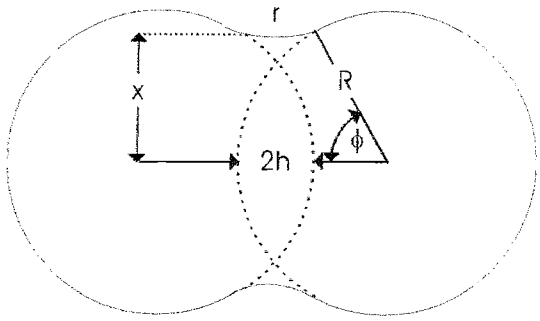

Figure 2.6, Necking of two particles during sintering

The rate of consolidation at a given temperature is directly related to the degree of consolidation that occurs for a given time and temperature. In reality, there is a point at which the rate of consolidation is so slow as to be effectively nonexistent, in which case sintering can be deemed not to be occurring. The occurrence of sintering under a given set of conditions has therefore been shown to be dependent upon the temperature-viscosity relationship for the material in question and the particle sizes present within the soot layer.

2.3.2 Glass Formation verses Crystal Growth

Unfortunately, the process of sintering amorphous silicate particles into fully dense layers exposes the material to conditions suitable for crystal growth. The thermodynamic driving force behind sintering that results in densification through the minimisation of free energy, is similar to the minimisation of free energy associated with crystallisation of amorphous solids. If crystallisation occurs during sintering at a temperature below the melting point of the crystalline phase, then consolidation will stall. It is therefore necessary to consider the factors that dictate glass formation and crystallisation characteristics of materials and in particular weakly doped silicates.

A glass is formed when a material is cooled from an amorphous liquid phase at a rate greater than crystal nucleation and subsequent growth can occur, therefore resulting in a solid with "frozen" amorphous structure [Varshneya, 1994]. For a specific material, the

critical cooling rate (CCR) dictates the rate at which the viscosity of the material increases rapidly enough to halt the molecular rearrangement associated with crystal growth. The reheating of amorphous solids and the associated reduction in viscosity introduces the possibility of molecular rearrangement and thus crystal nucleation and subsequent growth. The relative temperature dependence of viscosity, nucleation rate and crystal growth rate all play an important part in determining the devitrification resistance for a material. A plot combining variation of crystal growth rate and nucleation rate with temperature in the form of a time-temperature-transform (T-T-T) diagram allows heat treatment regimes that do not

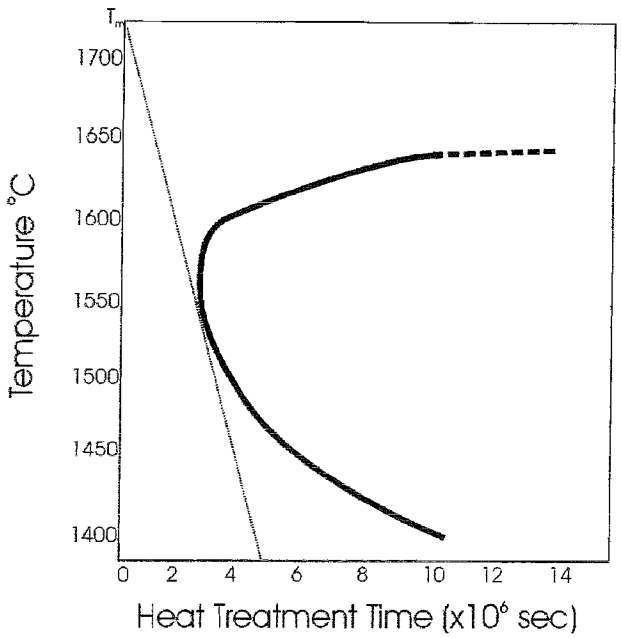

Figure 2.7, Time-Temperature-Transform diagram for silica [Varshneya, 1994]

result in crystallisation to be determining, see figure 2.7. Near the melting point, the time required for crystal, growth to occur is essentially infinite, due to nucleation and growth rates being effectively zero because of the lack of thermodynamic driving force. At low temperatures, the time required is also very large due to the significant reduction in molecular mobility. For intermediate temperatures where the occurrence of nucleation and growth overlap, there is a finite time until appreciable crystallisation is observed. However, for the temperature regimes proposed for consolidation of FHD soots (1200-1400°C) it is clear that the occurrence of crystallisation is very unlikely unless exceedingly long process times are used. The addition of dopants into the silica matrix will alter the crystallisation behaviour of silica, but P_2O_5, B_2O_3 and GeO_2 are also known to have high viscosities and low crystallisation velocities therefore dictating high degrees of devitrification resistance.

2.3.3 Specifics of FHD Densification Process

As highlighted in section 2.3.1 the primary mechanism for FHD soot layer densification at elevated temperature is viscous sintering. This requires having a sufficient volume of the amorphous material at a viscosity for which particle coalescence and pore-closure takes place without the occurrence of crystallisation. For multicomponent systems, viscosity is dependent upon the relative amounts of the components present. A single viscosity-temperature dependence for a system can only be assumed once a solid solution has formed. The formation of a solid solution between the host matrix and lower melting point dopants lowers the viscosity of the whole system, therefore allowing viscous sintering to take place at a lower temperature. The production of a glassy layer using FHD and consolidation techniques can therefore be summarised by the following stages [Sakaguchi, 1994a]:

1. Dopants are independently deposited in soot layer and do not form a solid solution.
2. Upon heating soot for consolidation, dopants diffuse into the silica matrix to form a solid solution.
3. Formation of a solid solution leads to a reduction is viscosity.
4. Consolidation is completed at a lower temperature and an amorphous doped silica layer is formed.

Due to the various melting points of the dopants used, there is a considerable temperature range over which consolidation can occur. The determination of the theoretical effect of dopants upon consolidation conditions can take place using sintering kinetics [Sherer, 1977b] [Sherer, 1977c] Such calculations are dependent upon experimental determination of soot density and temperature dependent viscosity, which are not easily determined. Subsequent work has relied heavily upon Differential Thermal Analysis (DTA) and Thermo Gravimetric Analysis (TGA). The well-developed nature of DTA and TGA techniques has allowed the classification of consolidation behaviour for a number of soot layers produced using FHD [Sakaguchi, 1994a] [Sakaguchi, 1994b]. Although no chemical reactions actually take place within the soot an endothermic peak is produced. The peak value determines the onset of densification, due to the quasi-heat exchange associated with the increase in density of the soot, resulting in an increase in thermal conductivity. The TGA measurements are used to confirm that no significant chemical reaction or dopant volatilisation takes place. From these types of procedures the graph in figure 2.8 showing the effect of dopant upon threshold consolidation temperature has been produced.

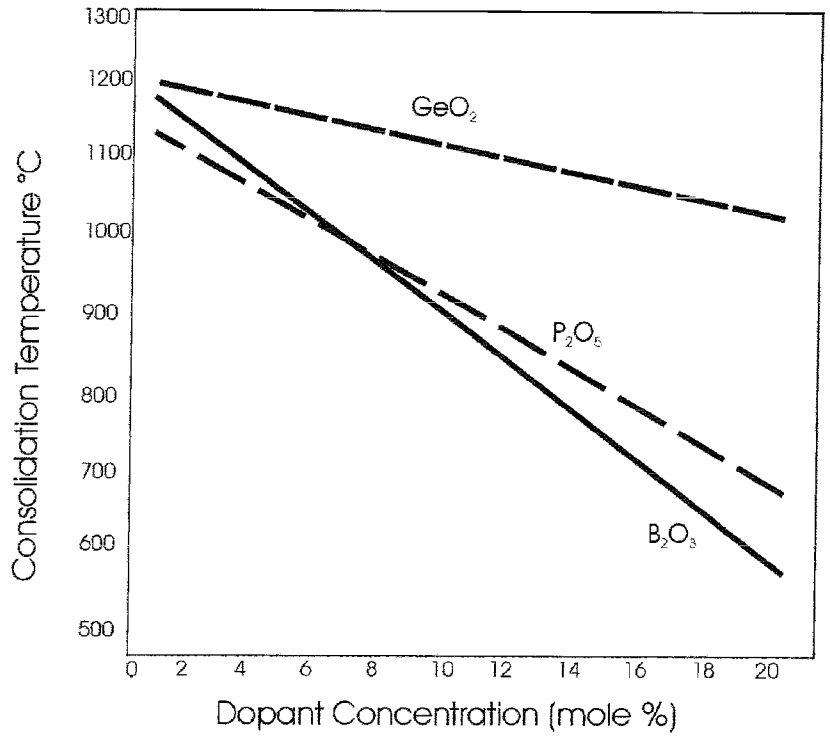

Figure 2.8, Effect of dopant concentrations upon consolidation temperature [Sakaguchi, 1994b]

The thorough understanding of the mechanism behind FHD and sinter processing is a required prerequisite if such processes are to be fully applied to the production of Germanosilicate layers suitable for construction of planar waveguiding structures. The ability to tailor the nature of the deposition process through controlling the flame characteristics and subsequent deposition parameters will allow a high degree of flexibility with respect to the soot layers that can be produced. The effect of soot characteristics and compositions upon the consolidation process facilitates rapid attainment of processing parameters suitable for soot densification resulting in high quality optical layers. The intimate knowledge of microscopic scale processes with respect to soot deposition and consolidation greatly aids the trouble-shooting process when a specific layer is required. Knowledge of prior art and theory has been an indispensable backbone to the work undertaken.

2.4 Conclusion

The various fabrication routes suitable for the production of doped silicate layers have been identified, in particular FHD, PECVD, and Sol-gel have been highlighted as techniques with considerable potential that are already being widely applied both academically and industrially. The specific merits of FHD, with respect to its high degree of flexibility and its relative ease of implementation under the specific circumstances, readily lends itself to a research environment.

The theoretical mechanisms inherent to the FHD process have been discussed in a logical progression from the flame where oxides are first produced, through to the consolidation process required for forming fully dense amorphous layers. It is with this knowledge that the development and optimisation of the FHD processing equipment and subsequent layer production has taken place, as discussed the following Chapters.

3 Design, Construction and Operation of Experimental Equipment

The development of the flame hydrolysis deposition process including design, construction and utilization of systems fundamental to the deposition and consolidation processes represents a key part of the work undertaken. This chapter outlines the equipment that has been developed and that was used on a daily basis during the project. The various elements are presented as a linear progression through the workings of the three main systems (FHD rig, Gas supply system and consolidation furnaces) used in the FHD production of silicate layers. However, the actual progressive development of the various systems was far from that highlighted by the following sections. Figure 3.1 indicates the progressive nature of the development involved in attaining the deposition system subsequently outlined in the chapter. The first incarnation of the FHD rig was only capable of static soot depositions and extract was supplied by a single point deposition chamber extract. Subsequent development saw the implementation of the translation system (section 3.1.5), sliding seal (section 3.1.7) and deposition head extract (section 3.1.4). The deposition of soots under controllable thermal conditions was realised through use of the first generation halogen heating system (section 3.1.3).

The first major evolution of the FHD rig took place when the previously used reagent supply system borrowed from a fibre preform lathe was replaced by the construction of a dedicated FHD reagent supply system (section 3.2). At this time, the FHD rig was reconstructed into a freestanding unit and housed in a dedicated lab within a 10,000-class cleanroom. The implementation of system integration through application of dedicated control hardware and software (section 3.3) also took place at this stage. Subsequently the substrate heating systems were further developed through design and implementation of an improved halogen heater and latterly a resistive heater (section 3.1.3). The introduction of the new resistive heating system required construction of a new deposition chamber lid, at which point a deposition head cleaning port was included, allowing in-process cleaning and a subsequent increase in soot deposition flexibility. The deposition of layers with relatively independent optical and processing characteristics was realised through the development of the Boron Trichloride reagent supply system (section 3.2.4). The implementation of a dedicated scrubber unit (section 3.1.8) allowed a degree of system separation from the service extract, and therefore afforded greater process stability due to non-dependence upon

other processes using the service extract. Finally the replacement of flame gas system reliant upon gas metering via rotameters with a mass flow controller based system (section 3.1.6) and the associated increase in flame uniformity, completes the progression to the systems current state that is present in the following sections.

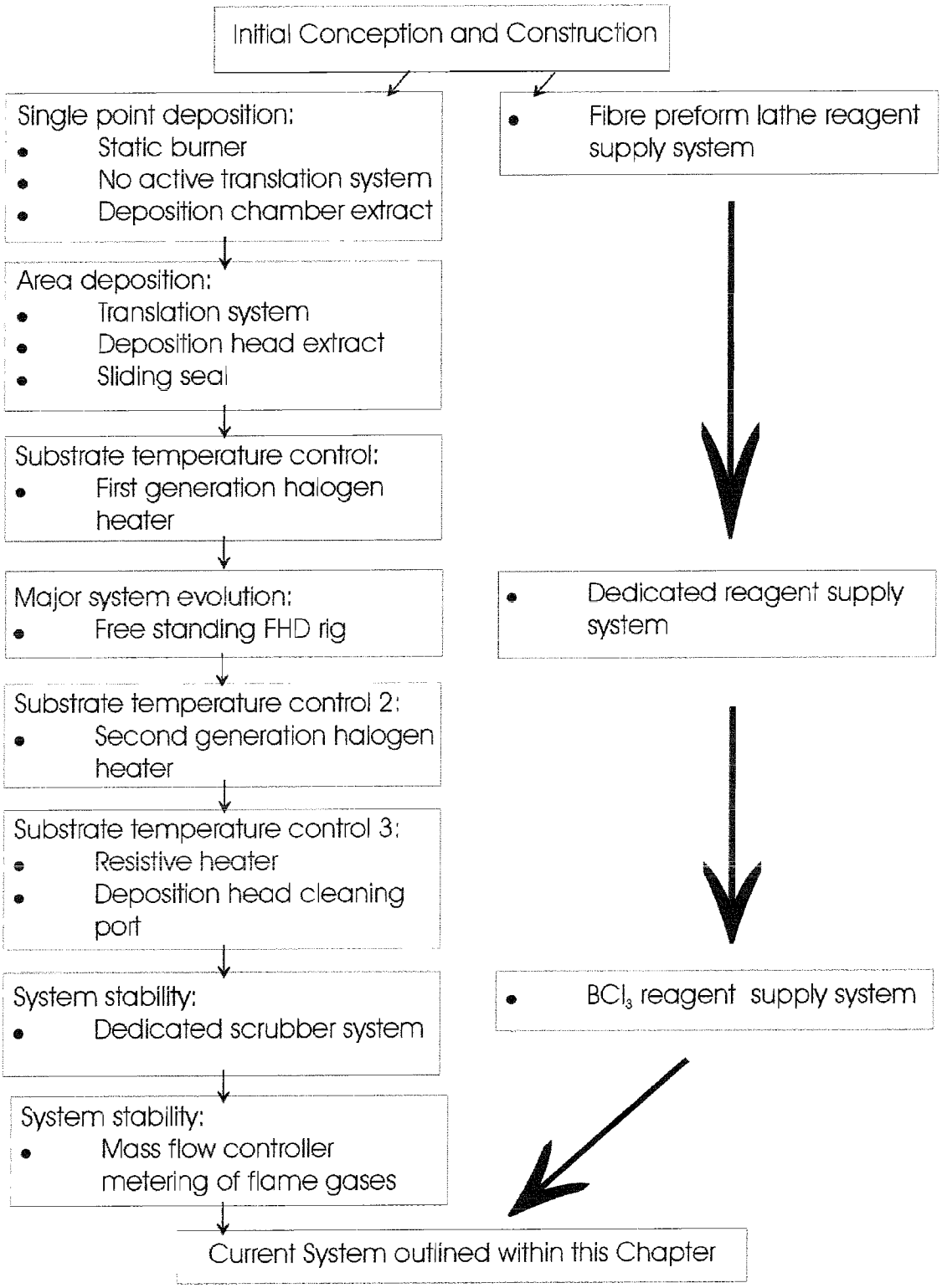

Figure 3.1, Progression of Equipment Development

The nature of the project and the continued optimisation of layer production has led to continual feed back with regards to the fabrication characteristics and solutions in the form of equipment development. Therefore, the system outlined and the development routes pursued are intimately connected with the discussion of deposition and consolidation properties within chapter 4.

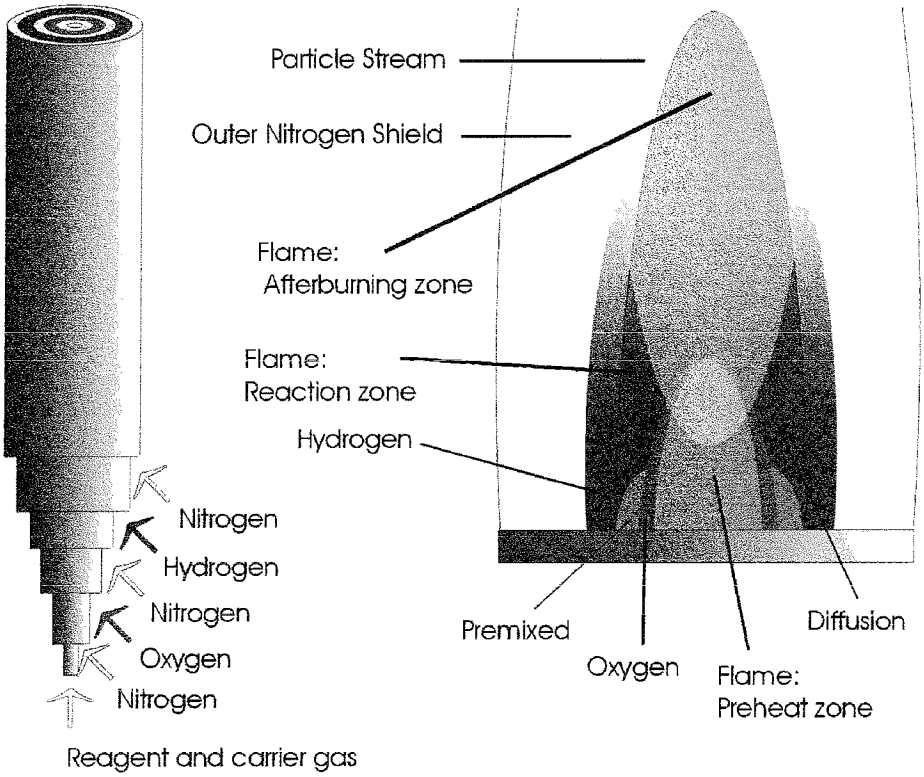

Figure 3.2, Schematic of six ringed burner

3.1 Flame Hydrolysis Deposition equipment

The design and construction of the equipment used for the deposition of doped silicate layers using the FHD process represents a considerable amount of effort and is the centre from which all subsequent work has developed. A thorough understanding of the FHD process and the requirements of equipment have been attained during the continued development of the deposition system. The following section outlines the reasoning behind the systems employed and the physical workings of the various subsystems, which form the FHD system that has been constructed.

3.1.1 Burner configuration

The burner used within the FHD rig is of six-ringed design shown in figure 3.2. Burners of this type have been used previously in commercially available Vapour Axial Deposition systems used for preform fabrication in the fibre industry. The burner consists of six concentric tubes; each flame gas is individually introduced into its respective tube. The larger diameter tubes have two gas inputs, insuring that gas flow up the tube is uniform and that resulting flow out of the rings at the burner nozzle is not affected by the position of gas injection into the tube.

The first ring is used for introducing the carrier gas and reagent into the flame. The third ring supplies the oxygen required for combustion. The fifth ring supplies the hydrogen that is used as the fuel in the flame. The second, fourth and sixth rings all flow nitrogen that is used to shield the reactive gases from each other when in close proximity to the nozzle. The flow velocity from each ring is scaled relative to ring area such that a stable flame is produced. This is achieved through increasing flow rate as the ring number increases and results in a tightly confined flame with high gas velocity. The minimisation of flicker, a stable reaction zone and a high soot particle velocity are therefore easily achieved.

The general flame shape produced using a six-ring burner with the gases previously outlined can be characterised as a confined cone. Understanding the effect that the various gas flow rates have upon the flame is of critical importance when using a flame as a reaction medium. The flame-front forms a cone burning at the interface between the hydrogen and oxygen jets. The nature of the flame, diffusion or premixed, will depend upon

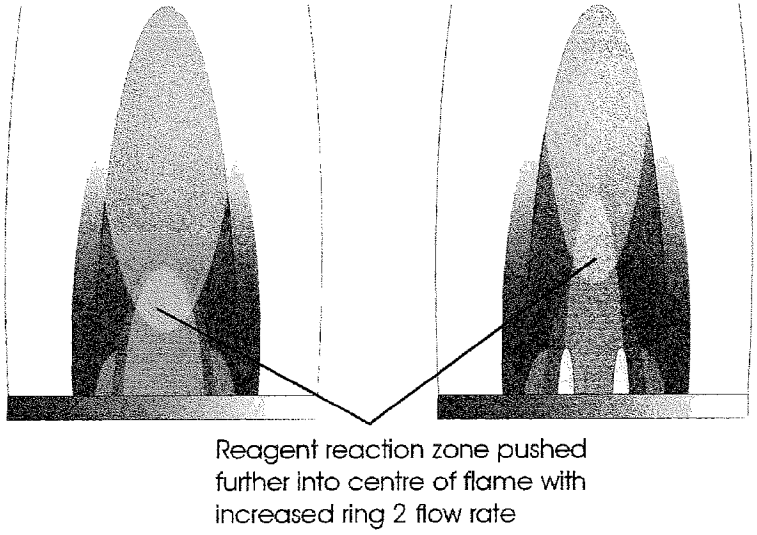

Figure 3.3, Schematic showing theoretical effect of first nitrogen shield

the specific gas flow rates. It is normally found with jet flames of this type that premixing occurs at the base of the flame-front near the nozzle and diffusion is dominant for the rest of the flame-front, as previously explained in chapter 2. The integrity of the cone will also be dependent upon gas flow rates. For low flow velocities, the flame-front may become diffuse at the tip of the cone due to diffusion being the dominant process and afterburning occurring simultaneously. A stable preheated zone is predominantly present within the flame front cone. Preheating of the hydrogen must also occur outside of the flame front cone, however this is likely to overlap with the afterburning zone. The afterburning zone is likely to extend vertically and to some degree laterally from the flame front. The volume of the afterburning zone will be dependent upon the fuel to oxidiser ratio used in the flame. The reaction zone for the reagents that result in soot production can occur at any stage within the flame. Particle creation is dependent upon the specifics of the reactions taking place as mentioned in a Chapter 2. The high gas flow velocities result in a high velocity particle and exhaust gas stream, which is tightly confined above the flame.

The flame characteristics can be tailored within the stable regime outlined through modification of the relative flow rates for individual rings. In particular the role of the shield gases can greatly affect the flame dynamics and therefore the nature of soot production and deposition. The shield produced by the second ring has the effect of separating the reagent and carrier gas stream from the flame gases, see figure 3.3. The higher the shield flow rate the lower the lateral diffusion of reagent relative to the distance from the nozzle. The in-diffusion of water from the flame front is also impeded by higher shield flow rates. It is

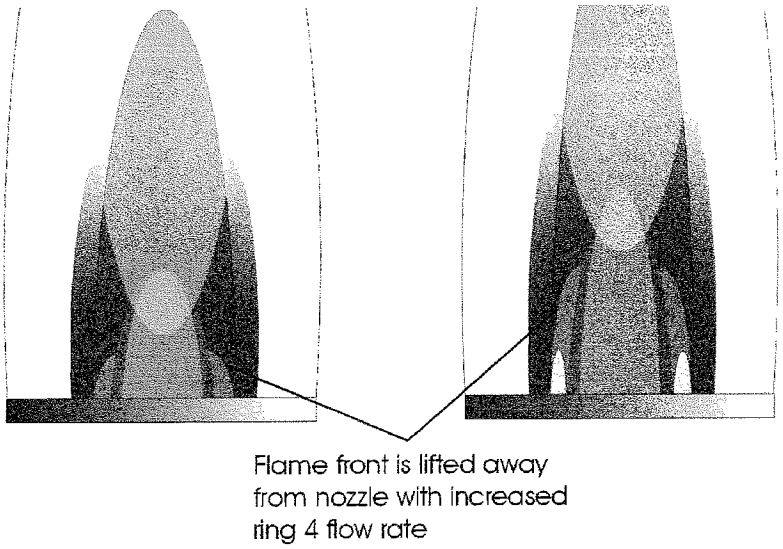

Figure 3.4, Schematic showing theoretical effect of second nitrogen shield

therefore possible to control the nature of the reagent injection into the flame and the resulting reaction through modification of the shield flow rate from the second ring. The ability to modify the reagent injection characteristics and resulting reaction without modifying carrier gas or reagent flow rates is important. It is effectively possible to leave reagent supply parameters constant and vary the injection dynamics through shield gas flow rate tailoring. The separation of such process parameters is useful in the characterisation and optimisation of the Flame Hydrolysis Deposition process.

The flow rate of the shield produced from the fourth ring has the effect of lifting the flame off the burner nozzle as shown in figure 3.4, thereby increasing the diffusion distance required for fuel and oxidiser to come into intimate contact. Increasing the fourth ring flow rate therefore has a direct effect upon the distance between flame front and burner nozzle, thus controlling the heating effect of the flame upon the nozzle. Minimisation of nozzle temperature reduces the likelihood of reagent reacting in the burner prior to injection into the flame. The degree of flame lift-off must be carefully controlled in order to maintain flame stability. The flow rate for the fourth ring is therefore limited to a range that produces significant lift off, resulting in burner temperature reduction, but does not result in significant flame instability.

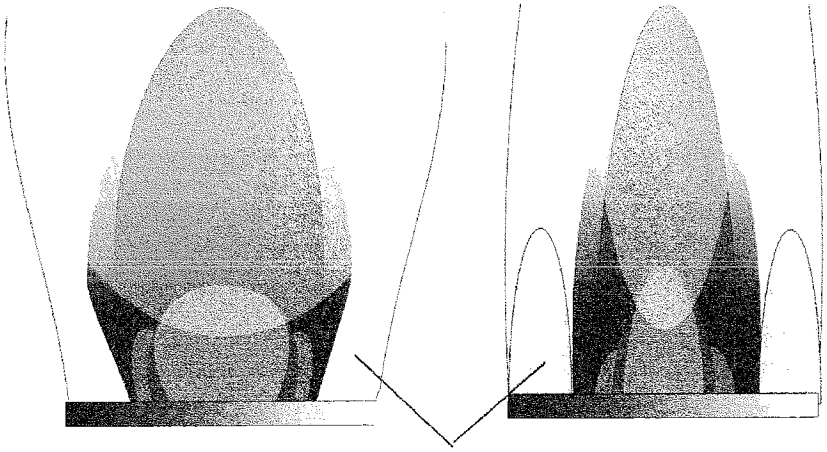

Figure 3.5, Schematic showing theoretical effect of third nitrogen shield

The shield produced from the sixth ring effectively shrouds the flame in nitrogen. The flow of nitrogen minimises the re-circulation of particles back into the flame, thereby reducing particle size variation that would result from multiple passes through the reaction zone, see figure 3.5. High flow rate through the sixth ring produces a tightly confined flame and particle stream. The ability to influence the particle stream velocity and cross-section is

important in controlling the deposition dynamics and the particle-particle reactions prior to deposition. The temperature of the particle stream will also be affected by the nitrogen flow through the sixth ring. The outer shield flow rate must therefore be tailored so that suitable confinement of the particle stream results, but its effect upon particle stream temperature must also be taken into consideration. It should be noted that the total amount of nitrogen used in all of the shields has a considerable affect upon the flame temperature.

The flame temperature is also directly dependent upon the hydrogen to oxygen ratio, as previously explained in Chapter 2. It is normal practice for the flame to be run oxygen rich, to ensure that there is sufficient oxygen present to result in soot formation. Excess oxygen within the flame also ensures that the flame dynamics are easily controllable. If insufficient oxygen is present within the flame gases then atmospheric oxygen will be scavenged, which may result in flame flicker and excessively large afterburning zones.

3.1.2 Substrate configuration

The burner is aligned vertically with the substrate inverted above it, the majority of FHD systems use alignments similar to figure 3.6a. The vertical alignment of the burner means that convectional effects do not distort the flame or resulting particle stream as showing in figure 3.6b. If the burner were to be inclined at an angle, the flame-front and resulting reagent reaction zone would deviate from the symmetry of the burner. The large range of gas densities present within the flame could result in considerable deviation from the expected structure. Any affect upon relative gas flow velocities would have a significant effect upon particle production and transport. Distortion of the reaction zone may result in particles being produced at considerably different points within the flame, this would be likely to increase in the particle size distribution for a given set of flame parameters. The transport of particles from the reaction zone to the substrate within the particle stream is

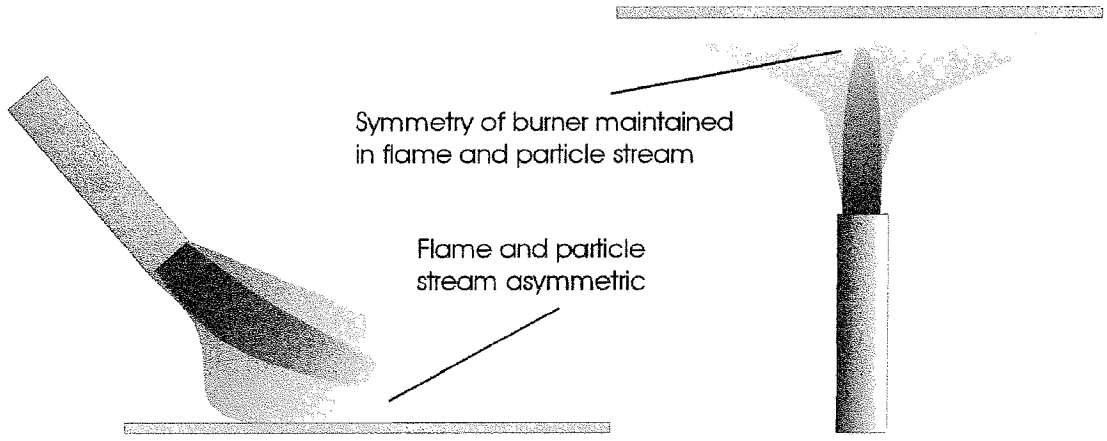

Figure 3.6, a) conventional FHD burner alignment, b) symmetrical burner alignment

also likely to be affected by any deviation from vertical alignment of the burner. Smaller particles are more likely to be affected by thermal currents within the flame, therefore rising within the particle stream. Larger particle are more likely to be directly affected by gravity, therefore falling within the particle stream. Particles stream deviation from vertical alignment is likely to result in a degree of particle size sorting. Transferral of this spatial variation in particle size to the deposited soot is likely to cause non-uniform consolidation characteristics.

The perpendicular alignment of the substrate relative to the burner also has an effect upon the deposition characteristics. In particular, the maintenance of particle stream symmetry thus leading to a homogenous layers both compositionally and with respect to particle size. Any deviation from perpendicular alignment may result in a degree of directionality within the deposited soot layer. If the particle stream were to be incident on the substrate at an angle, particle movement across the substrate surface could occur. If particle adhesion varies with particle size, a degree of particle size distribution across the deposition area could result due to weakly bound particles being blow across the substrate prior to deposition. In general it is expected that a higher deposition rate will be achieved with perpendicular alignment since maximum decrease in particle stream and exhaust gas momentum occurs. The occurrence of soot being blown off the substrate by exhaust gases should therefore be minimised, and resulting in a homogenous and uniform soot layer.

The inverted nature of the substrate has several advantages, in particular the inherent maintenance of cleanliness. Only particles that have come directly from the particle stream will be deposited. Secondary particles occurring due to soot delamination from surfaces within the deposition rig will not fall onto the substrate. Minimisation of contamination from other sources such as atmospheric dust during sample loading and unloading also helps maintain sample cleanliness.

3.1.3 Sample heater

The need to heat the sample during deposition required the development of heaters with a specific set of requirements. The temperature range within which deposition can take place is of importance. Temperatures of 400-600°C are of significant interest for two reasons that have been previously discussed in detail in Chapter 2. The first reason is that the temperature at which maximum deposition rate occurs is ~600°C. The second reason is that the transition temperature between depositing crystalline and amorphous Germania lies

within the range 400-600°C. The highest temperature envisaged to be used is therefore 600°C. The lower end of the temperature range that the heater must operate within concerns the presence of large amounts of water during the deposition process. In order to make sure that liquid water does not become included within the soot layer a temperature greater that 100°C must be maintained. The highly hygroscopic nature of silica soot suggests that once water is present it may considerably alter the character of the soot, such that upon dehydration the structure becomes altered. It is thus necessary to be careful that liquid water does not come into close proximity with soot layers during deposition. This is achieved through heating the substrate to a temperature above 100°C such that the atmosphere around the soot is also above 100°C. The criterion for minimum heater operating temperature during deposition has therefore been set at ~200°C.

The uniformity of the heater and the resulting thermal uniformity of the substrate surface directly affects the uniformity of the soot deposited. As mentioned in Chapter 2 the primary soot deposition mechanism that results in soot-substrate adhesion is thermophoretic. The rate of soot deposition is directly dependent upon the temperature of the substrate. Any thermal gradient across the substrate will result in a variation in deposition rate. During the process of soot deposition, soot thickness variation will mirror thermal non-uniformity. In order to maximise the thickness uniformity of deposited soot layers it is necessary to have a heater that is as spatially uniform as possible across the scale of a substrate.

The dependence of soot thickness uniformity upon thermal uniformity extends to the influence of the flame upon the substrate temperature. It is important that when the flame is traversed under the substrate it has a consistent effect upon the temperature observed by the soot being deposited. There must be minimal net change in the substrate temperature due to flame heating or heater temperature variation as the deposition takes place.

The inverted nature of the substrates introduces a need for secure fastening of the substrates to the heater plate. It is important that a continuous soot layer is deposited across the substrate, since a break in the soot layer results in problems during the consolidation process. It was therefore necessary to hold the substrates without touching the deposition surface. The application of a vacuum to a port in the heater plate behind the substrate was found to be the most suitable method of holding substrates. Any heater design must therefore include suitable vacuum ports for holding the variety of substrates that were to be

deposited on. It is important that the vacuum ports do not have a significant effect upon the thermal uniformity of the substrate surface for the same reasons as previously outlined.

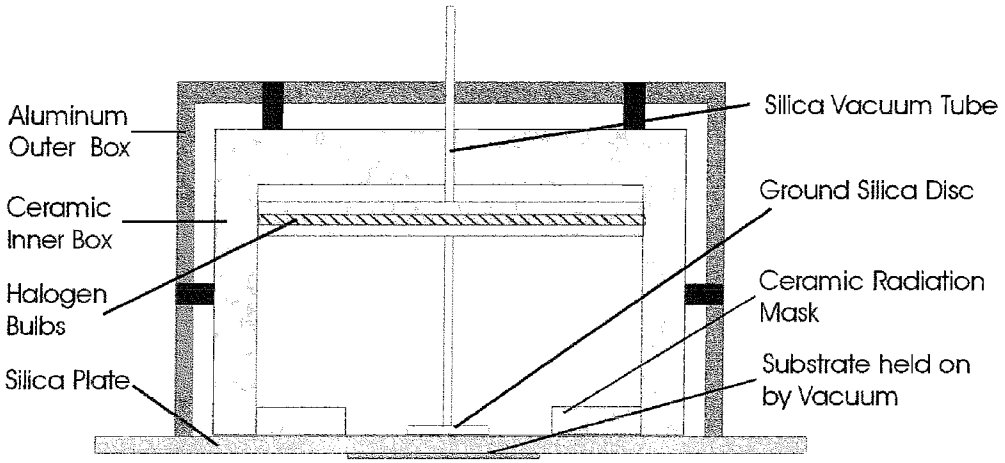

Figure 3.7, Radiative substrate heater

The first heater designed for substrate heating during deposition worked on the principle of direct radiative heating of the substrate, a schematic of which is shown in figure 3.7. The heating power was supplied using three 1kW halogen bulbs housed within a box fabricated from Duratec™ (a pressed ceramic insulating board which is machinable). The Duratec box was then hung from an Aluminium box with a suitable air gap between inner and outer boxes. Forced air-cooling of the outer box and the use of heat sinks in addition to forced circulation within the air gap, ensured that the outer Aluminium box maintained a suitably low temperature. It was important to minimise the temperature of the outer box so that the electrical connections to the bulbs would not over heat and the Aluminium support structure would maintain its integrity. It was necessary to cut a hole in the underside of the Duratec box such that illumination is masked and is only incident upon the back of the substrate. Radiative heating takes place through the mask and through a fused silica window onto the underside of which the substrate is held using a vacuum. Vacuum is supplied to a port in the silica window using a silica tube that passes through the Duratec box. A vacuum seal is achieved between a ground disc attached to the end of the tube and the surface of the plate. Deposition thus takes place across the total surface of the silica plate. A K-type thermocouple is mounted through the silica window such that the junction touches the back surface of the substrate, allowing the degree of heating to be determined.

Some of the advantages of such a radiative system include the short time taken for the substrate to reach and cool down from the required deposition temperature. This is due to the low thermal mass of the heating system, the substrate is the only component where

deposition temperature is achived. The majority of the radiative energy produced by the bulbs is coupled in to the back of the substrate either directly or due to reflections from the inside of the white Duratec box. Any convection or conduction that does occur still results in heating of the substrate since it is the least insulated route for heat flow out of the system. The relatively direct nature of the energy transfer between source and substrate results in minimal heating of the support structure relative to the substrate temperature. It is therefore possible to achieve the high temperatures required with comparatively low power consumption.

The primarily radiative nature of the heating allows easy access to the back of the substrate. Direct measurement of substrate temperature is possible through simple introduction of a fine gauge thermocouple. The determination of substrate temperature has very little effect upon the heating of the substrate. The ability to directly determine the deposition temperature during processing is of great use in characterising and optimising the deposition mechanism.

Although there are obvious advantages to the radiative heating technique outlined previously, there are also some unfortunate disadvantages;

- The power control of the system has been purely within the constant power regime, since halogen bulbs are not suitable for binary switching of power and analogue power controllers are prohibitively expensive.
- Active power controlling would require a feedback loop in order to calculate the heating power required to achieve a given temperature and the substrate is the only place that absolute temperature is achieved, which is directly affected by the translation of the flame during the deposition process.
- The direct power coupling between bulbs and substrate transfers any non-uniformity from bulb directly to the substrate.
- The low thermal mass of the heated body leads to translation of the flame having a large effect upon the temperature of the substrate.
- Any power fluctuations within the system are directly transferred to the substrate is a very short length of time.
- The overall thermal stability of the heating system is dependent upon the thermal mass of the substrate, which will not be constant for different sizes and types of substrates.

- The nature of the heating process limits substrate materials to those that adsorb the output of the halogen bulbs.

An alternative heater used for substrate heating during depositions employs a resistive heating element and conductive heat transfer to the substrate, a schematic of which is shown in figure 3.8. The element used within the heater is Thermocoax™, a high temperature resistive heating element surrounded by alumina/silica spacers and sheathed in Inconel alloy. The heated length is five meters and has a total power rating of 3.5kW. The heating element is bent into a uniform zigzag shape approximately 300mm square. The element is then sandwiched between a 10mm thick Duratec plate faced with alumina fibre wool, and a 10mm thick Copper plate backed with a 15mm thick Aluminium plate. The element is held laterally within the sandwich by Macor™ (high precision machinable ceramic) blocks. The primary heater structure, the sandwich, is hung from an air-cooled Aluminium box. Vacuum is supplied via stainless steel pipes that are screwed into the Aluminium deposition plate. The vacuum pipes pass through the heater sandwich and protrude a significant distance out of the top of the Aluminium box, so that thermal conduction to the rest of the vacuum system does not occur. The substrates are therefore held onto the underside of the Aluminium deposition plate, across the entirety of which depositions take place.

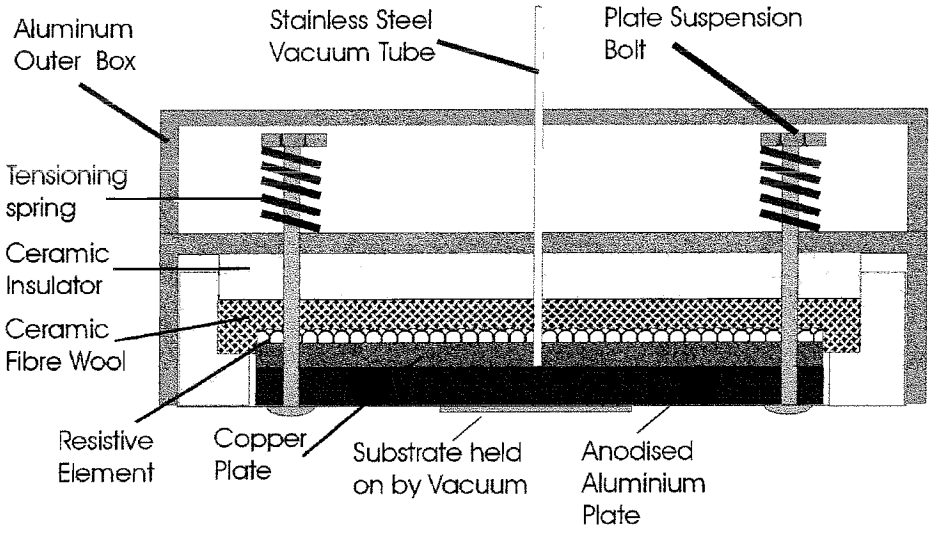

Figure 3.8, Resistive substrate heater

The power of the element is regulated using a digital temperature controller. The feedback for the temperature control is supplied by a stainless steel sheathed K-type thermocouple placed in the heating element void at the centre of the sandwich. The

thermocouple is positioned such that it reads the temperature of the copper plate and not the element directly. The temperature of the deposition plate and substrate is calibrated to the temperature of the Copper plate, allowing measurement of substrate temperature during depositions.

The significant merits of this heating system lie in its inherent high uniformity and stability. The high degree of thermal uniformity experienced by the substrate arises due to the large path length for thermal conduction between the element and the substrate. The fact that there is a significant amount of material with high thermal conductivity leads to little thermal gradient on the deposition plate due to the element pattern. The size of the deposition plate is considerably larger than the substrates, thus the heating of the substrates is effectively two dimension and no edge effects are experienced by the substrates.

The high thermal stability of the heating system arises from the high thermal mass of the heater sandwich. In particular the Copper and Aluminium plates act to average any of the temperature variation due to switching of the element. The heating effect of the flame upon the substrate during deposition is also minimised. The use of active temperature control also greatly aids the thermal stability of the system. If any net increase in deposition plate temperature does occur during deposition the system should automatically compensate by reducing the power supplied to the element. The use of active control also gives much greater resolution in the temperatures that can be applied to the substrates during depositions. Although precise substrate temperature cannot be determined during deposition due to the hostile environment, the temperature is considered to be as observed during calibration.

The disadvantages of the conductive heating system outlined mainly arise due the same characteristics that make it advantageous. The large thermal mass of the system imposes very slow heating and cooling cycles, thereby considerably lengthening the total deposition process. The purely conductive nature of the heating system also imposes a significant set of limitation. The presence of material in between the heat source and substrate limits the maximum temperature, to which the substrate can be heated, to the serviceable temperature of those materials. The direction of heating is also difficult to control, requiring the use of a large amount of insulation in the direction which thermal conduction is not desirable. Limitations upon the amount of insulation and cooling that can be practically used enforce a maximum operating temperature upon the system.

3.1.4 Extract Configuration

The primary deposition extract is designed to be omnidirectional with respect to the burner and deposition zone, and is shown in figure 3.9. The burner extract consists of two borosilicate tubes, with approximately a 10mm difference in radius, mounted concentrically. The height of the inner tube is also approximately 10mm less than the outer tube. The two tubes are mounted on an Aluminium plate with eight extract holes symmetrically arranged between the two tubes. The application of extract to the eight ports results in a reduction in pressure within the void in between the two tubes. Extraction of gases present within the region of the burner and substrate therefore takes place over the lip of the inner tube, down the void in between the tubes and ultimately out of one of the eight extract ports. The small gap between the top of the outer tube and the roof of the deposition chamber ensures that a small but consistent amount of extraction occurs for the rest of the deposition chamber. Minimal leakage of exhaust gases and particulates into the rest of the deposition chamber has therefore been achieved.

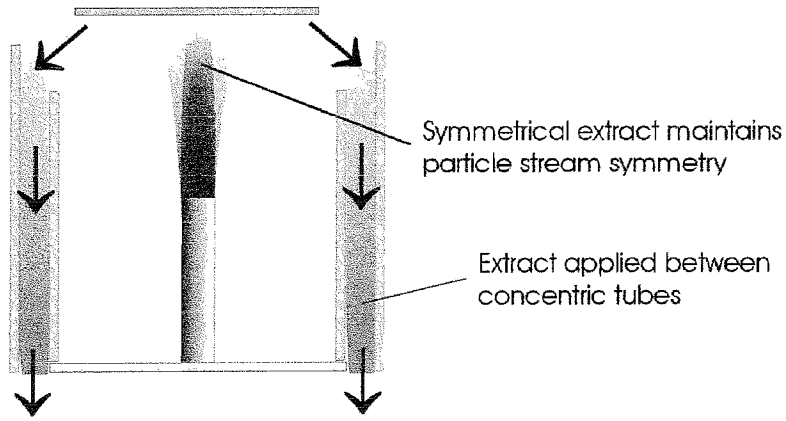

Figure 3.9, Deposition head extract

The extraction system outlined is inherently symmetrical due to the concentricity of the two tubes relative to each other and a constant distance between the extract and the roof of the deposition chamber, therefore maintaining flame and particle stream symmetry. Flexible PTFE tubes are used to supply the extract to the ports, the lengths of which are all similar, thus leading to comparable extract rates. The PTFE tubes are then fed into a larger flexible PVC tube. Assuming that the pressure at the point of connection is constant for all eight tube and the lengths are sufficiently similar, then the extract is found to be symmetrical. The constant position of the extract relative to the deposition zone insures that extract rate and symmetry are stable under all deposition conditions. The inherent stability

of the extract insures that the deposition process always take place under the same conditions.

3.1.5 Burner Translation

The deposition head consisting of the burner and primary deposition extract are mounted on a translation system allowing positioning of the deposition zone onto the deposition plate. The translation system consists of two stepper motor controlled linear stages. A dedicated hardware computer board controls the stepper motors. The linear stages are mounted in an x-y configuration such that the two stages are mounted perpendicular to each other, a schematic showing this can be seen in figure 3.10. The bottom stage is fastened to the FHD rig structure, the top stage is mounted to the linear actuator on the bottom stage and supported at each end by roller bearing that run of tracks formed by the FHD rig structure. The deposition head consisting of burner and primary deposition extract is mounted on the linear actuator of the top stage. The total length of the translation stages are 600mm, however the translation area is limited to approximately 400mm square due to fouling of the extract and associated piping on the FHD structure.

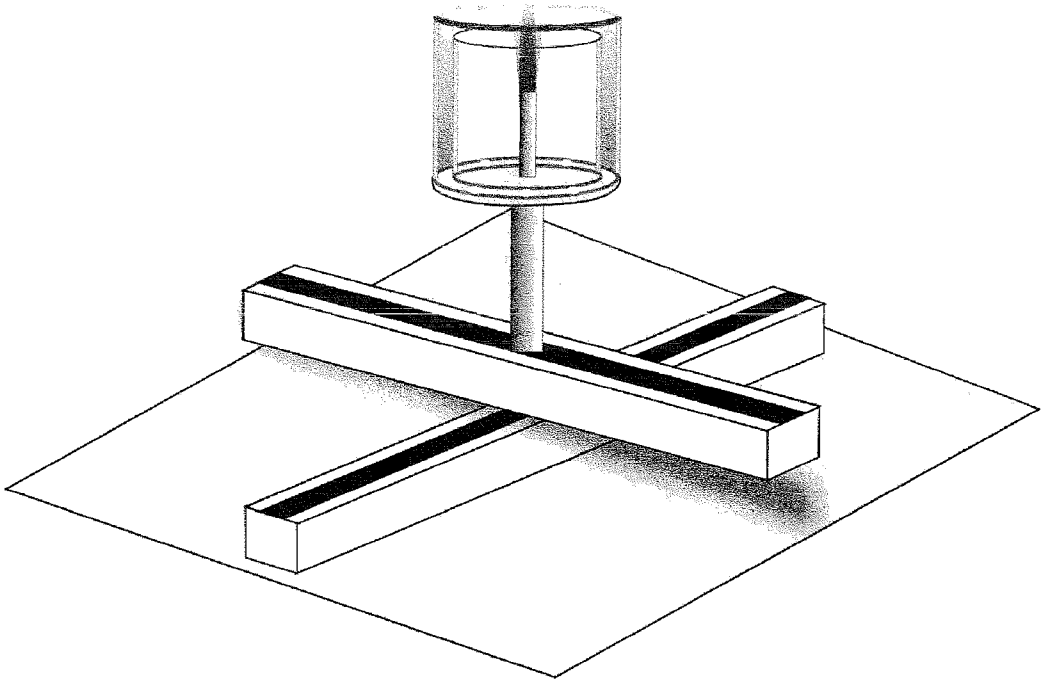

Figure 3.10, x-y translation via perpendicular alignment of linear stages

The maximum speed at which translation can take place is limited by the occurrence of stalling. Stalling occurs due to the increased chance of gear slippage and the reduction of torque associated with high-speed stepper motor operation. The maximum speed achievable

with the use of ramped acceleration is ~25mm per second, without the use of ramped acceleration speed is limited to ~10mm per second. The higher speed translation is only possible under automatic control where the total translation distance is known prior to translation starting. Ramping occurs over a set distance of ~25mm regardless of total translation distance. If the translation system is to be manually controlled, such that the total distance moved it not predetermined, then the maximum speed it limited to ~10mm per second since ramped acceleration cannot be employed.

The translation system gives positioning accuracy with an error of <1% in a single direct with no load and ~2-3% when the system is loaded during standard deposition conditions. The accuracy of the translation system can by compromised if stalling of a stepper motor occurs under excessive loading. Stalling is particularly noticeable at the start of translation and is normally associated with excessively fast translation speeds, but more specifically with the transition from zero to steady rate movement. If stalling occurs positional errors as large as 20% can occur. The minimisation of positional errors due to stalling has required the use of long ramp distances up to maximum translation speed. The use of ramped speeds has resulted in average positional errors of <5%. Positional errors also result from backlash that occurs upon translation direction reversal. The backlash associated with the translation system is fairly consistently ~10mm, but does depend to a degree upon the loading. The effect upon deposition uniformity of the errors outlined so far can be minimised by taking them into consideration during the design of translation patterns that are be used. The errors are only effectively noticeable at the end of the translation distance since steady rate translation occurs, and the majority of error occurrence is at the start of the translation period. Positional errors are allowed for by ensuring that the translation distance is larger than the distance over which uniform deposition is required. It is found that errors in the positive translation direction are matched by errors in the negative translation direction. Although positional errors are commonplace during translation, the total position error after a number of actions is normally insignificant due to positive and negative error cancelling each other.

The complete control of x-y position for the deposition area with a known degree of accuracy has made it possible to construct computer controlled overlapping scan patterns of intricate design. An area of >300mm square can be uniformly deposited upon with a high degree of flexibility using the translation system outlined.

3.1.6 Flame Gas System

The flame gases used at the burner are controlled and metered by a dedicated supply system, schematics and operation procedure of which are included in Appendix 1. The Oxygen and Nitrogen originate from cryogenic liquid boil-off; the hydrogen is sourced in zero-grade bottled form. The gases are supplied to the FHD laboratory via shared service lines, at a pressure greater than 2Bar. The FHD flame gas system is connected to the shared gas lines and a supply at 2Bar is provided using dedicated regulators. The use of independent regulators ensures that the pressure supplied to the FHD rig is constant, regardless of other processes that use the shared gas supply, as long as the service line pressure remains above 2Bar.

Upon entering the FHD rig both Hydrogen and Oxygen lines are fitted with flashback arresters. This avoids the consequences of flame burn-back for the Hydrogen line, or the flame being forced down the Oxygen line. The flashback arrestors are of "single shot" design. The two main active components within the flashback arrestors are a one-way valve and a ceramic flame-stop. The one-way valve makes it impossible for gas to be actively forced the wrong way down the supply line. The ceramic flame-stop is porous in nature thus allowing gas to flow but not allowing a flame front to pass through it, due to the shockwave and rapid increase in pressure associated with a propagating flame front.

The Hydrogen and Oxygen lines are also fitted with solenoid actuated cut-off valves of normally closed configuration. The cut-off valves are controlled using a key switch and emergency stop button circuit. Supply of fuel and oxidiser to the burner cannot take place without direct intervention from the operator. The inclusion of the emergency stop button also allows quick extinction of the flame if required. The normally closed nature of the cut-off valves also insures that the system is failsafe in the event of power failure.

The individual gas flow to each ring of the burner is metered using a dedicated mass flow controller (MFC), specifically calibrated for the gas being used. The advantages of using MFCs include the minimisation of flow rate fluctuation that can occur due to fluctuations in supply line pressure or flame stability. The dynamic nature of the MFC insures that constant flow is supplied to the flame. The MFCs can be operated in manual or computer controlled modes. Manual control is facilitated through potentiometer controlled 0-5V inputs, used to vary flow relatively between zero and maximum for a given MFC. Computer control involves the use of RS232 communication protocol to individually

address each MFC, allowing complex command structures to be issued and data read. The MFCs supply a 0-5V output that represents zero to maximum flow for the given MFC. The output signal is scaled through the use of potential dividers, such that the reading is representative of the flow rate in standard cubic centimetres per minute (sccm), and displayed using digital voltmeters.

The first ring is the only ring of the burner that is not controlled by a flame gas MFC. The reagent and carrier gas that are supplied to the FHD rig can be switched between flowing to the burner and being vented directly to the extract system. The ability to run the flame with or without reagent is of obvious benefit when it comes to lighting and stabilising the flame. Reagent flow switching also allows deposition to be turned on and off without altering the flame conditions. In order to insure that flame gases and moisture are not forced down the first ring, nitrogen purging takes place when reagent is not being supplied. The Nitrogen purge is controlled by a solenoid valve that works in antiphase with the solenoid used to switch reagent between vent or burner. When reagent is being supplied to the burner the purge gas is shutoff, when reagent is not being supplied nitrogen is purged down the burner line and out of the first ring. The flow rate of the purge gas is controlled using a simple rotameter since absolute flow rate is not of importance. The use of a permanent purge has several advantages. Minimal moisture ingression into the reagent line minimises the chance of reaction prior to exiting the burner. The burner can also be purged while reagent is still supplied to the FHD rig thus allowing mid-process cleaning of the deposition head with minimum time require for burner purging upon ceasing deposition.

3.1.7 Sliding Seal

The deposition chamber and the main body of the FHD rig are separated using a "sliding seal". Separation is necessary due to the incompatibility of many of the components required for the operation of the FHD rig, to the high temperatures and corrosive gases which occur during the deposition process. The translation system and the flexible pipe used to supply flame gases and extract to the deposition head are all susceptible to damage from high temperatures or corrosive gases. Limitation to the deposition chamber of the particulate contamination that occurs during deposition is also preferable. The general longevity of components and operating safety can be assured through application of the sliding seal to contain exhaust gases, particulates and high temperatures within the deposition chamber.

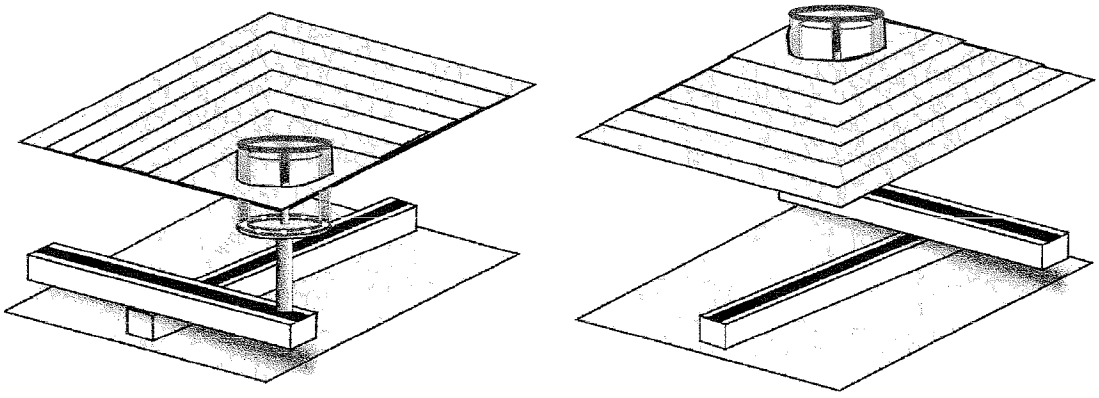

Figure 3.11, Formation of a sliding seal through stacking concentric plates

The sliding seal consists of a number of square Aluminium hoops of increasing size, mounted concentrically with the largest plate held by the FHD rig frame and the smallest held by the burner extract, thus forming a flexible floor to the deposition chamber shown in figure 3.11. Initially the sliding seal relied on the natural low friction nature of the Aluminium plates resting on top of each other. However, high temperatures and the introduction of particulate contamination resulted in excessive loading of the translation system due to increased sliding seal friction. The addition of PTFE feet for each plate significantly reduced the friction, but decreased the degree of separation between deposition chamber and the rest of the FHD rig internal systems. The integrity of the deposition chamber and translation chamber separation is therefore maintained through careful tailoring of pressure and extract rates.

The extraction of the deposition chamber takes place from a single point at the rear of the deposition chamber and is designed to be the secondary deposition extract shown in figure 3.12. The primary and secondary extract routes are common prior to routing through the scrubber. The sum of the primary and secondary extract rates is always constant. The blocking of the primary extract due to excessive soot production does not result in zero extraction. The secondary extract is capable of complete exhaust gas extraction. As the primary extract becomes compromised, the relative extraction rate from the secondary extract is increased. The pressure due to the secondary extract, and therefore the pressure in the deposition chamber, is higher than that of the deposition head. The direction of flow is from the chamber into the primary extract, insuring that during normal operation all exhaust gases and soot particles are extracted via the primary extract. The secondary extract is purely a backup designed to extract the deposition chamber if the primary extract is not 100% efficient. Extraction via the secondary extract during processing is not desirable,

since soot deposition on chamber walls takes place and resulting sample soot layer may be of dubious quality.

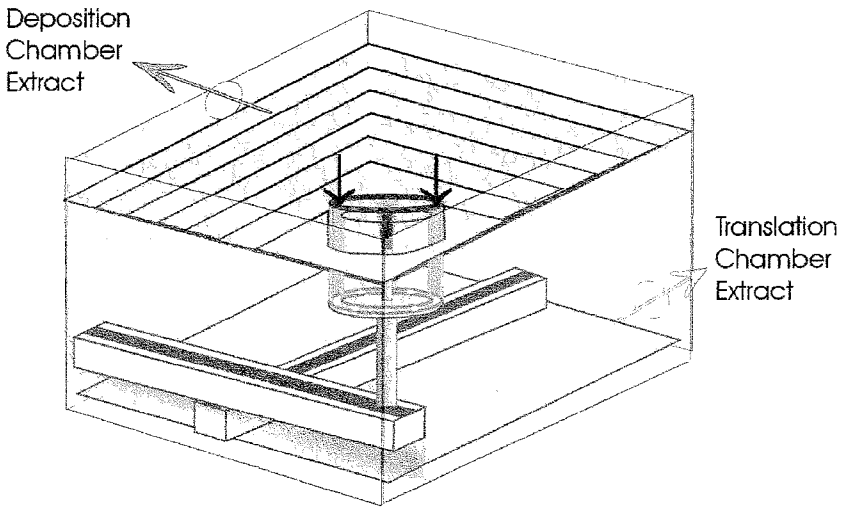

Figure 3.12, Deposition head, deposition chamber and translation chamber extract routes

The translation chamber is purged with dry Nitrogen and extracted to a non-scrubbed extract. The Nitrogen purge ensures that in the unlikely even of reagent leakage within the translation chamber, minimum reaction will occur or at least the reaction ferocity will be minimised due to the low moisture levels. The purging of the translation chamber also prevents corrosion of the sensitive FHD rig components. The translation chamber is extracted from a single point opposite the point of nitrogen purge introduction. The extract rate is tailored so that the translation chamber has a higher pressure than the deposition chamber. This means that under normal operating conditions gas flow is from translation to deposition chamber. The leakage of exhaust gases and particulates from the deposition chamber into the translation chamber is therefore minimised to a nominally zero level. Assuming that either primary or secondary extracts remain operational it is impossible for exhaust gases to be present in the translation chamber. If however the scrubbed extract that supplied both the primary and secondary extracts were to fail then release of exhaust gases into the laboratory atmosphere does not occur. Extraction of exhaust gases through the translation chamber is not intended to happen during normal operation and is purely a safety feature.

The scrubber extract that supplied both the primary and secondary deposition extraction routes, and the non-scrubbed extract that supplies the translation chamber extraction route are all alarmed independently from the FHD rig. All extract systems within the FHD rig are regularly maintained and monitored to insure the safe and consistent running of the system.

3.1.8 Extract and Scrubber Unit

Extract to the deposition head is supplied via a flexible PVC pipe, so that regardless of translation system position uniform extraction is supplied. Prior to the extract route exiting the FHD rig, the burner vent line used to vent reagent that is being supplied to the rig but not to the burner is teed into the extract. The reagent is introduced into the extract stream using a shielded vent line shown in figure 3.13. A high flow of nitrogen is passed down the shield tube, and has the effect of diluting and increasing the velocity of the reagent gas prior to injection into the extract stream. The use of a shielded vent line minimises moisture ingression into the vent line from the flame exhaust gases present in the extract. The chance of vent line blockage due to the inevitable soot production reaction between exhaust gases and reagent is minimised due to shielding. The gas from the primary extract and the secondary are then combined and routed to the scrubber unit.

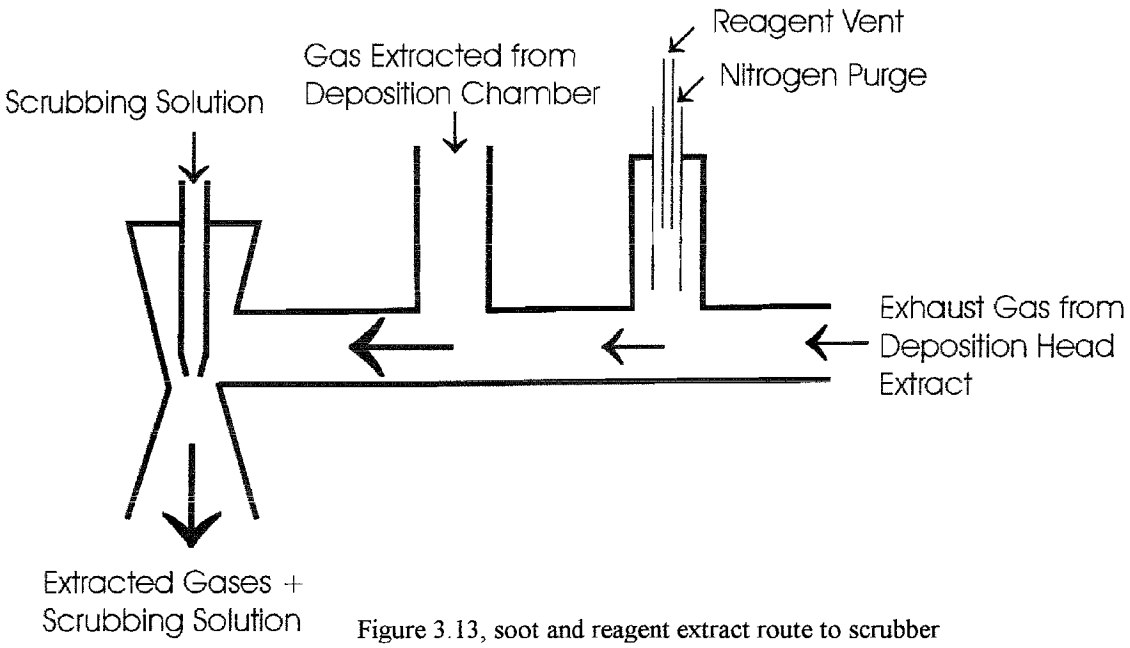

Figure 3.13, soot and reagent extract route to scrubber

The FHD system has its own dedicated scrubbing system situated in close proximity to the FHD rig thereby minimised the length of extract pipe which can become clogged by soot, a schematic of which can be seen in figure 3.14. The scrubber was introduced in order to minimise the affect of pressure fluctuation within the service extract upon the FHD process. The scrubber system consists of a liquid driven venturi, a scrubbing solution reservoir and a pumping system. The gases extracted from the FHD rig are drawn into the venturi by the low pressure induced in the expansion chamber due to the movement of the scrubbing solution. The pressure drop and incidence with the diffuser acts to atomise the

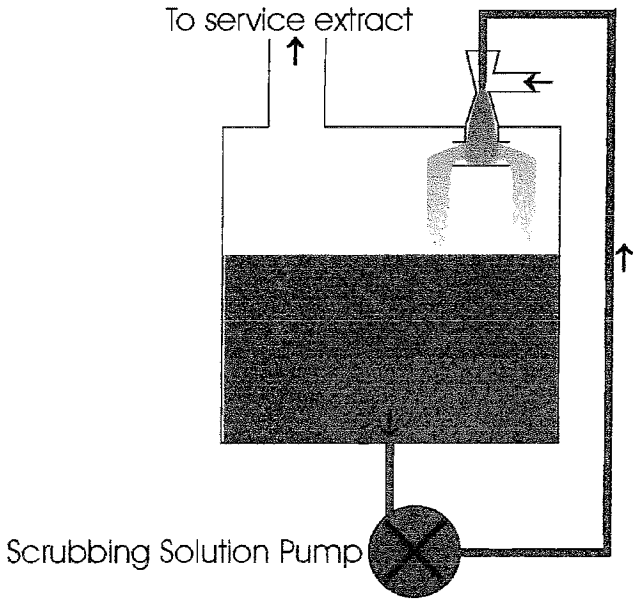

Figure 3.14, FHD scrubber system

scrubbing solution, thereby encouraging intimate contact between scrubbing solution and extracted gases. The scrubber gas above the scrubbing solution is removed to the service extract via a condenser. The building extract insures that the scrubber unit operates at below atmospheric pressure, increasing the extraction rate experienced within the FHD rig.

The scrubbing liquid used is a solution of Sodium Hydroxide with deionised water, and removes Hydrogen chloride via the following reaction;

$$HCl + NaOH \Rightarrow NaCl + H_2O$$

The pH levels within the scrubber are maintained between 4 and 10. This range allows approximately 1-3months of scrubber operation without the need for additional Sodium Hydroxide to be added. The scrubbing solution is initially prepared to a concentration of approximately 0.1M. The scrubber tank is filled using a dedicated pumping system. For complete filling of the system 10 litres of 1M NaOH, produced by dissolving solid NaOH pellets in deionised water, is pumped into the scrubber tank. Filling is completed by topping the tank up to its full capacity, approximately 100 litres, using deionised water. The level and pH of the scrubbing liquid is thoroughly checked on a monthly basis. If the pH level drops below 4 then the system is topped up with additional 1M NaOH solution. The level normally drops due to evaporation during the proceeding month, if the pH is still within limits then topping with DI water takes place. Emptying and refilling of the system takes place every 3-6 months depending upon the number of depositions that have taken place. Complete emptying and flushing of the system is necessary to ensure that the scrubbing liquid does not become overly concentrated and that the system does not clog with soot

particulates. Emptying takes place using a gravity drain system, and the system is flushed using DI water to remove residue.

The use of the scrubber to neutralise the HCl present within the exhaust gas has already been outlined, but it also has several other beneficial functions. The nature of the venturi action and the large free volume above the scrubbing solution in the tank has the effect of smoothing extract rate. Short period pressure fluctuations that occur within the service extract are effectively cushioned, increasing the consistency of the extract rate within the FHD rig and thereby increasing deposition uniformity. The scrubbing action also removes a high percentage of the soot particles present within the extracted gas. This reduces clogging of the service extract down stream from the FHD system. The large thermal mass of the scrubbing solution also acts to significantly cool the exhaust gases. In general the use of a dedicated scrubbing system for the FHD rig greatly simplifies the down stream handling of extracted gases.

3.2 Vapour Production

The production of reagent vapours, the injection of which into the flame results in the formation of soot, takes place within a dedicated vapour production system. The various subsystems that lead to vapour production and subsequent delivery to the FHD rig are outlined in this section.

3.2.1 Bubblers

The bubblers are the point within the vapour production and handling system at which the vapour is actually produced, schematics of the bubbler systems is included in Appendix 1. The bubblers are fabricated from borosilicate glass, and consist of a cylindrical container with gas input and output, a reagent fill port and a submerged thermocouple port. The carrier gas input is directed to the bottom of the bubbler and through a submerged fret. The line pressure forces the carrier gas through the pores in the fret producing bubbles in the liquid reagent held within the bubbler. Saturated vapour is produced in the free volume above the reagent, and the carrier gas laced with vapour exits the bubbler via the gas output. All direct ports into the bubbler can be sealed using PTFE ball valves, the fill port remains sealed except during fill procedures. The valves on the input and output allow the bubbler to be sealed during maintenance operations. All bubblers have a volume of approximately

600ml, but are not filled with more than 500ml of reagent. The primary reagent bubbler has an additional reservoir with a
volume of approximately 1000ml. The reservoir minimises the need for bubbler refilling, but does not actually increase the bubbled volume. The use of the reservoir allows the level within the primary bubbler to be maintained from deposition to deposition, ensuring that vapour production for the primary reagent and therefore the primary constituent in deposited layers remains constant. Each bubbler is individually temperature controlled using silicone embedded resistive heating elements. The temperatures of the heaters are measured using Pt100 resistance thermometers. The feedback provided by the thermometers is used by CAL3300 digital temperature controllers to switch the current being supplied to the heaters. The bubblers and heating jackets are contained within borosilicate beakers producing an approximately 10mm insulation air gap between bubbler and beaker. The beakers are submerged in tanks containing silicon oil, which is maintained at a temperature below that of the lowest bubbler temperature. The silicon oil temperature is maintained using a heat-exchanging loop containing water. The water is circulated and maintained at a temperature of 5°C by an external refrigerating circulator unit.

The large thermal mass of the silicon oil baths induces inherent stability to the reagent temperatures within the bubblers. A relatively low voltage is used to power the bubbler heater jackets thereby also inducing a stable elevated temperature for the reagent. The heater jacket temperature can be maintained to ±0.1-0.2°C as measured by the resistance thermometers. The actually resultant temperature of the reagent is measured using K-type thermocouples place in the submerged ports and shows a temperature stability of ±0.1°C. The reagent temperature is maintained at ~10% below that of the heater jacket due to the cooling nature of the evaporation process used in vapour production.

The use of individually temperature-controlled bubblers has many advantages for the production of reagent vapour. A large range of reagent vapour pressures can be accommodated, allowing maintenance of relative volatility between reagents. The carrier gas flow rates used during vapour production need not be vastly different for reagent with different vapour pressures. Tailoring the temperatures of the bubblers as well as the flow rate of the carrier gas through the bubblers gives a high level of flexibility with respect to the production of vapour.

The primary reagent available are Silicon Tetrachloride ($SiCl_4$), and the secondary reagents are Germanium Tetrachloride ($GeCl_4$), Phosphorous Oxychloride ($POCl_3$) and Tin

Tetrachloride ($SnCl_4$). All bubblers are run with a heater temperature of 19.5°C, this gives relative vapour pressures of $SiCl_4$> $GeCl_4$> $POCl_3$>> $SnCl_4$, which mirrors the relative range of doping levels being investigated. Under the isothermal temperature regime outlined, relative carrier gas flow rate through the bubblers is used to control relative concentrations of vapour stream produced.

The filling procedure for the $SiCl_4$ and $POCl_3$ bubblers involves the use of a pressurised bulk-filling system. Dry Nitrogen is used to drive the reagent from a bulk vessel into bubblers via PTFE fill lines that are attached to the fill valves on top of the bubblers. A two-line construction allows fill line purging prior to and preceding the flow of reagent. The entire bulk-filling equipment and procedure are designed to maintain the low moisture and high purity nature of the reagent. The remaining bubblers are filled with reagent from ampoules. The ampoules are cracked under a dry nitrogen atmosphere and reagent introduced into the bubblers using borosilicate funnels attached to the fill valve.

3.2.2 Gas Supply System

Dry Nitrogen and Dry Oxygen are both available within the carrier gas supply system. Moisture content of ~0.1ppm water is achieved through the use of thermally regenerating molecular sieve columns. Oxygen and Nitrogen are supplied to the system at a pressure of 2Bar through the use of dedicated regulators. Upon introduction into the system Oxygen and Nitrogen are switched by five three-way ball valves, allowing either gas to be separately supplied to all four bubblers and to the dilution line, schematics of the gas supply system are included in Appendix 1. The valves also provide a positive shut off which allows the system to be sealed from input gases.

After the selector valves carrier gas flow is metered using MFCs. Each bubbler line has a separate MFC capable of a maximum flow of 250sccm, and the dilution line has a single MFC capable of 500sccm. The MFCs are completely computer controlled and their operation is fully integrated with the rest of the gas supply system, complete system operation is discussed in detail in a later section.

After the carrier gas has been metered for each line by its respective MFC, routing of the gas through the rest of the system takes place using solenoid actuated PTFE valves, and associated PTFE tube and connectors. For the bubbler lines the first routing choice is either input into the bubbler or to by-pass the bubbler and associated vapour pickup. The bubbler/ bypass routing takes place using two valves, the first switches the incoming gas to

the bubbler input, and the second switches the outgoing gas from the bubbler. The dual operation of the valve set allows the bubbler to be completely sealed when carrier gas is required to bypass the bubbler, thereby facilitating a positive shutoff to vapour production and insuring gas cannot be forced backwards into the bubbler. The bubbler/ bypass valves are operated electronically in series, thus insuring that if one valve fails the remaining one will not switch. The possibility of over pressuring the bubbler by supplying gas to the input while the output is sealed will be avoided. The second routing choice within the gas supply system involves a choice between the vent and supply lines. The vent line routes the gas to the scrubbed extract and the supply line routes the gas FHD rig. The dilution line is not switchable within the gas supply system, and is permanently directed down the supply line. All lines are fitted with pressure relief valves directly after metering, insuring that it is impossible to over pressure the gas supply system to the point at which catastrophic failure of a bubbler or gas line connection occurs. The various switchable gas routes allow a variety of process stages to take place within the gas supply system. The default gas route is for bubblers to be bypassed and the gas to be directed to the vent, resulting in all lines being purged by vapour free carrier gas. Supplying carrier gas to the bubblers and routing the resulting vapour and carrier gas to vent allows the stabilisation of the vapour pickup process, while the supply line is still being purge by vapour free carrier gas from the dilution line. Having the bubblers bubbling and the resulting vapour rich carrier gas routed to the supply line allows mixing of the vapour stream and dilution gas, which is then supplied to the FHD rig. The independent nature of each bubbler gas route allows a free choice with respect to the combinations of the reagents that can be supplied to the FHD rig. It is possible to supply only one reagent to the FHD rig while the other reagent gas lines are simultaneously being purge to the vent by vapour free carrier gas.

3.2.3 Glove Box

All of the valves and associated connections used for gas routing within the gas supply system are housed inside a glove box see figure 3.15. The sealed environment insures that any leakages from the gas supply system do not result in the release of reagents into the lab atmosphere. In the unlikely event of leakage or a gas system pressure relief valve venting, safety of the operator is assured. The use of a glove box also allows gas supply system maintenance and bubbler filling procedures, which may result in the presence

of reagent vapour outside of the gas supply system, to take place remotely from the operator.

The body of the glove box is constructed from fibreglass. A PVC window and fibreglass frame are clamped onto the front of the glovebox. A seal between window and body is achieved using closed pore PVC foam strip, which under pressure produces a completely gas tight seal. The window allows the operator to observe the gas supply system, giving visual information regarding bubbler reagent level and visual checks of approximate carrier gas supply rate to bubblers. The side of the glove box is fitted with a posting port, which is also constructed from fibreglass, sealing from both lab and glove box atmospheres takes place using expanding O-ring bungs. The posting port allows introduction of items into the glove box without directly venting the glove box atmosphere to the lab. The glove box window is fitted with two medium thickness nitrile rubber gloves, which are normally sealed from the glove box atmosphere using expanding O-ring bungs to stop glove pressurisation. The gloves allow the manipulation of items within the glove box such as the actuation of manual valves and the fitting of pipes required during bubbler filling procedures.

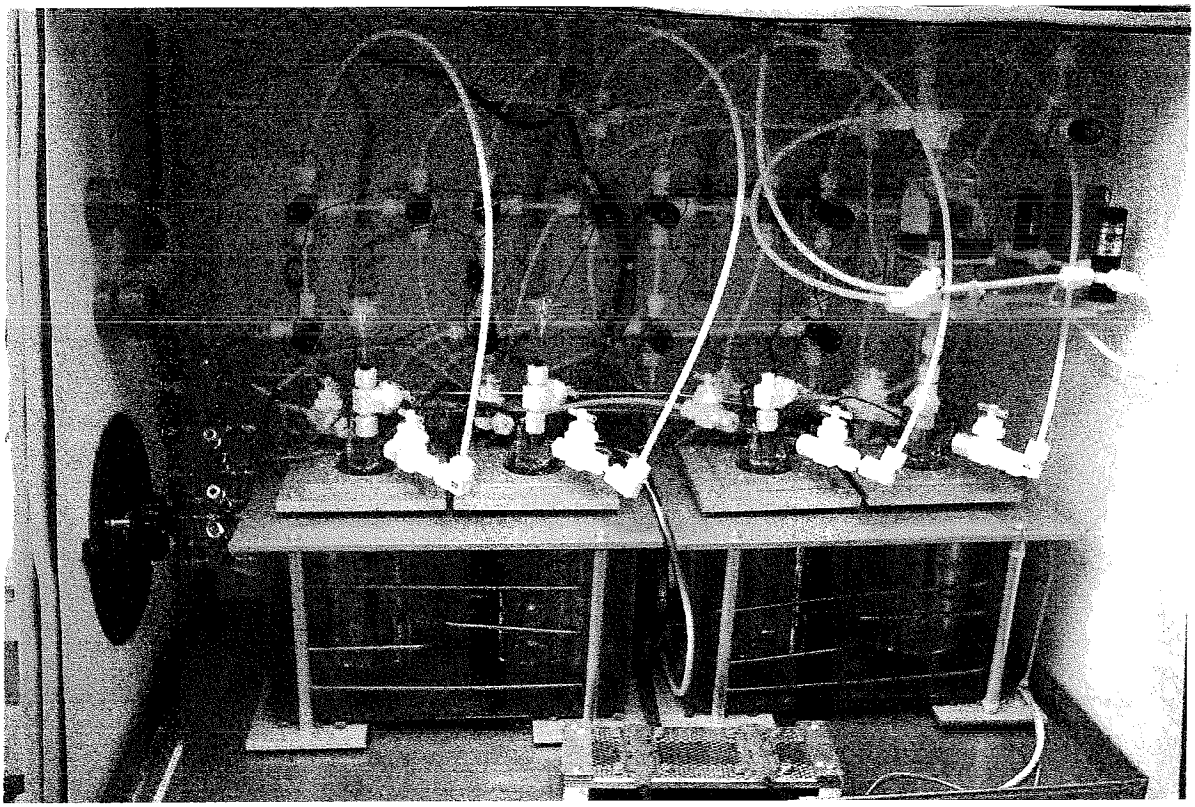

Figure 3.15, Glove box containing bubbler set and gas supply systems

The glove box is permanently purged using dry nitrogen. Controlling the purge flow rate and vent aperture allows a pressure of 5mBar to be maintained within the glove box. The elevated pressure means that the glove box atmosphere is continually purged, thereby extracting any reagent vapours that are present due to leakage or filling procedures. The dry atmosphere and elevated pressure within the glove box also insures minimal moisture ingress through seals or down the glove box vent line. The posting port is also purged with dry nitrogen during the posting process. The small volume of the posting port requires a relatively low flow rate and a finite purging time in order to achieve adequate dryness and cleanliness for posting to take place.

The glove box is fitted with a double redundancy automatic pressure relief system. Firstly a pressure switch controlled solenoid actuated valve allows venting through a permanently purged ½" PTFE pipe. The pressure switch is set to 7mBar, venting takes place at ~8mBar and resealing at ~6mBar. The purge insures that the emergency vent line is dry, and therefore minimises any possible moisture ingression into the glove box when the valve is opened. The second pressure relief valve vents to the lab atmosphere and trips at 3psi. The valve is not connected to the vent since it has been observed that the glove box window lifts off its seal at >20mBar. Secondary relief valve actuation is only expected to occur under very extreme conditions, at which point the operator is likely to be aware of the situation. The primary pressure relief valve can be manually actuated, allowing the pressure within the glove box to be controlled during glove insertion and general posting procedures. A manual ½" non-purged vent line is also included, the use of which is intended to occur if excessive reagent leakage and resulting soot production results in the blockage of the primary relief valve. The actuation of both ½" vent lines allows a considerable increase in the glove box purge rate, in the case of excessive reagent leakage this would be used to rapidly remove reagent vapour and soot from the glove box.

The glove box atmosphere is heated using self-regulating resistive heaters with a maximum operating temperature of ~100°C. A temperature controller using a Pt100 resistance thermometer for feedback regulates the power supplied to the heaters. The heaters are positioned on the plate upon which the gas routing system is mounted. The plate is maintained at an elevated temperature relative to the bubblers. The heating of the valves and pipe work insures that vapour condensation does not occur within the routing system. Heaters are also mounted at the front of the glove box. The combined effect of all the heaters elevates the temperature of the glove box atmosphere. The normal operating

temperature is ~40°C, this further reduces the chance of moisture ingression and condensation in the glove box. Minimisation of moisture is particularly important for the bubbler cooling tanks, which would act as moisture traps due to their low temperature. The combined effect of cooling tanks and plate heaters allows the total control of glove box atmosphere temperature. Normal operation requires that the tank temperatures are suppressed and that the plate temperature is elevated relative to the bubbler temperatures. Glove box drying, which is needed to initially minimise moisture, requires that both tank and plate temperatures are elevated above ambient. During filling minimal reagent volitisation is achieved through cooling the atmosphere by running the tanks at below ambient temperature and not heating the plate.

The supply line that runs from the gas supply system to the FHD rig is shielded, the ¼" PTFE supply line is fed through a 1" PVC tube through which dry nitrogen is flowed. The purged shield line insures that if reagent leakage from the supply line does occur then the vapour is contained and minimal soot production takes place. The supply-line can be heated via heating of the shield line purge gas. Heating is maximised down the length of the line through thermal insulation of the shield line. In the case of bubbler temperatures above ambient temperature supply-line heating is desirable in order to minimise condensation. The shield line purge gas is vented into the translation chamber of the FHD rig and forms the dry nitrogen purge for this chamber. Additional heating of the purge gas within the FHD translation chamber, and associated reduction in supply line condensation, is achieved through the use of a fan heater.

3.2.4 BCl_3 system

The final reagent used in the gas supply system is Boron Trichloride (BCl_3). Unlike the bubbler set-up previously outlined, where carrier gas is required to pick-up and carry vapour from the liquid reagents, the high vapour pressure of BCl_3 at ambient temperature means that it can be treated as a gas in its own right. BCl_3 is supplied in a sealed flask in liquid form, upon opening to ambient pressure BCl_3 gas is evolved with a pressure equal to its equilibrium vapour pressure. The high vapour pressure of BCl_3 allows it to be treated as a gas, and independent carrier gas is not required or transport purposes. However, dry Nitrogen is still required within the system for purge purposes.

The BCl_3 system is purged in much the same way as the bubbler systems, a schematic of which is included in Appendix 1. When BCl_3 is not being supplied and the

flask is sealed, dry Nitrogen is purged through all lines. Purging with dry Nitrogen insures that lines are free from reagent and that minimum moisture ingression occurs, both of which minimise the chance of reactions within the lines. During supply of BCl_3 to the rest of the gas supply system, metering takes place using a dedicated MFC with a maximum flow rate of 20sccm. Purging of the BCl_3 supply line takes place through switching a solenoid actuated two-way valve situated directly after the MFC, acting in much the same way as the bubbler/ bypass arrangement for the bubbler set-up, allowing either vapour production or purge. The BCl_3 supply line is fed into the glove box at which point it is switched between vent/ supply routes using a solenoid actuated valve, again in a analogy to the bubbler set-up.

Operational procedure for the BCl_3 system is similar to those for the bubblers. Filling of lines with reagent and general vapour production stabilisation involves opening the flask and flushing lines through until a saturated vapour is assumed to be present. Line filling for BCl_3 takes considerable longer than for other reagents due to the lower flow rates involved and the long line length. Once the BCl_3 supply line is full and mixing with other reagents and carrier gases has taken place the system is operated as normal. Upon completion of vapour supply, lines must be thoroughly flushed of vapour using dry Nitrogen. Flushing the BCl_3 only section of the system requires that the line running up to the bottle must be cyclically pressurised and depressurised since flow past the end of the bottle is not possible. Lines that cannot be permanently purged with dry nitrogen are sealed while at a pressure of 2Bar, thus minimising the possible moisture ingression.

The BCl_3 system is housed within an extracted enclosure such that only the "single piece" supply line running to the glove box is not enclosed. All valve work and connections within the system are housed within either the extracted enclosure or the glove box. In the case of leakages any reagent will be removed from the immediate atmosphere by the extract.

3.3 Control systems

The control of the FHD rig and vapour supply system required the construction and development of a system centred around a high level of hardware and software integration. A considerable degree of automation has been possible resulting from the inherently integrated nature of the FHD rig and vapour supply system through the control system. This section outlines the design, construction and operation of the various control systems.

3.3.1 Electronic control systems

The gas supply system and the FHD rig are controlled by a custom built electronics system, the construction of which involved the integration of a large number of standard hardware components, A relay board is used to control the position of all of the solenoid-actuated valves used for routing process gases within the gas supply system. The dedicated relay board housed within the electronic control system is linked to a digital input/output board in a PC. The relay board uses opto-isolated relay modules. Output modules are used to switch the circuits controlling the valves. Inputs modules are used to monitor the voltages within the circuits thereby monitoring valve positions.

All of the thermocouples within the system are of K-type and are connected to a thermocouple hardware board. The board measures the voltages across up to sixteen thermocouple junctions and references them to an onboard cold junction. The interpreted temperatures are then supplied to the PC via the parallel port.

The CAL3300 digital temperature controllers used to control bubbler temperatures are located within the electronic control system. Manual control of operating parameters and monitoring is possible through the use of the individual controller fascias. Integration to the PC is via RS232 communication protocol, and allows full remote control of all temperature controller functions.

The stepper motor controller used in the FHD rig translation system is linked to the PC via RS232 connection allowing control of up to three motors (although only two are used in the current set-up). Command lists can therefore be issued from the computer and interpreted by the controller that directly influences the power supplied to the different phases in the motors resulting in translation of the deposition head within the FHD rig.

The electronic control system has a custom designed and built display panel, showing flow rates, temperatures and valve positions within the gas supply system. The flow rates provided by the carrier gas MFCs are displayed using digital voltmeters and suitable potential dividers, thus converting the 0-5V MFC output signals into values representative of the flow rates in sccm. The CAL3300 temperature controllers are mounted on the panel thus giving a direct read out of the bubbler heater jacket temperatures. The circuits used for controlling the solenoid-actuated valves include LED which are mounted on the panel and indicate visually the valve positions. The convention employed places the LEDs on a schematic of the pipe and valve work within the gas supply system. A red LED is used to indicate a valve in its closed position and a green LED indicates a valve in its open position. Manual thermocouple read out is achieved via a separate thermocouple

interpretation unit, mounted on the panel, which runs in parallel to the computer interfaced board. The temperature controller that controls the glove box atmosphere temperature is also mounted on the front panel. The layout of the display panel is intended to represent the physical lay out of the gas supply system, thereby aiding intuitive interpretation of the information displayed relative to the state of the system.

The electronic control subsystem that powers the solenoid-actuated valves within the gas supply system in manually primed via the use of a key switch and emergency stop button circuit. The power to the solenoid circuits is not provided unless the key switch is in the on position and the stop button is reset. When the switching circuit is not powered it is indicated by the non-illumination of the LEDs on the front panel. Such intrusive control of the switching circuit means that vapour production cannot take place under any circumstances within prior intervention by the operator. The fast shut down of vapour production in an emergency is also an advantage of such control.

3.3.2 Software control

The integration of hardware components within the electronic control system, thereby allowing a high level of automation, required the design and coding of a dedicated piece of software. The software was designed to be easy to use and intuitive, thus allowing process parameters to be conveyed quickly to the operator in a way that can be easily interpreted with respect to the parameters effect upon the process. Issuing of commands from the software takes place in a clear unambiguous manner, in which the operator has no doubt as to the effect of the command upon the system. The issuing of multiple commands is simplified through the ability to integrate hardware operation within the software.

The use of Visual Basic™ as a software language and programming environment has allowed the production of a graphical interface. Graphical representation of process steps increases the operator's data interpretation rate and reduces ambiguity. The environment produced allows control of hardware components within the gas supply system and FHD rig to take place in a simple straightforward manner, without the need for intimate knowledge of the individual systems being operated.

The nature of the hardware being controlled required two distinct operating regimes. The software is required to directly control the actions of the hardware during parameter changes, and is also required to continually monitor the system parameters whether commands are being issued or not. Hardware that is controlled by the software falls into two

distinct categories, "dumb" components and "smart" components. "Dumb" components require instruction on a base level, such as switching individual relay positions. The amount of code required for communicating with "dumb" components is minimal, however large amounts of code is required to operate such components in a complex manner. Any computation required for "dumb" component operation must be undertaken within the software by the host computer. "Smart" components require instructions on a higher level, but can undertake computations without the intervention of the host PC. The code regarding communications protocol for smart components can be complex, but the actually issuing of commands within the protocol is relatively simple. The ability to integrate the operation of hardware components from within the software has allowed a number of common processes to be automated. Due to the nature of the gas supply system, such as the relatively constant time required to fill or purge lines, it has been possible to automate such operations. Issuing of a single command from the software results in multiple hardware actuations, flow rates and valve positions are automatically controlled, without the need for further operator intervention. These complex command strings can be further integrated with other operational parameters such as the translation system, thus allowing full automation of the deposition procedure. Non-standard deposition parameters, such as those that vary depending upon desired composition, can be saved and reloaded into the software. The ability to recall previous deposition parameters allows easy repetition of depositions. The deposition parameters are saved as text files, it is therefore possible to write or interpret sets of deposition parameters without access to the dedicated software.

The monitoring of deposition parameters involves the direct display of relevant information to the operator. A large amount of the data taken from the FHD system is not directly relevant to the deposition. If all data were displayed in real-time it would result in undesirable complexity of system monitoring. Data that is not deemed directly relevant to real-time processing is recorded along with the displayed data so that it may be reviewed offline. Log files that are created and written in real-time as the process is carried out are saved as text files. Data is taken and saved so that commands issued and their effect upon the system is recorded against a common time base. The flexibility of data in text format allows it to be interpreted in a number of ways. Plotting process parameters graphically against the common time base allows easy characterisation and optimisation of the FHD process. Detailed log files are of particular use when it comes to trouble shooting, and greatly eases the process of erroneous result explanation.

3.4 FHD System Operational Safety

During all stages of equipment development, the nature of the reagents and the system as a whole has required that safety be continually considered. The high level of automation present within the system has allowed a degree of automatic failsafe operation that does not require operator input. However, automation has also dictated that conditions leading to control system failure also be considered in detail. This section treats the inherent dangers associated with various aspects of the system and its operation, and illustrates the systems and procedures that have been implemented in order to achieve a maximum level of safety.

3.4.1 Gas Supply System Safety

The gas supply system has been designed and constructed to be inherently safe, the inclusion of several features within the system insure that a satisfactory level of safety is achieved. The bypass/ bubbler double valve system previously outlined ensures that it is impossible to supply gas into a bubbler without the output being open. Only the advent of a physical blockage would result in gas being inadvertently routed without the operator's knowledge.

The default positions for all gas routing valves is to by-pass the bubblers and vent the gas present within the system. The occurrence of a power failure results in the halt of vapour production and dry gas purging of all lines. The system is designed to be failsafe due to reversion to the standby condition upon power failure. The standby condition for the gas supply system involves continual purging of all lines to vent, other than those that are sealed internally. Continual purging insures that all lines remain clean and moisture-free when vapour production is not in progress.

The inclusion of pressure relief valves within the gas supply system insures that it is impossible for catastrophic failure to occur due to blockage induced over-pressuring. The location of the pressure relief valves insure that if a blockage does occur then carrier gas is vented prior to vapour production. The pressure relief valves are situated so as to vent in a controlled manner into an extracted volume, and therefore impossible for reagent to leak into the lab atmosphere due to relief valve actuation.

If a blockage occurs within the gas supply system that results in gas being forced backwards, the MFCs will crash if negative flow occurs. An MFC crash during vapour

production results in the system reverting to a failsafe condition. The likelihood of MFC crashes due to negative flow is minimal since relief valve failure must simulatiously occur with gas pressure failure, since a pressure greater than that supplied by the regulator must occur.

3.4.2 Glove Box Safety

The entire gas supply systems valve work is enclosed within the glove box. The double skinned nature of the system ensures that even a primary gas system failure, such as a leaking joint or relief valve actuation, does not result in reagent being vented to atmosphere. The leaked reagent remains contained and the fault can be dealt within an enclosed environment with minimal risk to the operator.

The glove box has been designed with triple redundancy vent lines, one which is in continual use, one which actuates automatically upon pressure rise, and one which must be manually operated. The chance of a glove box breach due to catastrophic over pressuring as a result of reagent leakage and vent line blockage due to soot production is minimal. The numerous systems present within the glove box to ensure that the atmosphere has a minimum moisture content insure that if reagent does become present within the glove box it will remain in vapour form and will not react to form soot.

3.4.3 Computer Control Safety

The computer control of the system introduces a number of risks. The possibility of spurious commands due to a software crash may result in an unsafe state. A general PC crash may result in the system being locked into its current state until the software can be brought back online. The chance of an unsafe system state due to control software or hardware crashes has been dealt with through the development of a "crash protection system". As has previously been mentioned the valve system requires activation from a key switch, this controls a relay, which in turn powers the valve circuit. The controlling relay is not only dependent upon the key switch and emergency stop, but also on a timer relay. The timer relay must receive a signal every five seconds from the software in order to remain active. The software must therefore be running in a stable state for the valve circuit to be powered. If the system crashes than the relay is opened and the gas supply system reverts to a failsafe condition. The activation of the crash protection system is accompanied by an audible alarm to alert to operator to the crash. There are three possible routes to actively

reverting the system to its failsafe state; firstly the crash protection system outline, secondly the emergency stop button, and finally the software process stop button which issues a command set that reverts the system to its failsafe state.

3.4.4 Flame Gas Safety

There are a number of complementary safety systems built into the flame gas system with the aim of maximising safe operation. The provision of automatic and operator influenced safety measures further increases the safe nature of the system. The flashback arrestors ensure that any possible occurrence of burn-back or blow-back will not result in flame propagation down the supply lines and the associated consequences. Both Oxygen and Hydrogen lines are switched using solenoid-actuated stop-valves, the use of which insure lines remain sealed during system stand-by and facilitate quick flame shut off during processing via an emergency stop button arrangement. The use of a Nitrogen shielded burner also imparts an inherent degree of safety. If flame extinction occurs it has been found impossible to relight the flame without first ceasing nitrogen supply to the burner. It is however possible that a flammable gas mix may result as some point within the extract system if the flame goes out, it is therefore necessary for an operator to always be present when the flame is in use. Continual visual checks of the flame condition take place so that flame gas shut off occurs in the unlikely even of the flame blowing out. It should however be emphasised that the chances of explosion due to unexpected flame extinction are minimal.

3.5 Advantages of Self Built System

Through in-house design and development of the system outlined, it has been possible to produce equipment that has a considerable degree of flexibility. As many parameters as possible that have a direct effect upon the FHD process can be modified. The use of alternative reagents in liquid or gases form, other than those outlined, would be relatively straightforward.

The advantages of intimate knowledge of the construction and internal working of the system cannot be over emphasised. The increased ease of trouble shooting and inherent knowledge of the FHD process has been invaluable with regards to process development and optimisation. The system was envisaged to be continually developed and therefore the construction of the system is conducive to future modification with the minimum of

alteration to the existing systems. The cost of developing for such a flexibly piece of research equipment both temporally and financially, has been considerable reduced through in-house design and construction compared to that if work has been outsourced.

3.6 Consolidation Furnaces

The thermal processing required for the densification of FHD soot layers via the sintering mechanism has been achieved using a variety of furnaces. The large range of soot layers that can be produced have a correspondingly wide range of consolidation parameters, not all of which can be achieved using a single furnaces. It has therefore been necessary to use a number of furnaces in order to achieve thermal regimes that allow full investigation of the consolidation process. This section describes the furnaces that have been employed and the thermal regimes that they offer.

3.6.1 Soot Storage Oven

In the event that samples are not consolidated directly after the deposition process, they are stored prior to subsequent consolidation. Samples are placed within petridishes in order to minimise particulate contamination of the soot layers. The storage oven has a maximum temperature of 200°C and is operated at this temperature. The fan-assisted nature of the oven insures isothermal conditions for all samples regardless of position. The oven allows simultaneous storage of up to 6 full 100mm wafers at any one time, although less are normally stored due to the maximum deposition capacity of the FHD system being 4 full wafers.

The samples are stored within the oven due to the highly hygroscopic nature of silica soot. It has been discovered experimentally that unconsolidated samples stored at ambient temperature do not consolidate consistently. This is assumed to be due to moisture adsorption within the soot, the minimisation of moisture incorporation through storage at elevated temperatures results in greater consolidation consistency. Any samples not consolidated immediately upon removal from the deposition plate are routinely stored at 200°C. Although consolidation does not take place within this oven, its use is of paramount importance to the subsequent consolidation of stored samples.

3.6.2 Elite Furnace

The Elite furnace is a lift-fronted furnace, heated by 6 silicon carbide resistive heating elements with a combined heating power of 16.6kW. The maximum sustainable temperature for the furnace is 1600°C, with an absolute maximum temperature of 1700°C however stability at this temperature is not specified. The maximum heating ramp rate is ~30°C per minute although a more stable rate can be achieved for 20°C per minute. The heating ramp rate is limited by the power supplied from the elements and can be dependent upon starting and target temperature. The maximum cooling rate is highly dependent upon the temperature range being cooled through. Cooling at greater that 500°C can be achieved at rates of 10-20°C, at temperatures below 500°C achievable cooling rate steadily slows and final cooling from 200°C to ambient can take hours. Cooling rates of 100-200°C can be achieved by opening the front of the furnace, however cooling from high temperatures using this method cannot take place for extended periods of time due to over heating of external furnace components. The ability to open the furnace while at elevated temperature allows for extreme sample ramp rates to be achieved through direct sample insertion and removal. Depending upon the thermal mass of the sample and associated elements, ramp rates of greater than 100°C per second can be achieved for both heating and cooling.

Temperature stability of the furnace is normally maintained to within $<\pm 0.5$°C by the temperature controller. The thermal uniformity within the furnace is specified by the manufacturer to be nominally isothermal. Independent verification of the thermal uniformity within the sample zone proved to be greater than the 1°C resolution of the measurement system used at a temperature of 1400°C. The uniformity and stability of the furnace are greatly affected by the sample insertion and removal processes. Practiced sample insertion results in the core temperature dropping by 20-30°C from the target temperature. After the furnace is closed the temperature overshoots by less that 2°C within 30 seconds and reverts back to the set temperature within 5 minute.

The furnace is insulated using low-density fire brick, which has proved to be a major source of particulate contamination for samples during consolidation. A silicon carbide liner has been employed to minimise contamination, although the open fronted nature of the liner still allows a degree of contamination to occur. The furnace is regularly cleaned in order to minimise the amount of loose particulates present. Care must also be taken when opening and closing the furnace in order to minimise the production and circulation of particles within the furnace.

The furnace has a volume of approximately 300x200mm, however the silicon carbide liner reduces this to approximately 200x120x120mm. The consolidation of full 100mm wafers is possible, although simultaneous consolidation of multiple full samples is not possible.

3.6.3 Other Available Furnaces suitable for consolidation

Thermal regimes other than those previously mentioned have been achieved using a number of additional furnaces. The Lenton tube furnace has a maximum operating temperature of 1700°C. The tube is constructed from alumina, which due to its poor thermal shock resistance requires careful profiling of temperature along its length. The furnace has three heated zones; a central working zone and two outer zones which act to smooth the temperature gradient along the tube. The remaining temperature profiling along the tube is achieved through the use of variable insulation. The thermal sensitivity of the tube dictates that furnace temperature ramping is not achievable on a time scale shorted than hours. Any ramp rates that are required for sample processing must be achieved through sample insertion and removal. Entrance to the hot zone is approximately 1 metre into the tube, ramp rates are therefore limited by the rate at which samples can be inserted and removed for the tube. Ramp rates of greater than 50°C per seconds are estimated to be achievable, although care must be taken not to thermally shock the tube due to heat transfer from sample and carrier. The tube has a diameter of 100mm and an isothermal hot zone of approximately 150mm in length. It has been found difficult to process samples larger than $50mm^2$ within the Lenton furnace. A sample degree of tube degradation can result in minor particulate contamination of samples, however the Lenton furnace is inherently cleaner than the Elite furnace.

The GEC furnace is another tube furnace, but its maximum operating temperature is limited to 1200°C due to its silica tube. The lifetime of the tube would be seriously reduced if operation at above 1200°C takes place, for significant lengths of time result, due to tube crystallisation. The silica tube does however have very high thermal shock resistance making it possible to very quickly insert and remove samples from the hot zone without fear of damaging the tube. The tube has a diameter of 75mm and an isothermal hot zone of approximately 50mm, greatly limiting sample sizes that can be processed.

The low temperature elevating hearth furnace has maximum operating temperature of 1200°C imposed by its silica liner, although actual maximum temperature is 1400°C. The

hearth has a diameter of 100mm and heating of the hearth is assumed to be relatively isothermal. Although when the hearth is actuated the sample is directly removed or inserted from the hot zone, the large thermal mass of the hearth limits the ramp rates that are achievable. Ramp rates are likely to be slower than those achievable using the Elite furnace due to the indirect access to the hot zone.

The high temperature elevating hearth furnace for all intents and purposes is operationally the same as the low temperature elevating hearth furnace but has a maximum temperature of 1700°C. The ramp rates are still limited by the indirect insertion and removal of sample from the hot zone and the large thermal mass of the hearth.

The diversity of the furnaces that have been available during the investigation of the consolidation process, has allowed a large range of thermal processing regimes to be used. Standard processing and development work has subsequently mainly taken place using the Elite furnace due to its high degree of flexibility.

3.7 Conclusion

This chapter has highlighted the highly complex nature of the systems that have been developed and employed in the investigation of the FHD process and related fabrication procedures. The FHD rig and reagent supply systems in particular represent equipment that is continually developing as additional feedback is gained from the increasing numbers of samples that are produced. The systems have been designed to be as flexible as possible and encompass as many possible future directions as is practical. One of the inherent advantages of the FHD process is it flexibility with respect to the inclusion of novel dopants, with this in mind the vapour supply system is designed to be conducive to future development. It is also envisaged that the FHD rig will see future development in the pursuit of ever better layer uniformity and flexibility of deposition parameters. The system as highlighted within this section is therefore a snapshot of the current system that has been used to produce the layers discussed in latter chapters.

4 Characterisation of FHD and consolidation, processes and optimisation

The continual development and optimisation of the FHD process and equipment with the ultimate aim of producing FHD layers suitable for UV direct writing, involved a considerable amount of feedback with respect to process parameters and resultant affect upon layer properties. This chapter highlights the experimental work undertaken that led to the development of the equipment discussed in chapter 3, but also outlines the intricacies of the FHD process that must be mastered if layer properties are to manipulated in the required manner.

The complex nature of the FHD process and in particular its reliance upon three sequential stages (vapour production, soot production, and soot consolidation) has led to a huge number of samples being produced during the characterisation and optimisation of the FHD process. A particular difficulty arises from the fragile nature of the as deposited soot, imposing the need to consolidate layers prior to full characterisation, thus leading to trouble determining at what processing stage various mechanisms have occurred. During the characterisation of the FHD process, over two hundred samples have been produced investigating areas a diverse as flame dynamics to silicate crystallisation. The driving force behind the work embarked upon has always been the optimisation of the FHD process to produced silicate planar waveguiding structures, thus leading to a problem-solving approach that often did not allow the luxury of time to investigate scientifically, all of the phenomena that occured.

4.1 Summary of Analytical Techniques used for Process Optimisation

The nature of the FHD process dictates that mechanisms crucial to the production of high quality layers of known composition require the macroscopic and microscopic analysis of physical and compositional behaviour. It was therefore necessary to implement a number of techniques to allow the characterisation of the samples produced. In some cases, the macroscopic observation of samples with either the naked eye or low magnification microscope could impart a significant amount of information. However, the need for accurate and reproducible, quantitative and qualitative analysis led to the use of a number of analytical techniques. This section highlights the operating principles and factors relevant to the use of a number of analytical techniques that were regularly employed during the characterisation of FHD layers.

4.1.1 Scanning Electron Microscopy

i) Electron Imaging

The main advantage of electron microscopy used for the characterisation of samples is the production of extremely high-resolution images with a large depth of field. However, the reality of electron imaging systems also imposes some limitation upon the samples that can be characterised. The use of electron microscopy to analyse samples can allow topographic imaging resolution of approximately 3nm. Compositional contrast can be achieved on images with a resolution of approximately 10nm. The need for imaging to take place within a vacuum system imposes a limit upon sample size due to the limited chamber size. The low pressure is required to allow a suitable mean-free path length for the electrons, thereby increasing the resolution of imaging. The posting port on the system used for the analysis undertaken forces a limit on maximum sample size of approximately $10mm^2$. Samples are required to be coated with a conductive layer in order to minimise the build up of surface charge. If charge build-up due to the electron beam does result then image distortion will occur, due to charged areas being imaged with high brightness. Sample damage caused by ablation may also result from charge build-up, which can result in possible chamber coating and detector damage. For high-resolution imaging, samples are coated via sputtering with a fine layer of gold particles. The small particle size and high conductivity allow high-resolution images to be acquired.

The electron-specimen interactions that take place determine how the sample is imaged and what type of detector is used. Elastic and inelastic scattering events are the basic atomic interaction mechanisms that occur. However, the final signal formation is not generally the result of a single scattering event. Complete electron diffusion due to multiple large angle scattering events normally results in the gradual loss of electron energy. The diffusion of the probe electrons within the material being analysed results in a finite range over which the electrons can interact with the sample, this range R is commonly 0.1-10μm and is dependent upon the electron energy and the density of the material. However, R does not solely define the resolution since signals of one form or another must leave the sample in order for information to be gained. This information volume is considerably smaller than the interaction volume, and defines resolution for the material and probe current being used. There are a number of interaction processes that can yield useful signals from the

information volume, see figure 4.1. The energy of the electrons emitted from the sample can be used to classify them, and allows insight into where the electrons originated.

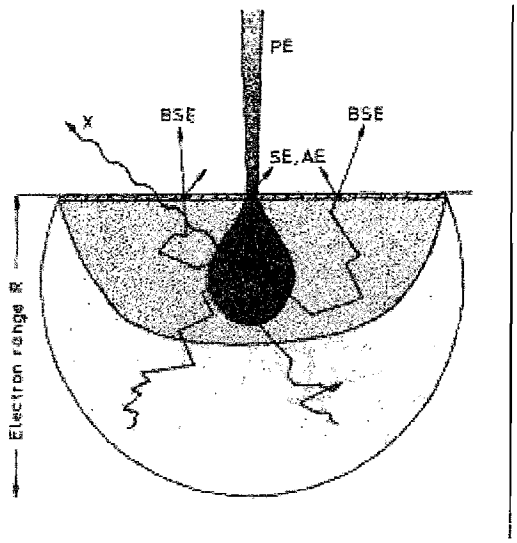

Figure 4.1, electron interactions with materials [Reimer, 1985]

Secondary electrons, SE, are generated by inelastic excitation to an energy high enough to allow dissociation and emission from the material. The most probable energy for secondary electrons is 2-5eV. The low exit energy means that they can be collected relatively easily using a positively biased collector grid. More importantly, the low exit energy of secondary electrons means that they can only escape from the top few nanometers of the material, thus giving excellent topographical information. About 20-50% of the secondary electrons come from the area directly illuminated by the probe beam, giving resolutions of 5-20nm. The remainder of secondary electrons come from interactions with backscattered electrons in the surface region of the information volume.

Backscattered electrons, BSE, are primary electrons from the probe beam that have been decelerated due to multiple energy losses and multiple large angle scattering events. This results in electron energies between 50eV and the energy of the primary electrons. This high energy means that BSE collection requires a high angle detector, since backscattered electrons travel in straight lines when outside the material. BSE surface emission is dependent upon surface tilt and surface topography and can therefore result in better shadow effect than for SE. However, magnification cannot be as high as for SE. The most important contrast mechanism for backscattered electrons is the dependence of backscattering coefficient upon the mean atomic number. This allows recognition of phases with different compositions. It is also possible to gain this compositional contrast from the SE signal due to the occurrence of backscattered electrons producing secondary electrons outside of the probe beam illumination area.

Auger electrons are produced after the ionisation of an inner shell of an atom within the material. The de-excitation energy released when an electron from an upper shell fills the vacancy in the ionised shell can be transferred to another atomic electron. Auger electrons like secondary electrons are highly susceptible to elastic and inelastic scattering, meaning that they are only produced from the top few nanometers of the sample surface. Both primary electrons and backscattered electrons can produce Auger electrons in the surface region, and for all intents and purposes can be treated in the same manner as secondary electrons.

ii) Energy Dispersive X-ray Analysis

In addition to the direct imaging and compositional contrast that is achieved from the electrons returned from the sample, the production of characteristic x-rays also occurs. The use of Energy Dispersive X-ray analysis (EDX) can result in compositional information for the material being analysed. Compositional resolution of approximately 5μm can be achieved using EDX analysis. Samples must be coated for the same reasons as for electron imaging, however gold is not suitable since it confuses the interpretation of x-ray spectra. Carbon coating is used in place of gold, the larger particle size and lower conductivity results in a reduction in imaging resolution. Carbon is used since it is too light to be detected by EDX and therefore does not effect the characteristic x-ray spectrum produced.

Characteristic x-ray emission after the ionisation of an inner shell is produced as an alternative to Auger electrons. Characteristic x-rays will only be excited in the volume in which the electron energy exceeds the ionisation energy of the inner shell involved. Secondary x-ray emission or x-ray fluorescence can occur if atoms exist within the material that have suitable ionisation energies. The information volume of x-ray fluorescence depends on the absorption of both the primary and secondary radiation, and can exceed the electron range. Imaging or compositional analysis using x-rays therefore has a considerably lower resolution than either secondary electrons or backscattered electrons, this leads to x-rays being largely used for compositional analysis.

Energy dispersive lithium-drifted silicon detectors are employed for detection of characteristic x-ray lines, allowing both qualitative and quantitative composition analysis of samples. However, problems do exist when quantitative analysis is required. The use of pure elemental standards are required in order to calibrate the system, this on its own is not a problem but the likelihood of a pure elemental sample accurately representing the inclusion of that element within a compound is slight. Problems also exist with detecting

elements lighter than and including boron. Technically this should be possible through the use of standards, as has already be mentioned this is not always practical. These various limitations have limited EDAX to a largely qualitative technique in this case.

It can be seen that SEM with EDAX is a very flexible and useful technique for analysis of samples. In particular, the high resolution and magnification combined with the large depth of field make SEM indispensable as an imaging technique when materials characteristics are occurring on a submicron level. The compositional analysis possible using EDAX has also been invaluable. Although absolute data is not practically achievable, the ability to compare compositional variation between samples is very important when investigating deposition processes.

4.1.2 Mechanical Profiling

Quantitative and qualitative analysis of layer thickness and surface roughness is important for any layer deposition process. A quick and easy method for comparing layers allowing accelerated process optimisation was achieved through using a Tencor Alpha-Step, a computerised step profiler with a programmable x-y translation stage.

Profiling takes place by tracking a stylus across the surface that is being analysed, measurements are digitised and stored, finally being displayed as a height against scan length plot. Scan lengths from 80-10,000μm with 400Å resolution and maximum profile heights of either 160kÅ with 5Å resolution or 160μm with resolution of 5nm are possible. The scanning stylus has a radius of 12.5μm and can be applied to the surface with a tracking force of 1 to 25mg, although 6mg is normally used.

The technique with which the profile plot is attained requires care to be taken when interpreting the results. Although the digitisation takes place with the accuracies mentioned previously, the stylus may not be gaining a true representation of the surface profile. Rapid variation in height may not be picked up if the probe cannot penetrate to the bottom of features. The tapered nature of the stylus can result in the misrepresentation of vertical surfaces, although this effect is slight. Finally, the possibility that the stylus is altering the surface must also be taken into consideration.

The use of the Alpha-step has given valuable qualitative information, particularly with respect to production process optimisation. However, the use of this technique for quantitative analysis has been less successful. Problems concerning the absolute accuracy of

this technique have already been raised, and are further compounded by the nature of the samples being analysed. Factors such as substrate flatness will greatly affect results; the process for producing a step suitable for thickness measurements also appears to confuse matters. Both of these points will be further explained in section 4.4.

4.1.3 Optical Profiling

The Nanospec is an instrument designed for measuring the thickness of optically transparent films typically on silicon wafers. It is widely used in measuring oxide thickness in the field of semiconductor microelectronics, but is also more widely applicable to any optically transparent material layer. The Nanospec works on the principle that the intensity of monochromatic reflected light depends strongly on film thickness, due to interference occurring when the film thickness is comparable to the wavelength of the incident light. The equation for measuring the interference is:

$$x_0 = \frac{\lambda}{2n_i}\left[g - \left(\phi_s - \phi_f\right)\right]$$

Where x_0 is film thickness, λ is the wavelength of the incident light, ϕ_s is the relative phase shift at the film/substrate interface, ϕ_f is the relative phase shift at the air/film interface, n_i is the refractive index of the film, and g is the order of the interference. The intensity is at a maximum when the bracketed term is an integer and a minimum when it is an integer plus ½.

The sample is mounted on an x-y translation stage along with a bare reference wafer. Spectra over 350-800nm are then taken from both the reference and sample wafers, and given a refractive index for the layer being measured, a layer thickness can be determined. The point at which the spectrum is taken can be scanned across the wafers following a predetermined grid, allowing three-dimensional information to be attained for the layer being analysed. The data can then be converted to a contour plot, allowing easier interpretation.

There are several limitations that affect the accuracy of the Nanospec in terms of analysing novel films. Firstly, the technique relies upon an accurate refractive index being given for the layer that is being analysed; this means that an additional complementary technique must be used in order to ensure absolute accuracy. The spatial resolution is also limited by the size of the spot with which the sample is illuminated during the spectrum

acquisition. Finally, any surface irregularities or contamination can cause scatter, resulting in the possibility of misleading results.

The nanospec is however very useful in terms of qualitative analysis. The production of contour plots showing the layer thickness across a whole wafer has allowed insight into layer dynamics during the production process. The ability to measure layer thickness regardless of wafer bowing is also of great use. Although the Nanospec is rarely used as a stand-alone technique, it does complement both Alpha-step and prism coupling analysis.

4.2 Theoretical Effect of Doping Silica

The manipulation and accurate control of material properties through the doping of pure silica is of paramount importance, firstly in order to control the processing properties of layers during FHD fabrication, and secondly to allow control of optical properties relevant to the construction of planar waveguiding structures. This section treats the theoretical effect of introducing dopant species into the nominally fully connected tetrahedral structure typified by pure silica. The discussion of dopant effects upon parameters relevant to processing such as melting point or more precisely viscosity and glass transition temperature is important to the layer optimisation process. The effect that dopants have upon properties such as thermal expansion coefficient and refractive index are of great importance with respect to ultimately production planar waveguiding structures. The particular dopants primarily used in the FHD process have been Phosphorus, Boron and

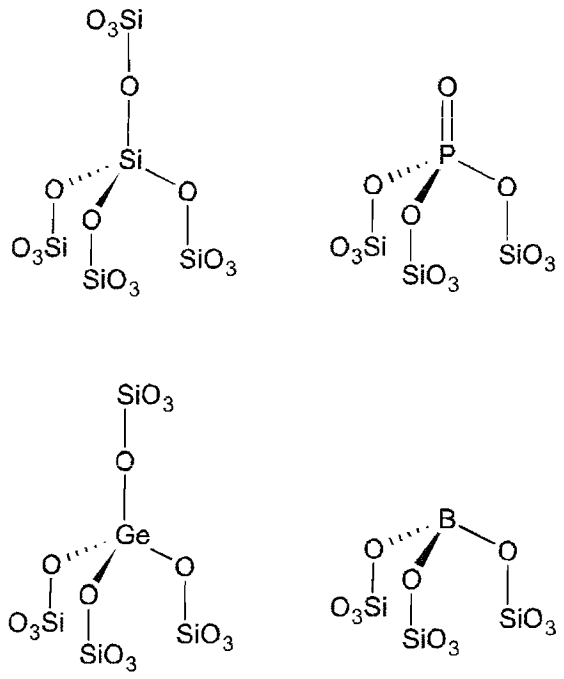

Figure 4.2, Inclusion of dopant atoms within silica matrix [Varshneya, 1994]

Germanium, the theoretical effect of each is discussed independently and the resultant modification of properties relative to silica is highlighted.

4.2.1 Phosphorus Doping

Phosphorous co-doping of silica to produce phosphosilicate glasses SiO_2: P_2O_5, results in PO_4 tetrahedron being substituted into the silica matrix. However, due to the pentavalent nature of the P ion, one of the oxygen atoms from each tetrahedron remains non-bridging thereby satisfying charge neutrality, see figure 4.2. The presence of non-bridging oxygen atoms within the silica matrix can result in the termination of ring, or chain structures. The formation of isolated chains, which cannot normally occur at non-defect sites in pure silica, is therefore possible through P doping. The less connected nature of the matrix results in a significantly less rigid structure, decreasing melting points and glass

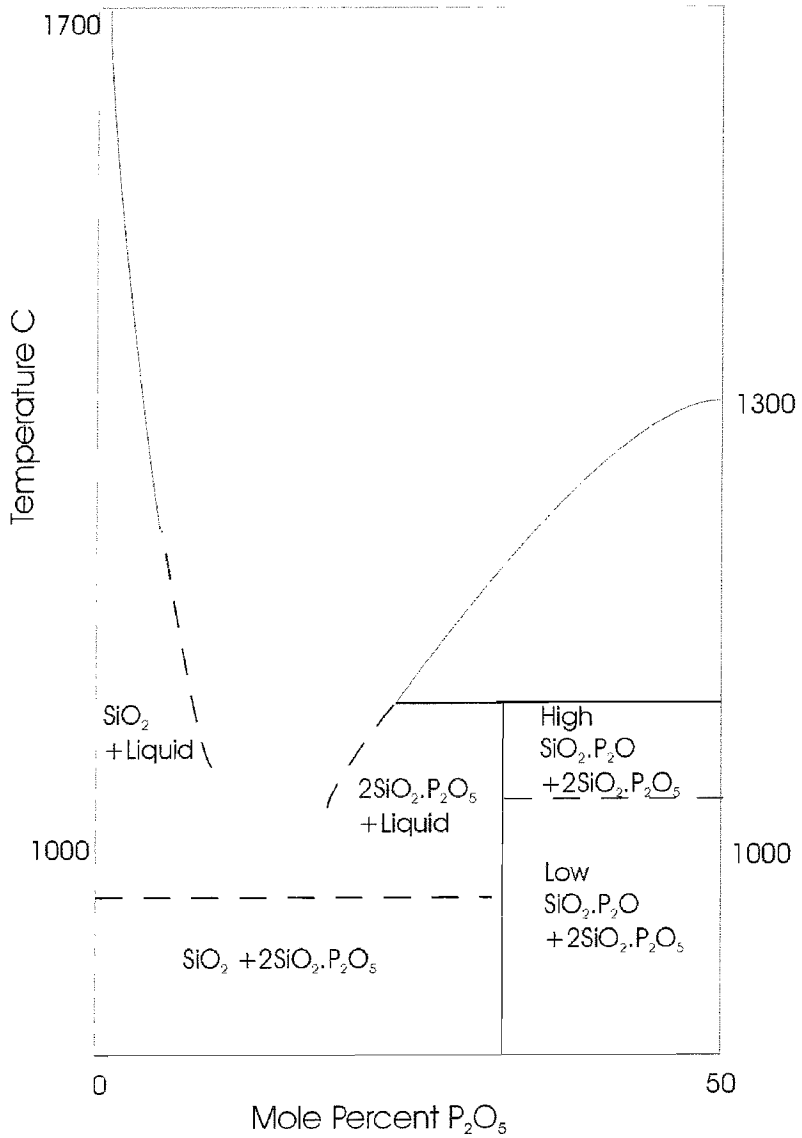

Figure 4.3, Phase diagram representing Phosphorus doping of silica [Tien and Hummel, 1962]

transition temperatures for phosphosilicate glasses when compared to pure silica.

The effect of P_2O_5 doping on SiO_2 can clearly be seen on the P_2O_5: SiO_2 phase diagram shown in figure 4.3. It is clear that phosphorous doping has a profound effect on the liquidus line and that the eutectic point occurs at ~20 mole percent P_2O_5. It is however unlikely that doping of this level will be required since a melting point of ~1200°C is possible at ~10 mole percent, which should be suitable for waveguide processing. Analysis of the phase diagram does not give information about the glass forming capabilities of the material. It does however give an insight into when a single amorphous liquid is produced, which is a precursor for glass.

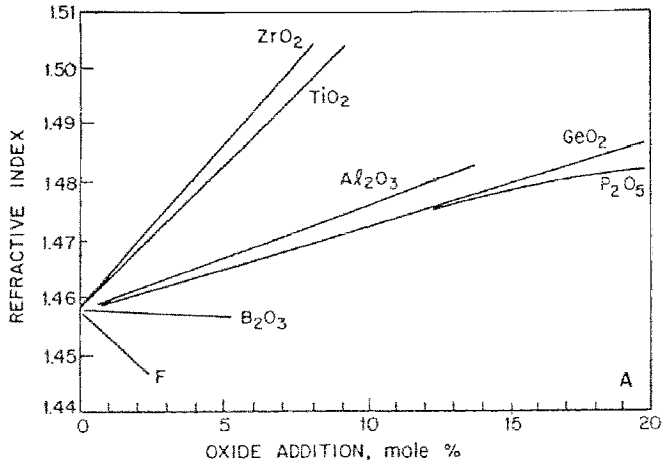

Figure 4.4, Affect of dopants upon refractive index at 598nm [Miller and Chynoweth, 1979]

Increasing the doping level of phosphorous has the general effect of increasing the refractive index of the doped silica glass, seen in figure 4.4. The increase in refractive index is likely to be due to the double bond and resulting "tighter" structure of the PO_4 unit compared to a SiO_4 unit. An increased absorption in the ultraviolet leads to a higher index of refraction via a Kramers-Kronig relationship [Ward, 1988]. The refractive index of a medium; the ratio of the speed for a propagating wave in free-space and in the medium, is related to absorption in the deep UV if the spectral absorption from zero to infinite frequencies are considered. This may be formulated in terms of Kramers-Kronig relations, relating the relative refractive index change $\Delta n(\lambda)$ to the changes in the absorption coefficient $\Delta\alpha(\lambda)$;

$$\Delta n(\lambda) = \frac{1}{2\pi^2}\int_0^{\infty} \frac{\Delta\alpha(\lambda')d\lambda'}{1-(\lambda'/\lambda)^2}$$

where λ is the free space wavelength. Thus, an increase in deep UV absorption results in an associated increase in refractive index.

The addition of phosphorous to silica-based glasses has the affect of increasing the thermal expansion, which can be seen in figure 4.5. Doping levels above ~15 mole % could result in phosphosilicate layers having a thermal expansion coefficient greater than that of a Silicon substrate which is 2.5×10^{-6}. Care must therefore be taken to ensure that deposited layers are not exposed to unfavourable strain conditions. The effect of substrate materials will be discussed in section 4.5.1.

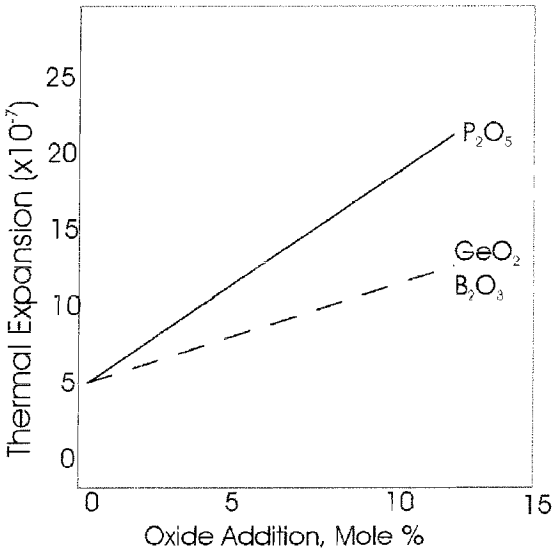

Figure 4.5, Affect of dopants upon Thermal Expansion Coefficient [Miller and Chynoweth, 1979]

Several additional potential problems could arise with phosphorous as a dopant. Besides the large increase in thermal expansion coefficient, which has already been mentioned, P_2O_5 sublimes at 358°C or melts at 569°C, and is highly hydroscopic at elevated temperatures. Despite these problems, phosphosilicate glasses are chemically stable and easily produced, resulting in widespread use in the field of fibre and planar optics.

4.2.2 Boron Doping

In borosilicate glasses the silicate matrix, SiO_2, is doped with boric oxide, B_2O_3. The oxygen coordination around each boron atom is 3, resulting in a triangular structural unit consisting of BO_3. It is widely believed that the B atom sits slightly above the plane of the three oxygen atoms, all of which are bridging [Varshneya, 1994]. The addition of these triangular units to the tetrahedral structure of the silicate matrix has much the same effect as the addition of the phosphorous non-bridging tetrahedron. The BO_3 units can act as terminators for the silica matrix, thereby leading to a less interconnected structure. The fact that the structural unit of BO_3 is also a considerable departure from the tetrahedron of the matrix adds an additional degree of disorder. The co-doping of silica with boron therefore

has the effect of producing a less rigid glass, which has a lower melting point and glass transition temperature when compared to that of pure silica.

The effect of boron doping upon refractive index results in the decreasing of refractive index with increasing doping level. It should be noted that the magnitude of the effect induced by boron doping is relatively slight when compared to other dopants. A increase in deep UV absorption results with associated effect upon refractive index. The addition of boron into the silica matrix has the effect of increasing the thermal expansion, but not to the same degree as for phosphorous doping.

Historically Boron doping of silicate glasses has been widely used in the field of fibre optics to reduce refractive index. Although, due to the relatively low wavelength of the fundamental absorption for the B-O unit at 7.2μm, its absorption tail can effect attenuation within the 1300-1550nm wavelength range commonly used in telecommunications systems. The comparatively low fundamental absorption wavelength also increase the effect of overtones present within the telecoms window. Thus, modern low loss fibre systems rarely use Boron in large amounts, although it has found widespread use in planar optics. Boron doping is particularly useful in FHD not only to reduce the index but to also to reduce the melting point of the glass. Pure boric oxide glass has a melting point of 450°C, compared to the 1710°C melting point for silica. This gives an indication of the degree of melting point reduction.

4.2.3 Germanium Doping

The addition of germanium to a silica matrix is subtler than for the previous two dopants mentioned. Germanium, like Silicon, forms a fully bridging tetrahedral structure, which results in the simple substitution of Ge atom into the silica matrix. However, this causes the matrix to be stressed for several reasons. Firstly the Ge-O bond length is ~8% longer than the Si-O bond, and secondly the Ge-O-Ge bond angle is 133° compared to the Si-O-Si bond angle of 144°. Although it is unlikely that a germanium tetrahedron will actually be bonded to another germanium tetrahedron, the difference in bond angle gives an indication of the type of effect that Ge substitution has on a silica matrix. The stressing of the matrix not only has a direct effect on the physical properties of the material, but also increases the chance of defects occurring within the structure. It can therefore be seen that a silica matrix is weaker due to the introduction of Ge atoms; it is again this disordering effect that causes a reduction in the melting point and glass transition temperature for the material.

The refractive index of a silicate glass is increased through the addition of germanium. The effect is very similar to that seen for phosphorous doping and the index is increased as doping levels are increased. The reason for index increase is likely to be due to the increased stress in the structure and the "tighter" bonds resulting in a increase in deep UV adsorption.

There is an increase in thermal expansion coefficient, which is associated with germanium doping of silicate glasses. The nature of the thermal expansion dependence on doping level is approximately the same as that found for boron doping.

Germanium doping of silicate glasses has found widespread use in the fields of fibre and planar optics. It has a limited affect in reducing melting point of silica due to the relatively high melting point of 1110°C for pure germania. However, germanium doping is more normally included for optical purposes. Not only does germanium doping have a significant affect on refractive index, it also introduces defects that play a part in photosensitivity. The role of germanium defects in promoting photosensitivity is discussed in Chapter 6.

4.2.4 Multi-dopant Silicate Glasses

So far the doping of silicate glasses purely in terms of binary compounds has been considered. However, the ability to tailor glass properties more precisely than is achievable through single dopant incorporation is required if useful PLC devices are to be fabricated. The combination of several dopants and doping levels allows greater freedom in modifying properties. For instance the ability to lower the melting point of a glass but maintain its refractive index would not be possible using single dopants, but in theory is relatively simple if complementary dopants and doping levels are employed.

The combination of dopants to produce multi-component silicate glasses is already well proven in the field of fibre optic fabrication processes. Historically amounts of work using ternary systems have taken place, and have found widespread use in fibre systems. The work has tended to focus on fibre production rather than material theory. The investigations regarding quaternary systems have little literary substance, and are not regularly used in fibre optics. When quaternary systems have been investigated, the work has tended to be of an experimental nature regarding fibre processing rather than materials properties. A lack of theoretical literature is likely to be an indication of the high complexity associated with considering quaternary systems.

The modification of refractive index and thermal expansion has however been shown to be largely additive for the dopants outlined in this section. This approximation is assumed consistent for FHD layers, at least for first order effects and for low dopant concentrations. The modification of melting points and glass transition temperatures is more complicated, and there has been little work published specifically in this field. However, precise definition of melting points and glass transition temperatures are not fundamental to this research.

4.2 Flame Hydrolysis Deposition Process

The FHD production of soot layers is a multistage process originating with reagent production and transport and resulting in the deposition of a uniform soot layer. The number of intervening mechanisms all of which must proceed in a suitable manner in order to result in the production of the required layer leads to the highly complex nature of FHD. This section deals with the characterisation of the FHD process and attributes various observed effects to specific mechanism that occur during fabrication. Many of the effects mentioned were brought to attention by specific problems that arose during the development and optimisation of the deposition process. The experimental work is presented as a linear progression through soot layer production, however this does not accurately represent the actual historical progression. A number of the problems associated with soot layer production only become apparent upon consolidation of layers, however this is considered separately in section 4.4. Thus, it was regularly the case that problems that arose upon consolidation were solved through modifying the soot layer deposition process.

4.2.1 Theoretical Consideration of Reagent Pick-up

As previously mentioned in Chapter 3 the reagents that are delivered to the flame are in vapour form, having been produced through evaporation from a liquid precursor. When considering the FHD process it is therefore necessary to understand the fundamental processes involved in the initial production of vapour from the liquid precursors. The implications of the vapour pressure for the reagents at a given temperature and the rate of vapour pick-up due to carrier gas flow through a bubbler must be well understood.

The vapour pressure of a liquid can be defined as the equilibrium pressure that occurs in the free volume above a liquid when contained within a sealed vessel. The equilibrium pressure indicates that evaporation from the liquid phase is occurring at the

same rate as condensation from the gas phase. The vapour pressure for a material can be used as a comparable measure of its volatility, such that a higher vapour pressure indicates a material that is more easily evaporated. Vapour pressure for the reagents used in the FHD system have been calculated using the Antoine equation;

$$\log_{10}(P) = A - (\frac{B}{T+C})$$

were P is the vapour pressure, T is the temperature of the system, and A, B, and C are all experimentally determined materials dependent factors.

The vapour pressure for a substance can be seen to be dependent upon the temperature of the material. It should be noted that all phase changes that result in transition to the gas phase have associated activation energies, and therefore associated vapour pressures. However, the temperature and pressure have to be suitable to allow the phase change to take place.

It is not practical to try to measure the amount of vapour being produced from the bubblers directly. It is however possible to gain an approximation for both the molar composition of the vapour stream and the corresponding flow rate components for each vapour. This was done by considering the "Perfect gas equation of state":

$$pV = nRT$$

Where p is the pressure within a system, V is the volume of the system, n is the number of moles in the system, R is the Gas constant and T is the temperature of the system. By treating both the vapour and the carrier gas as components within the system, and making assumptions concerning the pressure at various stages, the following expression was acquired:

$$n_v = \frac{P_v P_{in} V_c}{(P_A - P_v)RT}$$

Where n_v is the number of moles of vapour picked up, P_v is the vapour pressure of the reagent, P_{in} is the pressure in the bubbler, V_c is the volume of carrier gas and P_A is atmospheric pressure. The following assumptions were made in order for the above expression to be valid: i) The pressure at the outlet of the bubbler is atmospheric, ii) the sum of the carrier gas pressure and the vapour pressure for the reagent is atmospheric, iii) temperature and volume are the same for both carrier and vapour, and iv) equilibrium between liquid and vapour is reached while gas is flowing. The fact that the perfect gas equation of state is only valid for ideal gases means that any calculations using the above

expression must be considered as estimates. However, through using the derived equation to represent the various molar flow rates for the vapours in the vapour stream, it was possible to calculate the mole percent composition of the vapour stream with respect to its constituents.

The following expression is of use when considering vapour supply to the burner, it gives the flow rate of vapour out of the bubbler [Bonar, 1995];

$$F_v = \frac{(F_c \times P_v)}{(P_{in} - P_v)}$$

where F_v is the flow rate of vapour and F_c is the flow rate of the carrier gas. It relies on the assumption that the ratio of carrier pressure to vapour pressure is the same as for carrier flow rate to vapour flow rate.

The use of the two expressions outlined above allows the approximate composition and the total flow rate of the vapour stream being supplied to the burner to be calculated. Both pieces of information although approximate are important for process control, optimisation and repeatability. The advantage of knowing what composition you are likely to be depositing is obviously of great use, and allows calibration of the equipment between theoretical values and actually determined compositions. The knowledge of the total vapour stream flow rate supplied to the burner is of slightly more subtle importance. The ability to maintain the flame size and to a certain degree the flame dynamics through knowledge of the vapour stream flow rate, allows the system to be relatively stable regardless of the flow rates being bubbled. To this end, the vapour stream being supplied through the central ring of the burner is maintained at 0.5lpm. This is done through varying the dilution flow rate to compensate for variation in the carrier gas flow rates.

4.2.2 Comparison of Nitrogen and Oxygen as Carrier Gases

It was necessary to investigate the effect of Nitrogen and Oxygen carrier gases upon the FHD process. The use of Oxygen as the carrier gas would appear to be the natural choice since intimate mixing between reagent vapour and Oxygen may result in greater completion of reagent oxidisation in the flame. However, the use of Oxygen as a carrier gas may not always be possible due to constraints imposed by the reagents being used. Reactions between carrier gas and reagent prior to injection into the flame would not be preferable. It is therefore necessary to investigate the use of an inert carrier gas as well as Oxygen The easy availability of dry Nitrogen made it the natural choice.

The effect upon the flame that occurs due to the change of carrier gas must be taken into consideration. In order to maintain the H_2/O_2 ratio within the flame, and hence maintaining consistent flame kinetics, it was necessary to balance the Nitrogen flow from the second burner ring and the Oxygen flow from the third burner ring. This makes the absolute volume of Nitrogen and Oxygen being delivered from the first three rings the same regardless of the carrier gas being used. Changing the relative flow rates from the second and third rings in order to maintain flame kinetics has the adverse affect of altering the gas flow velocity profile for the burner. It is therefore possible that the reagent injection dynamics into the reaction zone are also changed.

Experimentally it has been possible to observe the effect that carrier gas species has upon the particle production mechanism within the flame. When O_2 is used as the carrier gas a bright tightly confined reaction zone is visible, this is consistent with direct oxidation of the reagent [Bautista and Atkins, 1991]. It is assumed that that the premixed nature of the reagent vapour and O_2 carrier gas allows a degree of oxidation to occur in the preheat zone prior to intersection with the flame front. The remaining reagent reaction and resulting luminescence occurs at or very near to the flame front. Although it is unlikely that soot production is purely due to direct oxidation, it is assumed that oxidation is a significant mechanism when O_2 is the carrier gas.

When N_2 is used as the carrier gas, the reaction zone is seen to be of low brightness and highly diffuse in nature. This is thought to be due to the increased dominance of hydrolysis as the primary soot production mechanism. The fact that reagent vapour has to diffuse within the flame until it encounters a reactant species implies that the associated reaction zone is likely to be large. The diffuse nature of the observed reaction zone and its low luminescence is assumed to be due to a considerable amount of hydrolysis occurring in the afterburning region of the flame.

The production of a tightly confined reaction zone, as has been observed when O_2 is used as a carrier gas, suggests that initiation of particle growth and aggregation for all particles is temporally and spatially similar. The reaction zone to substrate distance is therefore likely to be similar for all particles deposited. Deviation in deposited soot particles size is likely to be minimised if a small tightly confined reaction zone occurs. In contrast, a large diffuse reaction zone is likely to result in a large range of particle nucleation to substrate distances. The diffuse nature of the reaction zone may also lead to more reactive reagents actively scavenging H_2O within the flame, resulting in less reactive reagents not forming particles until higher in the flame. Large diffuse reaction zones may not only

induce a large spread of particle sizes, but particle composition may also vary depending upon nucleation point.

It can be seen that the carrier gas has an observable effect upon the flame dynamics and resulting soot production mechanism. The possibility that the carrier gas type also influences the particle size and compositional distribution has been highlighted. It should be noted that any variation is particle size or composition will ultimately affect the consolidation characteristics for a given layer. In the aim of consistency, all subsequent depositions mentioned take place with O_2 as the carrier gas and no further investigation of the oxidation verses hydrolysis reaction within the flame has taken place.

4.2.3 Burner Profile

The uniformity of a deposited soot layer is ultimately dependent upon the uniformity of the deposition zone produced when the particle stream is incident upon the substrate. The size and profile of the deposition zone dictates how the deposition stripes, produced by translation of the deposition zone across a substrate, should be overlapped. A completely symmetrical flame and extract should result in a stripe with an approximately Guassian profile. Determining the dimensions of the profile produced allows derivation of a scan pattern required to fabricate known layer thickness and maximum uniformity.

In order the produce a burner profile the deposition zone was translated along the same axis numerous times, thus building up a single deposition stripe with exaggerated profile. The composition used was a Phosphosilicate produced with a vapour stream calculated to be carrying 18.5mole% P, which had been previously been seen to consolidate to a high quality layer. The stripe was deposited using a total of 10 passes across the centre of a silicon wafer held at 400°C. The direct physical analysis of soot layers is not possible due to their extremely fragile nature, therefore mechanical profiling of the deposition stripe was not possible. Optical profiling was also not suitable due to the highly scattering nature and resulting non-transparency of soot layers. The layer was therefore consolidated at

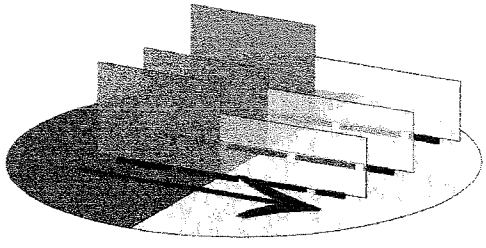

Figure 4.6, Measurement of layer thickness via surface profiling

1350°C for 3 hours, under which conditions a high quality fully dense layer had previously be observed to occur for the composition being used. The resulting layer was found to still be representative of the soot profile. Prior to consolidation a proportion of soot was removed perpendicular to the axis of the profile, thereby producing a cross-section. The consolidated layer was analysed by mechanically profiling the thickness difference between layer and substrate in the direction of the profile axis, see figure 4.6.

Using multiple measurements of layer-substrate height difference, it was possible to build up a profile of thickness across the layer cross-section shown in figure 4.7. It was observed that the profile appeared asymmetric, this is consistent with observation of the flame which also show a slight tendency to asymmetry. Asymmetry of the flame is likely to be due to a minor non-concentricity in the burner rings. Detailed flow measurements of the deposition extract also highlighted a minor asymmetry. It was concluded that the relatively minor deviation from symmetrical deposition was not a significant problem, and that any asymmetry could be eliminated through scan pattern manipulation.

4.2.4 Scan Patterns

The production of uniform soot layers is a prerequisite in the production of high uniformity fully dense layers. The relative size difference between the deposition zone and the substrate require that multiple deposition zone passes are needed to cover the substrate.

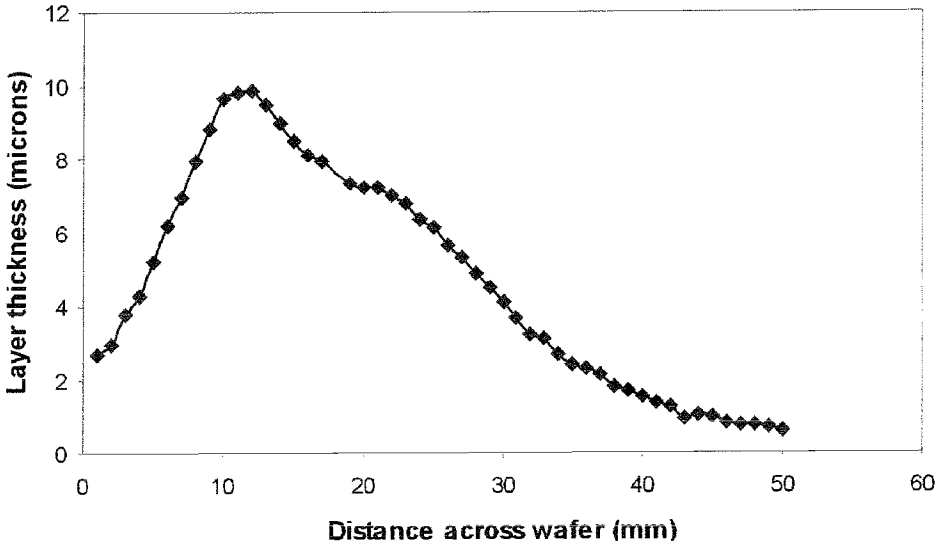

Figure 4.7, layer thickness profile due to burner asymmetry

The ability to control soot layer thickness through the number of deposition zone passes is also of importance when it comes to flexibility within the structures that can be deposited. The exact uniformity of the soot layer is dependent upon how the multiple passes, used to

cover large deposition areas and produce variation in soot thickness, superimpose upon one another. The use of multiple passes should allow the asymmetry observed within the deposition zone to be washed-out. The overlap between individual stripes, which form the scan pattern, must also be significant enough to allow for the Guassian nature of the deposition zone. It is preferable to build layers up with small amounts of soot deposition per pass, and use a high number of passes. Any short scale temporal fluctuations within the flame or extract characteristics therefore has minimum impact up the resulting soot layer uniformity.

In order to describe the scan patterns used for soot layer deposition, it was necessary to construct a consistent notation, a schematic of which is showing in figure 4.8. A scan

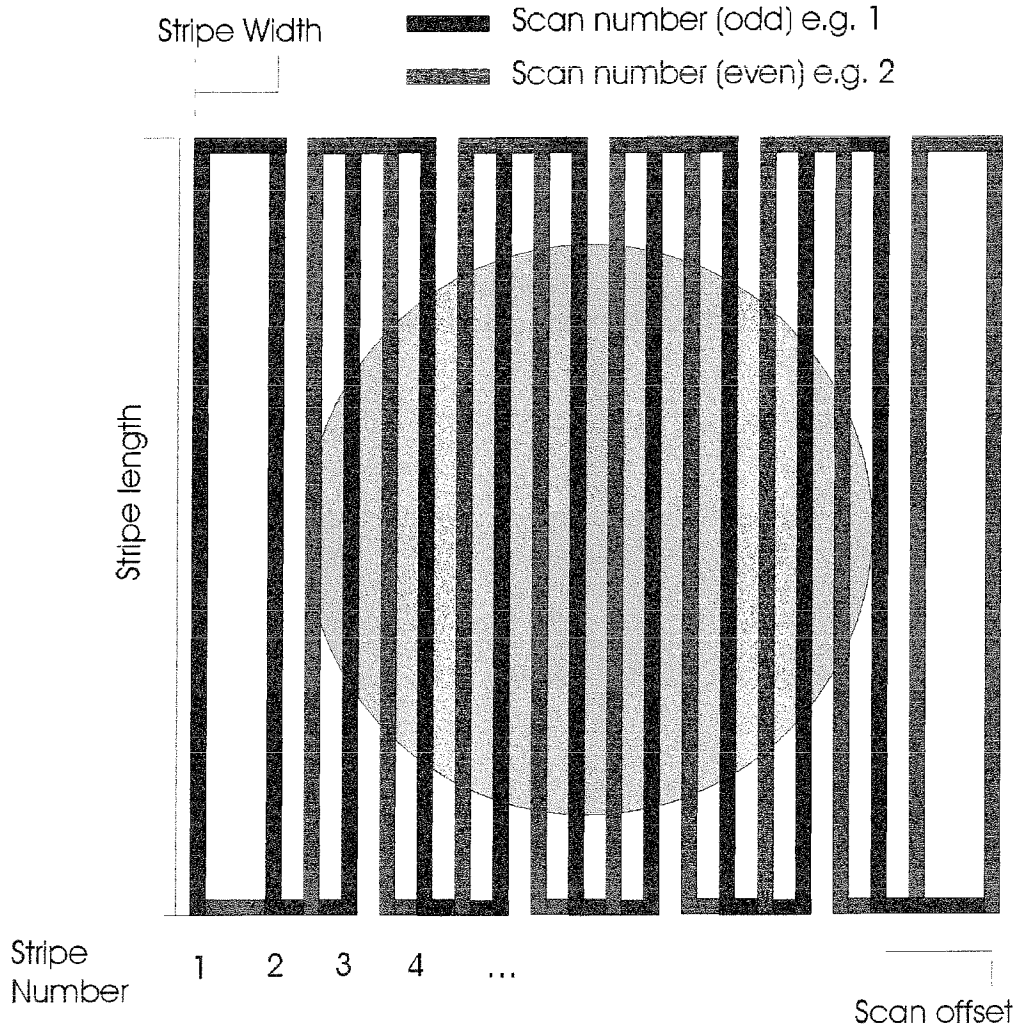

Figure 4.8, Schematic of scan patterns and relevant terminology

consists of a number of stripes with a given length and width, the width is effectively the stripe spacing not the size of the deposition zone. Subsequent scans are offset to result in the interlacing of current stripes with those produced by the preceding scan. Stripe width controls the degree of overlap of stripes produced within a given scan. The scan offset sets

the degree of overlap between stripes in separate scans. The total deposited area is defined by the stripe length and the number of stripes multiplied by the stripe width. The degree of stripe and scan overlap along with the number of scans directly affects the thickness of the soot produced for a given vapour supply rate to the burner and constant translation rate.

The direct observation of the soot layer produced allowed the stripe width range to be narrowed down to 1.25-5mm wide. If stripe widths are greater than 5mm, a soot layer that is visibly striped is produced. The use of stripe widths smaller than 1.25mm cause problems due to the inaccuracy of the translation system, the variability in translation distance becomes a considerable component.

The further determination of deposition uniformity due to the manipulation of scan parameters required the consolidation of layers, since soot layer uniformity could no longer be directly determined by eye. Upon consolidation it was possible to determine the uniformity of the deposition through direct observation of the interference fringes, produced by variation in layer thickness and resulting influence upon the path length and interference effects for light reflected by the substrate-layer interface. Visual observation was found to be the best and quickest method of relative comparison between the scan pattern-induced uniformity for consolidated layers. It was found that the best uniformity was produced by using a stripe width of 2.5mm and an offset of 3.75mm. A steady increase in uniformity was observed up to four scans, above which no significant increase appears to occur. The highest uniformity soot layers were found to occur under the maximum translation rates consistently achievable (~25mm/sec). The minimisation of substrate heating or cooling due to the deposition head is thought to be the likely reason for the translation rate dependent uniformity. The increased smoothing of any temporal deposition fluctuations across a larger area is also a probable contributing factor.

The relative size of the deposition area compared to substrate area was also found to affect the uniformity of soot deposition onto the substrate. As has been previously shown the deposition zone for approximately 90-95% of the soot is approximately 20mm in radius. The occurrence of deposition between the primary deposition zone and the deposition extract was found to have an effect upon the total soot layer uniformity. If the dwell position of the extract, during stripe width stepping, coincided with the substrate then particulates and crystal growth within the consolidated layer appeared. The general thickness uniformity of the layer seemed also to be affected by any deposition head dwell over the substrate. This was assumed to be due to the exaggerated temperature variation caused by the extract. It has therefore been necessary to always have a total deposition area

that is larger than the substrate area, so that the deposition head is completely translated off the substrate at the extremities of the scan pattern. The optimisation of scan patterns has taken place to allow deposition on to a number of different sized samples. The ability to deposit onto multiple samples has also been achieved using suitably large area deposition parameters.

4.2.5 Burner Substrate Distance

The distance between the burner nozzle and the substrate has a direct effect upon the nature of the soot that is deposited. Larger distances between the reagent reaction zone within the flame and the primary deposition zone, result in greater dwell times for particles in the particle stream. This leads to increased particle growth and coagulation, resulting in the deposition of coarser soot. The increased particle stream length will result in a lower particle stream velocity at point of deposition, and a possible associated increase in turbulence. A change in burner-substrate distance will also affect the temperature of the particle stream at the point of deposition, and the relative heating effect that the flame has upon the substrate. It can be seen from these arguments that the distance between burner nozzle, and more specifically the reagent reaction zone, and the substrate may have a considerable effect upon the nature of the soot deposited and therefore its subsequent processing characteristics.

The soot particle size dependence was directly observed when depositions where completed with different burner-substrate distances. SEM images of both soots were produced in order to quantify the effect upon soot characteristics. The SEM image of the soot produced with a 90mm burner-substrate distance showed particle sizes of >100μm, the general nature of the soot also appeared to be relatively dense. Decreasing the burner-

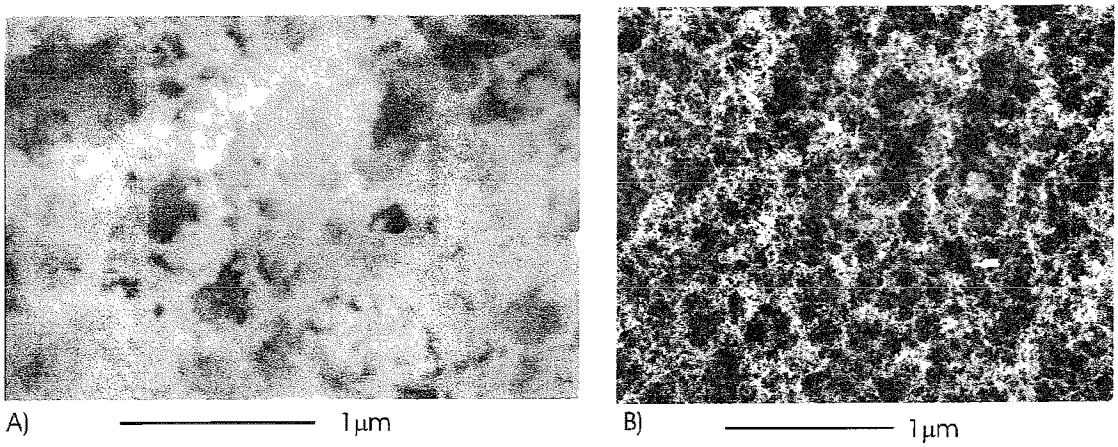

Figure 4.9, SEM micrographs of FHD soot with varying burner to substrate distance: a) 90mm; b) 50mm

substrate distance to 50mm had an observed effect of decreasing particle size to <50μm. The soot also appeared to be generally of a lower density and to consist of particles with a more uniform particle size distribution, as can be seen in figure 4.9.

Upon consolidation of soots produced using the two different burner-substrate distances it was found that the 90mm soot consolidated at unexpectedly high temperatures. It was in fact found impossible to consolidate to high quality layers a large range of the soots produced using 90mm spacing. An increased degree of contamination and associated cracking of the consolidated layer was also noted, an example of this is shown in figure 4.10. The problems with consolidation can be directly linked to the large average particle size of the soot resulting in an insufficiently high surface energy to result in consolidation at lower temperatures. The high occurrence of contamination is assumed to be due to the large particle size variation, resulting in some particles that are of such considerable size that they appear as particulate contamination due to the non-occurrence of sintering mechanisms. A detailed discussion of sintering dynamics and the factors that influence consolidation is dealt in Chapter 2.

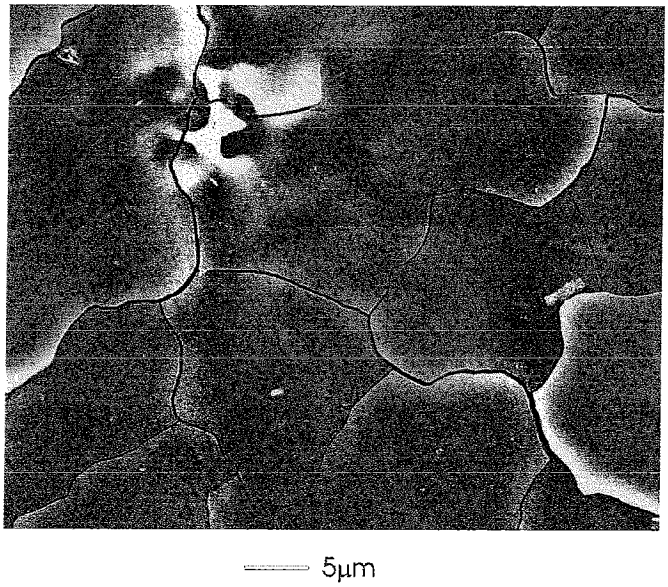

Figure 4.10, SEM micrograph showing layer cracking associated with large particle inclusion

The consolidation to full density for soot layers produced with a burner-substrate spacing of 50mm were found to occur at considerably lower temperatures, a significant decrease in particulate contamination was also encountered. The generally observed increase in layer quality and ease of consolidation is assumed to be associated with the production of soot having characteristics that are more conducive to densification due to sintering.

The further characterisation of burner-substrate distance effects upon soot and resulting consolidation characteristics were not undertaken, beyond noting that for distances appreciable less that 50mm flame heating of the substrate became significant. The results outlined here are intended to indicate the trends with burner height that were observed, and the optimisation process undertaken during the solution of consolidation problems through manipulation of soot production process. All subsequent deposition processes occurred with a burner-substrate spacing of 50mm.

4.2.6 Effect of Deposition Temperature upon Soot Layer

The temperature of the substrate during deposition has a direct effect upon the moisture content of the resulting soot layer. Regardless of the composition of the soot being deposited the lower the deposition temperature the higher the moisture content of the soot. The main source of moisture during depositions is the large amount of water present within the H_2/O_2 flame exhaust. It can be assumed that a substrate temperature of greater than 100°C will result in a decreased amount of moisture incorporation. However, the highly hygroscopic nature of silica soot and some of the dopants results in a more complex relationship between substrate temperature and the effect of moisture incorporation.

The general mechanical nature of the soot has been observed to be highly dependent upon the temperature at which deposition takes place. The higher the deposition temperature the higher the relative friability of the soot. This is thought to be due to a decreased level of moisture incorporation resulting in a reduction in intra-soot adhesion. For deposition temperatures above 500°C, soot layers have been observed to become highly friable, to the point that intra-soot and soot-substrate adhesion is tenuous to the point of extreme fragility and almost powder like properties. As the deposition temperature decreases, within the range 200-500°C, soot becomes increasingly plastic in nature. The assumed relative increase in moisture content results in increased particle-particle bonding within the soot, increasing the tendency for layers to behave as single materials and not a collection of individual particles. However, the overriding nature of the soot is to readily return to a powder-like substance under minimal physical interference. For temperatures below 200°C soot layers exhibit such plasticity that upon removal of layers from substrates, through scraping with a razor blade, layer "curling" occurs. For the temperature range below 150°C water becomes present within the deposition extract and the non-heated regions of the chamber roof where deposition occurs. Moisture inclusion does not occur

within the soot layers to a point at which they physically appear "wet", except for the special case of Phosphorus doping. For all non P-doped compositions, moisture incorporation is only observed by the physical changes outlined. It is assumed that flame heating maintains the substrate at a temperature above that for which physical large-scale condensation occurs.

The presence of Phosphorus within compositions considerably enhances the moisture sensitivity of soot layers, specifically for the temperatures below 200°C. For soots that are deposited below 100°C, P doping results in an oily substance being deposited. A pH of 1-2 suggests that condensation of Hydrochloric acid and the formation of Phosphoric acid from the combination of water with the highly hygroscopic Phosphorus oxide have occurred. The presence of both acids and residual water results in a suspension of silica particles that is observed as an oily substance. Deposition temperatures above 100°C do not result in the appearance of liquid water, either due to condensation not occurring or re-evaporation taking place prior to the completion of deposition. The deposition of P-doped compounds within the temperature range 100-200°C results in a gel-like substance, which although not a liquid does have a very high water content. The gel-like tendencies decrease as deposition temperature is increased. Above 200°C Phosphorus doped soot layers exhibit the same temperature dependence as previously outline for general soot layers.

It was highlighted in Chapter 2 that there is a theoretical temperature dependence for the deposition states of both Boron and Germanium doped compounds, both B_2O_3 and GeO_2 can exhibit crystalline forms. It was noted that the production of Boron oxide crystallites is theoretically unlikely due to the rapid formation of particles within the flame, at a temperature above which the crystalline phase occurs. The Germanium oxide case, as previously mentioned, can possibly exhibit an amorphous and a crystalline phase separately or simultaneously. However, the formation of GeO_2 crystals has not been observed in the quality of the soot produced. It is possible that GeO_2 formation occurs at a point within the flame where temperatures are above the transition temperature, resulting in the formation of amorphous particles. The other possibilities are either that the crystalline phase is present in the form of discrete GeO_2 micro-crystals, or that the Germanium oxide directly crystallises onto other particle in the particle stream. The result of which is that the general nature of the soot remains unchanged, and consequently no temperature dependent Germanium doping effect are observed at this stage of the process. The direct observation of the presence of

crystalline GeO_2 within soot was attempted using x-ray diffraction techniques, however the low diffraction efficiency due to the low soot density resulted in inconclusive results.

4.2.7 Effect of Composition on Soot Layer

The general physical nature of pure silica soot produced using FHD can be summarised as very bright white, powdery and of low density. The colour is associated with the very small particle sizes and the resulting scattering of incident light. The powdery nature results from the exceedingly weak inter-particulate bonding present within the layer. The density of soot is characterised by a void volume within layers of approximately 90%.

The doping of silica soot with Phosphorus exhibits a compositional ceiling of 35mole% Phosphorus in the vapour stream, above this a gel like substance is deposited for all deposition temperatures below 600°C. Decreasing the relative amount of Phosphorus within the soot, at a constant deposition temperature, has the effect of decreasing the plasticity of the layer produced. As previously mentioned the hygroscopic nature of P_2O_5 and it associated moisture trapping ability is accountable for the change in soot character. The production of suitable Phosphorus doped soot layers were found to occur with theoretical vapour stream concentration of less than 20mole%, and with substrate temperatures above 200°C.

The doping of soot with Boron and Germanium individually has a considerably more subtle effect upon soot characteristics compared to Phosphorus doping. Generally, as doping levels are increased a subtle decrease in friability is observed. This is assumed to be due to the decrease in relative viscosity of particle within the flame resulting in greater inter-particulate bonding during deposition. At very high doping levels of Ge and B (approximately 40 and 20mole% respectively), a degree of plasticity for soot layers becomes apparent. The use of such high doping levels was not expected to be commonplace, due to possible problems regarding inhomogeneous compositions resulting from phase separation.

In summary the effect of Boron and Germanium doping, within the compositional ranges of interest, are very slight compared to that observed for phosphorus. It was therefore not deemed necessary to impose a compositional doping ceiling upon Ge/B, to ensure soot layer quality, as was the case for P doping.

4.2.8 Dopant incorporation in soot layers

The method for deriving a theoretical concentration for the vapour stream depending upon the carrier gas flow rates and corresponding reagent vapour flow rates has been discussed in Section 4.3.1. It is assumed that the vapour conversion rate from halide to oxide is likely to be 100%, since the vapour must traverse a flame front and the amount of halide/water diffusion after the flame front is likely to be high. However, the theoretical model used to calculate vapour pick-up is likely to be flawed. The incorporation rate of dopant into the soot layer is also likely to be skewed, due to potential dopant volitisation and the formation of gaseous oxide during the deposition process. It is therefore necessary to gain an indication of dopant incorporation rate within the deposited soot layer.

The investigation of dopant incorporation was undertaken using Phosphorus doping since it was renowned for being problematic, probably due to its low melting and sublimation points. A number of P doped samples were prepared using various relative $SiCl_4$: $POCl_3$ flow rates. The carrier gas flow rates were also manipulated to ensure that the soot layers were all of similar thickness. The deposition temperatures remained constant with the aim of avoiding temperature dependent compositional and thickness effects.

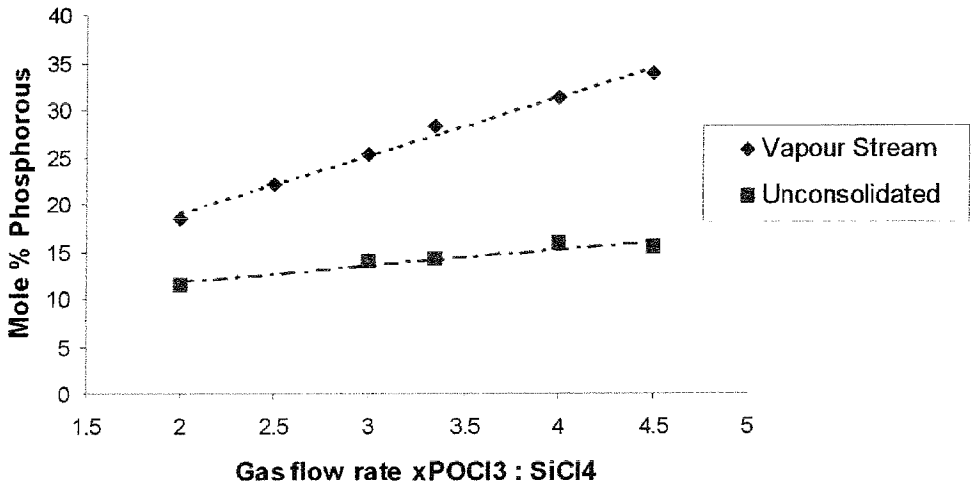

Figure 4.11, Dopant incorporation in soot layers

The soot samples produced were analysed using relative EDX compositional measurements. Multiple measurements were taken across the area of the samples in order to make sure that a representative composition for the whole layer was attained. The results of the analysis can be seen in figure 4.11. The results show a discrepancy between the

theoretical model and the actual incorporated composition. There are two possible explanations for this, either the model is inaccurate or there is a degree of preferential deposition occurring. Any error in the model is likely to occur due to non-equilibrium vapour pressures, the assumption of a system at equilibrium or the assumption of the pressures at various points within the system. The possibility of preferential deposition due to P_2O_5 not being as stable as SiO_2 cannot be overlooked as an explanation for the discontinuity.

It is likely that a large amount of the discrepancy is due to the complicated nature of P_2O_5 as previously highlighted in Section 4.2.1. At the flame temperature of approximately 2000°C it is possible that a percentage of the P_2O_5 will be in gaseous form, the resulting deposition efficiency is therefore likely to be low if the primary doping mechanism is the in-diffusion of gaseous oxide into the soot layer. It is also possible that P_2O_5 already present within the soot will be continually evaporating out, especially for the higher range of deposition temperatures.

The analysis of other dopants and their incorporation rates into soot has not been investigated in this manner. The apparent greater stability of other dopants and much higher melting points suggest that significant volitisation, of the type thought to occur for P doping, will not take place. Ultimately the soot composition is of little importance, the final consolidated composition is of greater interest. The incorporation of dopants into consolidated layers via the combined processes of deposition and sintering will be considered in a later section.

4.3 The Consolidation process

The production of high quality soot layers with appropriate properties is a prerequisite to producing high quality fully dense layers. However, the consolidation process introduces a number of problems the occurrence of which can hamper the consolidation of otherwise suitable soot layers. It is required that a soot layer experiences a suitable sintering regime if a optical quality layer is to be produced, matching of consolidation parameters to soot properties is therefore essential. This section focuses on the specific problems that occur during consolidation, and the solutions found via modification of sintering parameters. Thus taking the production of suitable soot layers, discussed in section 4.3, as a prerequisite.

4.3.1 Effect of Ramp Rates upon Consolidation Process

The time that it takes for a sample to be heated to or cooled from the required consolidation temperature can have several possible effects upon the sintering and ultimately the glass-forming mechanisms required to produce high quality layers. Heating to the temperature required consolidation can possibly affect the sample processing in a number of ways. The occurrence of sintering being initiated prior to the target temperature being reached may lead to the inability to accurately determine when consolidation has started for a given sample. If a sample is held at an elevated temperature for an excessive amount of time prior to the onset of sintering, the possibility of dopant volatisation must be considered.

It was found experimentally that satisfactory consolidation of layers using heating ramp rates of less than 20°C/min was not possible. The inability to consolidate samples using slow ramp rates was particularly notable for compositions containing Phosphorus. It was therefore assumed that dopant volatilisation was a key factor due to factor mentioned in section 4.2.1. The full consolidation of layers was realised using high heating ramp rates, in particular those experienced by direct insertion of samples into the furnace hot zone. The estimated ramp rates of greater than 100°C/sec appear to result in the almost instantaneous onset of sintering, quickly producing a sealed structure and reducing surface area and thereby minimising dopant volitisation.

The effect that cooling rates have upon layer processing is more destructive in nature. Cooling rate were estimated using surface temperature measurements and in the case of extreme cooling conditions the time take to reach room temperature was used, the rates given are therefore only approximate. The return of a sample from consolidation to ambient temperature is the stage at which glass-forming criteria must be adhered to. For pure silica heterogeneous nucleation occurs at cooling rates in the range of 2×10^{-1} to 1×10^{-5} °C/sec, cooling rates must exceed this to avoid crystallisation [Varshneya, 1994]. It was found experimentally that cooling rates of approximately 1×10^{-1} °C/sec did not result in any signs of large scale bulk crystallisation, or the apparent formation of visible crystallites. However, the use of cooling rates within this range has a tendency to produced cracked layers, shown in figure 4.12. It was found that slow cooling rates resulted in a greater degree of cracking. The size of plates and the ratio of cracked to non-crack area seemed to be directly dependent upon cooling rate. The cracking is thought to be due to the formation of

microcrystallites within the amorphous layer. The layers are under considerable stress due to the thermal expansion mismatch between the substrate and layer. Any crystallites present

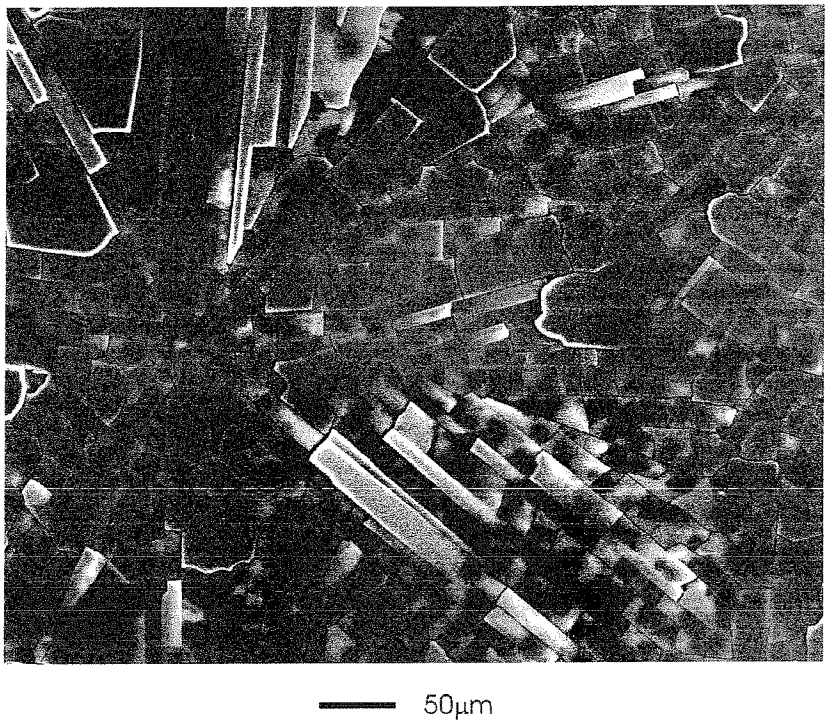

Figure 4.12, SEM micrograph showing cracking associated with unsuitable cooling rates

would act as stress concentrators inducing crack formation and propagation due to the stress field. The higher the number of the crystallites the more severe the resulting cracking will be. In order to minimise cracking and therefore improve layer quality it was found necessary to use very rapid cooling rates. Rates of approximately 200-300°C per second were found to minimise the cracking, which could be attributed to the growth of microcrystals, any subsequent cracking can be directly linked to particulate contamination.

The production of high quality layers is a compromise between rapid cooling rates in order to minimise crystallisation induced cracking, and wafer warping. High cooling rates can result in significant distortion of Silicon wafers upon returning them to ambient temperatures from consolidation temperatures. In particular, it was found that handling samples directly with metal tongs and the resulting heat-sinking action resulted in considerable deformation. The stress due to handling can be easily seen in the way in which wafers warp, and in severe cases wafer shattering occurs. The warping was found to be additive and therefore a particular problem during the repeat thermal processing required for multiple layered samples. It was therefore necessary to find a suitable compromise between cooling rates that minimised cracking and substrate deformation.

The ability to indirectly handle samples and decrease their cooling rates was achieved using silica tiles as sample carriages. The tiles were preheated within the furnace; insertion of samples involved the rapid removal of tile onto which the sample was placed, and then tile and sample were replaced into the furnace hot zone. The relatively high thermal mass of the tile ensures that the sample is rapidly ramped to the required consolidation temperature, and is only slightly decreased relative to that for insertion without the use of a tile. Sample removal involves removing both sample and tile, the sample is left on the tile for 30 seconds during which time it experiences a cooling rate of approximately 20°C/sec, after which time it is removed and remaining cooling takes place at approximately 100°C/sec. The initial cooling rate is fast enough to minimise crystallisation and associated cracking, but is slow enough to minimise wafer warping.

The use of a tile uniformly drops the substrate temperature through the critical range, below which the viscosity of the layer is too high to allow crystallisations as described in Chapter 2. The sample is removed from the tile to speed processing time, thus allowing rapid sequential processing. The use of a tile also theoretically allows the subtle modification of ramp rates through varying the thermal mass and surface area of the tile. This has not been investigated further since the current technique produces samples of adequate quality.

4.3.2 Consolidation Temperature

The theory of sintering is discussed in Chapter 2. The following sections treating both temperature and time of consolidation involve application of this theory to the specific case of consolidation and attempt to explain experimental observations. The rate at which consolidation takes place is directly dependent upon the consolidation temperature. This is because the higher the temperature for a given composition the faster the formation of a

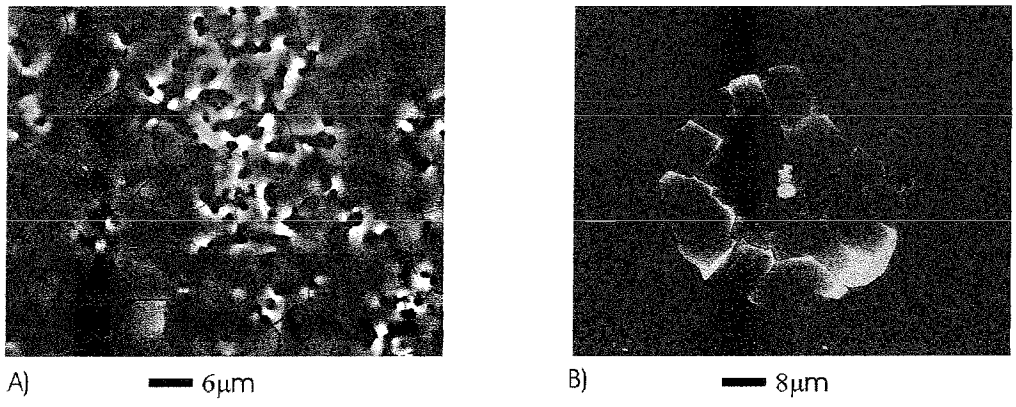

Figure 4.13, SEM micrographs showing typical examples of a) under-consolidation and b) over-consolidation

solid solution occurs, the viscosity of the particles is therefore lowered more rapidly and to a greater extent. A higher consolidation temperature generally produces a higher energy system that is more mobile. A lower viscosity allows greater flow to occur and will result in a flatter, less porous layer.

The occurrence of under-consolidation and over-consolidation, due to too high or too low a temperature has been observed during the experimental investigation of sample consolidation characteristics, examples of which are shown in figure 4.13. The case for under-consolidation occurs when the temperature is high enough to cause a lowering in viscosity that results in particle coalescence. However the resulting viscosity is not low enough to allow pore closure and the layer still exhibits an interconnected porous nature, but on a considerably larger scale than for soot. The case for over-consolidation occurs when the temperature is high enough to result in a significantly low viscosity and resulting particle coalescence, pore closure and pore gas out-diffusion. However, after a fully dense layer is achieved the viscosity is still low enough to allow the initiation of crystallisation, which upon cooling results in cracking due to microcrystallites.

As mentioned in Chapter 2 the driving force behind sintering is the need for the system to reduce its surface energy, hence the reason that sintering takes place at a temperature below the melting point of the material. The elevated consolidation temperature makes available sufficient energy for the system to reduce its viscosity, but less energy than would be required to reduce the viscosity to the same point for a fully dense material of the same composition. Lower consolidation temperatures result in less energy being available for the system, and hence a lower relative decrease in viscosity leads to a slower rate of consolidation. As the material becomes more dense the surface energy associated with the system is reduced due to reduction in surface area, and therefore the mobility for a given temperature decreases. If the consolidation temperature is not sufficiently high in the first place, the mobility will drop to a point where sintering no longer takes place. The result of which causes the consolidation process to stall, or slow to such a rate as to have effectively stalled.

A higher consolidation temperature results in a higher energy system and an associated greater decrease in viscosity. Initial reduction in viscosity must be low enough to allow consolidation to continue even although decreasing surface energy increases the viscosity for a given temperature. Full density must be achieved prior to reduction in surface energy causing sufficient increase in viscosity to stall consolidation. If the

consolidation temperature is too high then the viscosity is low enough after full density is achieved to allow the atomic rearrangement required for microcrystal nucleation.

4.3.3 Consolidation Time

As mentioned in the previous section there is a considerable amount of interdependence between consolidation temperature and time. If the consolidation temperature is low then a long consolidation time is required, despite the associate lower viscosities full density can often be achieved. If the consolidation temperature is high then a short consolidation time is required. The sample is removed once full density is achieved prior to the onset of significant crystal nucleation. The rapid increase in viscosity associated with sample cooling upon removal from the furnace ensures that there is no opportunity for crystal growth to occur. Experimentally significant similarities have been observed between low temperature and short time resulting in under-consolidation, and high temperature and long time resulting in over-consolidation.

There is a specific set of problems that can be directly attributed to extremes in consolidation time. Dopant evaporation becomes a significant problem when excessively long consolidation times are used, and can be a contributing factor to consolidation stalling. If the layer experiences elevated temperatures for excessive lengths of time prior to pore sealing, then an associated increases in dopant evaporation results. The composition shift due to dopant volatisation results in the material becoming more viscous as consolidation proceeds. Experimentally, dopant volitisation effects are particularly notable for Phosphorus compounds due to its volatile nature, as explained in sections 4.4.1 and 4.2.1. Problems were also experienced for very short consolidation times and the associated high temperatures. The rapid sealing of the porous structure and rapid volitisation of dopants results in vapour being trapped within the sealed structure. The very low viscosities associated with high temperatures result in the trapped vapour forming large surface bubbles. In the case of Phosphorus doping a structure resembling glass bubble wrap was formed!

It has been possible to characterise the consolidation process through observing the physical changes in the layer as sintering occurs, this has allowed the optimisation technique for producing high quality layers to be defined. Assuming the temperature is constant and minimal compositional changes, the following illustrates the mechanisms associated with stable consolidation. i) An interconnecting porous structure typical of soot

coalescence due to initial reduction in viscosity, particle size grows from approximately 50nm to approximately 1μm. ii) Increasing degree of particle coalescence, a degree of pore shrinkage and closure is also observed. iii) Complete pore sealing resulting in a non-interconnecting structure, the layer surface is non-flat due to residual pores within the layer. iv) The viscosity is still low enough to allow further layer flattening and pore gas out-diffusion. v) Further extension of the consolidation time results in the appearance of rosette like crack features. vi) As consolidation time is increased rosette cracked regions grow in size and increase in number. vii) Excessive consolidation time results in total coverage of layer surface with cracks due to complete growth and coalescence of rosette cracks. This

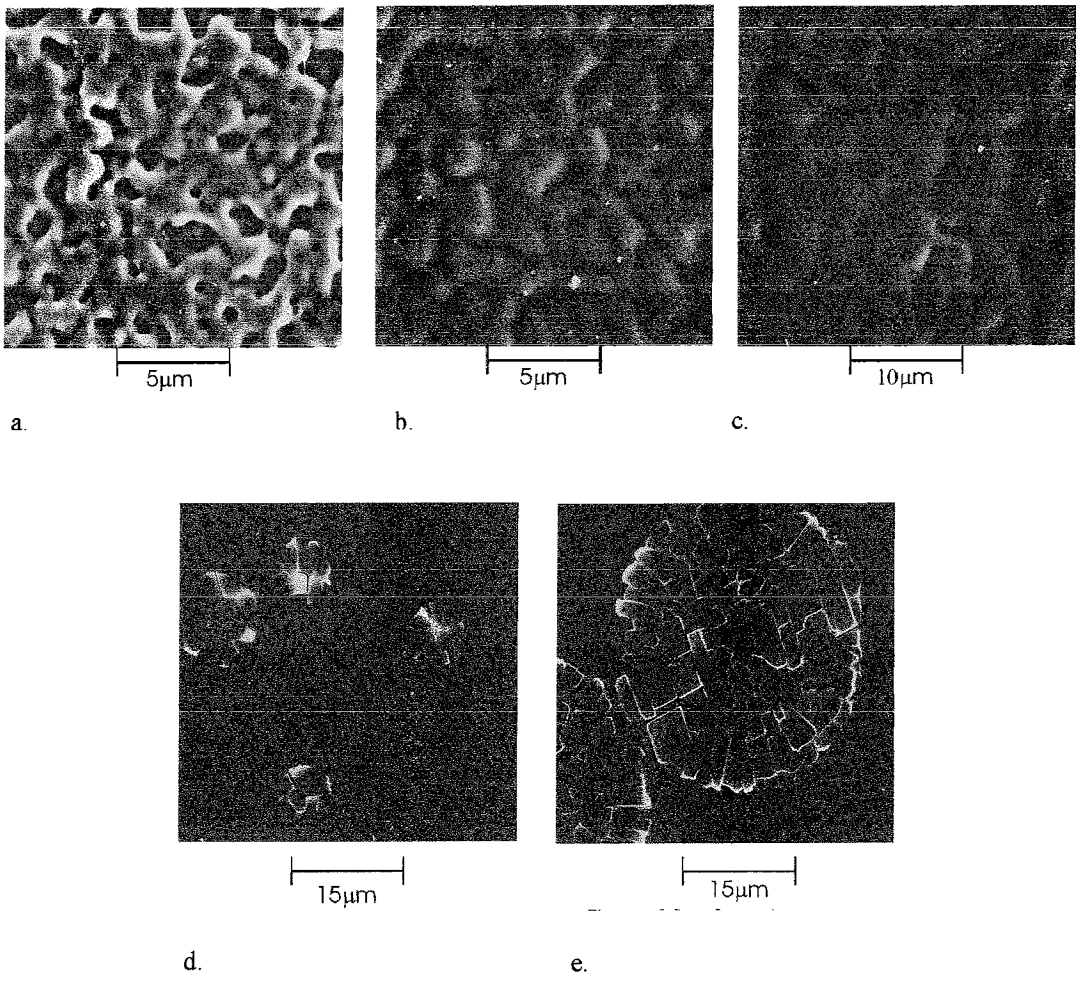

Figure 4.14, SEM micrographs showing the various progressive stages of consolidation; a) particle coalescence, b) pore closure, c) layer flattening, d) appearance of rosette crack features so time after optimal consolidation has been achieved, and e) growth of cracked regions

progressing is shown in figure 4.14.

The production of a summary containing the relative temporal occurrence of the various stages of consolidation has greatly added the development of further composition

dependent consolidation processes shown in figure 4.15. The schematic represents the various stages highlighted using the previous micrographs during a theoretical consolidation process. Stages (a) and (b) occur within the first 25%, progression from (c) to a layer of maximum quality occurs between 25 to 100%, and (d) to (e) occurs for times greater than 100% with (e) typifying approximately 115%. The actual rate of layer quality progression is

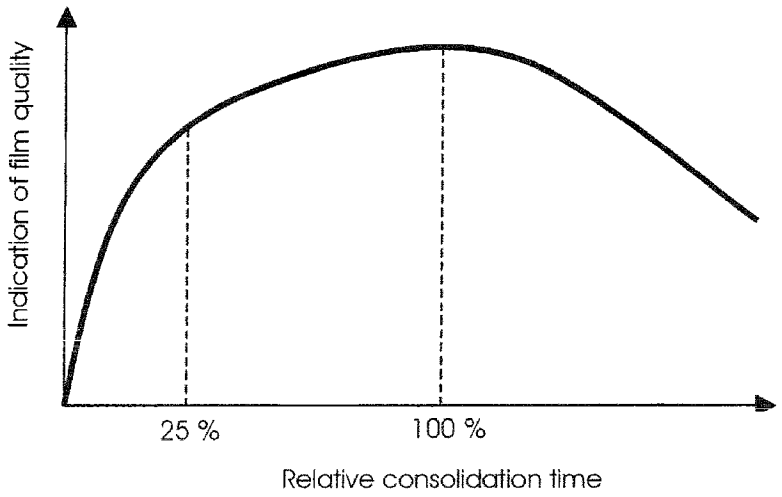

Figure 4.15, schematic showing the summary of consolidation progression

dependent upon the consolidation temperature used.

4.3.4 Determination of Composition Dependent Consolidation Parameters

The previously outlined relative interdependence of consolidation time and temperature, if extremes are ignored, has allowed simplification of the consolidation process. The use of a constant consolidation time was imposed in order to reduce the number of variables, which must be optimised when determining the consolidation parameters required to give greatest layer quality for a given composition. A period of one hour was identified as a suitable length of time, long enough to ignore the stabilisation period of the furnace after opening, short enough to allow a relatively quick turn around of samples. A consolidation time of one hour also forced consolidation temperatures for required compositions into a suitable temperature range.

A simple technique was developed for optimisation of consolidation temperatures for varying compositions. Initially a suitable temperature is estimated from previously knowledge of similar compositions and the known effects of the dopants being used. After consolidation the sample is assessed, preliminarily by ocular inspection, observing colour, particulate nature, flatness and cracking. If the layer appears consolidated to a fully dense amorphous layer then further analysis using mechanical or optical profiling and either

optical or electron microscopy. If required the consolidation temperature is modified in the direction expected to produce a better quality layer. The process is repeated until a layer of suitable quality is produced. After gaining considerable experience, it was possible to determine the degree of consolidation purely by manual inspection.

The nature of the consolidation process previously outlined in section 4.4.3 results in consolidation temperature windows of approximately 50°C. Heavily doped compositions sometime require a more rigorous determination of consolidation temperature, but most consolidation temperatures are defined to ±25°C.

4.3.5 Dopant Incorporation in Consolidated Layers

It has been previously noted in Section 4.3.8 that the incorporation of dopants into soot layers is not 100% efficient. In particular, the volatile nature of Phosphorus within the silica matrix has been highlighted as a potential cause for deviation from theoretical doping levels. The investigation regarding Phosphorus incorporation within layers was extended to include consolidated layers as well as soot layers. EDX analysis of a Phosphorus doped layer allowed relative comparisons to be made between theoretical doping levels and the actual dopant incorporation observed within in soot and consolidated layers, the results of which are shown if figure 4.16. It can be seen that there is a considerable decrease in Phosphorus concentration that occurs due to the consolidation processes. Incorporation efficiency for Phosphorus doping has been widely determined to be less than 20% of the theoretical composition of the vapour stream. Compositions containing Phosphorus show a very large range of incorporation efficiency, apparently dependent upon the absolute consolidation temperature for the compound. The highly volatile nature of Phosphorus, as previously discussed in section 4.3.8, is thought to be the primary cause of this effect.

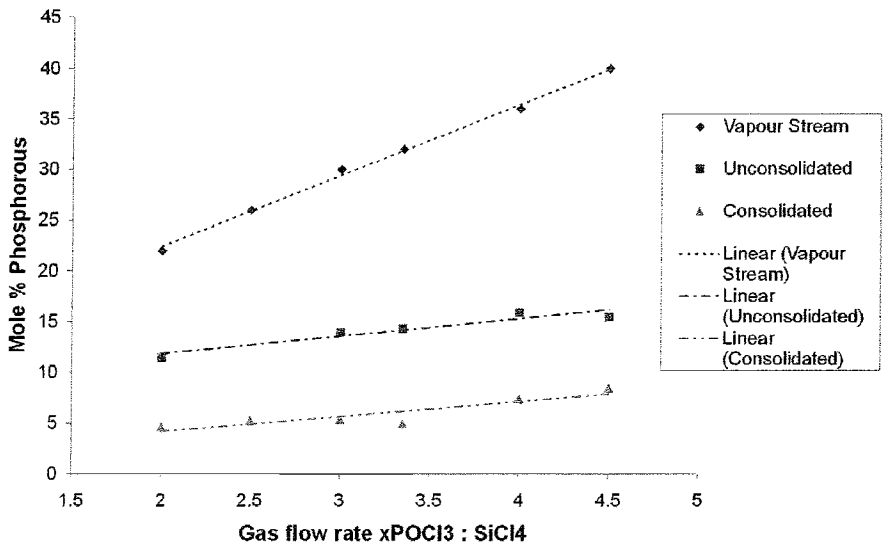

Figure 4.16, relative dopant inclusion within unconsolidated and consolidated layers

The incorporation rates from both Boron and Germanium appear to be considerably more stable that that observed for Phosphorus. Germanium has been observed to consistently have an incorporation rate of approximately 40% of the theoretical vapour stream composition. Incorporation rates for Boron have been difficult to determine due to problems associated with detecting Boron using EDX, however incorporation rate deduced from effect on refractive index discussed in Chapter 5, have suggested incorporation in the range of approximately 30%. It is thought that both Germanium and Boron will generally exhibit much more linear incorporation compared to Phosphorus, because of their more stable nature. The effect of dopant incorporation in fully dense layers is further discussed in Section 5.3.3.

4.4 Physical Summary of Layers Produced

The optimisation of deposition and consolidation processes, discussed in sections 4.3 and 4.4, has allowed the reproducible fabrication of fully dense layers with controllable composition. However, the production of fully dense layers of known composition does not necessarily imply suitability for construction of planar waveguiding structures. This section discusses the physical nature of the layers produced, in particular thickness and uniformity. Controlling the mechanisms that influence thickness and uniformity is ultimately required if optical waveguiding structures are to be produced.

4.4.1 Effect of Substrate Material

It has been found that substrate material and the nature of the deposited layer to substrate interface has a considerable effect upon the nature of the deposited layer. Two specific types of substrate have been investigated; crystalline p-doped silicon in the form of polished wafers, 100mm in diameter and with 1-1-0 orientation, and amorphous fused silica with 99.5% purity and 30×50mm in area. The silica substrates allow a range of compositions to be deposited that have a considerably higher consolidation temperature, due to relative melting points of approximately 1700°C and 1410°C for silica and silicon respectively. However, silica has the disadvantages that it experiences high temperature creep and crystal growth during extended consolidation periods.

The stress regimes, due to thermal expansion mismatch between layer and substrate, imposed by the two different substrate types are of great importance when considering the production of FHD layers. The larger thermal expansion coefficients, mentioned in section

4.2, for the layers compared to the silica of the substrate results in tensile stresses within the layer upon cooling from consolidation temperature. The resulting strain causes cracking within consolidated layers, which is visible to the naked eye as hairline fractures. A radial pattern of cracking is observed, possibly due to the non-uniform stress field induced by the rectangular substrate. The relatively large thermal mass of the silica substrates has a limiting factor upon the thermal ramp rates that can be used for consolidation. This may further increase the stress sensitivity of the layers due to crystal growth, which combined with the tensile stress regime increases crack initiation and propagation.

The use of silicon wafers as substrates imposes a consolidation temperature ceiling of 1400°C, in order to avoid melting and resulting deformation. However, the stress regime experienced by the layer is compressive, and therefore limits crack initiation and impedes propagation. The large mismatch in thermal expansion coefficient, up to five times, between substrate and layer leads to bowing of the wafer. The general cleanliness and high flatness of silicon wafers greatly benefits the FHD process. Any contamination that occurs at the substrate-layer interface can cause catastrophic failure resulting in delamination and large scale cracking. The many advantages of silicon wafers over bulk silica as a substrate material has resulted in the majority of work being carried out using silicon wafers.

As mentioned section 4.4, one of the main disadvantages of using silicon wafers is the wafer bowing that occurs due to thermal expansion mismatch. This problem was particularly notable with the standard 525μm wafers that were initially used. The composite nature of the layer-substrate unit suggested that increasing the substrate thickness would result in a decreased amount of deformation of the unit as a whole. The implementation of 1000μm thick wafers resulted in the subsequent reduction in relative bow to a point that is almost unperceivable. Although layers are now essentially flat, the increased stress in the layers will lead to an inevitable increase in birefringence.

The silicon wafers are supplied with a native oxide present, which is less than 50nm thick, resulting in depositions effectively taking place onto silica. However, preliminary depositions directly onto native oxide had a tendency for layers to "pull up" during consolidation. The appearance of droplet like structures upon consolidation suggested that the FHD layers were not wetting the surface sufficiently to result in adhesion. The implementation of deposition onto 1μm thick thermally grown oxides resulted in a subsidence of obvious wetting problems, however cracking and delamination especially under extreme quenching conditions occurred. The shift to using 2μm thick thermal oxides

solved all problems and resulted in good layer adhesion and crack resistance. It was concluded that the thick oxide acts as a stress gradient between the pure silicon and the FHD silica layers, thereby reducing the stress concentration that can occur at the layer-substrate interface.

4.4.2 Layer Thickness

The ability to accurately control layer thickness is of paramount importance for a deposition process such as FHD. The ability to gain quick feedback with respect to the parameters that influence thickness is fundamental to the efficient optimisation of layer thickness to a required value. The main technique for measuring layer thickness is as previously briefly outlined in section 4.3.3, and involves mechanical profiling of a step produced by scraping an amount of soot off the substrate prior to consolidation. Upon consolidation, the step is maintained and can be used as a representative measure of layer thickness. Subsequent measurements along an edge can be used to build up a profile of the thickness across a sample. The degree of consolidation only effects measurements to a small degree, allowing the thickness to be measured for layers that have not had consolidation parameters fully optimised or if contamination occurs. However, this relatively robust measurement technique does require that surface non-uniformities are not of a similar scale to the layer thickness, otherwise interpretation of data is virtually impossible.

It has been discovered that a minimum for high quality layer thickness occurs at 4μm, below this defects occur on a large scale most notably cracking although wetting problems resulting in layer pull-up have also been observed. When wetting problems occur large variations in thickness comparable with the total layer thickness result. It is assumed that layers below 4μm in thickness are not mechanically strong enough to resist the compressive stresses imposed by the substrate upon consolidation. To date it has been found impossible to consolidate layers less than 4μm thick, however the deposition of such layers onto the top of already existing FHD layers may be possible but has not been investigated.

The maximum producible layer thickness is purely dictated by the amount of soot that can be deposited in a single deposition. However, consolidation parameters would probably change for excessively thick layers due to the increased time required for pore gas out-diffusion. The current FHD system is limited by the primary extract capacity, since during a deposition soot also builds up within the extract. It has been found that excessively long deposition times or large vapour flow rates results in the extract flow rate being

compromised and runaway deposition occurring. This is not preferable since it results in excessively thick layers of unknown uniformity and deposition occurs within the entire deposition chamber. The current maximum consolidated layer thickness achievable through a single deposition is 16μm, although processes are not designed to result in layer thickness greater than 14μm. In process extract cleaning which involves shutting the flame off and purging the deposition chamber, allows multiple soot layers to be deposited prior to consolidation. To date only layers of the same composition have been deposited using the multiple soot layer deposition technique, since complication within the consolidation process may arise. These problems are highlighted in Chapter 5.

There are three main factor which determine the thickness of the deposited layer; reagent supply rate, extract rate and the number of passes or the effective deposition time. The reagent supply rate and extract rate determine the maximum amount of time over which deposition can take place, limited by extract blocking. Variation in the number of scans is used for coarse adjustment of thickness. Adjustment to the reagent flow to the burner is used for fine adjustment of thickness, scaling of relative carrier gas flow rates allows composition to be maintained while deposition rate is varied. A similar bracketing technique as used for determining consolidation parameters, is employed to achieve desired consolidated layer thickness.

The deposition rate due to subsequent scan is not linear and this must be taken into consideration at the process design stage. It is found that the first pass across the substrate produces a thin layer of soot, which is assumed to be due to the weak bonding between soot particles and the bare substrate surface. Subsequent passes result in an increased deposition rate, probably due to a degree of interlocking with particles that are already present on the substrate from the first pass. The nature of the substrate surface also has a direct effect upon the deposition rate. It was found that bare substrates have a lower deposition rate relative to substrates that already have a consolidated FHD layer present. This is thought to be due to FHD layers being rougher on a microscopic scale than bare wafers, it is also possible that the chemical similarity between soot and an FHD layer results in an increased degree of bonding. Maximum average deposition rates for the FHD system are approximately 10μm of consolidated layer per hour, this does not include the FHD system run-up and purge time or the hour consolidation period since they are constant and independent of total layer thickness.

There is a considerable difference between soot layer thickness and consolidated layer thickness, due to the very low density of soot layers. During the consolidation process a reduction in thickness by a factor of 50-100 occurs, such that a 1000μm thick layer of soot results in 10-20μm of fully dense glass. It is difficult to determine that rate of shrinkage accurately due to problems associated with determining the soot layer thickness. The increase in density associated with consolidation is most noticeable in the thickness reduction, however a small amount of shrinkage does occur within the plane of the layer

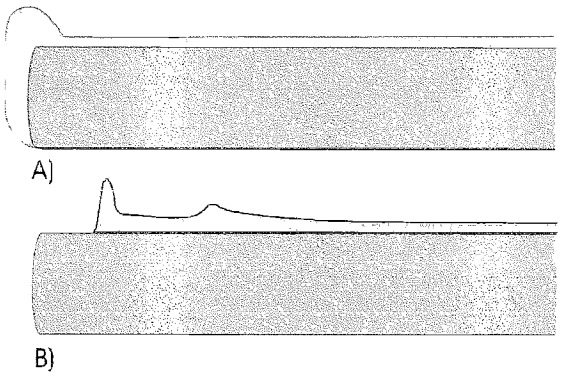

Figure 4.17, Schematic showing occurrence of "layer pullback"

under certain conditions. Lateral shrinkage or "layer pullback" occurs when soot is removed in the manner used for consolidated layer thickness measurements, a schematic of this effect is shown in figure 4.17. If the soot layer remains undisturbed and "wrapped" over the edge of the substrate, lateral shrinkage does not occur and a limited edge bead forms. Normal edge beads are confined to the outer 500μm or so of samples. When pullback occurs due to soot removal, edge bead formation occurs on a considerable larger scale. The primary edge bead is thicker but laterally of similar dimensions to a normal edge bead, the secondary bead by comparison can have an effect up to several millimetres radially into the layer. It has been found that the thicker the layer the greater the degree of lateral shrinkage, leading to greater bead stretching. In extreme cases exaggerated edge beads can cause problems with layer thickness determination, due to secondary bead formation dominating the majority of the Alpha-step scan length.

4.4.3 Layer Uniformity

There are various types of uniformity that are of importance when considering layers produced by FHD. Thickness variation across the substrate, resulting in wedged layers, will cause problems when a constant core size is required during the construction of guiding

structures. Surface roughness and its effect upon core-clad boundary layers, resulting in scattering out of the core is of importance. Intermittent changes in layer thickness, particularly for the core layer will effect the modal operation and possibly induce scattering within a waveguiding structure. A full explanation of uniformity effects upon optical properties for guiding structures is discussed in Chapter 5, the remainder of this section deals with the physical occurrence and minimisation of the non-uniformity at the processing

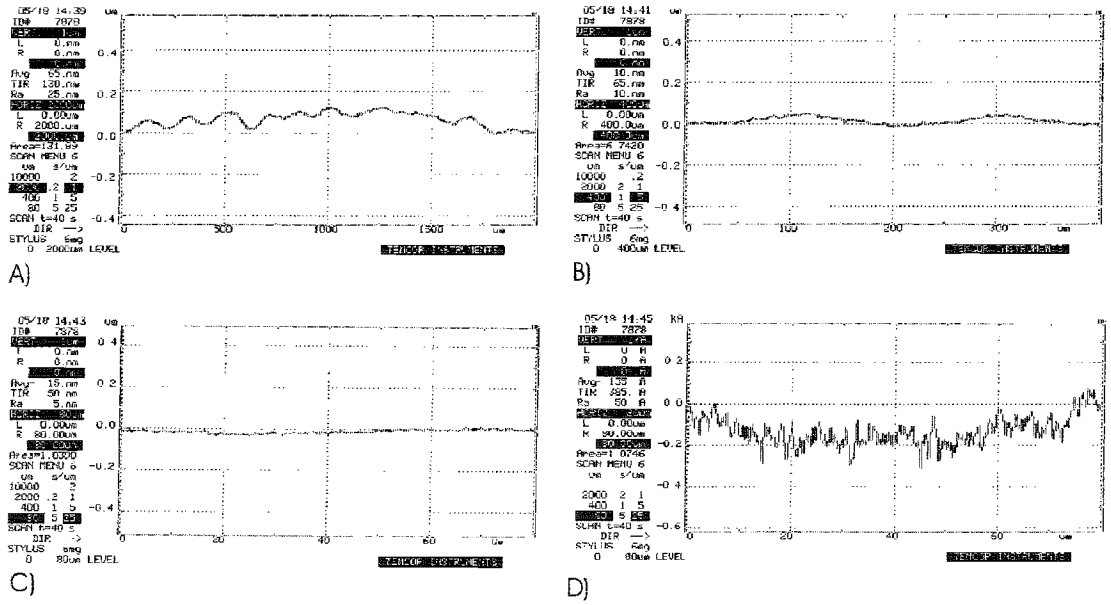

Figure 4.18, Alpha-step plots showing scale of non-uniformities

stage.

There are several length scales that non-uniformities have been observed to occur over, alpha-step plots showing the various effects included in figure 4.18. Over approximately 1000-2000μm layer thickness ripple has been observed, within the period of 100-200μm long period roughness can be seen, periods of 2μm and less typify short period roughness. Layer thickness ripple with a peak to trough value of approximately 100nm over a period of greater than 1000μm, can be seen optically due to distortion produced in the reflection from the layer surface. This is possibly caused during deposition, but is most likely due to consolidation. Long period roughness with a peak to trough value of 50nm over approximately 200μm, and short period roughness with a peak to trough value of less than 20nm over approximately 2μm are both likely to be residual structure remaining from the particulate nature of the soot. These values outline represent the current state of the art regarding uniformity of consolidated layers. Uniformity problems on a larger scale than those highlighted can normally be attributed to incomplete consolidation, particulate contamination or layer discontinuities such as cracking or delamination. Uniformity is normally directly related to degree of consolidation, assuming that the composition being

used is feasible, greater accuracy in determining correct consolidation parameters results in increased uniformity.

Non-uniformities in thickness occurring on the scale of the substrate are easily observed due to the interference fringes caused by the variation in thickness, although this

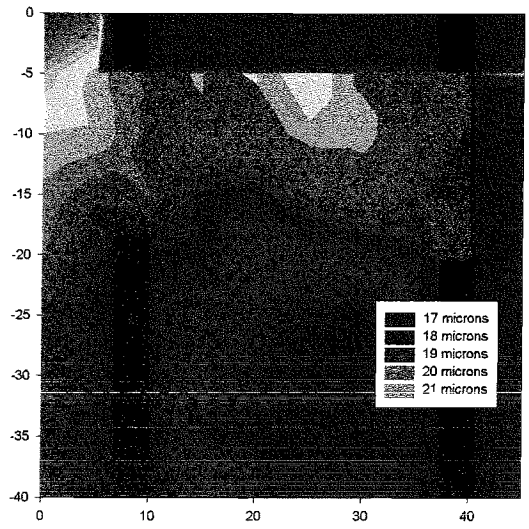

Figure 4.19, Nanospec scan showing layer wedging within a 40mm^2 area

does not give absolute data it does give quick relative feedback for process optimisation. For fringes to be observed the layer must be significantly flat and transparent. Some compositions result in the formation of pixelated fringe patterns due to layer rippling. When layer rippling is the dominant fringe production mechanism, a minimisation in layer wedging normally occurs. Independent quantitative data on layer wedging is easily achieved through use of the Nanospec, the results of which can be seen in figure 4.19, confirming what is observed by the naked eye.

There are several possible causes of layer thickness variation all of which could result in the production of a wedged layer. The reagent or flame parameters could vary during the deposition, the extract rate could vary, the heater temperature may not be constant during the deposition and the deposition temperature maybe non-uniform across the area of the substrate. It was necessary to individually investigate the various possible causes of the layer wedging in an attempt to solve the problem.

Observations of flame brightness during depositions revealed that flame flicker does occur, however the period is very short and probably caused by aerodynamic fluctuations rather than reagent or flame gas flow rate variations. The short period nature of the observed fluctuations meant that several occurred per stripe in the deposition pattern, it was therefore thought highly unlikely that repeatable wedging could result from flame flicker.

The uniformity of the extract rate from the deposition extract was investigated using a hot-wire flow meter. The variation around the deposition extract was found to be less than 10%, which is attributed to the difference in tube length between the deposition extract and the main extract pipe for the different extract ports. The variation in extract rate depending upon translation system position was also investigated. The deformation of the flexible extract pipe, which supplies extract to the deposition head, was found to cause a 15% variation in the resulting extract flow. The fitment of a 45° rigid PVC elbow at the point of maximum deformation was found to solve the problem of variable extract rate depending upon translation position. However, this did not stop the deposition of wedged layers. The constant variation in extract rate around the deposition extract was though unlikely to be the cause of wedging since multiple passes are used during the deposition process.

A variation in deposition temperature experienced by the substrate was found to coincide with the flame and resulting deposition area, and the region directly above the extract. During translation a temperature gradient is moved over the substrate with a maximum occurring above the flame and a minimum above the extract. The maximum temperature difference observed was ±100°C, although this was dependent upon the starting temperature of the substrate. It was found that the induced temperature gradient was constant for the deposition area, and since that area is uniformly translated across the substrate layer wedging is unlikely to be a result. The fact that the heating and cooling effect of the deposition head results in no net temperature change of the substrate further suggests that the induced temperature gradient is not the cause of layer wedging.

The uniformity of the temperature at which the substrate is held during deposition was monitored using a thermocouple probe, it was found that a ±5°C temperature gradient occurred across the substrate area when heated by the halogen heater system. It would appear that the masking of the radiation used to heat the substrates resulted in non-uniform temperature across the samples, leading to a temperature gradient and the deposition of a wedged layer due to the thermophoretic dependency of deposition (see Chapter 2). The implementation of the resistive heating system increased thermal uniformity to ±1-2°C across the deposition area, this is on the resolution limit of the thermocouple system used to measure temperature. The resulting fringe pattern produced using the resistive heating system is probably the best measure of thermal uniformity. Layers produced using the resistive heating system have wedging that is on average less than 5% of the total layer thickness across a full wafer.

The thermal characteristics of the substrate directly affect deposition efficiency. The presence of a previously deposited and consolidated FHD layer appears to improve the uniformity of the deposition temperature experienced by the soot. This is probably due to the composite nature of the substrate, the high thermal conductivity silicon wafer is covered by a low thermal conductivity FHD layer, resulting in a more uniform temperature on the surface of the sample. This can be readily seen by the apparent decrease in wedging for layers that are deposited onto previous layers, such that subsequent layers only have a minimal effect upon the fringe structure observed. The deposition of thick underclad layer will possibly result in greater uniformity core layer being subsequently deposited.

4.5 Conclusion

The development, characterisation and optimisation of the FHD technique and associated processes have been discussed thoroughly in this chapter. The understanding of the various mechanisms that lead to layer production has allowed the various problems encountered during the work to be overcome. The table below summaries the main difficulties encountered and the solutions that were employed in order to produce layers with suitable properties;

Problem Encountered:	Solution Found:
Non-uniform burner profile and implications to soot layer uniformity (4.3.3).	Development of a suitable scan pattern, resulting in a uniform soot layer (4.3.4).
Unexpectedly high consolidation temperatures assumed to be due to deposition of large soot particles.	Reduction of burner-substrate distance, associated reduction in soot particle size, and reduction in relative consolidation temperature (4.3.5).
Incorporation of water within soot, leading to non-uniform layer.	All depositions take place with a substrate temperature greater than 200°C (4.3.6).
Unfavourable soot structure/ physical properties.	Implementation of dopant dependent maximum concentration ceiling (4.3.7).
Discrepancy between theoretical vapour stream composition and actual soot composition.	Calibration of reagent flow rates to required soot layer composition (4.3.8).

Discrepancy between soot layer composition and consolidated layer composition, due to dopant volitisation during consolidation.	Maximisation of heating rate to consolidation temperature, resulting in rapid production of a sealed structure (4.4.1)
	Calibration of reagent flow rates at deposition to allow for volitisation during consolidation (4.4.5).
Cracking upon cooling from consolidation temperature, assumed to be due to crystallisation.	Modification of cooling rate from consolidation temperature to regime in which crystallisation does not occur (4.4.1).
Over and under consolidation.	Optimisation of consolidation temperature and time (4.4.2 and 4.4.3)
Excessive Silicon wafer bowing upon production of fully dense layer.	Increase in substrate thickness from 525μm to 1000μm (4.5.1).
Layer pull-up and delamination during consolidation process.	Increase in thermal oxide thickness resulting in increased wetting and graduated stress field (4.5.2).
Non-uniformity of layer thickness.	Implementation of more uniform substrate heater during deposition (4.5.3).

The work presented represents a considerable effort and required the fabrication and characterisation of a large number of samples, and was intimately connected with the development of equipment previously discussed in Chapter 3. This has lead to the ability to reliably fabricate high quality layers, of known composition and thickness, therefore providing the foundations for all subsequent work involving the production of planar waveguiding structures using the FHD process.

5 Production of Layers and Structures Suitable for Waveguiding Applications

The application of the FHD process to the fabrication of planar waveguiding structures is the primary goal with respect to the motivation of the work highlighted in Chapters 3 and 4. This Chapter discusses the application of the equipment and knowledge already gained, to the specific task of producing a set of compositions suitable for the further construction of three-layer planar waveguiding structures.

A number of analytical techniques centred on excitation of guided modes via prism coupling are discussed, and their suitability for determining specific optical properties primarily refractive index is highlighted. A theoretical review is included in order to determine the required properties that must be taken into consideration when constructing waveguiding structures.

Finally, the FHD production of layers suitable for construction of waveguiding structures is discussed, and particularly focuses on the calibration of deposition and consolidation parameters. Thus, allowing the subsequent combination of layers from a fully characterised database of compositions and therefore giving a variety of samples suitable for the investigation of direct UV writing within doped silicate layers.

5.1 Summary of Analytical Techniques used for Characterising Layers

The production of optical quality layers with controllable properties requires feedback in order to calibrate the fabrication processes employed. This section discusses the use of prism coupling and various associated techniques that have been used in the determination of refractive index, thickness and propagation loss. Prism coupling is particularly suitable since it offers rapid data acquisition regarding fundamental optical properties, which are inherently linked to the composition and quality of layers. The techniques outlined in the following have therefore been indispensable in the rapid acquisition and subsequent feedback of data to the fabrication process.

5.1.1 Prism Coupling

Prism coupling is a method of analysis that involves coupling light into the layer being studied, and the conditions under which waveguide excitation takes place allows calculation of both waveguiding layer thickness and refractive index. The ability to

determine parameters that are fundamentally important to final waveguiding devices is of considerable significance, this makes prism coupling a powerful technique for characterising waveguiding materials and structures. The following section describes the principles of prism coupling, and the calculation of refractive index and thickness from measured parameters, in terms of an analytical technique.

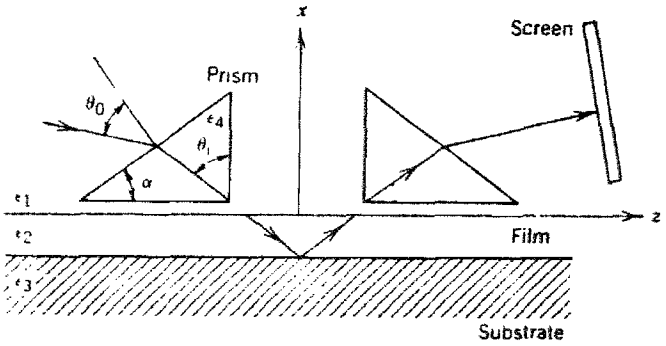

Figure 5.1, schematic of the prism coupling technique [Lee, 1986]

Strong excitation of a guided mode requires very precise phase matching with the incident launching beam. This implies that there is a finite angular dependence for the incident beam that will successfully couple to a waveguide mode. Prism coupling allows the incident beam angles that produce strongly excited guided modes within the waveguide to be determined, shown in figure 5.1. The angle θ_0 is varied which in turn varies θ_i through the following relationship:

$$\theta_i = \alpha - \left(\sin^{-1}\left(\frac{n_1}{n_4} \sin\theta_0 \right) \right)$$

It is possible to determine when coupling is taking place through either observing the cleaved edge of the waveguide, or by observing minima in the light coupled straight out of the layer when waveguiding conditions do not exist.

The determination of θ_i for at least the lowest two modes (p = 0,1) supported by the waveguide, allows the index of the core region, n_2, and the thickness of the core region, d, to be calculated. Iteration of the following equation allows n_2 to be determined due to the functions converging nature:

$$n_2^2 = \frac{(n_{eff})_0^2 \psi_1^2 - (n_{eff})_1^2 \psi_0^2}{\psi_1^2 - \psi_0^2}$$

Where

$$\left(n_{eff}\right)_p = n_4 \sin\theta_i$$

$$\psi_p = p\pi + \tfrac{1}{2}\phi_1 + \tfrac{1}{2}\phi_3$$

$$\phi_1 = \tan^{-1}\left[\frac{\left(\left(n_{eff}\right)_p^2 - n_1^2\right)^{\frac{1}{2}}}{\left(n_2^2 - \left(n_{eff}\right)_p^2\right)^{\frac{1}{2}}}\right]$$

$$\phi_3 = \tan^{-1}\left[\frac{\left(\left(n_{eff}\right)_p^2 - n_3^2\right)^{\frac{1}{2}}}{\left(n_2^2 - \left(n_{eff}\right)_p^2\right)^{\frac{1}{2}}}\right]$$

The use of additional θ_i for subsequent modes allows n_3 to be fitted to data acquired using the prism coupler, thus allowing the refractive index of both layers in a two layer structure to be determined. The thickness of the guiding layer can be determined through use of the following relationship:

$$d = \frac{\lambda}{2\pi}\frac{\psi_p}{\left(n_2^2 - \left(n_{eff}\right)_p^2\right)^{\frac{1}{2}}}$$

It is therefore possible to calculate the refractive index of the core and underclad layers, and the thickness of the core layer using prism coupling.

A Metricon™ automatic prism coupler was used for the majority of the index measurements during the characterisation of processing parameters against optical layer properties. Standard measurements involved the use of a 633nm Helium Neon laser source. The Metricon uses a stepper motor controlled rotation stage with angular resolution of 0.45', giving a theoretical effective index resolution of $\pm 5\times10^{-5}$. An interchangable prism allows the measurement of materials within the index range of 1-2.6 to take place. A prism of index 1.9648, allows the measurement of all indices within the range likely to be produced by doped silicates and was used in the characterisation of FHD layers. A photodiode placed at the output face of the prism determines the relative intensity of the incident beam that is not coupled into the guiding layer. Modification of the incident angle by actuation of the rotation stage, through a range known to produce phase matching for the layer being characterised, results in an angularly dependent intensity that is detected by the photodiode. A piece of dedicated software is used to record and plot the relative intensity against incident angle. Upon completion of a scan, the software employs pattern recognition routines to highlight the minima in intensity, which are associated with coupling.

Calculation of guiding layer characteristics are then undertaken automatically, using the techniques previously outlined, resulting in an index and thickness for the guiding layer.

There are a number of practical considerations and limitations that must be considered when prism coupling is used to analyse layers. The flatness of the sample must be sufficient to result in a uniform prism-layer distance for the area of the incident beam. Any roughness present in the layer will result in significant errors for the prism coupling data. The parallelism between prism and layer surfaces must also be high enough if errors in the angular determination of coupling conditions are to be avoided. Problems that arise due to coupling inefficiencies and uncertainties result in the resolution of measured indices decreasing below the theoretical maximum, repeatability of better than $\pm 5\times10^{-4}$ is normally possible. The use of 633nm as the measurement wavelength limits the thickness of layers that can be analysed due to the inaccuracies involved in resolving a highly multimode structure. It has been found experimentally that doped silicate layers greater than 5-6μm in thickness result in excessively complex and error prone measurements due to high numbers of modes closely packed relative to incident angle.

5.1.2 Critical Angle Measurement

The critical angle for a given interface between two regions of different refractive index is the angle for which transition between reflection and refraction occurs. The refraction that is observed for a ray incident upon an interface can be described by Snell's law of refraction;

$$n_1 \sin\theta_1 = n_2 \sin\theta_2$$

Where n_1 and θ_1 are the refractive index and incident angle in the initial medium that the ray is propagating through. The refractive index for the second medium and the refraction angle

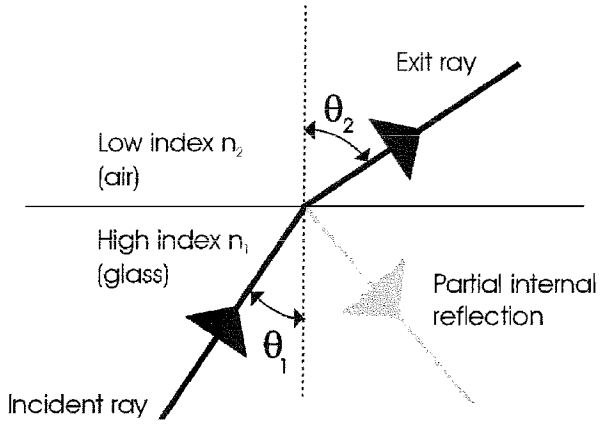

Figure 5.2, diagram illustration Snell's law of refraction

are represented by n_2 and θ_2 respectively, shown if figure 5.2. A small amount of light is reflected back from the interface this is known as partial internal reflection. When n_1 is greater than n_2 the refraction angle must always be greater than the incident angle, and when the refraction angle is 90° (parallel to the interface) the incident angle is less than 90°. The limiting case for refraction is when the incident angle exceeds that for which a refraction angle of 90° occurs, resulting in total internal reflection. The critical angle for an interface is the incident angle for which transition from refraction to total internal reflection occurs, and is given by;

$$\sin\theta_c = \frac{n_2}{n_1}$$

The dependence of critical angle upon the indices of the two dielectric materials that form an interface, allows the experimental determination of critical angle to be used to determine the unknown refractive index for one of the media. The apparatus previously described for prism coupling is ideally suited for determining critical angle, the Metricon software in fact offers this mode of operation. Figure 5.3 shows a schematic of the Metricon operating in critical angle mode.

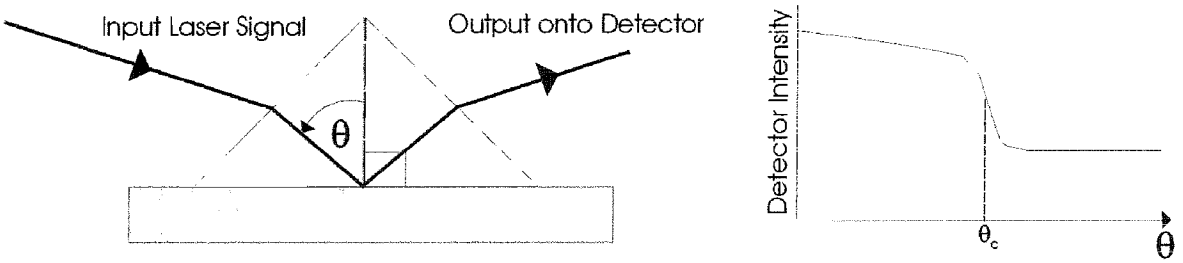

Figure 5.3, determination of critical angle

The determination of refractive index for bulk samples can be done to a very high degree of accuracy. Errors of less than 1×10^{-4} are achievable if absolute index standards are used (from Metricon literature). The high accuracy associated with bulk samples arises due to the large spatial separation between reflections that occur due to the top and bottom interfaces of the sample. As samples deviate from the "bulk" case, errors can arise due to confusion between rays resulting from prism/layer and layer/substrate interfaces. However, it is possible to use the determination of critical angle to infer the refractive index of thick layers. The incident angle at which reflection decreases due to coupling into the first mode is taken as the critical angle. As a film with fixed index gets thicker the angle at which the first propagation mode occurs asymptotically approaches the critical angle. As the layer thickness increases the error in refractive index determination can be seen to decrease. A

3μm layer gives an error less than 4×10^{-3}, a 5μm layer an error less than 1×10^{-3} results, and a 10μm layer an error less than 3×10^{-4} occurs. It can therefore be seen that for layers in the range of 6-10μm, determination of refractive index through critical angle measurement is of comparable if not greater accuracy than prism coupling.

As for prism coupling, critical angle measurement requires layers of a high enough quality to result in a reflective surface. Any defects of surface roughness that result in scattering will directly affect the accuracy of refractive index measurements. The prism base and layer surface must be parallel to avoid angular errors. However, it has been generally found that critical angle measurement is less sensitive to layer quality than full prism coupling. The natural range of layer thickness that can be easily produced using FHD fall within the range for which the accuracy in measured refractive index is better for critical angle compared to prism coupling. Although critical angle measurements of refractive index are apparently more suited to FHD layers, thickness data is not attainable and the absolute accuracy compared to prism coupling is likely to be lower.

5.1.3 Measurement of Loss due to Scattering

Observing scattering loss is a simple method for measuring the propagation loss of a layer, without the need to produce a fully guiding structure or the requirement of end polishing to allow efficient end launch. Assuming that the primary loss mechanism is scatter caused by physical and compositional imperfections, then upon excitation of a guided mode an associated guided-wave streak will result due to light scattering out of the waveguide plane. The peak intensity and the decay rate of the streak with respect to distance can be used to interpret the loss of the guiding layer. Scanning a pinhole or fibre along the guided streak and detecting the light selected through use of a photodiode, allows determination of the loss for the guiding layer, as shown in figure 5.4. The Metricon automatic prism coupler

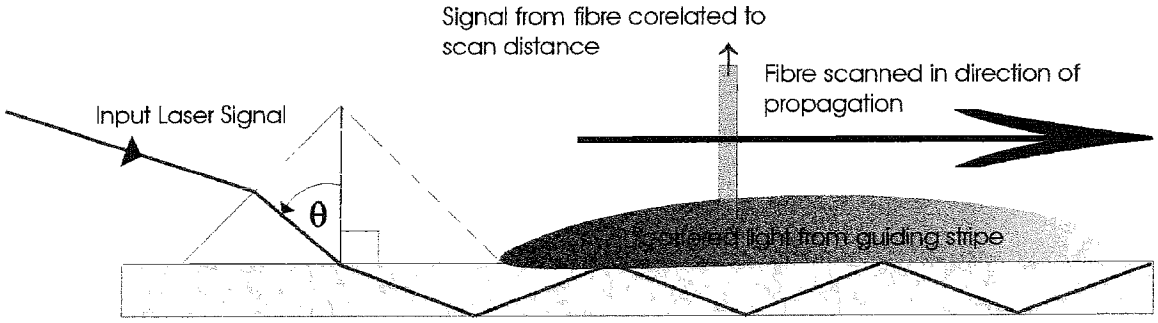

Figure 5.4, determination of loss through detection of scattered radiation

is equipped with such a scanning detector and allows calculation of propagation loss due to scattering once a guided mode has been excited in the same manner as for prism coupling.

Measurement of loss due to scattering relies on the assumption that the primary loss mechanism is scattering and that the primary direction for scattering is out of plane. Sensitivities down to less than 1dB/cm are routinely possible with an error of ±0.1dB/cm, maximum measurable loss for this system is 30dB/cm. The maximum sensitivity to date as reported by the manufactures is 0.2dB/cm, although the likelihood of achieving this experimentally is thought to be remote.

The limitations for the measurement of loss due to scattering centre on the use of the prism coupling technique to initially excite a guided mode, which has been previously outlined. The resulting restrictions regarding the amount of power it is possible to couple into an excited mode may have a considerable affect upon the measurement of propagation loss. The fact that it is not possible to measure losses for realistic guiding structures due to the need for the core to be exposed, further limits the breadth of situation to which the technique can be applied. It has been noted experimentally that any deviations from exponential decay for the guided streak, results in spurious loss measurements. The occurrence of large-scale scattering events such as those caused by particulate contamination or surface irregularities are particularly notable for their ability to distort the guide-wave streak and therefore inhibit accurate loss measurement.

5.2 Layer Properties required for PLC construction

The fabrication of layers suitable for constructing planar waveguiding structure requires a fundamental understanding of the theory that determines the nature of light propagation within dielectric materials and ultimately the phenomena of waveguiding. From an understanding of the basic theory, it is therefore possible to realize the properties that are required of layers in order to form planar waveguides.

This section identifies the attributes that are required of fully dense FHD layers if suitable planar waveguiding structures are to be constructed. The purely optical properties necessary are identified, as well as the physical properties that ultimately affect waveguide operation.

5.2.1 Propagation of Electromagnetic Waves within guiding structures

The propagation of electromagnetic waves within dielectric media can be described vectorally using Maxwell's equations relating electric field **E** to magnetic flux density **B**, and magnetic field **H** to electric flux density **D** via the following curl equations;

$$\nabla \times \mathrm{E} = -\frac{\partial \mathrm{B}}{\partial t}$$

$$\nabla \times \mathrm{H} = \frac{\partial \mathrm{D}}{\partial t}$$

and the divergence conditions indicating the lack of free charges and poles;

$$\nabla \cdot \mathrm{D} = 0$$

$$\nabla \cdot \mathrm{B} = 0$$

where the four field vectors are related by the following relationships;

$$\mathrm{D} = \varepsilon \mathrm{E}$$

$$\mathrm{B} = \mu \mathrm{H}$$

ε is the dielectric permittivity and μ is the magnetic permeability of the medium. Through substituting for **D** and **B** into Maxwell's equations, and taking the curl, the following can be arrived at;

$$\nabla \times (\nabla \times \mathbf{E}) = -\mu\varepsilon \frac{\partial^2 \mathbf{E}}{\partial t^2}$$

$$\nabla \times (\nabla \times \mathbf{H}) = -\mu\varepsilon \frac{\partial^2 \mathbf{H}}{\partial t^2}$$

It is then possible to apply the divergence conditions and use the vector identity;

$$\nabla \times (\nabla \times \mathrm{Y}) = \nabla(\nabla \cdot \mathrm{Y}) - \nabla^2 \mathrm{Y}$$

to obtain the nondispersive wave equations below;

$$\nabla^2 \mathrm{E} = \mu\varepsilon \frac{\partial^2 \mathrm{E}}{\partial t^2}$$

$$\nabla^2 \mathrm{H} = \mu\varepsilon \frac{\partial^2 \mathrm{H}}{\partial t^2}$$

The above wave equations hold of each component of the field vector, all satisfying the scalar wave equation expressed in rectangular Cartesian coordinates below;

$$\nabla^2 \psi = \frac{1}{v_p^2} \frac{\partial^2 \psi}{\partial t^2}$$

where ψ may represent a component of **E** or **H** field and v_p is the phase velocity in the dielectric medium. It follows from the above that;

$$v_p = \frac{1}{(\mu\varepsilon)^{1/2}} = \frac{1}{(\mu_r\mu_0\varepsilon_r\varepsilon_0)^{1/2}}$$

where μ_r and ε_r are the relative permeability and permativity for the dielectric medium, μ_0 and ε_0 are the permeability and permativity of free space. It therefore follows that the velocity of light in free space if given by the following;

$$c = \frac{1}{(\mu_0\varepsilon_0)^{1/2}}$$

For a planar waveguide described using rectangular Cartesian coordinates (x,y,z) it is possible to expand the scalar wave equation previously shown into the following more explicit form;

$$\nabla^2\psi = \frac{\partial^2\psi}{\partial x^2} + \frac{\partial^2\psi}{\partial y^2} + \frac{\partial^2\psi}{\partial z^2}$$

The basic solution of this wave equation is a sinusoidal wave, the most important form of which is a plane wave described by;

$$\psi = \psi_0 \exp j(\omega t - \mathrm{k}\cdot\mathrm{r})$$

where ω is the angular frequency, t is time, **k** is the propagation vector and **r** specifies the coordinate point at which the field is observed. When λ is the optical wavelength in a vacuum, the magnitude of the propagation vector $|\mathbf{k}|$or the vacuum phase propagation constant k is given by;

$$k = \frac{2\pi}{\lambda}$$

It is therefore possible to describe propagating electromagnetic waves within a dielectric medium as a periodically varying electric field **E** and a corresponding magnetic field **H** orientated at right angles to each other.

Having described the nature of electromagnetic waves propagation within dielectric media, further development allows the occurrence of waveguiding to be explained. The planar waveguide is the simplest form of optical waveguide, consisting of a dielectric slab

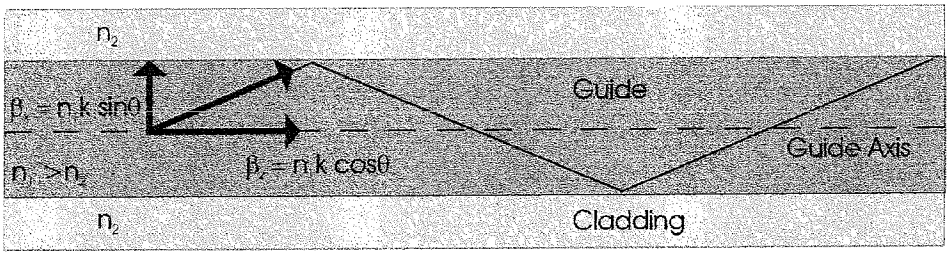

Figure 5.5, electromagnetic wave propagation in a planar waveguide

with index n_1 sandwiched between two slabs of index n_2, where $n_1 > n_2$, shown in figure 5.5. The treatment of electromagnetic wave propagation within a planar waveguide can be simplified by considering a plane monochromatic wave propagating in the direction of a ray path. The optical wavelength for such a wave is reduced to λ/n_1 and the vacuum propagation constant is increased to $n_1 k$. When θ is the angle between the wave propagation vector and the guide axis, the plane wave can be resolved into two components propagating in the z and x directions. The phase propagation constants in the two directions are given by;

$$\beta_z = n_1 k \cos\theta$$
$$\beta_x = n_1 k \sin\theta$$

The x component is reflected at the interface between n_1 and n_2. When the total phase change after two successive reflections between upper and lower interfaces is equal to $2m\pi$ radians, then constructive interference occurs. A standing wave is therefore obtained when the mode number m is an integer value. When m is equal to zero the resulting standing wave forms with a maximum in electric field at the centre of the guide, decaying towards the boundary. Continuation of decaying electric field across the boundary leads to the formation of Evanescent fields, which will be discussed later in this section. The optical wave is effectively confined within the guide, and electric field distribution in the x-direction does not change as the wave propagated in the z-direction. A stable field distribution in the x-direction with only periodic z dependence is known as a mode. The mode number m effectively denotes the number of zeros present in the standing wave across the guide, and signifies the order of the mode.

A specific mode is obtained only when the angle between the propagation vectors and the interface have a particular value. Light propagation within the guide is thus formed into discrete modes, each typified by a distinct value of θ. The periodic z dependence for a mode can be described by the form $\exp(-j\beta_z z)$. The invariance of the modal field pattern in all but the z-direction allows the propagation constant in the z-direction to describe the propagation constant for the mode (i.e. $\beta = \beta_z$). Assuming a time dependence with angular frequency of $\exp(j\omega t)$, allows a mode propagating in the z-direction to be described by $\exp j(\omega t - \beta z)$.

Dominant modes propagating in the z-direction may be considered as plane waves corresponding to different specific vector angles in the planar guide. Plane waves giving constructive interference result in standing wave patterns across the guide, following sine or cosine formulae. Transverse Electric (TE) modes occur when the electric field is

perpendicular to the direction of propagation hence E_z is equal zero. Transverse Magnetic (TM) modes occur when a component of the electric field is in the direction of propagation, but H_z is equal to zero, a schematic of mode formation is shown in figure 5.6.

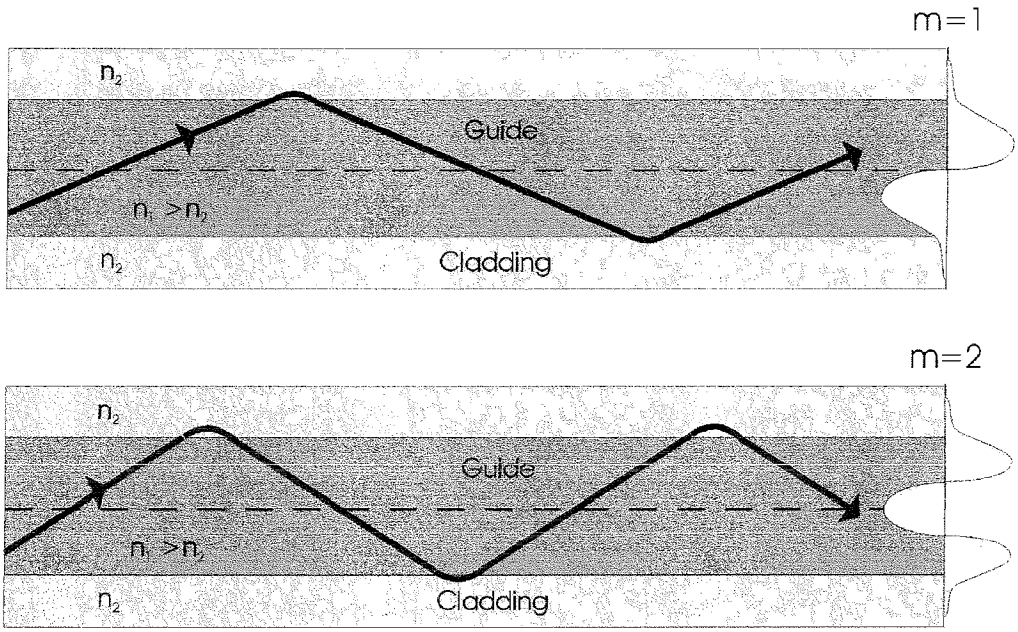

Figure 5.6 guided mode formation in planar waveguides

As has been mentioned the electric field decays within the clad as the mode extends outside of the guide. In order to appreciate the formation of Evanescent fields it is necessary to use the wave theory model of total internal reflection at a planar interface, schematically shown in figure 5.7 and 5.8. The wave equation in Cartesian coordinates for an electric field

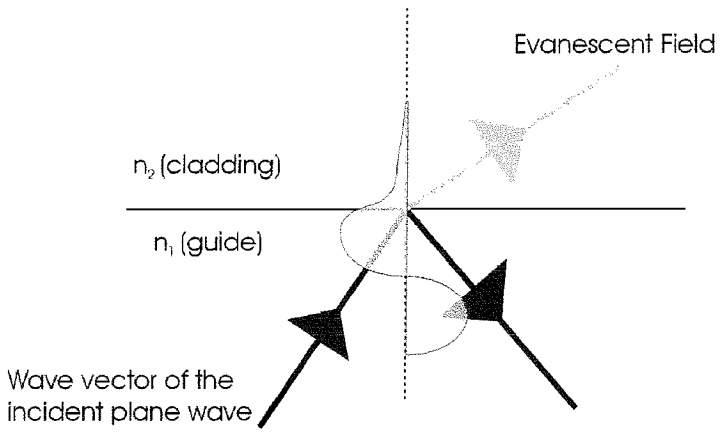

Figure 5.7, formation of evanescent fields in cladding

in a loss-less medium as has been previously shown is;

$$\nabla^2 E = \mu\varepsilon \frac{\partial^2 E}{\partial t^2} = \frac{\partial^2 E}{\partial x^2} + \frac{\partial^2 E}{\partial y^2} + \frac{\partial^2 E}{\partial z^2}$$

Since the guide-cladding interface lies in the *y-z* plane and the wave is incident on the interface in the *x-z* plane, $\partial/\partial y$ may be assumed to be zero. Along the interface in the *z*-direction, due to the phase fronts matching at all points, the incident, reflected and transmitted waves all have the same propagation constant. As previously mentioned a wave propagating in the *z*-direction maybe described by exp $j(\omega t-\beta z)$. Additionally there is

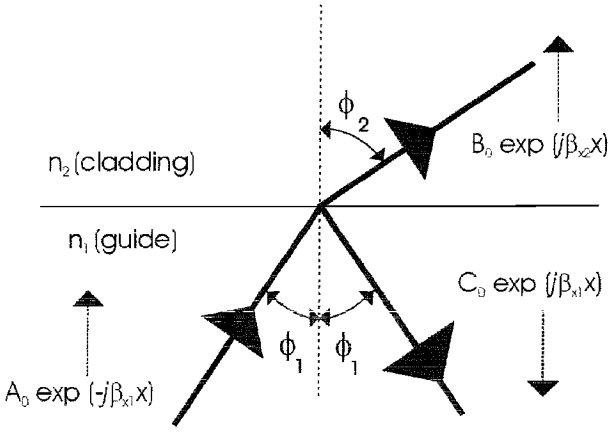

Figure 5.8, resolved wave vectors for incident, transmitted and reflected waves at a dielectric interface

propagation in the *x*-direction, resolving components in this plane gives the following propagation constants in the *x*-direction for the guide and cladding;

$$\beta_{x1} = n_1 k \cos\phi_1$$
$$\beta_{x2} = n_2 k \cos\phi_2$$

Thus incident, transmitted and reflected waves will have amplitudes A, B and C respectively of the following form;

$$A = A_0 \exp-(j\beta_{x1}x)\exp j(\omega t - \beta z)$$
$$B = B_0 \exp-(j\beta_{x2}x)\exp j(\omega t - \beta z)$$
$$C = C_0 \exp(j\beta_{x1}x)\exp j(\omega t - \beta z)$$

Using $\cos^2\phi + \sin^2\phi = 1$ it is possible to express the propagation constant in both core and clad in the following forms;

$$\beta_{x1}^2 = (n_1^2 k^2 - \beta^2) = -\xi_1^2$$
$$\beta_{x2}^2 = (n_2^2 k^2 - \beta^2) = -\xi_2^2$$

When an electromagnetic wave is incident upon an interface between two dielectric media, Maxwell's equations require that both the tangential components of **E** and **H** and the normal components of **D** and **B** are continuous across the boundary. If the boundary is defined by x equals zero then both TE and TM modes can be considered. Applying the boundary conditions to a TE mode, the normal components of the **E** and **H** fields may be equated giving;

$$A_0 + C_0 = B_0$$

The electric field component in the *y*-direction is related to the tangential magnetic field component H_z by the following;

$$-H_z = \frac{1}{j\mu_r\mu_0\omega}\frac{\partial E_y}{\partial x}$$

Applying the tangential boundary conditions and equating H_z gives;

$$-\beta_{x1}A_0 + \beta_{x1}C_0 = -\beta_{x2}B_0$$

It can therefore be shown that;

$$C_0 = A_0\left(\frac{\beta_{x1} - \beta_{x2}}{\beta_{x1} + \beta_{x2}}\right) = A_0 r_{ER}$$

$$B_0 = A_0\left(\frac{2\beta_{x1}}{\beta_{x1} + \beta_{x2}}\right) = A_0 r_{ET}$$

Where r_{ER} and r_{ET} are the reflection and transmission coefficients. When both β_{x1} and β_{x2} are real the reflected wave *C* is in phase with the incident wave *A*, corresponding to a partial reflection of the incident beam. However, as ϕ_1 is increased the component β_z increases resulting in a decrease of β_{x1} and β_{x2}. Continuation of this process results in β_{x2} passing through zero, corresponding to ϕ_1 reaching the critical angle for total internal reflection. As ϕ_1 is further increased β_{x2} becomes imaginary and maybe expressed in the form $-j\xi_2$. During this process β_{x1} remains real since $n_1 > n_2$. Under the terms for total internal reflection;

$$C_0 = A_0\left(\frac{\beta_{x1} + j\xi_2}{\beta_{x1} - j\xi_2}\right) = A_0 \exp(2j\delta_E)$$

where δ_E is the phase shift of the reflected wave relative to the incident wave and is signified by;

$$\tan\delta_E = \frac{\xi_2^2}{\beta_{x1}}$$

It should also be noted that under the conditions of total internal reflection the magnitude of the incident and reflected beams are identical (i.e. $|C_0| = |A_0|$).

Similar analysis as has been applied to TE polarisation can be applied to TM polarisation giving;

$$C_0 = A_0\left(\frac{\beta_{x1}n_2^2 - \beta_{x2}n_1^2}{\beta_{x1}n_2^2 + \beta_{x2}n_1^2}\right) = A_0 r_{HR}$$

$$B_0 = A_0\left(\frac{2\beta_{x1}n_2^2}{\beta_{x1}n_2^2 + \beta_{x2}n_1^2}\right) = A_0 r_{HT}$$

As for the TE case, increasing the angle of incidence such that β_{x2} goes to zero and then becomes imaginary leads to a phase shift when total internal reflection occurs such that;

$$C_0 = A_0 \exp(2j\delta_H)$$

where

$$\tan\delta_H = \left(\frac{n_1}{n_2}\right)^2 \tan\delta_E$$

It can therefore be seen that the phase shift due to total internal reflection is dependent on angle of incidence and the polarisation of the beam.

The phase shift of the mode has a direct effect upon the nature of the electric field within the cladding, and is directly related to the formation of evanescent fields. Before total internal reflection occurs, at angles below ϕ_1, partial reflection is dominant and β_{x2} is real. However, upon total internal reflection β_{x2} becomes imaginary and can be expressed in the form $-j\xi_2$, therefore;

$$B = B_0 \exp(-\xi x)\exp j(\omega t - \beta z)$$

Thus the amplitude of the field in the cladding is observed to decay exponentially in the *x*-direction. The formation of Evanescent fields upon total internal reflection has therefore been explained.

To summarise, a guided mode must obey Maxwell's equations, form a stable standing wave propagating in the z-direction, and have tangential components of **E** and **H** and normal components of **D** and **B** that are continuous across the boundary and decay exponentially once across the boundary. A wave that does not match these conditions will not be guided and therefore will not form a mode.

So far the discussion has been solely concerned with planar waveguides, however the consideration of three-dimensional guiding structures is necessary in order to understand practical waveguide devices. A large amount of theoretical work treating fibre guides exists. UV written planar waveguides are unlikely to be identical to fibre guides, but are suitable for indicating the parameters that are important during the design, fabrication and characterisation of three-dimensional guiding structures. Exact solutions of Maxwell's equations for cylindrical guides in a dielectric waveguide are extensive and yield complex

results, therefore the complete derivation will not be tackled. However, discussion of similarities to planar waveguides and the development of some of the phenomena previously discussed does aid the understanding of three-dimensional guides.

Both TE ($E_z = 0$) and TM ($H_z = 0$) modes form within cylindrical guides in the same way as for planar guides, but are bound in two directions rather than one. Modes are therefore described by two integers l and m as opposed to just m as in planar guides. The radial nature of the guide allows the formation of hybrid modes where E_z and H_z are nonzero this corresponds to skewed rays. Hybrid modes are designated as HE_{lm} and EH_{lm} modes, thus allowing the formation of TE, TM, HE and EH modes within cylindrical guides. However, weak guides corresponding to small grazing angles form modes that are dominated by forward propagation. It is therefore possible to approximate for HE, EH, TE and TM modes using two linearly polarized (LP) components. LP modes do not represent the exact modal structure for a guide except for the fundamental mode. However, within weakly guiding fibres HE-EH mode pairs occur known as degenerate modes, which have almost identical propagation constants. The superposition of degenerate modes corresponds to a particular LP mode regardless of their HE, EH, TE or TM configurations. This linear combination of degenerate modes obtained from the exact solution produces a useful simplification in the analysis of weakly guiding structures.

When considering the formation of LP modes within a guiding structure it is possible to derive from Maxwell's equations or modified Bessel functions both normalised frequency V and normalised propagation constant b;

$$V = ka\left(n_1^2 - n_2^2\right)^{1/2}$$

$$b = \frac{(\beta/k)^2 - n_2^2}{n_1^2 - n_2^2}$$

Using the above allows the determination of propagation characteristics for the various modes from their dependence upon optical wavelength and guide parameters such as core size a. The normalised propagation constant must lie between 0 and 1 since β has the bounds of n_2k and n_1k. On the limit of mode propagation when $\beta = n_2k$, the mode phase velocity is equal to the velocity of light in the cladding and the mode is no longer guided properly, the mode is said to be "cut-off". Unguided or radiation modes have frequencies below cut-off where $\beta < n_2k$. Leaky modes exist below cut-off and behave as very lossy modes rather than radiation modes, this happens because cut-off does not occur abruptly at $\beta \leq n_2k$. As β is increased above n_2k less power propagates in the clad and more power is

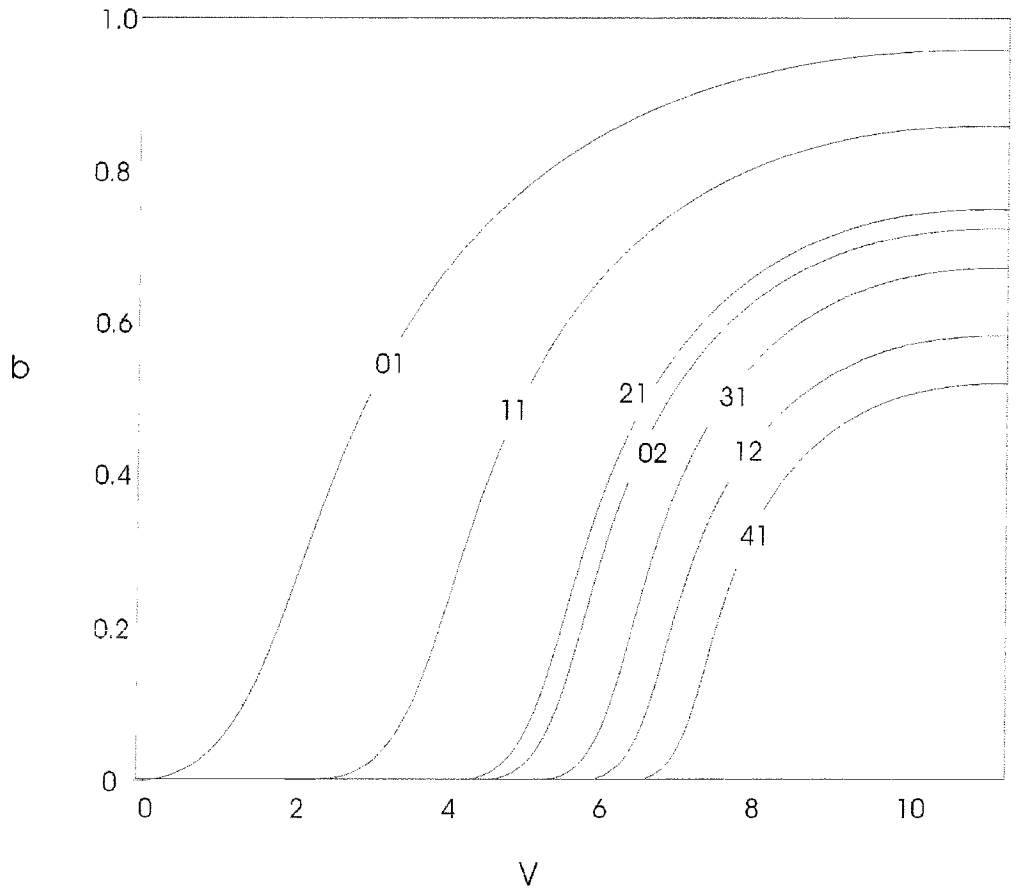

Figure 5.9, b/V plot showing a number of LP modes

confined to the core region, until $\beta = n_1 k$ at which point all of the power is confined to the core. The cut-off point for a particular mode corresponds to a distinctive value of normalised frequency V_c. It is possible to numerically solve V_c as a function of b against V, a plot of which can be seen in figure 5.9.

Such b/V plots can be used to determine the modal structure for a given guide. It can be seen that the cut-off for the LP_{01} mode corresponds to a normalised frequency of zero. Cut-off for the next mode LP_{11} occurs at $V_c = 2.405$, therefore for values of V between 0 and 2.405 only the LP_{01} mode will be supported and the guide is effectively single mode.

5.2.2 Effect of Refractive Index upon PLC Design

Having already discussed the theory that determines the nature of light propagating within waveguiding structures, it is worth highlighting the specific dependence of guiding characteristics due to controlling the refractive index profile. The normalised frequency or V-number, which has been described in section 5.2.1, implies that the higher the index difference between core and clad the smaller the area of guide required to maintain constant

V-number and therefore constant modal operation. A greater waveguide Δn has the effect of allowing smaller physical device sizes.

The use of high waveguide Δn also allows tighter bend radii to be achieved. Bend loss in the form of radiation occurs due to the energy in the evanescent field on the outside of the bend, exceeding the velocity of light in the cladding. Inhibition of the guidance mechanism results in energy radiating from the guiding region, as shown in figure 5.10. The loss can be generally represented using an attenuation coefficient of the following form;

$$\alpha_r = c_1 \exp(-c_2 R)$$

Where R is the radius of curvature of the guide and c_1, c_2 are constants that are independent of R. It should be noted that the bend loss increases exponentially with decreasing bend radius. Generally the higher the Δn for a guiding structure the tighter the bend radius that can be used for a given loss since the mode remains more tightly confined within the core region. The ability to use high Δn therefore allows the design of more compact PLC devices.

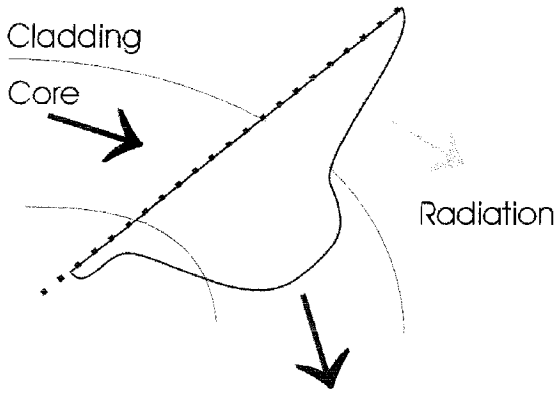

Figure 5.10, occurrence of radiation loss due to waveguide bend

The ultimate aim for any integrated optical device is for it to be used within larger transmission systems, in which case the compatibility of guides to fibre is of importance. The minimisation of insertion losses through approximate index matching of PLC structures to fibre guides both in size and index will ultimately allow more straightforward integration of PLCs into larger systems.

The use of direct UV writing to fully define the waveguiding structure, as will be discussed fully in Chapter 6, requires that an index matched structure results from the deposition stage. Rigorous control of index while varying composition and associated processing parameters is therefore required. The range of refractive indices thought to be achievable through compositional variation is approximately 1.46-1.50, as outlined in

Chapter 4. However, the need to produce sets of complementary layers is likely to reduce the range of indices that can be achieved for fully index matched three layer structures. The UV induced index that is likely to be achievable is in the range of 3×10^{-3}, which has been observed previously in germanosilicate glass systems (see Chapter 6). The enhancement of the UV induced Δn is hoped to be possible through the thorough understanding of the fabrication process, materials compositional systems and waveguide definition process. Ultimately the dimensions and geometries of waveguide devices will be dependent upon the range of refractive indices that can be achieved.

5.2.3 Effect of Consolidation Parameters

The range of compositions that can be used to form layers is limited by the melting point of the Silicon substrates used, as mentioned in Chapter 4. However, the range of compositions that can be used to form multi-layered structures is further limited by the need for compatible consolidation regimes as well as the index matching criteria outline in the previous section.

There are several possible routes that can be used to construct multi-layer structures; all layers should have the same consolidation temperature, or the consolidation temperatures should be stepped to result in sequential consolidation. The possibility of finding three compositions that all share the sample consolidation temperature and have the same index, but for which the core composition is higher in Germanium, is likely to be extremely remote. The need to modify consolidation temperature while maintaining index is therefore required. Deposition and subsequent consolidation of multiple layers can take place in two possible ways.

Sequential deposition and consolidation involves the independent deposition and consolidation of each layer, resulting in the construction of a multiple layered structure. The fact that subsequent layers are deposited and consolidated on top of existing layers requires that the consolidation parameters be tailored to ensure that previous layers are not further modified. The reflow of previous layers is unlikely, as highlighted in Chapter 4, however extended periods of time above an underlayer's consolidation temperature is likely to result in crystal growth. It is therefore necessary for subsequent layers to have a consolidation temperature that is lower than for any layers already present, such that Underclad T_c > Core T_c > Overclad T_c.

The second possible consolidation temperature regime for multiple layered structures is for parallel deposition and consolidation to take place. The deposition of all layers in soot form and subsequent consolidation of all layers simultaneously introduces the requirement for a different consolidation temperature system. As previously mentioned it is impossible to have all layers with the same consolidation temperature and still adhere to the other requirements for a multi-layered structure. However, stepping consolidation temperature so that Underclad T_c < Core T_c < Overclad T_c would allow simultaneous consolidation to take place. Any deviation from this structure would be likely to result in gas trapping within lower layers due to higher layers consolidating first and sealing the structure. The consolidation temperatures must also be close enough to allow consolidation to occur at the same temperature, but result in a consolidation rate difference that reflects the stepped consolidation temperatures.

All of the waveguiding structures produced during the work undertaken have used the sequential deposition and consolidation method. Although there is an increased susceptibility to contamination through subsequent processing, this far outweighs the increased likelihood of crystallisation occurrence within the bottom layer as is the case for simultaneous consolidation. This does not imply that simultaneous consolidation is not possible, the literature on the subject is vague and gives no precise indication as to how multiple layers are consolidated. However, it is the author view that simultaneous consolidation is widely used especially in commercial processes due to the associated reduction in processing time.

5.2.4 Thickness and Uniformity Requirements for PLC Construction

The thickness of the three layers which form the guiding structure have a profound affect upon the nature of the guide as highlighted by the discussion of V-number in section 5.2.1. Although the lateral guiding characteristics will be solely defined by the UV writing process, the physical vertical dimensions of any guide are defined by the deposited layer thickness. The underclad layer must be thick enough to isolate the evanescent field for the guided mode from the Silicon substrate. If the underclad is not thick enough, the high index of the substrate may strip the guided mode from the core, resulting in guides with high loss. Underclad layers are usually around 10μm thick, which is more than enough to significantly isolate the guided mode. The total underclad, including thermal oxide and FHD layer, used

in this project are normally approximately 20μm. The use of thicker underclad layers has been employed to aid deposition uniformity of core layers as highlighted in Chapter 4.

The core thickness required is dependent upon the required modal operation for the guiding structure. Using the V-number for cut-off to a single mode for a symmetrical guide as discussed in section 5.2.1, it can be shown that a 6μm core with Δn of 3×10^{-3} cuts-off to single mode operation at approximately 1480nm. Therefore a 6μm core is a suitable first approximation for single mode operation within the telecom range of 1300-1600nm, when the absolute UV induced index change can only be estimated. It is ultimately envisaged that vertical core size will have to be tailored to a value that matches the range of UV induced Δn found to be possible.

The overclad like the underclad must be thick enough to ensure that the guided mode is not affected by anything other than the intended guiding structure. The overclad used in all multi-layered FHD structures is 10μm thick, thereby ensuring that evanescent fields remain within the clad at all times, resulting in minimise of radiation loss due to mode leaking.

The absolute thickness of both clad layers is not ultimately relevant, as long as thickness exceeds the critical value enforced by the size of the evanescent field, therefore rigorous process control of clad thickness is not required. The tolerable thickness variation for both clad layers can be relatively large, since a thickness change outside of the critical thickness has no affect upon guiding characteristics. As outlined the thickness of the core layer is critical to the modal properties of the guiding structure, consequently any variation in core thickness within a layer will directly affect the guiding nature. Using V-number it can be shown that a thickness variation of ±50nm results in a shift in cut-off wavelength of approximately 10nm for the index regime previously defined. The affect of thickness variation upon modal structure can be minimised through ensuring that operating wavelength is significantly far from the cut-off condition.

The uniformity of layers also has an effect upon the inherent loss for a guiding structure. The interface between layers and the layers themselves must be free from particulate contamination. The overall roughness of the layer interfaces must be on a scale that does not cause scattering. Scattering centres that are on a similar scale to the wavelength of light being used will cause the most significant scattering. In general, the minimisation of scattering sites to a size significantly smaller than the operating wavelength will minimise loss due to scattering.

The occurrence of phase separation or crystallisation within the layers will also be a likely cause of scattering, the minimisation of such affects will reduce the loss for a given structure. It is well documented that rapidly quenched glasses, in particular silicates used in fibre production, form density fluctuations upon glass formation. It can be assumed that similar density fluctuations and corresponding spatial variation in refractive index occurs within FHD layers, loss due to this affect resulting from scattering is proportional to λ^{-4}.

5.3 FHD Layer Production Using the Quaternary Silica System

The production of optical quality layers for the subsequent construction of planar waveguides requires the optimisation of optical and physical layer properties that determine guiding through the manipulation of fabrication parameters. The simultaneous management of parameters that directly effect multi-layer sample production must also be taken into consideration. Resulting in the need to not only produce layers that are individually suitable, but that are also compatible with the other layers present within a multi-layered structure. The quaternary system formed by SiO_2:P:B:Ge was used for the investigation since it offer the greatest degree of flexibility, and allowed all layers produced to have a degree of processing similarity not found to exist to such a degree for other compositions.

The very large parameter space formed by the use of combined Phosphorus, Boron and Germanium doping of silicate glasses would be virtually impossible to completely characterise. A complete knowledge of the quaternary system is beyond the scope of the project, optimisation of processing parameters to optical properties therefore took place within a suitably small range of compositions. As has already been highlighted in Chapter 4 maximum stable doping ranges for Phosphorus, Boron and Germanium, theoretically in the vapour stream, have been defined as approximately 20, 20 and 40 mole percent respectively.

The detailed characterisation of optical and processing parameters exhibited by compositions within the parameter space outlined required a large number of process development steps. In particular, each composition deposited must have its consolidation conditions determined, which can take a considerable amount of time. Upon production of a layer with suitable quality measurement of refractive index can take place. The potentially excessive length of time required to fully define the parameter space outlined led to the use of the Taguchi method in order to reduce the number of experiments needed, however

subsequent full set analysis was require to fill in the gaps present within the data sets. This section describes the optimisation techniques employed and the results gained.

5.3.1 Taguchi Method

The Taguchi method, also known as orthogonal array analysis, allows the complete description of an experimental parameter space without the need for independent variation of all relevant parameters. Assumptions regarding the independence and linear affect of parameters upon a measurable outcome allow multiple variables to be modified simultaneously, and the independent affect of each variable to be extrapolated. The execution of experiments that fit into a known orthogonal array, and the subsequent measurable result for each experiment can then be used to describe the individual effect of each experimental element upon the observed set. The wider application of the effect determined for each element can be used to fully describe the parameter space within which the experimental set exists.

In order to successfully implement the Taguchi method it is important to carefully construct an experiment that fits one of the well defined orthogonal arrays. Eighteen standard arrays have been derived by Taguchi [Bendell *et al*, 1990], each subsequent array is increasingly complex and therefore defines more complex systems. All arrays revolve around assigning the relevant variables a number of levels, such that each variable is assigned a column in the array and the integers within the array indicate the relative level of the variable for the experimental set formed by the row across the array.

Experiment Number	Variable Number		
	1	2	3
1	1	1	1
2	1	2	2
3	2	1	2
4	2	2	1

The array illustrated uses an L4 standard matrix and can be used to define a system consisting of three variables, which can be set to two values. The effect of varying a specific variable from state 1 to 2 is extrapolated by subtracting the combined result of the two experiments with the variable at state 2 from the two experiments with the variable at state

1. As can be seen, only four experiments are required to fully define such a system compared to the nine needed to individually vary each parameter.

The application of Taguchi analysis to the quaternary silica system involved the use of an L4 matrix as outlined. The experiment designed to fit the array is outlined below;

	P	B	Ge	
1	L	L	L	R_1
2	L	H	H	R_2
3	H	L	H	R_3
4	H	H	L	R_4

The assignment of low (L) and high (H) values for relative doping levels for a given dopant allowed the derivation of four compositions the characterisation of which could be used to define the parameter space associated with the variable levels. Extrapolation of the individual dopant effects required the use of the expressions below;

$$P(L \rightarrow H) = (R_3 + R_4) - (R_1 + R_2)$$
$$B(L \rightarrow H) = (R_2 + R_4) - (R_1 + R_3)$$
$$Ge(L \rightarrow H) = (R_2 + R_3) - (R_1 + R_4)$$

The results used for the characterisation of the compositions were consolidation temperature and refractive index. The deposition and subsequent characterisation of any four compositions which match the criteria set out by the array can therefore be used to define the area of the parameter space bounded by the low and high extremes in composition. The application of the model formed by the Taguchi analysis therefore allows the calculation of a linear approximation for both the refractive index and consolidation temperature for any composition that falls within the parameter space investigated.

The initial set of compositions used within the Taguchi analysis represented the entire parameter space for which high quality layers within the quaternary system had been previously observed. The theoretical vapour stream composition in mole percent for the three dopants were varied from low to high between the following values;

	Low	High
P-doping	10	20
B-doping	6	12
Ge-doping	2	20

Although consolidation outside of the parameter space represented by these compositions is possible, the bounds represented by LLL and HHH must be achievable. For example, the use of lower Phosphorus doping levels is easily achievable when countered by increases in the other dopants, but the low value used in the Taguchi set must be sensible when combined with the low Boron and Germanium doping levels. A degree of educated estimation was used when constructing the initial set illustrated above, since the sets have to represent relative low and high doping levels for each dopant, and not the absolute limits possible.

Upon realisation of the initial set, a second set was constructed using the model produced by the initial set. The second set was devised not only to check the accuracy of the Taguchi method, but also to represent compositions that were closer to the type of layers required for three layer structures. The doping levels used for the second set are shown below;

	Low	High
P-doping	10	15
B-doping	8	12
Ge-doping	2	20

The results for the second set were included within the model of the parameter space described by the Taguchi analysis. The total affect of the dopants upon refractive index is included below;

Dopant	dn/mole %	Error
P	2.85×10^{-3}	$\pm2.6\times10^{-4}$
B	-5.63×10^{-4}	$\pm1.1\times10^{-4}$
Ge	3.76×10^{-3}	$\pm1.4\times10^{-4}$

The magnitude of the index changes due to doping for all three dopants is consistent with that presented in Chapter 4, regarding the individual affect of dopants upon the refractive index of doped silica. The errors that appear within the model would appear to be consistent with those previously outline for critical angle measurement of refractive index in section 5.1.2. However, the error for the affect of Phosphorus appears a little high with respect to both the Boron and Germanium, and slightly above that expected for refractive index determination. The explanation for the larger error associated with Phosphorus doping is

likely to be the instability of Phosphorus during processing, resulting in a non-linear relationship between vapour stream composition and the composition of the consolidated layer (this effect has been experimentally verified in Chapter 4).

The use of the model resulting for the Taguchi analysis to accurately determine consolidation temperature is considerably less consistent than that seen for refractive index. The affect upon consolidation temperature for concentration of each dopant is outlined below;

Dopant	T_c/mole	Error
P	-2.75°C	±15.8°C
B	-2.725°C	±11.5°C
Ge	-22.8°C	±9.7°C

The errors for all of the modelled dopant effects are within those expected for the technique used to determine consolidation temperature, as outlined in Chapter 4. The average effect of Germanium doping is also consistent with the majority of the previous work, and is therefore considered representative of a genuine effect. The modelled affect upon consolidation temperature for both Phosphorus and Boron doping is not consistent with that found from experience. All previous work shows that the independent use of both P-doping and B-doping have a larger reducing affect upon T_c than for Ge-doping, which is consistent with theoretical effects outlined in Chapter 4.

Further use of the model to predict compositions suitable for construction of guiding structures highlighted considerable inaccuracies within the model. It was found that both refractive index and consolidation temperature could not be predicted with a suitable degree of accuracy. An amount of model accuracy was observed for compositions nominally similar to those used to construct the model, however significant deviation resulted in model breakdown. The use of Taguchi analysis to characterise and optimise the FHD production of doped silicate layers within the quaternary system outline was deemed too inaccurate to aid fast suitable layer acquisition.

The source of the inaccuracies experienced for the Taguchi analysis constructed model is likely to be the initial assumption that dopants act to modify n and T_c independently and in a linear manner. A degree of accuracy was observed across the complete parameter space, particularly for refractive index. However, detailed modelling of effects is probably skewed by complex interaction between dopants at specific doping

levels, which will be discussed in detail in the next section. It is thought that complete modelling of the system using Taguchi analysis is probably possible, but would require a considerably more complex multi-levelled system. In view of maximising the information gained about compositions suitable for three layer structure construction, complete modelling of the system was not deemed that most efficient direction in which to proceed. Further analysis of the quaternary doping system was not under taken using Taguchi analysis.

5.3.2 Full Set Method

The failure of Taguchi analysis constructed models to fully define the effect of compositions within the quaternary system upon refractive index and consolidation temperature required the use of an additional technique. The method employed used the sequential bracketing of compositions to investigate detailed effects upon n and T_c. Using the comprehensive raw data already acquired during construction of the Taguchi sets, it was possible to bracket doping levels around compositions which gave the results most similar to those required. Homing in on suitable compositions took place by gathering further information regarding the affect of dopants upon n and T_c. The occurrences of combined dopant effects were also noted.

In total more than 30 different compositions were fully characterised before five suitable compositions allowing the construction of several consistent three layer guiding structures were achieved. The large number of compositions required to only partially describe the parameter space formed by the quaternary system of Phosphorus, Boron, Germanium and Silicon, highlights the complexity of the task undertaken. The full optimisation and characterisation of all layers that form the set represents a considerable amount of work. Illustrations of the problems encountered while investigating the full set are included below;

P (mole%)	B (mole%)	Ge (mole%)	n	T_c (°C)
15	12	2	1.4721	1200 to 1250
13	12	2	1.4714	1200 to 1250
10	12	2	1.4702	1200 to 1250 (DNC)

The example above shows the gradual decrease in P-doping level, the aim of which was to achieve a refractive index of 1.47. However, having achieved the refractive index required it

was found that the composition could not be consolidated to a high quality layer. The maximum in layer quality, normally associated with full density, occurs in the temperature range of 1200 to 1250°C, but does not result in a layer suitable for waveguiding structures. This example is one of many such occurrences in which a composition that was expected to have suitable characteristics, actually results in an inappropriate layer. Another effect that significantly hampered the optimisation of layers upon specific requirements is illustrated below;

P (mole%)	B (mole%)	Ge (mole%)	n	T_c (°C)
14	3	2	1.4701	1325 to 1350
14	8	2	1.473	1200 to 1250
3	10	20	1.4961	1300 to 1335
3	20	20	1.4965	1200 to 1250

It can be seen for the two different types of composition, for which, in both cases, the addition of Boron was intended to reduce the index in fact has the opposite effect. A significant reduction in consolidation temperature is observed to simultaneously occur. The explanation of this effect is discussed in detail along with other anomalous doping effects in section 5.3.3.

The use of the full set analysis previously outlined has allowed the production of compositions suitable for direct UV written waveguides. It has been possible to produce index matched clad layers with n = 1.47, and an approximation for an index matched core with n=1.48. It was decided to initially produce an approximation for an index matched structure in order to ensure that guiding within the core occurs even if determination of the core index has been significantly inaccurate. Core layers that are fully index matched to n = 1.47 have been achieved, but have not been used to construct waveguides to date due to the increased complexity associated with analysis. The consolidation temperatures have been stepped in a manner consistent with that outlined in section 5.2.3. Three core layers with high, medium and low relative Germanium doping that are all index matched to 1.48 have been achieved, with the aim of allowing Ge-doping level effects upon UV writing to be determined. The table below illustrates the compositions that have been determined suitable for three layer waveguide construction;

Layer Type	P (mole%)	B (mole%)	Ge (mole%)	n	T_c (°C)
Overclad	13	8	2	1.4706	1200 to 1250

High Ge Core	1	10	15	1.4803	1300 to 1350
Medium Ge Core	12	3	10	1.4810	1250 to 1300
Low Ge Core	20	10	5	1.4808	1200 to 1250
Underclad	14	3	2	1.4701	1325 to 1350

The incorporation rate for Germanium, the determination of which was discussed in Chapter 4, results in actual core layer compositions of approximately 6/4/2 mole percent Ge incorporated. The clad layers are estimated to contain approximately 0.8 mole percent Ge incorporated. As previously outlined Germanium is present within the clad composition in order to simplify the characterisation and optimisation of layers suitable for producing waveguiding structures. At the low level of 0.8 mole percent, it is not envisaged that a significant UV induced index change will result in the clad layers. Ultimately it is intended to completely remove Germanium from the clad layers in order to maximise possible UV induced Δn for the waveguiding structure.

5.3.3 Expected and Observed Dopant Effects

The relative effect of the dopants upon the structure of silica and resulting affects upon refractive index and consolidation temperature have already be discussed in detail in Chapter 4. However, it is worth reviewing the expected effects prior to discussing some of the unexpected affects that have been observed during the production of layers suitable for waveguiding structures.

All the dopants used have the theoretical effect of decreasing consolidation temperature relative to the composition in which they are included. The degree of structural deviation from the totally connected tetrahedral structure of pure silica, suggests that Phosphorus and Boron doping will have a greater effect upon consolidation temperature compared to Germanium doping. The melting points for Phosphate and Borate glasses are also considerably lower than for Germanate glasses, further indicating the expected effect of dopants included within silica. The effect upon refractive index for multiple dopants included within silica is also expected to follow that which is observed for single component doping of silicate glasses. The expected effect for Germanium and Phosphorus doping is for an increase in relative index, occurring at a similar rate until a concentration of approximately 15 mole% is reached. Doping above 15 mole% leads to the relative effect of Phosphorus decreasing with respect to Germanium. Boron doping is expected to have the

effect of decreasing relative index, but at a considerably lower rate than observed for the increase due to Phosphorus or Germanium doping.

Combining the effect upon refractive index of both Boron and Phosphorus is expected to allow index matching, such that clad layers with very low relative Germanium content can have indices similar to the high relative Germanium concentration core layers. The use of simultaneous Boron and Phosphorus doping is intended to allow relatively independent control of consolidation temperature whilst maintaining refractive indices and Germanium doping level.

The observed effect of dopants upon refractive index and consolidation temperature would appear to be considerably more complex than the expected effects. It has been observed that the effect that Boron doping has upon consolidation temperature directly affects the volitisation of Phosphorus during consolidation. Experimental sets have shown that independent control of Boron and Phosphorus doping levels is almost impossible when both are included within the same layer. Results would seem to suggest that Boron has a much greater effect upon consolidation temperature relative to refractive index, since this is not what is expected it is hypothesised that an additional effect is occurring. The high volatility of Phosphorus can be used to explain what is observed. As Boron doping level is increased then consolidation temperature is reduced thus allowing greater inclusion of Phosphorus within the composition due to its reduced volatility for lower temperatures. The resulting increase in relative Phosphorus doping further decreases consolidation temperature and increases refractive index, thereby increasing the apparent reduction in consolidation temperature and negating any decrease in refractive index induced by Boron doping.

The observed coupling of Phosphorus and Boron doping and the resulting effects upon refractive index and consolidation temperature can be used to explain some of the inaccuracy observed during the Taguchi analysis. Large-scale changes in doping level probably preserve the expected effects that can be assigned to individual dopants. However, incremental changes in doping levels actually result in the effective change of other doping levels. The effects for Phosphorus and Boron when combined are not independent and appear not to be linear when co-dependency is not taken into account.

The construction of three layered samples consisting of overclad and underclad compositions with one of the core composition already determined in section 5.3.2, allowed EDX to be used to determine relative dopant incorporation within each layer present in the resulting planar structure. The results from this analysis highlights the problems associated with calibrating dopant incorporation within layers, and can be seen in figure 5.11,

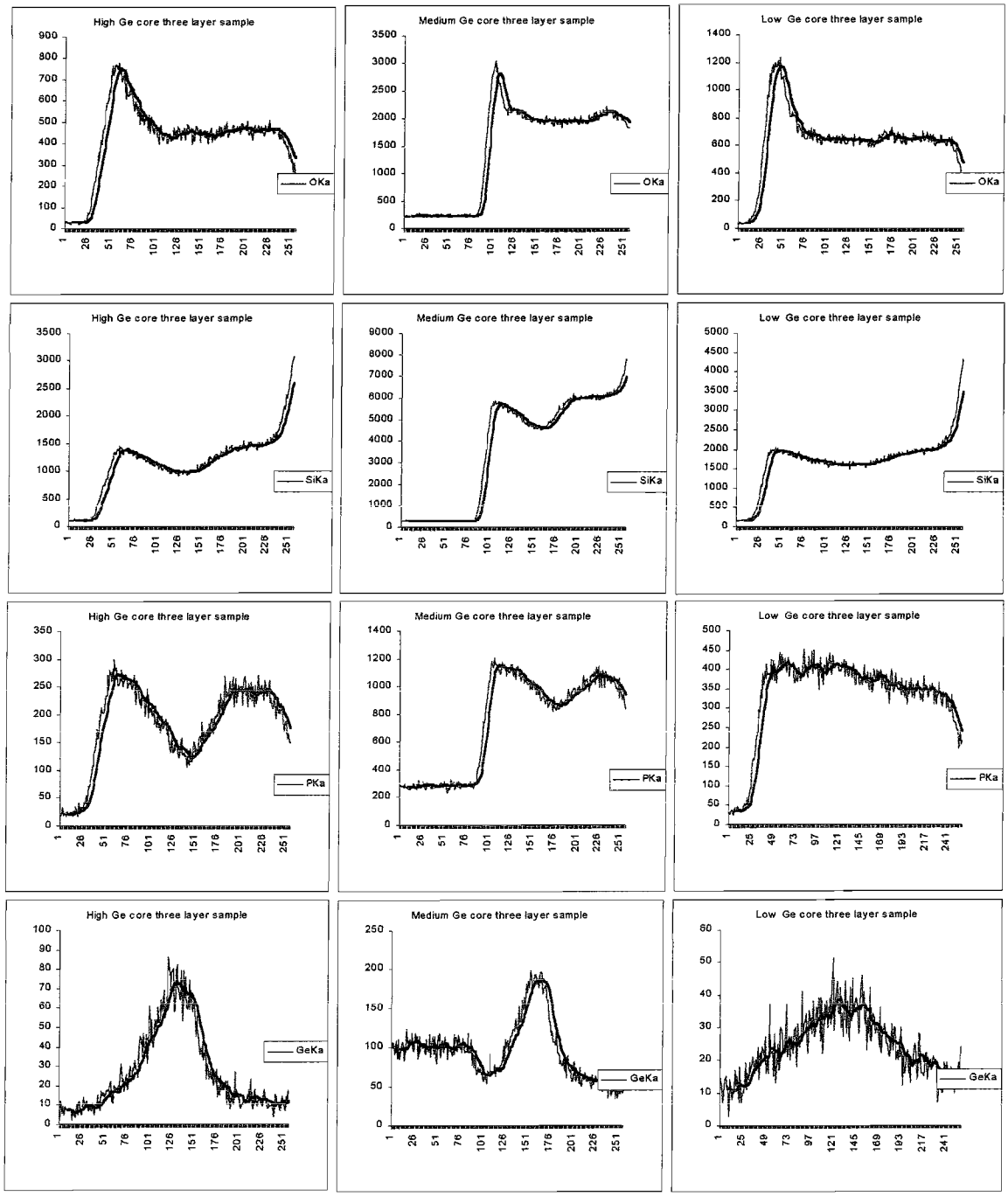

Figure 5.11, Linear compositional EDX scans, showing relative constituent concentrations resulting from 1μm^2 probe scanning from air-substrate in direction perpendicular to layer structure; a) high Germanium core, b) medium Germanium core, and c) low Germanium core. (note. Axes show arbitrary scan distance (x) and detector counts (y), therefore absolute values can not be attained)

(unfortunately only qualitative analysis was available at the time of writing due to the new nature of the SEM/EDX facility within the ORC, and in particular the lack of calibration). In the core layers (centre region of the scans) Germanium and Phosphorus behave as expected, with an obvious trend for decreasing relative P concentration with increasing Ge as expected. However, the relative P concentration in the clad layers (regions directly

adjacent to core region) does not appear to follow the doping trends intended. In particular the underclad layer (region to right of core) is expected to have a higher P doping level, but actually has a consistently lower concentration of P. It is clear from this qualitative compositional data that dopant incorporation is far from linear, as has already been highlighted by the refractive index data already presented. Unfortunately the compositional analysis undertaken has not included B due to lack of EDX calibration, in the future it is expected that full calibration of the EDX facility will allow conclusive determination of the complex nature of dopant incorporation within FHD silicate layers.

The occurrence of Phosphorus-Boron coupling has resulted in considerable problems with respect to tailoring refractive index. It has been necessary to increase indices to that of the highest layer in the structure, Boron doping has been limited to the tailoring of consolidation temperature. Fully independent control of refractive index will only be possible for layers that do not include Phosphorus. The use of alternative dopants that have a similar affect to Phosphorus would result in more complete control of the system. Conversely replacing Boron with a dopant that has a greater reducing affect upon refractive index would also result in greater control. Titanium could be used as a suitable replacement for Phosphorus since it has a considerable effect upon refractive index and does not suffer from any of the volatility problems associated with Phosphorus doping. However, Titanium does have a very large effect upon thermal expansion, which could lead to layer instability and increased wafer warping. Titanium Tetrachloride also has a very low vapour pressure, which may limit the maximum doping levels achievable. A suitable replacement for Boron maybe Fluorine since this is known to have a similar effect upon consolidation temperature, and a greater reducing effect upon refractive index. However, the very real possibility of Hydrofluoric acid being produced within the flame would result in a significant increase in complexity for the system and sample handling.

During the determination of dopant affects upon refractive index and consolidation temperature, the majority of indices were determined using critical angle measurement, as outlined in Section 5.1.2. However, occasionally a two-layer structure was produced to test underclad-core compatibility. The production of sensible guiding structures allowed the determination of index and core thickness using prism coupling. The prism coupling data confirmed the trends that had already been observed using critical angle measurement, and thickness measurement through physical or optical profiling as mentioned in Chapter 4. The production of a guiding structure also allowed the determination of propagation loss through the measurement of scattering induced radiation, as mentioned in Section 5.1.3. It was

found impossible to produce an accurate determination of propagation loss through the analysis of scattering induced radiation for all core layers investigated. There appeared to be several possible explanations for the lack of a suitable propagation stripe from which to determine scatter induced loss. The possibility that the core layers investigated have losses below the maximum sensitivity of the Metricon highlighted in Section 5.1.3 must be considered. The likelihood of all layers having losses less than 1dB/cm is possible, in which case loss maybe difficult to determine. However, it is expected that the highly doped layers will have losses of greater than 0.2dB/cm, which is the lower limit for observing any loss effects although accurate determination at this level maybe difficult. It is therefore not impossible that the reason scattering loss is not observed is due to relatively low loss guides. Alternatively, the power initially launched into the planar waveguides using the prism coupling apparatus maybe too low to be observed upon scattering out of the guiding layer. It is also possible that the relatively massive scattering regularly observed due to particulate contamination within the core layer has the effect of swamping the propagation streak. Thus impairing the measurement of the exponential decay against propagation length, required to determine loss. Any of the previous explanations, individually or in combination, maybe the cause of the inability to determine propagation loss through observing scatter induced radiation. Ultimately, the loss within planar guides is not of importance and therefore further work has not been undertaken to rigorously define it. The loss of UV written waveguides formed within the core layers is of great importance, and this is discussed and experimentally determined in Chapter 7.

5.4 Conclusion

The systematic optimisation of the FHD process has led to the determination of a number of compositions suitable for constructing three-layer planar waveguiding structures. In particular, index matched overclad and underclad compositions and three index matched core compositions with varying Germanium concentration have been identified. During the optimisation process a number of phenomena connecting composition to relative dopant incorporation rates have been identified. Most notably the Phosphorus-Boron coupling effect, which has led to a considerable amount of difficulty in accurately controlling refractive index independently from consolidation temperature.

It has been highlighted that a more predicable refractive index behaviour and increased freedom to independently vary consolidation temperature may be achieved by using alternative dopants. The deposition of core layers with higher Germanium

concentrations than those achieved may also require the use of alternative dopants in order to maintain index matching between core and clad layers while preserving required processing parameter. However, it is believed that the current sample set is suitable for the investigation of direct UV written waveguides within Germanosilicate layers produced using FHD.

6 Direct UV Writing

The waveguide definition process is a fundamental part of producing any waveguiding device. As has been previously mentioned in Chapter 5 the nature of the waveguide, in particular the relative refractive index and dimensions of the core, directly affects the devices that can be produced. The technique for defining the core region is therefore of paramount importance with respect to the final device that is produced.

This chapter compares the well-established techniques of photolithography and subsequent etching processes, to the UV direct writing technique. A comprehensive review is not given for other alternative techniques, rather an assessment of the merits between a well established and widely used technique, are compared to those of an emerging process. If the relatively new process of direct UV definition of waveguiding structures is to develop further it is required to have some elements that make its use advantageous. It is with this argument in mind that the review is presented.

The implementation of the direct UV writing process is discussed in detail, particularly focusing on the photosensitivity requirement for the materials used. The various mechanisms and enhancement processes that have been employed to develop suitable photosensitivity are highlighted, and a review of prior art within the field is given.

Finally using two and three-layer samples constructed from the compositional sets previously discussed in Chapter 5, the process of direct UV writing is investigated. In particular, the occurrence of physical damage and the associated imposed limit upon writing "strength" is treated, with the ultimate aim of determining writing conditions that are suitable for the production of UV induced index channels.

6.1 Review of PLC Definition Techniques

The following section discusses the definition of waveguiding structures, the theory of which has been previously discussed in Chapter 5. In particular, direct comparisons will be drawn between the well-established and widely used technique of photolithography and etching, and the newer technique of direct UV writing. Both techniques have obvious advantages and disadvantages, however it is not the aim of this review to conclude which technique is best, merely to put the operational requirements and subsequent results of such definition processes into context.

6.1.1 Photolithographic definition of waveguiding structures

The process of photolithography can be described as; the transferral of a pattern from plate to substrate through illumination of the plate, resulting in the production of a contrast pattern on the substrate. The basis of the technique stems from photo-printing of light sensitive media, and has been applied in fields as diverse as photography to bank note printing. The use of photolithographic processes to define features within the microelectronics industry is widespread. The definition of sub-micron features using deep-UV illumination and subsequent transferral of features into relief structures, has lead to the very large scale integration historically observed for integrated circuit manufacture. The application of photolithography to the field of integrated optics requires the use of complex multistage processes, including the initial production of the patterned plate or photomask, through to transferral of the photoinduced pattern into the substrate material. Figure 6.1 shows a schematic of the waveguide definition via photolithographic techniques.

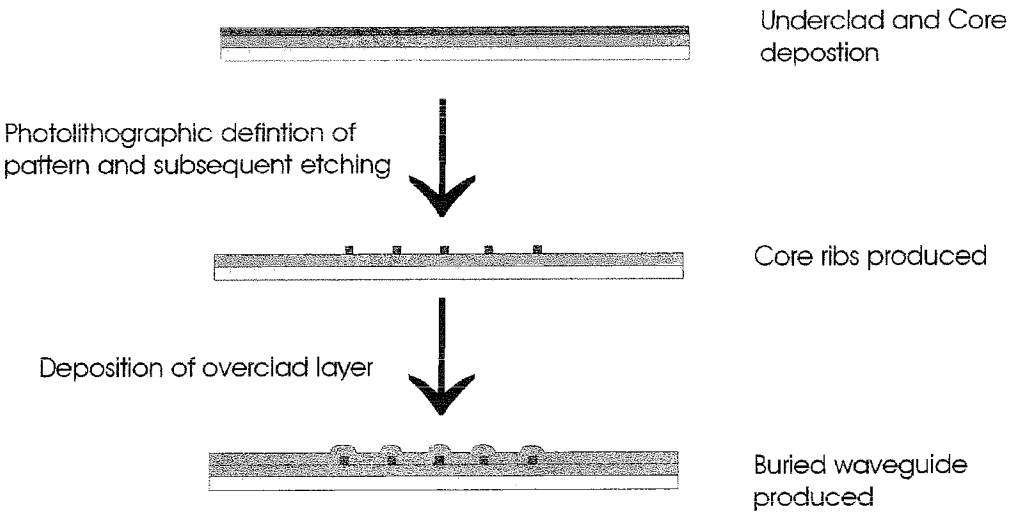

Figure 6.1, schematic showing photolithographic definition of waveguiding structures

Upon reproduction of the mask pattern into the photoresist and subsequent development, it is necessary to transfer the pattern onto the substrate material. A relief pattern is formed in the substrate material by etching through the windows in the resist mask. Selection of etching process is dependent upon the substrate material to be etched and the resist that has been used, the feature type and size must also be considered. The etchant used must have a significantly different etch rate for resist and substrate material, so that mask integrity is maintained for the whole etching process. The etch processes widely used fall into two categories, wet etching and dry etching.

Wet etching of silicates normally involves the use of solutions containing Hydrofluoric acid (HF) or a combination of HF and fuming Nitric acid (HNO_3). Etch rates are dependent upon the temperature and composition of the solution during the etching process. Etch processes are normally determined empirically depending upon the specific application. The isotropic nature of wet etching can cause problems associated with resist delamination and undercutting due to etch features increasing in size in all directions, schematically shown in figure 6.2. The sidewalls of features produced by wet etching are not normally straight as a result of undercutting.

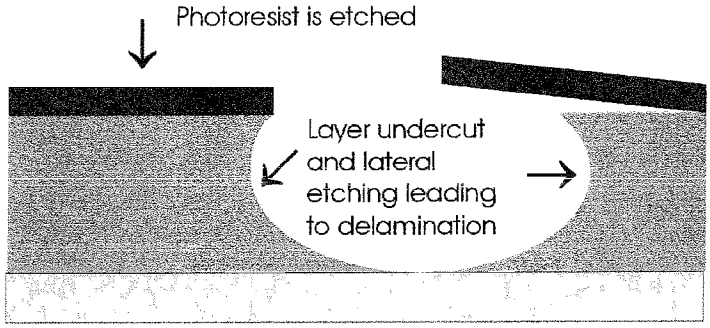

Figure 6.2, occurrence of undercut and delamination during etching

Dry etching uses gaseous etchants and tends to result in a higher degree of anisotropy than wet etching. Plasma etching involves the use of radio frequency (RF) excited plasma consisting of the etchant gases. When silicates are etched the plasma normally contains Fluorine and Chlorine ions. Sputter etching involves the ion bombardment of non-reactive ions to remove material by physically knocking atoms from the surface resulting in very high anisotropy but poor selectivity. Reactive Ion Etching (RIE) is a combination of plasma and sputter etching, and results in a relative increase of anisotropy and selectivity of the etching process.

RIE compared to wet etching has several significant advantages. Firstly, the degree of anisotropy is considerably greater, resulting in straight sidewalls and increased feature size consistency. Secondly, the occurrence of resist delamination for extended etch time is minimised, thus significantly deeper features can be produced with the only limiting factor being the selectivity of the etchant and the thickness of the resist.

There are several advantages in using photolithographic techniques to define structures for waveguiding devices when compared to competing technologies. The attainability of large-scale integration with little appreciable increase in processing time is perhaps the most obvious. The parallel nature of the process allows entire devices or multiple devices to be defined simultaneously on a single wafer, which has been

demonstrated in the IC industry and is potentially relevant to the growth of the PLC industry. The considerable knowledge regarding photolithographic and etching processes that exists within the field of microelectronics is directly applicable to the definition of features required for integrated optics, therefore development of dedicated processes and equipment is not required. From an industrial point of view the process is easily scalable allowing production line type processing. The mass fabrication already present in the manufacture of ICs allowing economy of scale, is as potentially applicable to PLCs. However, the inherently large size of PLC devices will ultimately limit the level of integration that occurs on single chips. A significant advantage of using etching techniques is the possibility of very large Δn between core and clad, since it is feasible to use entirely different materials for the two functions. The compositional effects of doping upon the index of silicate glasses allows Δn as large as $\sim 3\times10^{-2}$ to be easily achieved (see Chapter 4) if refractive index is the only important parameter.

Having outlined some of the significant advantages associated with photolithographic type process, it should be noted that there are also some disadvantages. The rapid prototyping of one-off structures is not easily attainable using photolithography due to the temporal and monetary expense associated with producing masks. The nature of the photolithographic technique requires the deposition of an overclad onto the etched structure, which increases the possibility of contamination at the overclad interface. Subsequent high temperature processing steps after the definition of waveguide channel can also lead to distortion resulting from reflowing of the core material. The etched nature of the core will lead to an inherent roughness on a microscopic scale, which may result in altered deposition conditions for the overclad and may ultimately effect the waveguiding properties of the device produced.

6.1.2 Direct UV Writing

The use of direct UV writing to define waveguide structures relies on photosensitive materials for which exposure to UV photons results in a permanent induced refractive index change. Employing a UV laser allows accurate control of exposure energy and area through the application of relevant optics, 244nm Frequency Doubled Argon Ion (FRED Ar^{+}) and 193nm or 248nm Excimer lasers are commonly used. Translation of a UV spot with suitable power across a photosensitive material results in a refractive index channel being written. The index change observed within a material is dependent upon the relative energy that is

coupled into the sample. The Lateral dimensions of the UV induced channel are dependent upon the writing spot size. The vertical dimensions of the channel are dependent upon the thickness of the UV photosensitive layer. Specifics of the photosensitivity mechanism and UV writing system used in this work is discussed in Section 6.2.

The advantages offered by the direct UV writing technique for defining waveguiding structures are wide ranging. The ability to rapidly prototype new structures and waveguide devices due to the lack of ancillary processes implies that UV writing will allow rapid development and quick feedback during the invention of novel structures and device configurations. The definition of refractive index structures using UV writing allows the index of a channel to be tapered, such that Δn is varied along the length of the device by changing the relative exposure conditions, this is something that is very hard to achieve by conventional methods. The nature of the UV induced refractive index change also allows active trimming of devices through altering core index and dimensions, meaning that devices can be altered in order to match requirements without the need to undergo all preceding steps. The use of UV writing and its similarity to UV definition of Fibre Bragg Gratings (FBG) suggest that the application of Bragg gratings to the planar geometry will be realisable, this will be further discussed in Chapter 8. The post deposition definition of the waveguiding structure allows the nature of the vertical core-clad interface to be entirely determined during layer fabrication, the minimisation of interface contamination is therefore expected. The lateral nature of the guiding structure is purely defined by the nature of the UV writing spot, it is therefore possible to modify the lateral index profile through tailoring the spot characteristics. In general, the speed of prototyping combined with the absolute flexibility of waveguiding structures and optically integrated devices that can be produced using UV writing is thought to be greater than for competing techniques.

When using UV induced refractive index change to define waveguiding structures, a number of limitations and general disadvantages must be taken into account. Most significantly UV induced refractive index change is limited in magnitude. As explained in Chapter 5 the Δn of a waveguide directly affects the size of devices. The production of symmetrical devices requires the index matching of core and clad layers, which is shown to be non-trivial in Chapter 5. The serial nature of the UV writing process does not readily lend itself to parallel processing or mass production, however these are technological problems and probably surmountable in the long-term.

6.2 Mechanism of UV Photosensitivity in Germanium Doped Silica

It is widely accepted that there is not a single mechanism responsible for UV induced index change. The nature of the material and exposure method can lead to a number of different effects, which in most cases are likely to occur simultaneously to varying degrees. The superposition of index modifying mechanisms leads to the complex nature of UV photosensitivity [Svalgaard, 1997]. The following section briefly outlines some of the accepted UV induced processes that take place within Germanosilicate glasses. A review of observed UV induced refractive index change within Germanosilicates will also be presented.

When considering the mechanisms that could be responsible for the positive refractive index change upon UV illumination, used for the definition of PLC components, it is important to note the molecular structure of the germanosilicate glasses used. As mentioned in Chapter 3, co-doping of the silica matrix with a few mole percent of Germanium results in a structure very similar to that of pure silica, because germanium also has a valency of 4. The properties of the material are however altered from that of pure silica as the melting point decrease and both refractive index and absorption in the UV increase. The introduction of both point and distributed defects that would not normally be present in the matrix, also occur due to germanium co-doping. It is generally accepted that the reaction of these defects to UV photons, and the energy that they impart to the matrix causes the photosensitive nature of germanosilicate glasses.

The point defects that are caused within a silica matrix through the inclusion of germanium can be classed in two groups; diamagnetic where electrons are paired and paramagnetic where electrons are unpaired, shown if figure 6.3. Diamagnetic defects often occur due to a deficiency of oxygen during glass formation resulting in Germanium related Oxygen Deficiency Centres (GODC). These commonly take the form of either a Ge^{2+} defect or a Neutral Oxygen Vacancy (NOV) in which a Ge atom bonds directly to a Si atom. Paramagnetic defects can take the form of Non-Bridging Oxygen Hole Centres (NBOHC), where an oxygen atom is only bonded onto one atom; GeE' defects where a Germanium atoms is only bonded to three other atoms; and Ge(1) defects where a fully bound Ge atoms traps a free electron [Sulimov *et al*, 1996]. It is currently thought that UV exposure of GODCs promotes the dissociation of electrons resulting in the formation of paramagnetic defects. The change in electronic structure of the matrix components through formation and modification of point defects is suggested as being responsible for a change in UV absorption and therefore refractive index. However, this by no means completely explains

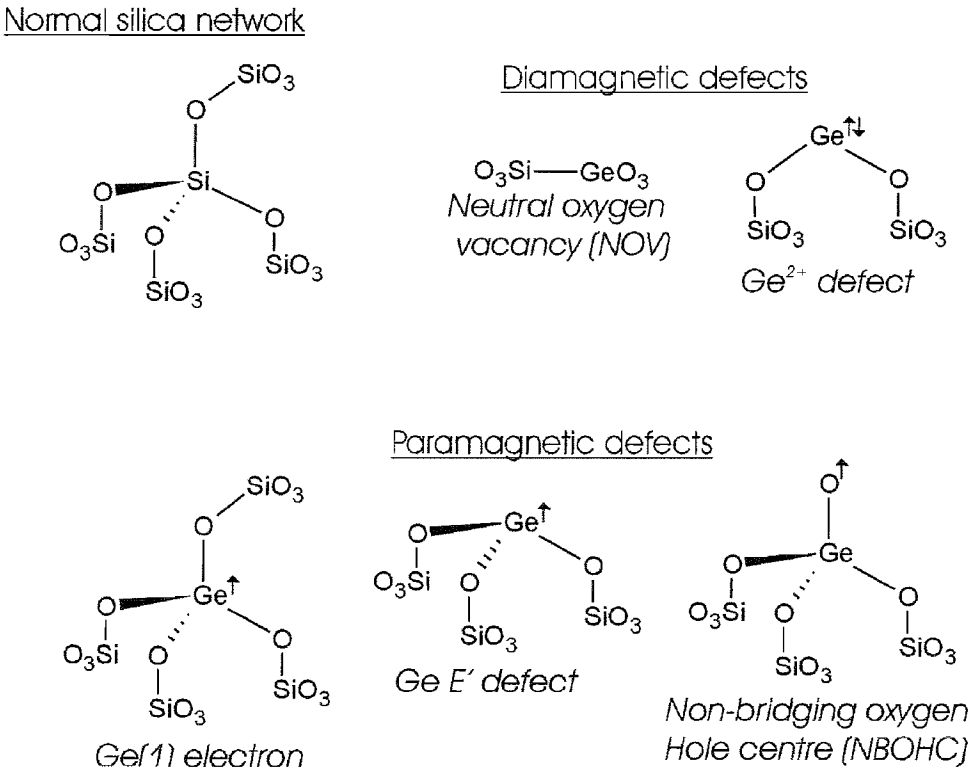

Figure 6.3, Germanium induced defects within Germanosilicates

all of the photosensitivity observed since changes in the stress and volume of the matrix will affect the refractive index. The modification of distributed defect can therefore not be ignored when discussing photosensitivity. In general, the formation or removal of defects within the matrix, either point or distributed in nature, will change the refractive index and the absorption of a material.

The photosensitive character of germanosilicate glasses is a complex matter, not only is the mechanism for index changes not fully understood, the nature of the index change itself is also not trivial. It has been shown in [Douay *et al*, 1997] that effectively three types of photosensitivity are exhibited. Type I; a monotonous increase in index with increasing UV exposure time. Type IIA; a time varying decrease in index, and type II a very large index change resulting from physical damage due to a single high intensity UV pulse. The combined effect type I and IIA can be characterised as follows: An initial positive index change occurs due to charge transport causing formation or erasure of defects or chemical species which result in an increase in the index consistent with type I photosensitivity. The reaction due to type IIA photosensitivity is slower than for type I, but results in a decrease in refractive index, this results in the erasure of any positive index change just after saturation due to type I. This competition between type I and IIA results in the varying nature of the index change observed when prolonged UV exposure takes place. However this problem may be solved when a positive index change is required through limiting the exposure time.

The magnitude of the induced index change within the region of the germanosilicate exposed to UV light, ultimately defines the devices that can be written. Typical UV induced index changes, demonstrated in single mode fibre doped with 3% germania, have been limited to ~3×10^{-5} [Atkins *et al*, 1993]. Raising the germania doping level to 10- 20% results in an increase of induced Δn to 1×10^{-4} to 4×10^{-4} [Cordier *et al*, 1997]. Further increases in UV induced refractive index change have been demonstrated through greater germania doping levels, co-doping with additional elements such as boron or tin, and by post fabrication processes such as Hydrogen or Deuterium loading which will be discussed in detail in section 6.4. Various combinations of UV induced index change enhancing processes have lead to induced Δn of up to the order of 1×10^{-2} [Mizrahi *et al*, 1993].

6.3 Review of Direct UV Writing in Planar Germanosilicate

The field of direct UV writing and it use to define waveguides is relatively new, and has stemmed from the discovery of high Δn produced during the UV formation of Bragg gratings within Germanosilicate fibres. As mentioned in section 6.2 the use of Germanium doped silica and hydrogen loading has seen induced indices of the order 2×10^{-2}, the same technique using a KrF excimer laser was used to expose three layer planar samples with Germanium rich cores [Mizrahi *et al*, 1993]. This was the first reported occurrence of "direct UV patterning" of planar samples, however the technique still involved the use of chrome-on-silica masks in order to define the waveguiding structures. Subsequent work using this technique has been demonstrated by various groups, and includes the fabrication of integrated devices such as directional couplers [Maxwell and Anslie, 1995] and Y-splitters [Hubner *et al*, 1996]. However, none of the work using the "masking" technique has reported waveguide propagation losses lower than 1dB/cm. Consequently the use of direct UV patterning of this type has not be widely adopted.

An alternative approach to UV induce waveguides within Germanosilicate planar geometry was proposed by Svalgaard [Svalgaard *et al*, 1994], in which the point to point direct writing of buried waveguides in the planar geometry was presented. In contrast to previous work a CW 244nm source was used to produce a focused spot within the photosensitive layer, the translation of which resulted in the definition of an increased refractive index channel and thus formation of a waveguide. Svalgaard *et al* have further developed this technique and demonstrated the fabrication of low loss (<0.2dB/cm) waveguides, low insertion loss waveguides, and symmetrical waveguide devices such as

splitters and couplers [Svalgard and Kistensen, 1997] [Zauner *et al*, 1998] [Faerch and Svalgaard, 2002]. All of this work has taken place in samples produced using PECVD, and has demonstrated the photosensitivity of Germanium doped layers fabricated using this technique.

The writing of UV induced index waveguides into the sample produced using FHD, outlined in Chapters 4 and 5, took place using the technique proposed by Svalgaard. The remaining sections of this chapter deal with the equipment required for UV sensitisation through H_2/D_2 loading, UV exposure using 244nm source, and the determination of suitable writing regimes.

6.4 Deuterium Loading and UV Writing Equipment

Deuterium loading is used in preference to Hydrogen loading due to avoidance of increased OH absorption in the 1300-1600nm transmission window. The mechanisms for enhanced photosensitivity via Hydrogenation and Deuteration are examined, in which species dependent effects are minimal. The theory and practice of loading via diffusion of D_2 into and out of silica is discussed, along with the calculation of relevant loading parameters. The equipment and operational procedure of the equipment used for UV exposure of FHD samples is presented, along with technical consideration regarding writing into Deuterium loaded samples.

6.4.1 Enhanced photosensitivity through Deuterium Loading

As mentioned in section 6.2 the photosensitivity for a given Germanosilicate composition can be enhanced through using Hydrogen or Deuterium loading. The process of loading involves the diffusion of H_2/D_2 into the silica matrix, upon UV exposure the loaded species are incorporated into the glass and result in a significant increase in the relative value for UV induced refractive index.

The mechanism responsible for enhanced photosensitivity through H_2/D_2 loading can be explained as a two-step process. The supply of sufficient energy either photolytically or thermally to a Germanium site within the silica matrix, that has a Hydrogen molecule in close proximity, results in the formation of SiOH silica matrix termination and corresponding GODC [Iino *et al*, 1990]. The presence of enough Hydrogen or Deuterium within the Germanosilicate matrix can therefore theoretically result in every Germanium site becoming a GODC, with the associated enhancement of Germanium dependent

photosensitivity resulting. An additional enhancement mechanism has also been observed in which the presence of Hydrogen or Deuterium acts as a catalyst for the photobleaching of GODCs associated with the transition from diamagnetic to paramagnetic defects and resulting in an increase of refractive index [Atkins *et al*, 1993]. It is clear that a number of mechanisms are probably responsible for the photosensitivity enhancement observed for H_2/D_2 loading of Germanosilicates, in much that same way as there are a number of possible mechanisms for the basic Germanium dependent photosensitivity highlighted in section 6.2. It is however clear that enhanced photosensitivity occurs due to an increase in the UV absorption during writing thus increasing the induced refractive index change regardless of the mechanism responsible.

The concentration of H_2/D_2 present within the silica matrix has a direct effect upon the photosensitivity for a given Germanosilicate composition, it is therefore necessary to understand the mechanism through which loading and unloading takes place. The high diffusivity of H_2/D_2 within the silica matrix allows any vacancies or voids present to be filled. The diffusion of H_2 within silica has been extensively investigated [Stone, 1987]. The diffusivity in square centimetres per second of Hydrogen may be expressed using a simple one-dimensional diffusion equation given below;

$$D = A\exp(-E/RT)$$

where A is a pre-exponential factor, R is the gas constant, T is the absolute temperature and E = 40kJ/mol [Lemaire, 1991]. Therefore the diffusivity is exponentially dependent upon the temperature of the system. The equilibrium concentration at room temperature has been determined to be;

$$c_{eq} = 116\,ppm/bar$$

where 1ppm is defined as 10^{-6} moles of H_2 per mole of SiO_2 [Shackelford *et al*, 1972]. It was also observed that solubility is weakly dependent upon temperature, with higher temperatures resulting in lower solubilities. The rate of outdiffusion in planar samples such as those produced using the FHD process was empirically determined at a loading pressure of 180bar and gave the following relationship;

$$\tau = -\ln[\alpha]\tau_0 \exp\left(\frac{E}{RT} - \frac{E}{RT_0}\right)$$

where α is the relative concentration of D_2 compared to saturation, τ is the decay time at temperature T, and τ_0 is the experimentally determined decay time at temperature T_0 resulting in a relative D_2 concentration of $1/e^2$ [Svalgaard, 1999]. The use of the values τ_0 =

11.8 hours and T_0 = 23°C allows the calculation of relative D_2 concentration for a given time and temperature. The calculation of indiffusion rate can also take place using the same expression since the same dynamics determine the diffusion process regardless of direction. The absolute rate of diffusion and resulting time taken to reach saturation are also dependent upon the pressure that defines solubility and the thickness of the sample that defines diffusion path length. However, if the samples and loading pressures are significantly similar, the previous relationship is believed to give an accurate approximation of the Deuterium loading characteristics for the FHD samples used.

The loading of the FHD samples, the fabrication of which is discussed in Chapter 5 took place using a high-pressure stainless steel cell. The samples are placed in the cell, which is then pressurised using high purity Deuterium to a pressure of between 180-220bar, giving equilibrium concentrations of D_2 in silica of between 2.1-2.6 mole percent. The time taken to reach 99.9% of saturation at a pressure of 180bar is approximately 3.5 days, loading times of 4 days or greater are normally used to ensure maximum loading with minimal turn around time.

6.4.2 UV writing technique and equipment

The time between unloading samples from the Deuterium cell and the definition of waveguide channels through UV writing is of critical importance with respect to the amount of D_2 present within the silica matrix. Upon removal from the pressure cell, prior to UV writing, samples are stored in solid CO_2 (-79°C) which significantly decreases the rate of D_2 outdiffusion. However, upon removal from the solid CO_2 and the initiation of the writing process the samples quickly return to room temperature. The effects of Deuterium outdiffusion during the writing process must therefore be taken into account, as discussed in Chapter 7.

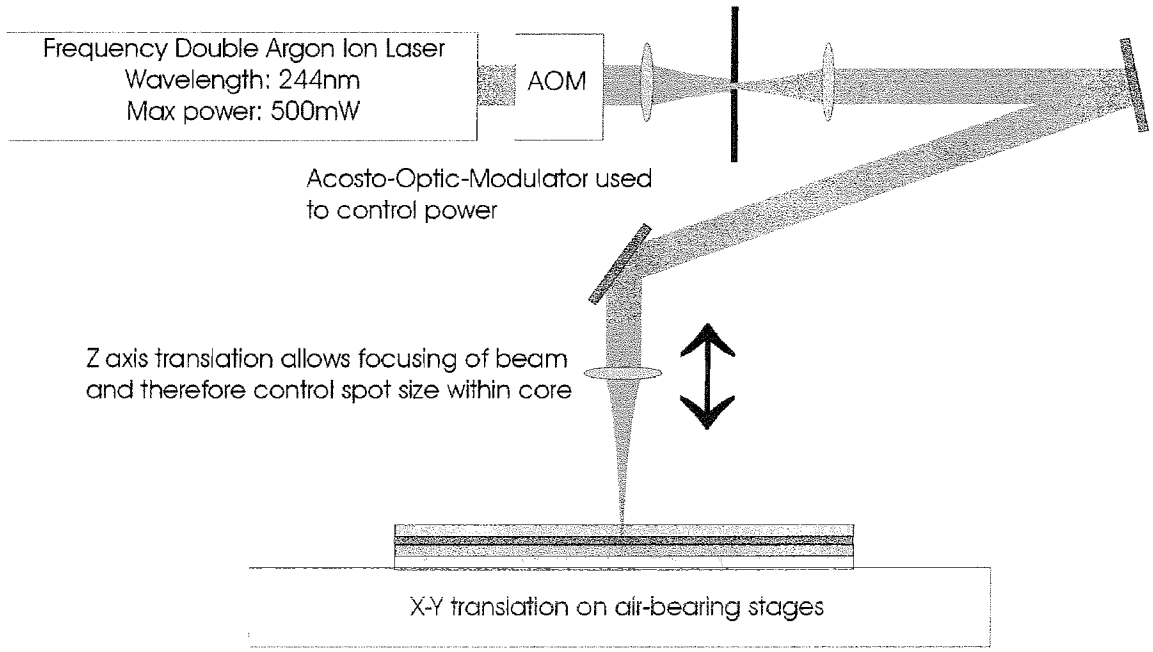

Figure 6.4, schematic of direct UV writing equipment

The equipment used for UV exposure of samples consists of a 244nm laser source, an optical system for modifying power and controlling beam direction, and a translation system for aligning the UV beam within the sample, shown in figure 6.4. The laser source used is a frequency doubled Argon ion laser operating at 244nm and capable of outputting continuous wave (CW) radiation at a power of 500mW. The maximum output power of the laser is normally reduced in the interest of stability and beam quality, therefore leading to an operational output of less than 500mW. The use of an acousto-optic modulator (AOM) allows the beam power to be further modified, facilitating accurate control of writing power through offline calibration using a UV sensitive power meter. The maintenance of beam quality and pointing stability is achieved using a spatial filter. The beam is focused to a waist larger than the pinhole thereby translating any dither in beam position into a fluctuation in power, thus maintaining pointing stability and removing any unwanted structure from the beam profile. The beam is subsequently delivered to the writing head using a number of UV mirrors.

The writing head consists of a cylindrical lens mounted on a vertical translation stage, the linear actuation of which along the axis perpendicular to the plane of the sample (z-axis) results in the modification of the beam focus with respect to the sample. The $1/e^2$ spot size at the beam waist is 3.3μm, thus allowing continuous variation of spot size to values larger than the focus through variation in the lens-sample distance. It is therefore

possible to modify the writing spot size experienced by the photosensitive core by selective defocusing of the writing beam.

The translation of the writing spot within the core region is facilitated through the movement of the sample relative to the writing beam. The sample is mounted on a vacuum chuck in order to allow alignment accuracy and minimal unintentional movement. The sample and chuck are then mounted on stacked air-bearing linear translation stages, the orthogonal alignment of which allows x-y translation. The x-y-z translation system is controlled using G-code executed from a PC running dedicated software, feedback from the stages via optical encoders allows alignment accuracies of ~3nm to be achieved.

The complete integration of the translation system and G-code operation allows the UV writing spot to be accurately positioned and translated within Germanium doped Deuterium loading cores of the FHD samples previously fabricated. The use of the UV writing equipment outlined has been invaluable, and the following sections highlight the use of the system in determining suitable UV writing regimes for the range of samples produced.

6.5 Determination of UV Writing Regime

When using the direct UV writing technique to define refractive index structures within photosensitive materials it is important to define the writing conditions for which a suitable result occurs. The act of focusing high energy into a small volume of material can have detrimental effects if the energy dissipation from the exposed region is not significantly rapid. A common problem occurs when thermalisation of a small volume results due to large amounts of energy being coupled into a material with a low thermal conductivity, thus resulting in local melting and in extreme cases vaporisation. The physical disruption of material through melting or vaporisation is undesirable since such damage does not result in low loss UV induced index channels. It is therefore important to determine the maximum power that can be coupled into a material without significant thermalisation and associated damage resulting. The following section focuses on the determination of suitable UV writing regimes for the FHD samples the production of which was discussed in Chapter 5.

The quantification of the UV writing "strength" that a sample is exposed to involves the calculation of fluence, which is a convenient measure of the energy per unit area. The

calculation of fluence F can take place from the focused spot intensity I, spot width a and the translation velocity of the spot across the sample v, using the relationship below;

$$F = I\frac{a}{v}$$

The correlation of fluence to induced refractive index assumes that a material is not being saturated such that additional exposure does not result in further change in refractive index, however this may not always be the case. The dominant index modification mechanism must also not be dependent upon peak power as would be the case for a thermally dependent process. The spot size used for writing is defined by the beam waist within the UV photosensitive layer, and is dependent upon the focal parameters of the writing set-up. Operational variation of the writing spot size is achieved through defocusing the beam relative to the UV photosensitive layer. The fluence calculations use the $1/e^2$ value of maximum beam intensity as an effective spot size. The Gaussian nature of the writing spot is not fully taken into account in the calculation of fluence since it assumes uniform intensity. However, for the characterisation of the writing process the assumption of uniform illumination within the spot and subsequent calculation of fluence is thought to be adequate at least as a first approximation.

6.5.1 Two Layer Samples

In order to determine the maximum fluence that can be tolerated by the core material without the occurrence of damage, two layer samples were produced from the compositions determined in Chapter 5. The two layer samples consist of an underclad and one of the three core layers, but the final overclad deposition did not take place. It was expected that the exposed nature of the core would result in a lower tolerable fluence than for full three layer samples, due to lack of absorption from the overclad and the relative reduction in physical confinement. However, the knowledge gained regarding the nature of the resultant damage was deemed to be of interest.

The three samples representing 2, 4 and 6 mol% Ge doping of the core layer, were exposed to a variety of writing conditions arising from four different spot sizes and twelve different writing velocities. The table below shows the resulting maximum and minimum fluences for the written channels, writing speeds where varied from minimum to maximum in steps of 10mm/min.

Laser power @244nm (mW)	100			
Writing spot diameter (μm)	3.3	5.0	7.0	10.0
Intensity (kW/cm^2)	1170	510	260	127
Translation speed (mm/min)	Fluence (KJ/cm^2)			
120 (maximum)	1.93	1.27	0.91	0.64
10 (minimum)	23.15	15.28	10.91	7.64

The resulting UV written channels were interrogated in order to determine the degree and nature of damage using surface profiling, with the Alpha Step and Atomic Force Microscope (AFM). The damage observed for the high germanium sample suggests that a purely peak power regime has occurred, shown in figure 6.5. The variation in fluence through modifying translation velocity at a constant spot size has little effect upon the type or degree of damage observed. However, variation in spot size has a very notable effect upon the damage that occurred. For the high intensities due to 3.3 and 5μm spot sizes, the energy coupled into the core layer has been sufficient to melt and eject material from the exposed region through either rapid expansion or vaporisation. The width of the ablated channels would appear to be dependent upon the spot size and not absolute intensity, suggesting that in both cases a threshold energy that is characteristic of ablation has been exceeded. For the 7μm spot size there has been insufficient energy supplied to result in ablation, but thermal expansion has occurred resulting in a raised ridge. It is thought that the heating due to exposure followed by rapid quenching leads to the "freezing in" of the thermal expansion thus resulting in a lower density state. The intensity due to the 10μm spot appears not to have caused any physical damage, suggesting that the threshold for damage due to peak power is in the range 120-260KW/cm^2 for the high Germanium core layer.

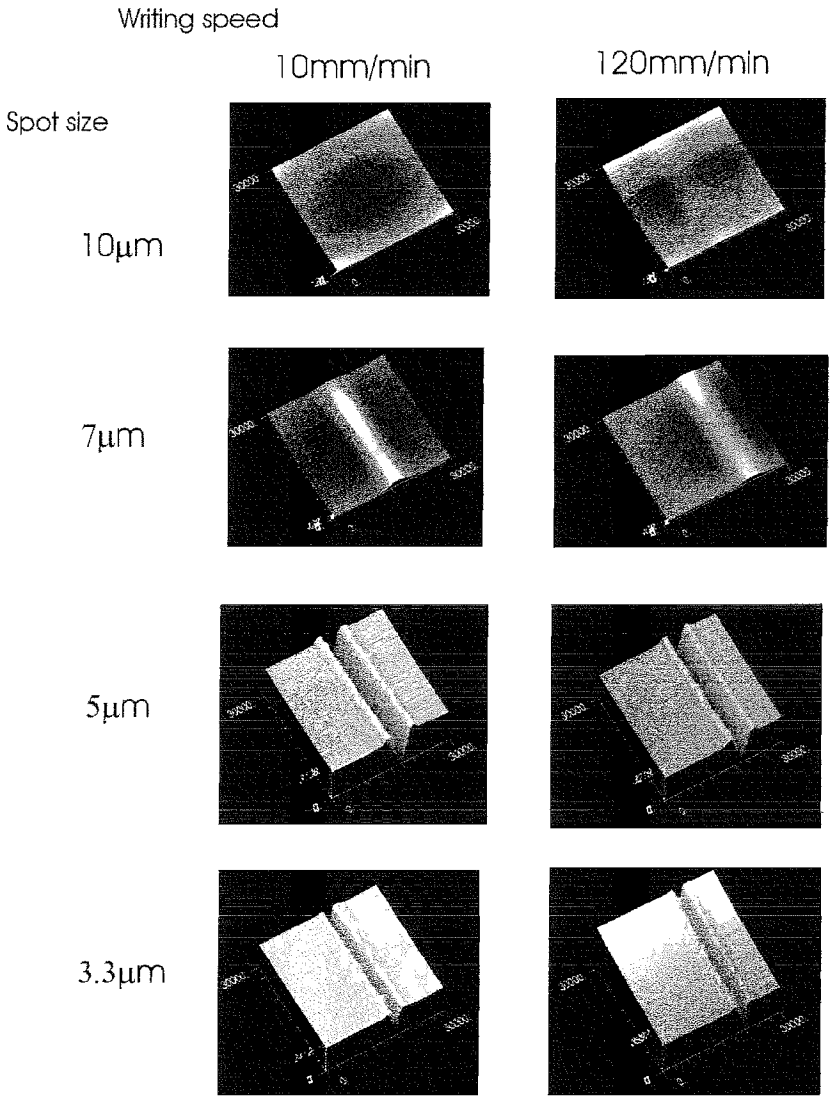

Figure 6.5, AFM scans 30μm^2 showing occurrence of UV induced physical damage on high Germanium 2-layer samples

The AFM scans for the medium Germanium sample generally shows that less energy is being coupled into the layer than for the high Germanium sample, shown in figure 6.6. This confirms that the level of Germanium doping has a direct effect upon the coupling efficiency of UV energy into the silica matrix. The writing regime appears to be dominated by the peak power effect, since spot size and resultant intensity has a more notable effect than translation velocity. However, when the spot size is constant, translation velocity appears to have a small effect upon degree of damage, implying that fluence is beginning to become important. It is clear from the scans that the intensity for which damage occurs within the medium Germanium sample is in the range 260-510KW/cm^2, and that intensity up to 1170KW/cm^2 do not result in ablation.

The AFM scans for the low Germanium sample show a further decrease in tendency to damage when compared to the high and medium doped samples, shown in figure 6.7.

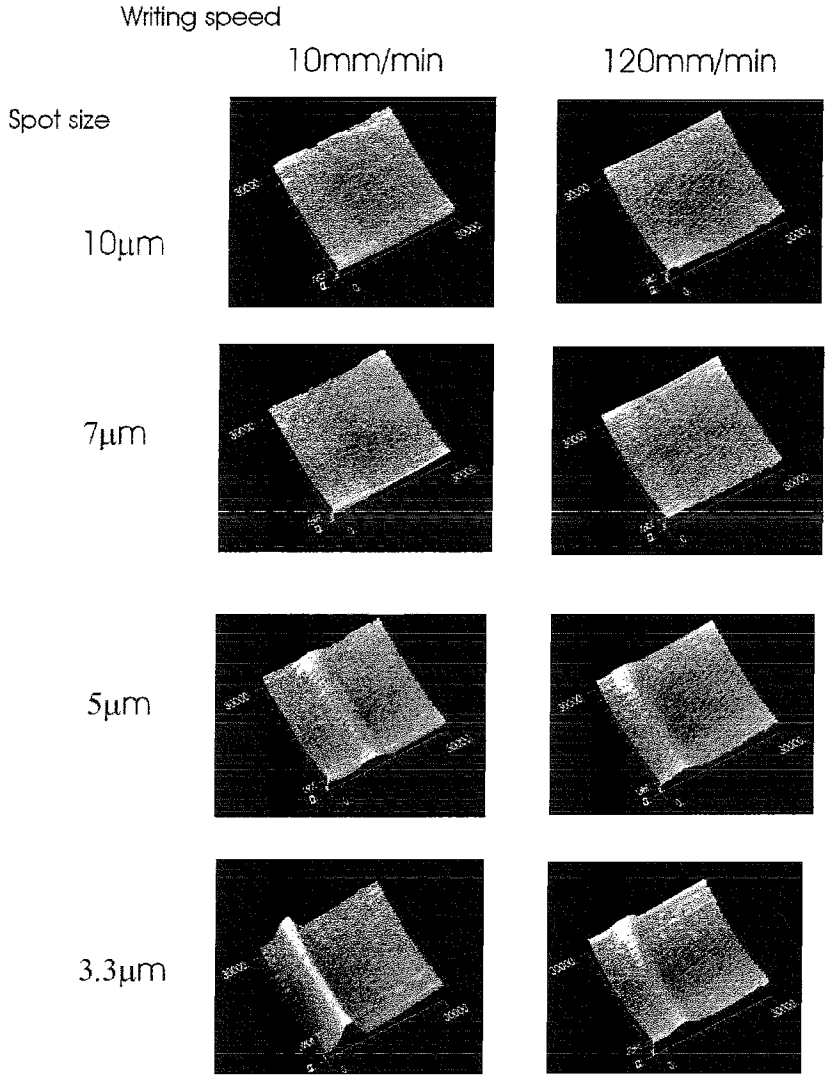

Figure 6.6, AFM scans 30μm^2 showing occurrence of UV induced physical damage on medium Germanium 2-layer samples

The dominant damage mechanism would appear to be peak power related as for the previous two samples. Intensity has the most notable effect upon the degree of damage, with fluence having little apparent effect. Ablation is not observed for any of the intensities used and the threshold for damage is between 510-1170KW/cm^2.

The analysis of the two layer samples indicates that two types of physical damage regularly occur when Germanosilicates are exposed to high intensity UV light. The occurrence of ablation due to rapid melting and expansion or vaporisation appears to have a characteristic threshold, above which ablation takes place over an area directly related to the spot size. It would appear that a lack of thermal conductivity leads to the spot size dependent effects, higher intensities result in higher temperatures. However, the lack of thermal conduction and the rapid ablation leads to features scaling with spot size regardless

of peak power. For intensities below the ablation threshold where energies are not sufficient to result in the ejection of molten material, a "frozen in" thermal expansion effect is

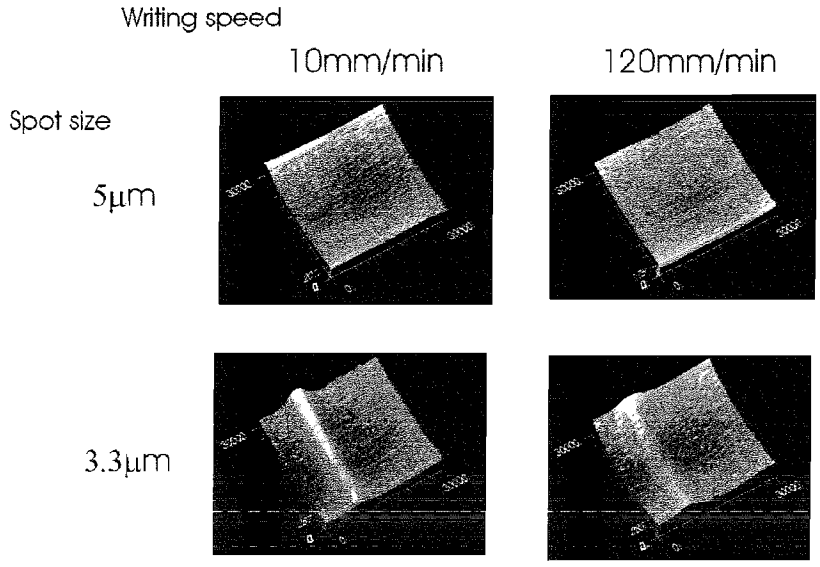

Figure 6.7, AFM scans 30μm^2 showing occurrence of UV induced physical damage on low Germanium 2-layer samples

observed. The dominant contributing factor for ridge formation would appear to be peak power, but a slight fluence effect may be present. The process of ridge formation is likely to be highly dependent upon quench rate, since rapid cooling would theoretically result in greater relative expansion freezing. A higher peak power will result in a higher maximum temperature and therefore a greater degree of expansion. A rapid quench rate would result in a greater relative amount of the thermal expansion being "frozen in". The quench rate is likely to be dependent upon translation velocity, thus it may be possible for fluence to have a small effect upon ridge formation.

The general trend for degree of damage against Germanium doping level has also been observed. It is assumed that where physical damage is not occurring, UV energy is being efficiently coupled into the silica matrix resulting in a potential index change. The damage thresholds determined using two layer samples illustrate the types of damage that can occur and give an indication as to the writing regimes that cause them. However, characterisation of suitable writing regimes required for the production of realistic waveguiding structures calls for the investigation of three layered samples.

6.5.2 Three Layer Samples

The three-layered samples used to determine suitable writing conditions were effectively overclad versions of the two-layered samples employed in section 6.5.1. The

addition of the overclad layer discussed in Chapter 5 allowed the production of a structure that was suitable for the UV definition of waveguides within the buried core layer. The overclad layer contained approximately 0.8mol% Germanium and from the results presented in section 6.2.1 it was not expected that overclad damage would result if similar exposure conditions were used. The determination of suitable writing regime for three-layered samples used the same exposure conditions previously highlighted in section 6.2.1, this range was expected to give an interesting spread of both physical and induce refractive index results. The following section discusses the physical results observed using mechanical profiling techniques.

The sample with the high Germanium core was found to be the only one for which physical damage occurred. The AFM scans for the high Germanium sample shows the occurrence of physical damage similar in nature to that seen for the two-layer samples, see figure 6.8. However, in this case fluence appears to be the dominant factor since both spot size and translation velocity can be seen to affect the nature of the resulting damage. The overlap in degree of damage between spot sizes strongly indicates that fluence is a suitable measure of the energy experienced by the core for three layer samples. The progression in the degree and nature of the damage in relation to fluence would appear to be similar to that observed for peak power in the two layer samples. When the fluence is increased to a point at which damage begins to occur, the formation of a ridge results. Upon further increase in fluence the size of the ridge increases proportionally, until the energy coupled into the core is sufficient to result in ablation. It would appear that in the case of three layered samples, due to the buried nature of the core, ridge formation precedes ablation as demonstrated by the low velocity 3.3μm channel. There also appears to be a significant difference in the quench characteristics for three layer compared to two layer samples, demonstrated by the low velocity 5μm channel. The periodic nature of the ridge is thought to arise from the difference in thermal conductivity between solid and liquid materials. Upon melting of the silica the thermal conductivity increases greatly when compared to the solid leading to rapid quenching after which point the heating process must be initiated again. The rapid change in thermal conductivity and resulting heat sinking effects would lead to an effective pulsing of the temperature experienced by the core. The height of the ridge will be directly dependent upon the temperature experienced during writing, as a result a periodic ridge height results. The confined nature of the core may also contribute greatly to this effect, since much greater temperatures may be achieved prior to ablation occurring. Any molten material that

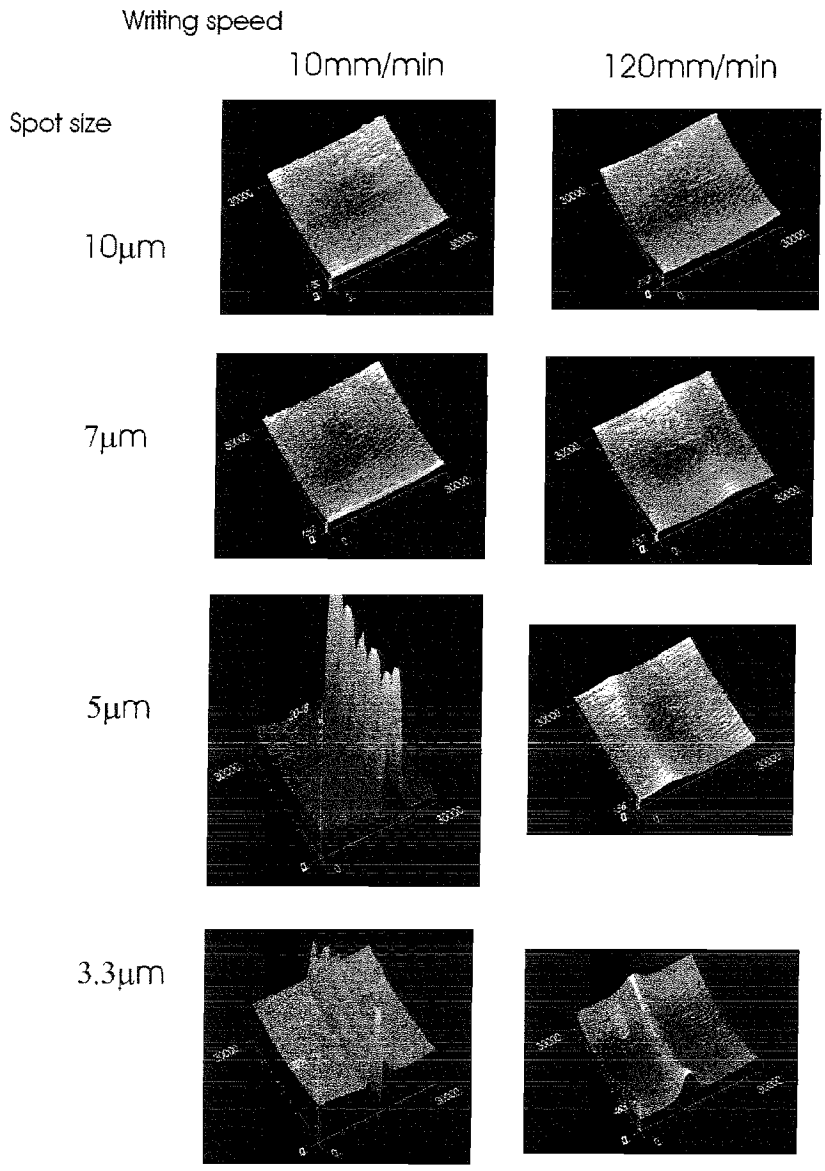

Figure 6.8, AFM scans 30μm^2 showing occurrence of UV induced physical damage on high Germanium 3-layer samples

breaks through the overclad but does not have sufficient energy to result in ejection will rapidly quench therefore enhancing the formation of a ridge with period height.

In general, the damage observed to occur for three layer samples appears to be dependent upon fluence. The total energy at which damage occurs is considerably higher when the core layer is buried, partially due to the absorption of the overclad layer but also due to the physical confinement. It was concluded that the range of fluences investigated were suitable for the further research of channel definition through the use of UV induced refractive index change within three layer samples. The exception being for high Germanium doping in which case fluences of between 10 to 15 KJ/cm^2 should not be used without taking into consideration the effects of physical damage upon the channels produced. It should be noted that the occurrence of physical damage within the layers that does not lead to topographic deformity has not been characterised. Chapter 7 investigates the optical properties of directly written UV channel, and therefore characterises the

occurrence of hidden damage within the layers and the effect of topographic damage upon optical properties.

6.6 Conclusions

The discussion of the widely used combination of photolithography and etching as a means of waveguide definition has highlighted the advantages of the UV direct writing technique. In particular the flexibility with respect to rapid prototyping, the ability to grade core index, and the possibility of direct application of FBG definition techniques in the planar geometry are all considerable advantages which are difficult to achieve using alternative methods. The main disadvantage identified is the limited magnitude of UV induced refractive index compared to compositionally defined structures. However, this can be taken into consideration during device design and is a limiting factor with respect to miniaturisation rather than a fundamental flaw of the technique. The difficulties associated with the mass production of devices using direct UV writing were also highlighted.

The mechanisms responsible for photosensitivity observed within Germanosilicate glasses have been presented and a review of the historically observed effects and the magnitude of induced Δn included. A "state of the art" review has shown the previous work undertaken within the field of direct UV writing, and has highlighted the feasibility of the work encompassed in this thesis. The process of photosensitivity enhancement and the equipment used for deuteration and subsequent UV exposure has been included.

Using the equipment outlined the process of determining suitable writing regimes to produce UV written waveguides has been presented. The mechanisms responsible for UV induced damage are highlighted and the range of exposure conditions apparently suitable for further investigation has been determined. Fluence up to 25kJ/cm^2 has been identified as a range that encompasses minimal effects through to damage. Further investigation of channels written within this range will offer additional information regarding the induction of UV written channels in three layer FHD samples.

7 Characterisation of UV Written Waveguides

The ultimate aim of the application of direct UV writing within planar Germanosilicate waveguides is the production of three-dimensional guiding structures, through inducing channels with increased relative index. The previous chapters have focused on the materials properties both during fabrication and with respect to the damage caused upon exposure to intense UV radiation. However, the goal of producing waveguiding structures requires that optical properties such as the induced refractive index and propagation loss are determined. It is important that the optical characteristic of UV written waveguides are determined if devices fabricated using this technique are to be further integrated into optical transmission systems. The calibration of UV writing parameters to the resultant optical properties of directly writing waveguides will greatly aid the future application of the technique, and liberate a vast amount of information regarding the mechanisms responsible for UV induced refractive index within Germanosilicate layers produced using FHD. This Chapter therefore focuses on the characterisation of waveguide properties, in particular the polarisation dependence, propagation loss, spectral response, and numerical aperture.

The samples used for the investigations discussed in this Chapter were identical to the three-layer, index matched clad, and high/medium/low germanium core, samples that have been described in Chapters 5 and 6. Two different sets of UV written channels were written for each type of sample. The first set of channels were identical to those used in Chapter 6, thereby giving a continuous range of fluences and allow correlation of the phenomena observed previously to be linked to optical properties. The second set of channels only encompassed a maximum and minimum value of fluence associated with a 10mm/min and 100mm/min translation speed, for each of the spot sizes. However, each channel type was repeated four times allowing multiple characterisation measurements of nominally identical channels. The entire set of channels were also repeated in the samples after a period of one hour, thereby allowing an indication of the affect of Deuterium outdiffusion upon optical properties of the UV written channels.

7.1 Polarisation Dependence

The majority of optical transmission systems do not rely on polarisation effects, and so ideally must have identical propagation characteristics for all possible polarisation states.

However, FHD layers are expected to be inherently birefringent due to the in-plane stress associated with the thermal expansion mismatch between substrate and layer as highlighted in Chapter 4. The inherent birefringence of the layered structure will have a direct effect upon UV written waveguides within the core layer. The nature of the FHD structures core-clad interface is also likely to be considerably different from the UV induced core-clad interface, therefore suggesting an inherent degree of polarisation dependent loss. The following section aims to determine the degree of polarisation dependence through investigating polarisation dependent loss and the polarisation maintaining abilities of UV written waveguides. Polarisation dependent loss is a comparative measure of the relative loss between two polarisation states, and gives an indication of the sensitivity of guiding structures to the launched polarisation state. Polarisation maintaining ability is a comparative measure of birefringence since a highly birefringent guide should maintain polarisation, assuming the launch polarisation is aligned with one of the principle axis of the birefringence. If the launch polarisation is not aligned with one of the principle axis then polarisation rotation will occur during propagation. The complementary determination of polarisation dependent loss and polarisation maintenance allows an indication of relative birefringence to be obtained, such that a sample with polarisation dependent loss and polarisation maintaining properties is likely to be birefringent.

The convention for describing polarisation within planar waveguides is as TE; component of the E- field is perpendicular to direction of propagation and TM; component of the H-field is perpendicular to the direction of propagation, as described in Chapter 5. However, the case of a 3-D guiding structure obviously complicates the matter, it is normal to orientate TE-TM such that the supposed planar structure is parallel to the air interface above the guiding structure. For the case of significantly buried waveguides TE-TM nomenclature obviously becomes less useful. In the interest of simplicity the following section assigns polarisation states as horizontal; being the alignment parallel to the planar structure or perpendicular to the direction of writing beam incidence and consistent with TE polarisation, and vertical; being the alignment perpendicular to the planar structure or parallel to the direction of writing beam incidence and consistent with TM polarisation.

7.1.1 Measurement Technique

The measurement of polarisation dependence for the samples prepared for characterisation took place using a 633nm HeNe source, objective launch and an output imaging system focused onto a photodiode. A schematic of the optical equipment is shown in figure 7.1. The objective launch allowed the focusing of the input signal onto the waveguide facet thereby maximising launch efficiency. The addition of a Polaroid sheet

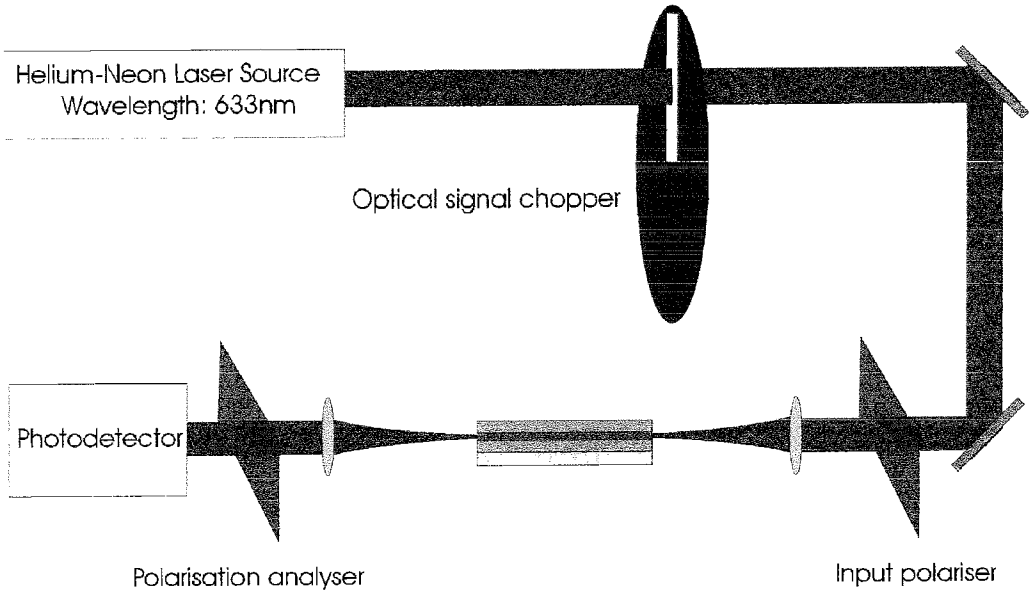

Figure 7.1, equipment used to determine polarisation characteristics of UV written waveguides

into the beam path prior to the objective lens and subsequent waveguide excitation, allowed the polarisation state of the guided mode to be controlled. The addition of an analyser, allowed the output polarisation state to be determined, and in particular allowed the polarisation maintaining properties of the waveguides to be determined. The output signal from the waveguide was imaged onto a Silicon photodetector, and the relative intensity determined using a lock-in amplifier synchronised to the beam chopper, thereby minimising the effect of background light and increasing the accuracy of the readings.

The analysis of the samples using polarised light took place through the comparison of the waveguide output signal produced by unpolarised excitation, to the output signals produced by the two orthogonal polarisation states orientated to the axis of the sample. Although a rigorous measurement of polarisation-dependent loss is not achieved using this method, it is possible to compare the relative propagation dependence due to polarisation.

Further information regarding the polarisation dependence of the waveguides was gained through exciting a mode with one polarisation state and analysing the output using the orthogonal polarisation state. If the waveguide is highly birefringent and therefore polarisation maintaining, a minimum signal will be observed. It is expected that the planar waveguide produced using FHD will be inherently birefringent due to the stress induced upon cooling from consolidation.

7.1.2 Effect of Writing Conditions

The determination of polarisation dependence for all three samples was undertaken using the technique outlined. The correlation of polarisation effects to writing conditions, in particular the fluence was therefore possible. Summary graphs showing the total loss for both orthogonal polarisation states relative to the output resulting from unpolarised launch, and percentage transmittance resulting from crossed input and analyser, are shown in figure 7.2. The error bars indicate the standard deviation from the mean resulting from the measurement of four channels written under nominally identical conditions.

The loss for the orthogonal polarisation states has a minimum value of 3dB associated with the presence of the polariser in the system before the launch. Assuming the output of the laser is unpolarised and that the polariser is 100% efficient then a minimum loss base of 3dB is established. However, an actual observed minimum in loss is likely to be lower than 3dB due to imperfect polarisation states produced by the polariser. If the laser output is polarised to some degree this will also lead to a shift in the loss measurements, although the measurement of identical channels and averaging of results is assumed to have taken this into account.

A highly birefringent sample is likely to have high polarisation dependence upon propagation loss, such that a guided mode of a specific linear polarisation will exhibit greater loss compared to an identical mode of orthogonal polarisation. Any differential loss arises from the different nature of the FHD and UV defined interfaces, such that if polarisation is not maintained then loss arising from the different interfaces is averaged. If polarisation is maintained it suggests that launch state is aligned with the axis of birefringence for the sample, if this is not the case polarisation rotation occurs.

The graph for the high Germanium sample clearly exhibits polarisation dependent loss and the associated polarisation maintaining properties. The divergence of the relative losses for both orthogonal polarisation states, the signature of polarisation dependent loss, is

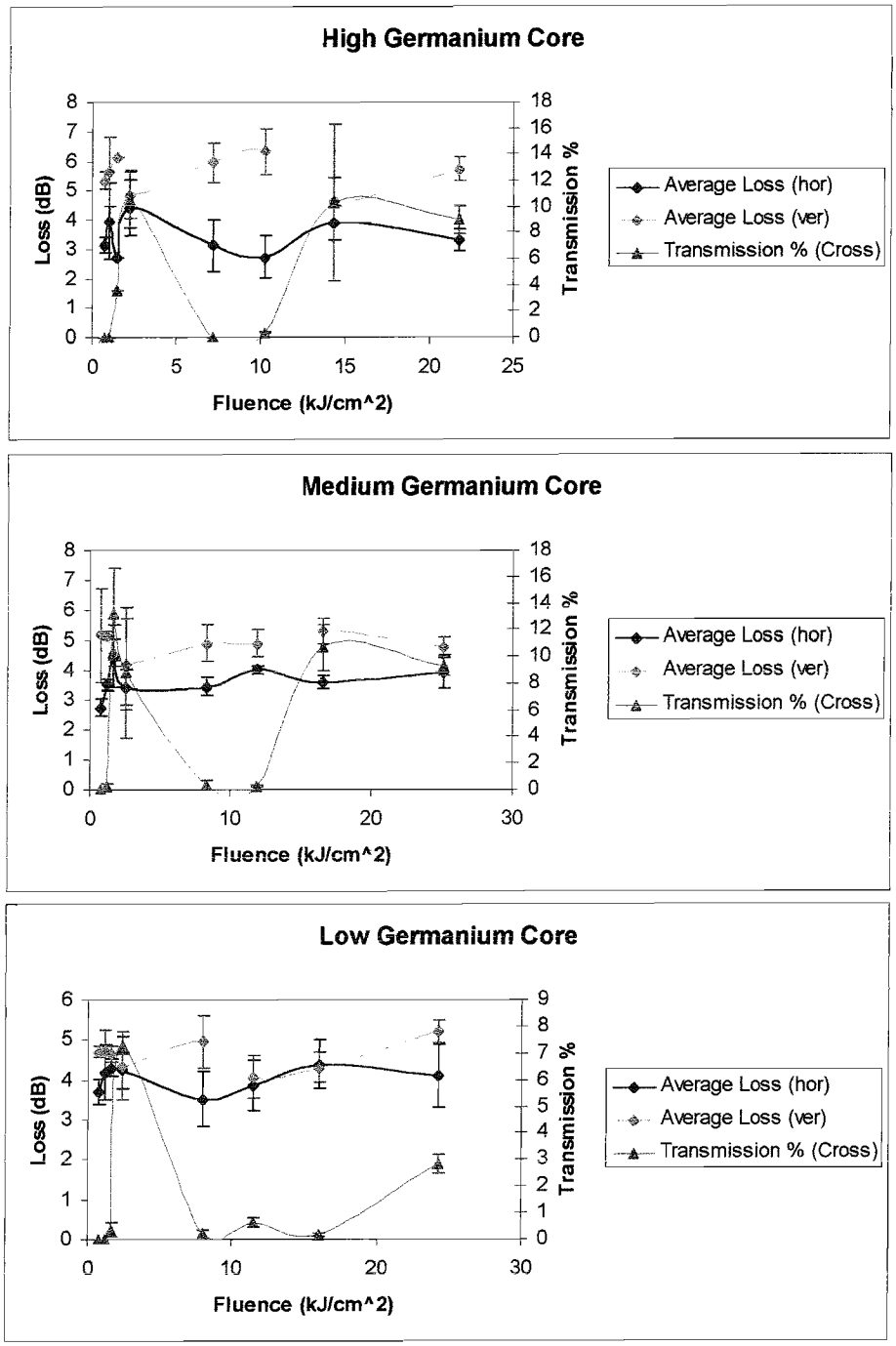

Figure 7.2, plots showing polarisation dependent loss and polarisation maintenance against UV writing fluence

accompanied by the minimisation of polarisation rotation during propagation through the waveguide. It is particularly notable for the fluence range ~5-12kJ/cm^2 that a decrease in loss for the horizontally polarised mode and increase in loss for the vertically polarised mode, coincides with apparent polarisation maintaining properties.

The graphs for the medium and low Germanium samples exhibit similar trends in polarisation maintaining properties. However, it appears that although the trends observed for polarisation dependent loss occur they are of a scale similar to the error of the

measurement system. The direct observation of polarisation dependence of propagation loss has therefore not been possible for the two lower Germanium samples. It is assumed that loss will follow a similar relationship depending upon polarisation maintaining properties as observed for the high Germanium sample.

The deviation from the expected polarisation maintaining properties associated with stress-induced birefringence suggests that the writing process is altering the stress field experienced by the waveguide. This is likely to be caused by thermalisation of the core during writing, resulting in the inherent stress being annealed out of the UV exposed region or a cancelling stress field being applied.

From the data presented it is clear that a high level of birefringence occurs within the waveguides, and that the degree of birefringence can be modified by the writing conditions. However, the degree of birefringence is difficult to determine absolutely with the current measurement technique. It appears that fluences below ~5kJ/cm^2 produce highly variable waveguides, the properties of which change rapidly with increasing fluence. The relationship for waveguide properties for higher fluences appears to be more stable. This combined with the writing regime information acquired in Chapter 6 suggests that channels written at fluences in the range of 7-15kJ/cm^2 are suitable for further investigation.

7.2 Propagation Loss

The transmission loss for an optical communication system is one of its most important attributes since it defines the distance between the need for signal amplification. In single mode fibre, loss is of paramount importance since this is the long distance transmission media. Losses of the order decibels per kilometre are achievable and commonplace in industrially produced fibre. The loss within integrated optical devices tends to be less critical since the primary purpose of such systems is not as a transmission media, but as a functional element. The path lengths for waveguides on a chip are dramatically shorter than repeaterless fibre lengths, therefore greater losses are tolerable. The losses for integrated optical devices tends to be higher due to larger concentrations of dopants required for processing, resulting in loss in the range of decibels per centimetre. The following section aims to determine the transmission loss for UV written waveguides within FHD samples, and attribute the losses to possible sources.

7.2.1 Measurement Technique

The determination of transmission loss due to a guided wave propagating through a guiding structure was undertaken using the "cutback" method. The standard cutback technique involves the measurement of transmittance for a waveguide of given length, and repeat measurement after subsequent reductions in path length. This is normally achieved by sequential measurement and dicing processes, thus allowing the waveguide length dependent loss to be calculated. Normally through using a single sample and reducing its length, the launch efficiency at the waveguide input facet remains constant, implying that any change in transmittance is purely due to the change in length. However, the time required to sequentially prepare and measure a sample with several different lengths is considerable. In order to reduce the time required to use the cutback technique a single sample was cut into three different lengths and all facets were polished to optical quality. Use of this modified method allowed the rapid acquisition of propagation loss data, however a moderate decrease in accuracy is to be expected since identical launch

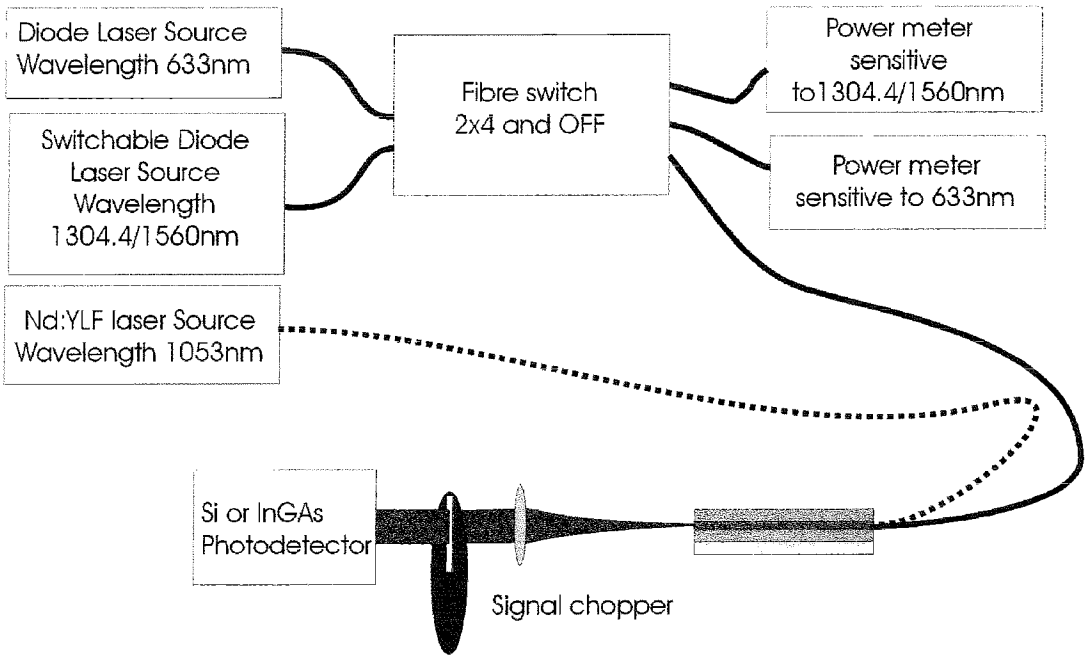

efficiencies are unlikely to occur for the different samples.

The determination of relative transmittance for the samples took place at four wavelengths ranging between 633 to 1560nm, guided wave excitation took place using a butt coupled launch fibre, and sample output power was measured using photodiode detectors, a schematic of the measurement equipment is shown in figure 7.3. A 633nm

diode source and switchable 1304.4/1560nm-diode source connected to a fibre switch allows selectability between the three wavelengths. The output from the fibre switch could be directed to a single mode 1310/1550nm standard telecom fibre or to fibre coupled visible and infrared detector heads. The use of the detectors allowed direct monitoring of the various sources output power prior to launch into a sample. An additional wavelength of 1053nm was supplied using a Nd:YLF source coupled to a dedicated single mode fibre. The power at 1053nm was found to be sufficiently stable during offline calibration of the onboard power selector, such that additional power monitoring was not deemed necessary during the sample measurement process. The light from the launch fibre was coupled into the sample being interrogated by simple "butt coupling", through the close proximity of fibre output and sample input facets. The accurate alignment of the fibre output facet to the waveguides present in the sample was achieved using micrometer-controlled stages, thus allowing guided wave excitation within the UV written channels. Launch efficiency was maximised by monitoring the power at the output facet of the sample while launch fibre alignment was modified. The output power was monitored by imaging the output facet onto a photodetector with suitable sensitivity. Two detector types were employed; a Silicon diode was used for visible wavelengths and an Indium-Gallium-Arsenide (InGAs) diode for infrared wavelengths. The imaging lens could be translated along the beam axis allowing the image of the sample output facet to be focused onto the photodiode. A degree of beam steering resulting movement of the image onto the photodiode could be achieved by alignment of the imaging lens in the plane perpendicular to the beam axis. The use of a signal chopper placed in between the output of the imaging lens and the photodiode allowed signal interpretation using a lock-in amplifier, thereby increasing sensitivity and removing error associated with background light. An adjustable aperture was placed in front of the photodiode, allowing the discrimination between signals originating from the planar and UV written waveguides present within the sample.

The use of the technique and equipment outlined allowed the accurate determination of material dependent propagation loss for the three layer samples previously outline in Chapter 6. After the completion of the writing process, each sample was cut into three lengths of 5, 10 and 20mm. Samples of the same composition were simultaneously polished to optical quality thus ensuring that the different length samples all had similar quality end facets. It was envisaged that it should be possible to determine the effect of UV writing conditions, Germanium doping level, relative deuterium level and transmission wavelength upon the material loss of UV written waveguides in FHD structures.

7.2.2 Effect of Writing Fluence

The propagation loss for all three samples with different Germanium doping levels largely follows the data presented in section 7.1, such that low loss with steady fluence dependence occurs between the fluences of 7 to 15kJ/cm^2. Loss was measured for all channels written into the samples, however low and high fluences produced data with a high variability and excessive error. For low fluence this is likely to be due to the very low induced refractive index, and therefore the guiding nature of the channels has a pronounced effect upon the loss properties. Higher fluences are more likely to cause significant damage through thermalisation of the core and therefore induce loss. The following discussion focuses on the loss data acquired within the "steady state" fluence-loss regime that is thought to be most likely to produce suitable waveguides.

The general trend for increasing writing fluence appears to be an increase in loss as shown in figure 7.4. In the low Germanium sample, it is difficult to observe any trend with increasing writing fluence, this is due to the limited sensistivity of the loss measurement technique. It was found that a maximum sensitivity of approximately 0.4dB/cm with an associated error of ±0.2dB/cm was achievable, therefore making it impossible to accurately determine losses lower that ~0.5dB/cm. If there is any effect induced by increasing writing fluence upon the loss for the low germanium sample then it is below the sensitivity of the technique used.

Both the medium and high Germanium samples show an increasing loss with increasing writing fluence. The nature and rate of loss variation appears to be similar for both sample types (high deuterium), suggesting that a similar effect is occurring within both samples. The rapid increase in materials loss with increasing writing fluence suggests that damage is occurring within the core during the writing process. There is likely to be an increase in loss due to the formation of defect centres mentioned in Chapter 6. The scale of the apparent damage in these cases suggests that thermalisation and resulting large-scale damage has occurred during the writing process. From the data it would appear that using fluences greater than ~10kJ/cm^2 for the high Germanium sample and 12kJ/cm^2 for the medium Germanium sample results in a considerable increase in loss compared to the background.

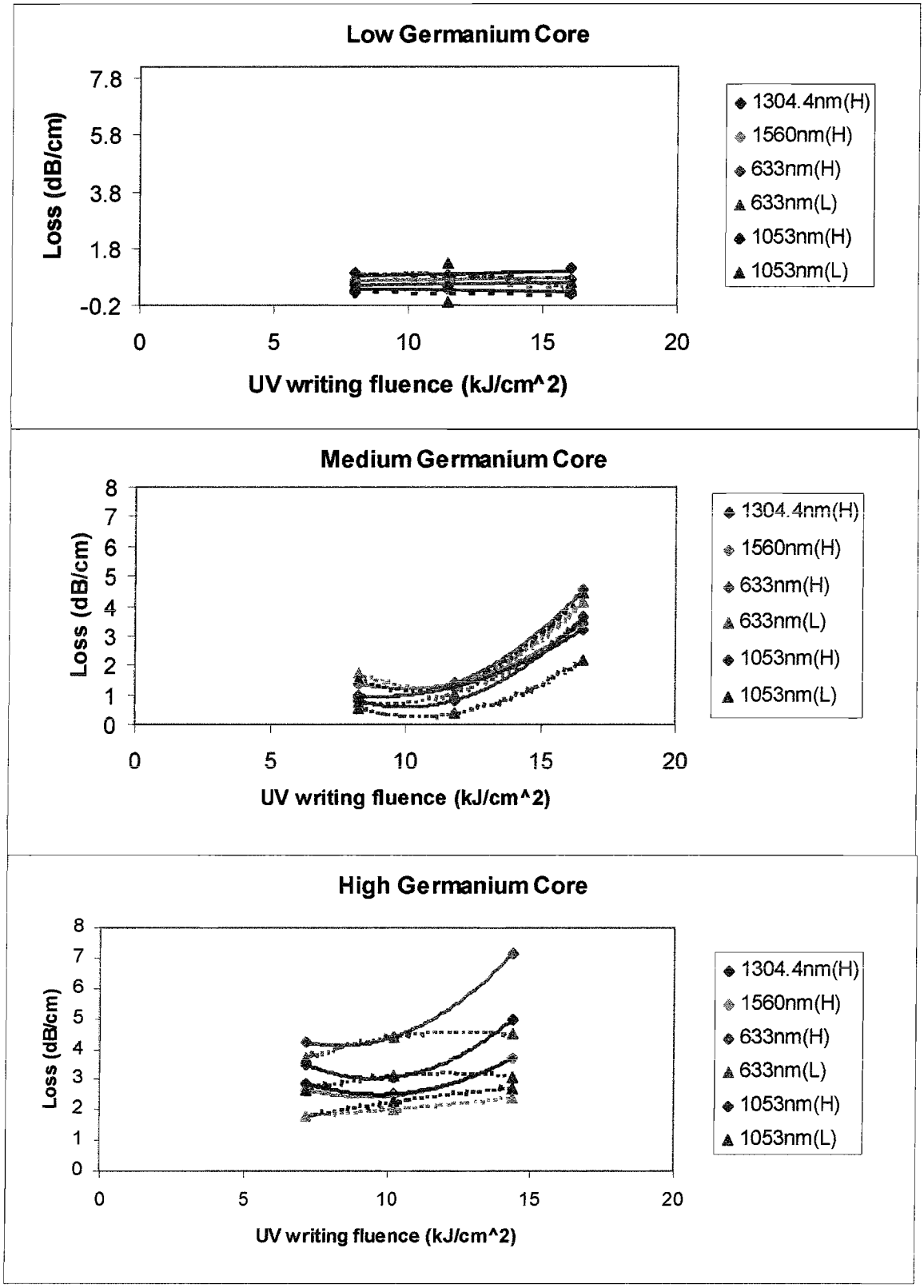

Figure 7.4, plots showing propagation loss at various wavelengths against UV writing fluence for high, medium and low Germanium samples with high (H) and low (L) relative deuterium levels

7.2.3 Effect of Germanium Doping

The direct effect of Germanium doping level upon propagation loss can be seen by comparing the graphs in figure 7.4. The average loss increases with Germanium doping level, such that for a constant fluence of ~7kJ/cm^2, propagation loss is <0.8dB/cm, <2dB/cm and <4dB/cm for the low, medium and high Germanium samples respectively.

The variation in loss due to Germanium doping level is likely to arise from two sources. Firstly, as mentioned in section 7.2.2, the relative level of Germanium directly affects the onset of fluence dependent loss that can be attributed to the initiation of UV induced damage. For a given fluence a sample with a higher level of Germanium doping is therefore likely to have a greater degree of UV induced damage. However, this assumes that significant damage and associated loss is occurring during UV induced index change, which is unlikely to always be the case.

The second explanation for the dependence of propagation loss upon Germanium doping level is the occurrence of absorption or scattering associated with increased Germanium content. The increase in loss due to absorption can be associated with the deviation from pure silica due to doping. However, since Germanium doping is not noted for introducing significant adsorption losses in the 0.6-1.6μm window this is thought to be an unlikely explanation for the magnitude of the effect observed. The introduction of scattering centres associated with Germanium doping level is of greater relevance. As discussed in Chapters 2 and 4, the temperature of the substrate during the FHD process has a direct effect upon the nature of Germanium incorporation into the soot layer. It is possible during the fabrication process for crystalline Germania to become incorporated within the layer. The presence of these crystallites either directly or as compositional inhomogeneities that may occur upon melting of the crystallites, could result in significant scattering centres. The effect of Germanium doping level upon propagation loss can therefore be explained by the relative introduction of scattering centres, this effect will be discussed further in section 7.2.5.

7.2.4 Relative Effect of Deuterium Loading Level

The determination of the Deuterium concentration and its effect upon the propagation loss observed for a UV induced waveguide is difficult to determine absolutely. As previously outlined in Chapter 6, as soon as a sample is removed from the Deuterium loading cell outdiffusion starts to occur. Samples are stored at "dry ice" (solid CO_2)

temperature for the short length of time between unloading and writing, and therefore outdiffusion during this time can be considered negligible. However, the room temperature nature of the writing process dictates that outdiffusion is continually occurring during UV exposure. The time taken to write a set of channels may therefore have an effect upon the optical nature of the waveguides produced. The difference in propagation loss for identical channels written approximately one hour apart can be seen from the graphs in figure 7.4.

For the low Germanium sample, any effect is on a scale too low to be observed using the current propagation loss measurement technique. However, both the medium and high germanium samples show an effect. The high germanium sample shows the most dramatic effect, with the dependence of loss upon writing fluence taking a different form according to the relative deuterium level. The low deuterium channels appear to have a fluence dependent loss which is of a much more linear nature, suggesting that damage has not occurred on the same scale as for the high deuterium channels. The medium Germanium samples show the same form of fluence dependent loss irrespective of relative deuterium level, but there is a general trend for lower losses associated with the low deuterium level.

The relative deuterium level seems to have a direct effect upon the loss induced by a given writing fluence, suggesting that the enhancement of UV energy coupling and resulting index change is extended into the loss induction mechanism. However, it is worth noting that increased losses due to higher deuterium level could be due to increased OD incorporation within the silica matrix, as well as an increased UV sensitivity. The following sections highlight the wavelength dependence of propagation loss and deals with the possibility of OD absorption.

7.2.5 Wavelength Dependence

The propagation loss for a guiding structure for a given wavelength is of great importance for determining the suitability of structures for device applications, since it directly dictates the transmission window for which a given material can be used. Additionally the information gained regarding wavelength dependence of loss can aid the identification of the mechanism that is causing the loss.

The wavelength dependence of propagation loss against writing fluence can be seen in figure 7.5. The propagation loss measurement technique employed does not have sufficient sensitivity to observe any trends for the low Germanium sample, therefore making it impossible to draw any conclusions for this sample. Both the high and medium

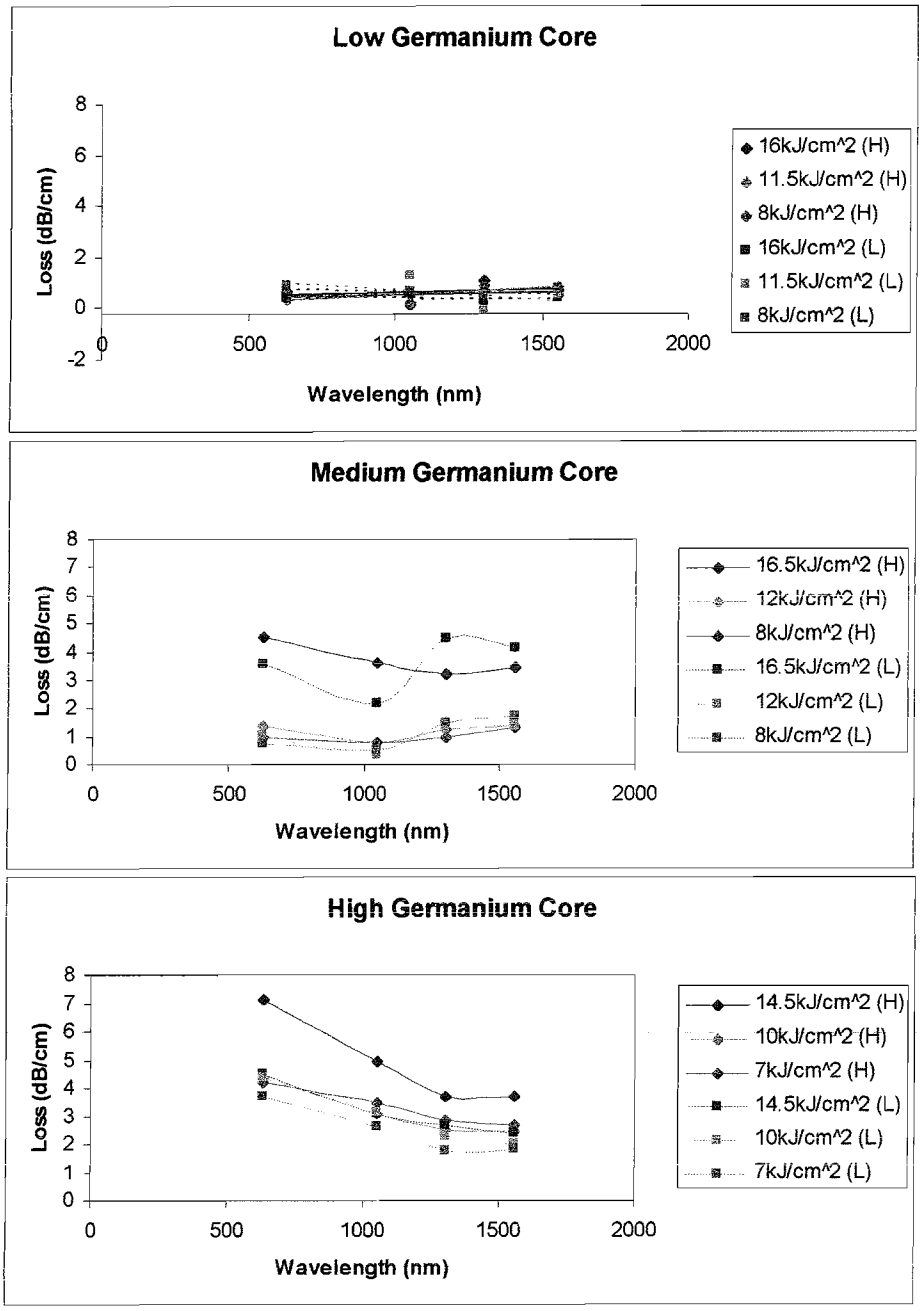

Figure 7.5, plots showing propagation loss at various writing fluences against wavelength for high, medium and low Germanium samples with high (H) and low (L) relative deuterium levels

Germanium samples do show interesting trends; a general decrease in loss can be observed with increasing wavelength for the lower end of the spectrum, which is consistent with scattering being the primary loss mechanism as discussed in Chapter 5. It is notable that higher fluences result in steeper decrease and higher initial value of loss, suggesting that part of the scattering is induced by the writing process. However, it can also be clearly seen that the high Germanium sample has a greater degree of inherent loss at lower wavelengths, suggesting that the Germanium concentration is also linked to the degree of scattering.

The total nature of the variation in loss across the whole spectrum is of interest since it gives information regarding the apparent guiding nature of the structures as well as the propagation loss. The change of gradient in the loss spectrum indicates that a mechanism with significant wavelength dependence is occurring. This may either be a specific absorption due to a component within the glass or due to the induced index structure. However, if the increase in loss was due to a specific absorption such as the first overtone of OH adsorption (1380nm) or the second overtones of OH (950nm) or OD (1240nm) [Stone, 1987], then it would be expected that all samples would exhibit the same effect to a similar degree.

It is likely that the changes in loss characteristics with varying wavelength are due to the guiding nature of the UV induced channel waveguides. The cut-off to single mode operation, as discussed in Chapter 5, can be used to explain the sudden increase in loss that is particularly notable for the channels written into the medium Germanium sample with low Deuterium level. However, it can be assumed that the relatively abrupt change in gradient for the other channels in both the high and medium Germanium samples are also due to cut-off. If V-number is used to calculate the UV induced refractive index from the cut-off values gained from the propagation loss measurements and assuming writing spot size represents channel size, then the medium Germanium sample has a range of Δn between 5.4×10^{-4} to 3.4×10^{-3} and the higher Germanium sample 8.4×10^{-4} to 4.5×10^{-3}. These values are only approximations due to the discontinuous measurement of propagation loss not giving a discrete value for cut-off wavelength.

A method for continually measuring the transmittance of the samples is highlighted in the following section. It is however apparent from the propagation loss data presented that samples doped with low Germanium and subsequently exposed to the UV writing regime highlighted results in the production of low loss waveguides (<0.5dB/cm). The medium and high Germanium samples show signs of a moderate change in refractive index, but the apparent occurrence of scattering as the primary loss mechanism suggests that inhomogeneities are occurring in the layers and to a certain degree is dependent upon writing conditions.

7.3 White Light Absorption Spectra

The measurement of relative transmittance over a continuous wavelength range allows an indication of wavelength dependent loss. Unlike the cutback technique described

in section 7.2 an absolute value for loss is not achievable, but the ability to measure the continuous variation in transmittance with respect to wavelength greatly aids the characterisation of waveguiding structures and materials. The measurement of white light spectra for a material allows the detection of absorption bands such as those associated with OH, which otherwise may be missed by a discontinuous measurement technique. The combination of the cutback technique and absorption spectra allows the complete determination of materials loss properties and the identification of probable sources, as well as waveguiding properties such as the wavelength for cut-off to single mode operation. The measurement of adsorption spectra in this case allowed trends observed using cutback to be confirmed and defined in detail.

7.3.1 Measurement Technique

The equipment required to attain absorption spectra, from the samples produced using the FHD process and the writing regimes outlined previously, consists of a broadband light source, a fibre launch set-up, a monochromator, and a suitable signal intensity

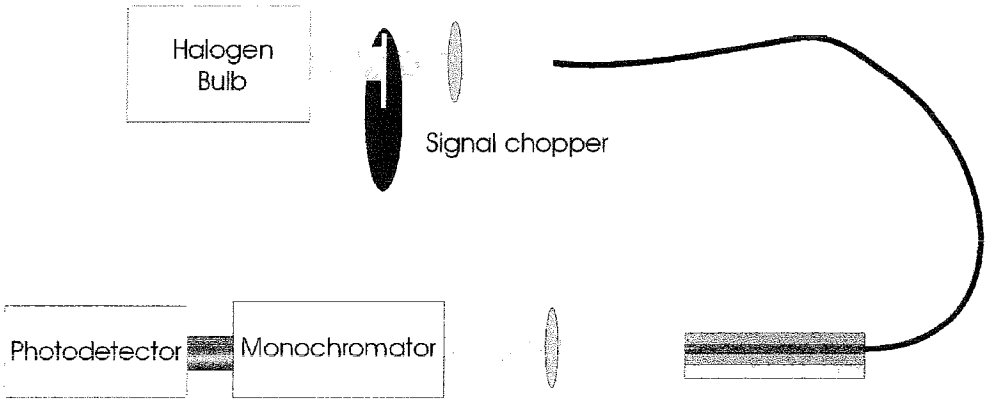

Figure 7.6, equipment used for obtaining white light spectra

monitoring system. A schematic of the white light measurement equipment is shown in figure 7.6. The white light source consists of an air-cooled halogen bulb, with an emission spectrum in the range 400 to 2000nm. The output for the bulb is collimated and chopped prior to focusing into the core of a multimode fibre, with parameters sufficient to allow highly multimode propagation for the entire wavelength range. The focusing of the signal into the fibre is optimised to result in maximum output at the other end of the fibre. The output of the fibre is then brought into close proximity with a UV written channel in a sample, resulting in simultaneous excitation of the waveguide for all supported

wavelengths. The launch fibre alignment is optimised to give maximum output from the UV written waveguide, using micrometer-controlled stages. The output facet of the sample is imaged onto the input slit of the monochromator, the width of which is adjusted until comparable with the image size thus resulting in only the waveguide output being spectrally analysed.

The monochromator is computer controlled allowing the accurate positioning of stepper motor aligned gratings, resulting in spectral resolution of <5nm. The absolute resolution of the monochromator is defined by the pitch of the gratings employed, and the width of the input and output slits. The minimisation of both input and output slits therefore results in the maximum resolution for the system. However, the input slit must match the size of the imaged output facet in order to ensure that only the modal structure associated with cut-off to single mode is observed. The output slit must also be of a width suitable to allow significant light onto the photodetector.

The photodiode used is of combined Si/InGaAs design, with the infrared sensitive cell positioned behind the visible range cell. Technically the use of such a detector should allow the continuous measurement of intensity in the wavelength range 400-1600nm. However, the misalignment of the two cells resulted in the peak sensitivity areas not coinciding, thus requiring the realignment of the detector head when the different cells are used. It was found that the sensitivities of the two cells were also not entirely compatible, resulting in a significant dead zone for the 1000-1050nm wavelength range. The signal from the detector head is interpreted using a lock-in amplifier synchronised to the modulation frequency induced by the optical chopper, thus allowing the minimisation of background noise.

The data from the amplifier is supplied to a PC allowing integration of monochromator operation and data acquisition within dedicated software. Automated operation allows discrete variation in wavelength and measurement of associated signal intensity. The use of the equipment outlined allowed measurement of relative sample transmittance with ~5nm resolution across the ranges of 600-1000nm and 1050-1600nm.

The interpretation of the data gained using the monochromator and associated equipment required the comparison with the spectrum for the launch fibre, thereby ensuring that any observed effects are solely due to the sample being analysed. The relatively high propagation losses previously observed for the samples dictated that a degree of output intensity normalisation was required when acquiring the fibre spectrum. The comparison of "raw" sample to fibre spectra took place using a pseudo attenuation calculation, such that

the fibre spectrum was treated as the power input into the sample and the sample spectrum was treated as the sample output power. The prior normalisation of fibre output power dictates that the derived sample spectra are purely relative, and absolute losses cannot be gained. However, the trends observed from the composite spectra do highlight the relative change in transmittance for a sample as the wavelength is varied, thus allowing the interpretation of wavelength dependent properties for the samples analysed.

7.3.2 Effect of Materials Properties and UV Writing Conditions

A typical transmittance spectrum for UV induced refractive index channels written with varying fluences is shown in figure 7.7. All of the spectra taken exhibit the same trends as highlighted in section 7.2; a steady increase in transmittance with increasing wavelength associated with loss occurring due to scattering, an apparent peak in transmittance which is assumed to be the point of cut-off to single mode operation for the waveguide, and finally a steady decrease in transmittance associated with the reduction in guided mode overlap with the core region.

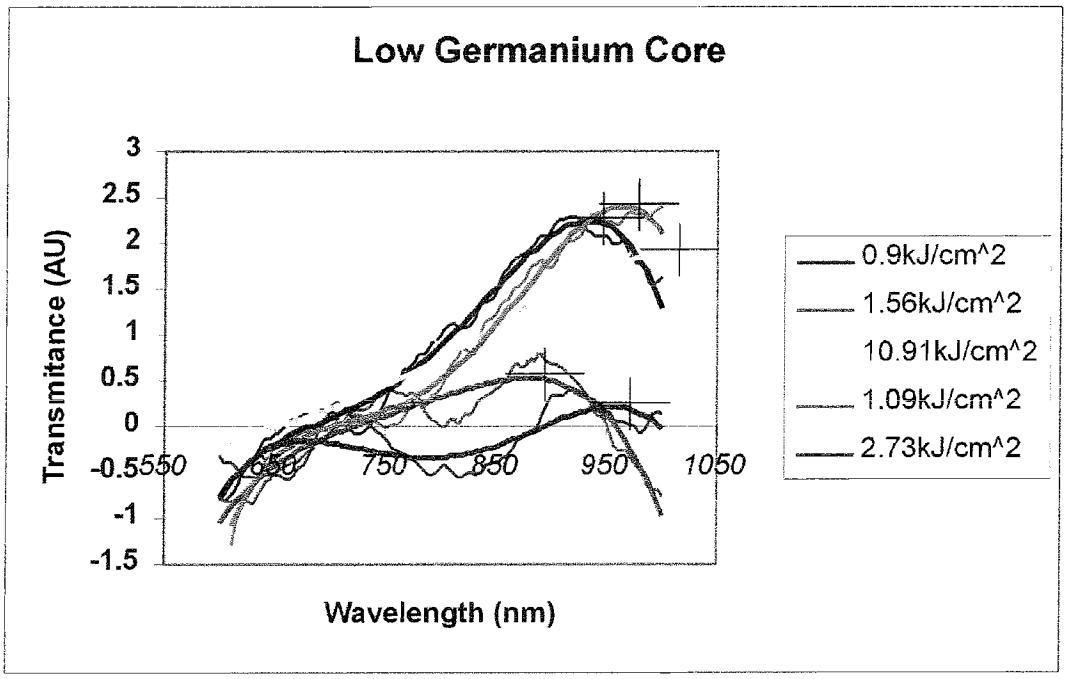

Figure 7.7, plot showing spectral propagation dependence for channels written with different fluences

In all spectra there is a notable lack of any specific absorption bands that can be attributed to contaminant species or the presence of OH/OD. This is likely to be due to insufficient sensitivity of the measurement technique and effects at wavelengths longer than

~1100nm being small comparable to the reduction in guiding associated with wavelengths beyond cut-off. The very short path length of the samples compared to similar measurements undertaken in fibre, dictates that any effects due to absorption species will be very small relative to the signal strength. It is therefore unlikely that the amount of OH incorporation within the FHD layers can be determined with the current samples.

The determination of the wavelength at which cut-off to single mode operation occurs has been possible through using the spectra acquired for various UV written channels. The point of cut-off has been assumed as the point at which the transmittance variation with increasing wavelength becomes appreciably negative. The determination of cut-off wavelength and calculation of the UV induce refractive index change has allowed the effect of writing fluence, Germanium level and relative Deuterium level to be resolved. Figure 7.8 shows UV induced Δn against writing fluence for the three samples previously characterised in section 7.2.

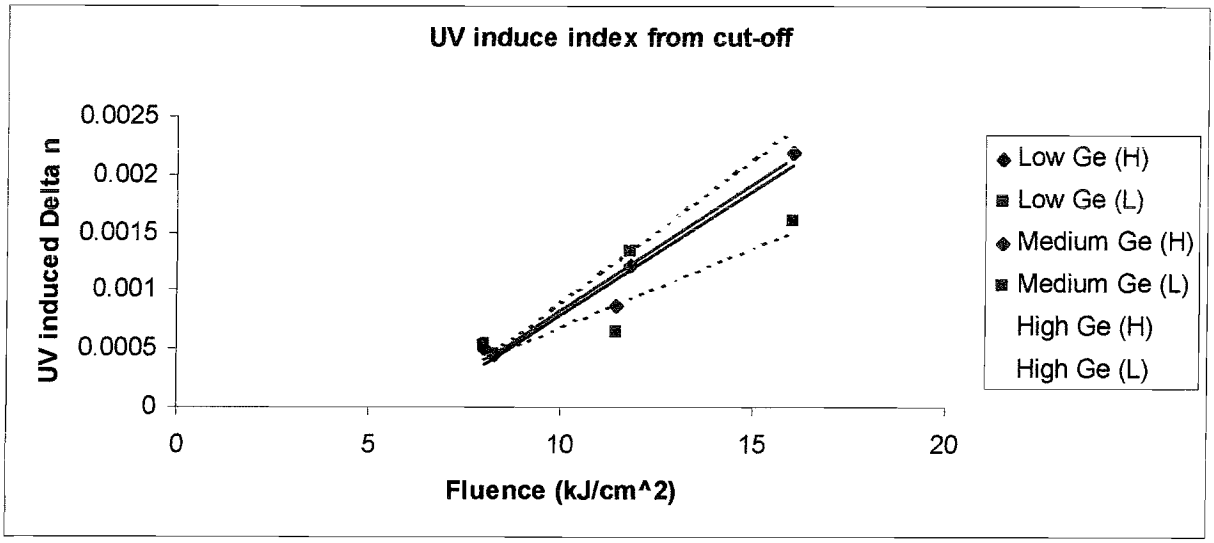

Figure 7.8, plot showing UV induced Δn determined from cut-off against UV writing fluence for high, medium and low Germanium samples with high (H) and low (L) relative deuterium levels

The general trend for increasing fluence is an increase in induced refractive index, as is expected. It is also clear that samples containing higher levels of Germanium are more photosensitive, as expected from the discussions in Chapter 6. It is less clear from the data presented what effect deuterium level has upon the induced refractive index, however this is possibly due to the inaccuracies in determining core index from cut-off wavelength. The indistinct nature of cut-off due to weakly guided modes continuing to propagate in the same direction as the waveguide will lead to considerable inaccuracies in determining the precise cut-off wavelength. The addition of high index fluid onto the top surface of the samples did

not result in a significant increase in weakly guided mode stripping, and therefore results more accurate than those presented could not be achieved.

The use of absorption spectra has allowed the trends previously observed using cutback measurements at discrete wavelengths to be confirmed. However, the accurate determination of UV induced refractive index as a function of writing fluence has not been possible. The assumption that the V-number used for symmetrical cylindrical guides is directly applicable to the UV induce planar case has possibly led to inaccuracies. It is therefore necessary to further determine the absolute values of induced refractive index achieved.

7.4 Numerical Aperture

The direct determination of the UV induced refractive index change produced within the FHD samples involved the measurement of the numerical aperture for the waveguides. The numerical aperture is effectively the acceptance cone defined by the conical half angles for which incoming rays are below the critical angle for mode propagation within a guiding

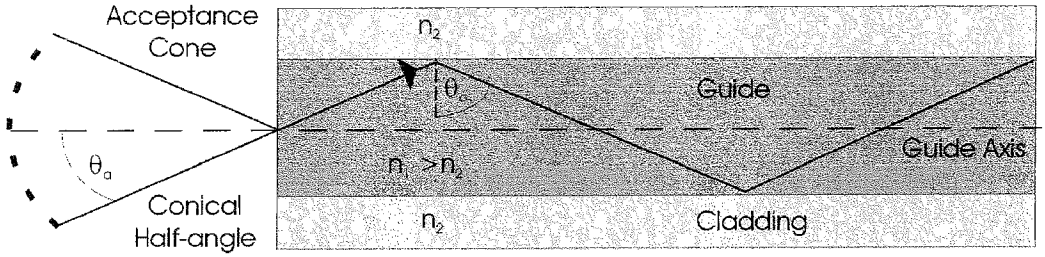

Figure 7.9, schematic showing Numerical Aperture and relevance to critical angle

structure, see figure 7.9. The relationship between acceptance angle and the critical angle for total internal reflection at the core-clad interface allows the refractive index difference between core and clad to be calculated. The definition of numerical aperture NA, is given below;

$$NA = n_0 \sin\theta_a = \left(n_1^2 - n_2^2\right)^{\frac{1}{2}}$$

It is therefore possible through direct measurement of the acceptance angle to calculate the NA for a given guiding structure, and subsequently derive the Δn, assuming that either the core or clad indices is defined.

7.4.1 Measurement technique

The direct measurement of the NA for a waveguide is possible using a variety of techniques, either through determining the range of input angles for which guided mode excitation occurs or through observing the range of angles output from a waveguide. The use of the latter technique proved to be the simplest to implement through measuring the divergence of the output signal relative to distance from the sample output facet. Accurate measurement of the farfield intensity pattern at a range of distances allowed the calculation of acceptance angle and therefore Δn for the waveguide being analysed.

The measurement of UV induce Δn for the FHD samples used in the previous sections took place using a 633nm HeNe source, a fibre launch and a CCD camera, shown in figure 7.10. The launch efficiency for each waveguide was maximised through the alignment of the fibre to the sample while observing output intensity and profile by forming an image of the output facet on the CCD array. Upon suitable waveguide excitation the image plane of the CDD array and imaging lens was moved away from the output facet, thereby imaging the farfield intensity pattern. The image plane was backed off by a suitable distance, normally ~300μm, the launch power was then modified to give a suitable image on the CCD array. The images formed on the CCD array for subsequent incremental increases in image plane to output facet distance, while the launch power remained

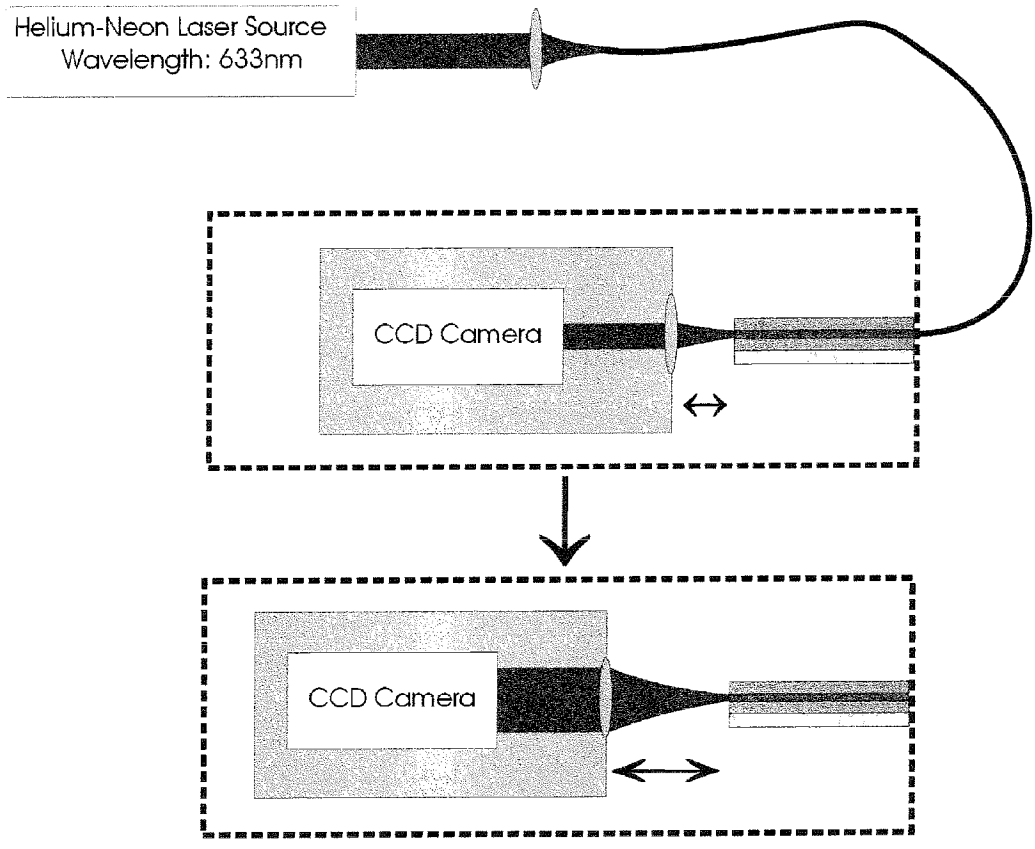

Figure 7.10, schematic of NA measurement equipment

constant, were acquired and stored digitally on a PC. It was therefore possible to build up a set of sequential images representing slices through the acceptance cone along the waveguide axis.

The images produced using the technique outlined were processed and the dimensions of the intensity pattern calculated using a piece of dedicated software written in Visual Basic. The height and width of the patterns were fitted using the first minima as the absolute dimension and by fitting a Gaussian function to the profile and assuming $1/e^2$ as the absolute dimension. Theoretically, both the minima fit and the Gaussian fit should be representative of the intensity pattern dimensions. In reality it was occasionally observed that one fit was considerably more suitable than the other. However, the absence of a consistently accurate method of attaining the dimensions of the intensity patterns led to the use of both sets to define the dimensions and therefore the NA for a given waveguide.

The measurement of the NA for both vertical and horizontal axis of the waveguides allowed the normalisation of the data to the Δn present between clad and core layers as measured in chapter 5. However, this assumes that the fabrication process required to produce three layer structures and the UV writing process does not significantly alter the relative index of the layers compared to that defined using prism coupling. The act of UV writing will obviously affect the Δn between cores and clad, but since the index change is expected to be positive it is assumed that any normalisation to the pre-UV exposure Δn will result in underestimation of UV induced index change.

The use of relative intensity patterns to infer the acceptance angle and therefore NA relies on the structure of the pattern purely arising from the "cut-off" associated with the critical angle for total internal reflection being exceeded. Any structure within the intensity pattern due to the modal nature of the waveguide will give rise to misleading results, therefore it must be assumed that all waveguides are highly multi-mode at 633nm if representative data is to be acquired. The use of a coherent light source is also likely to cause problems in accurately imaging the intensity pattern arising from the acceptance cone. It is very likely that the intensity patterns observed will be distorted to some extent by interference effects due to the defocused nature of the imaging process.

The limitation of the NA measurement system outlined must therefore be taken into consideration during the interpretation of the results. The follow section highlights the results that have been gained and the factors that contribute to them, whether inherent to the waveguiding structure or to the measurement technique employed.

7.4.2 Effect of Materials Properties and UV Writing Conditions

The results gained from the measurement of NA using the technique outlined previously are typified by the plot shown in figure 7.11, which shows the calculated NA for both minima and Guassian fitted data as well as the values normalised to the vertical NA defined by the FHD process. An effect similar to that observed in sections 7.1 and 7.2 for channels written with low fluences can be seen to occur. It was hypothesised in previous sections that the large variety in loss observed for low fluence may arise from excessively low Δn leading to very weak guiding and therefore pronounced loss effects. If the NA data

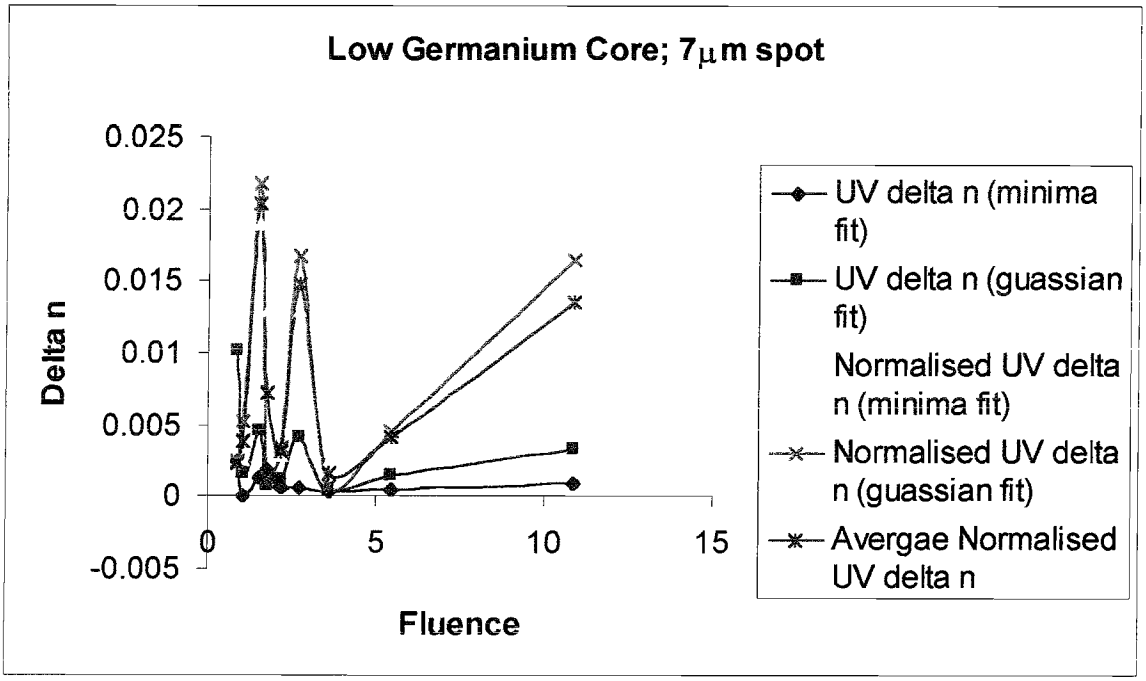

Figure 7.11, UV induced refractive index against fluence

in figure 7.11 is accurate then it would appear that a highly variable UV induced Δn may be the cause of the erratic variation of loss at low fluences. It is possible that such a variation in induced index could arise from the combination of type I and IIA index variation mechanisms mentioned in chapter 6, suggesting that for higher fluences the change in refractive index is due to type II damage related effects. The remainder of this section focuses on the apparent steady-state refractive index change with respect to fluence observed for the range greater than ~3-5kJ/cm^2.

The effect of Germanium concentration upon the UV induce refractive index change is demonstrated in figure 7.12, showing the measured Δn for the higher fluence ranges in both a high and a low Germanium sample. The large error apparent for some of the readings

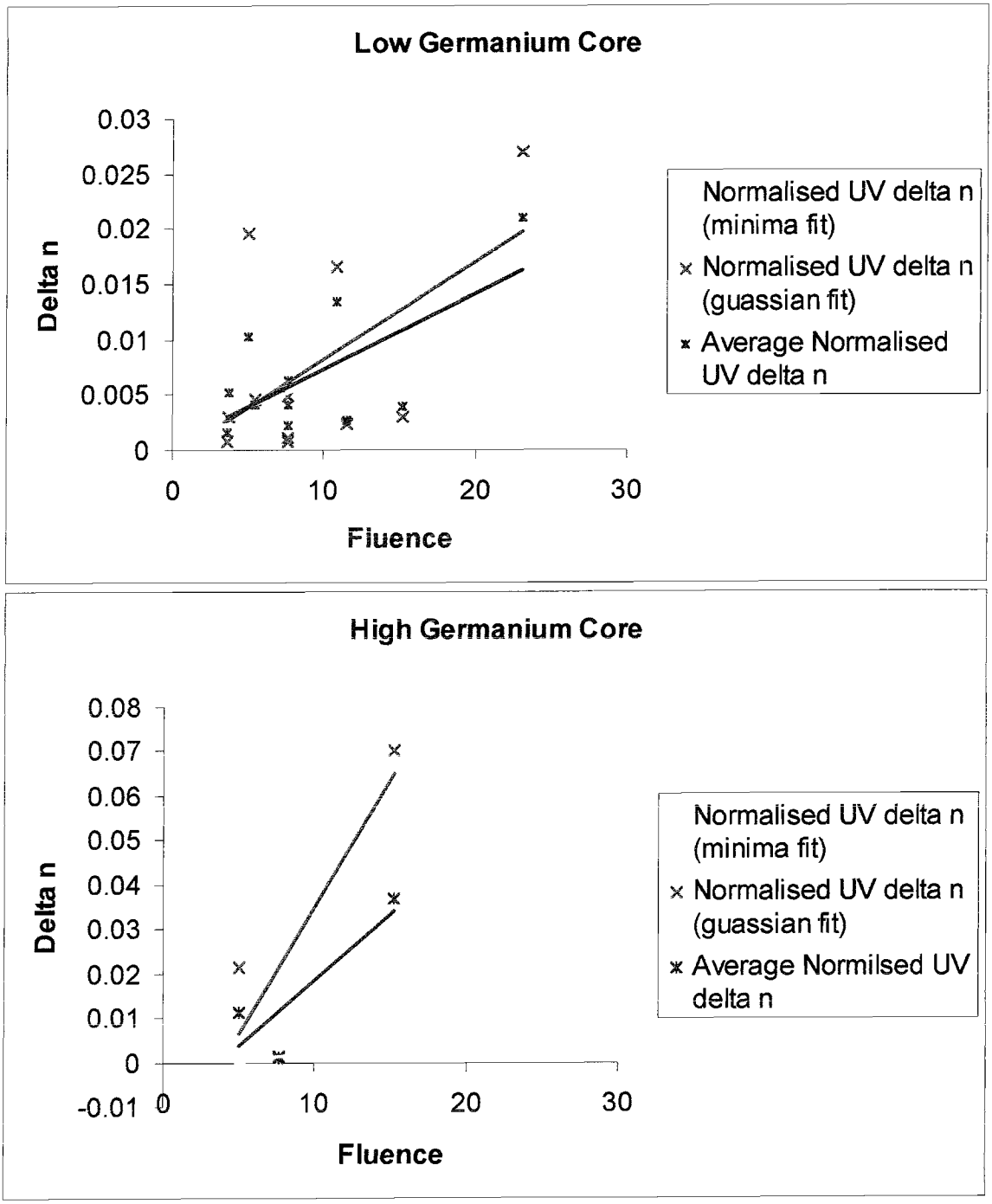

Figure 7.12, plots showing induced Δn against writing fluence for low and high Germanium samples

for the low Germanium sample is associated with inaccuracies in accurately controlling fluence through modifying writing spot size. The linear trend lines for both samples allow a relative measure of the accuracy of the NA measurement technique for the two samples to be determined. The error associated with the high Germanium sample is generated by the large scattering loss associated with such samples, as highlighted in section 7.2, leading to scatter induced structures within the intensity plots. If the "Average Normalised" induced index is taken as a representative measure of photosensitivity, it appears that the high

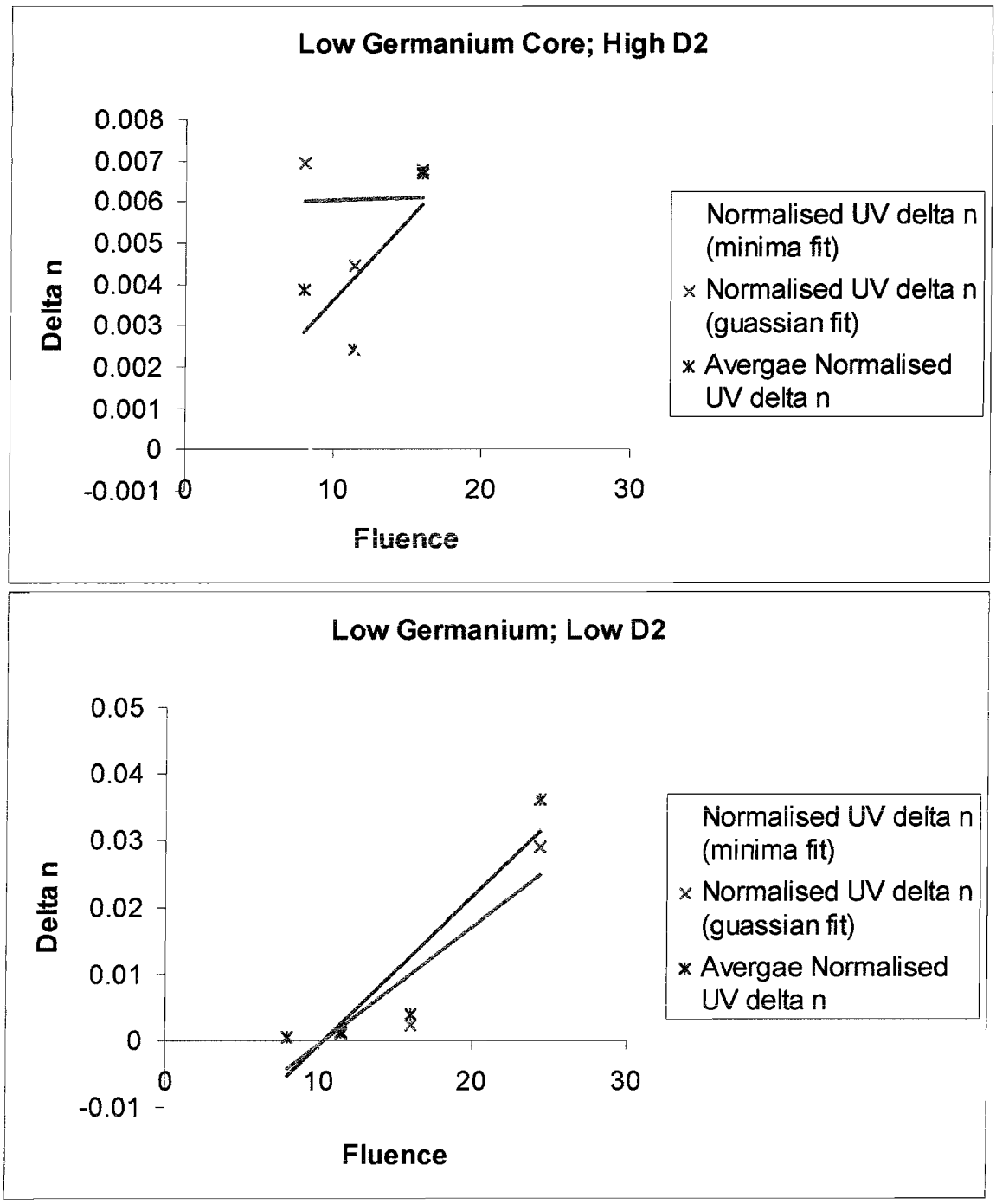

Figure 7.13, plots showing induced Δn against UV writing fluence for samples with varying levels of Deuterium

Germanium sample is approximately 40% more photosensitive than the low Germanium sample for the same fluence.

The direct comparison between waveguides written with high and low relative Deuterium levels is summarised in figure 7.13. The linear trend lines show a considerable degree of relative error associated with the measurement of NA for the high Deuterium sample, which is likely to arise for the low Δn observed in this sample for the fluences used to write the waveguides. However, by comparing the actual data for the two samples it

appears that the high Deuterium sample is approximately 25% more photosensitive compared to the low Deuterium sample written with the same fluence.

It has been shown using the NA measurement technique outlined in section 7.4.1 that it is possible to determine the relative refractive index of UV written waveguiding channels produced in FHD layers. The normalisation of directly observed data to known refractive index values determined by prism coupling, has allowed a method of determining refractive index. However, the imaging technique required to determine NA has a number of inherent errors originating from the coherent light source, the model structure of the waveguides and any scatter induced distortion of intensity profiles. It is unlikely that the data presented represents the absolute UV induce index of the waveguides measured, however the trends due to writing conditions and materials properties are likely to hold. The data indicates that modification of writing fluence during the waveguide definition process is a suitable method of controlling the magnitude of the induced index. In particular, the relatively steady-state variation associated with higher fluences would appear to be attractive for definition of PLC devices with varying index profiles. The maximum achievable UV induced index change appears to be dependent upon the level of Germanium doping and the Deuterium loading conditions. The data acquired suggests that UV induced indices in the region of 0.01 may be achievable through direct UV writing into FHD waveguiding structures.

7.5 Conclusions

It has been shown in this chapter that UV induced waveguides exhibit a significant degree of polarisation dependence, assumed to arise from the inherent birefringence of planar structures fabricated using the FHD process. However, it has also been observed that the writing conditions of UV induced channels have an effect upon the polarisation dependence of the resulting waveguides. It is concluded that deviation from the expected inherent birefringence is an indication of significant structural modification of the silica matrix.

An apparent correlation between Germanium doping and the magnitude of UV induced index has been strongly observed, however the large losses associated with high Germanium doping are of concern. The data presented in this chapter does however suggest that UV induced indices of the order 0.01 are achievable, and losses as low as 0.2dB/cm have been observed. It is however the opinion of the author that there is a very fine line

between inducing a high index and inducing a high loss, and unfortunately a more photosensitive material besides have a greater induce Δn for a given fluence may also have a lower damage threshold.

The affect of Deuterium outdiffusion during the UV writing process has been well characterised, and it is clear that repeatable writing into a single sample over a length of time has a considerable effect upon the induce Δn for a given fluence. The specific set of writing conditions used suggest that a 25% difference in relative photosensitivity is observed for identical channels written one hour apart, this is only an indication of the problem since absolute D_2 level is dependent upon the writing times relative to the initiation of the outdiffusion process. The data presented along with the outdiffusion discussion in chapter 6 indicates that the stable UV induction of a known refractive index will be extremely difficult while outdiffusion is occurring. Although not directly part of the work presented, a solution has been hypothesised and characterised but not in sufficient detail to allow full presentation. The initiation of the first stage of the Deuterium photosensitivity enhancement mechanism, as described in chapter 6, allows the minimisation of outdiffusion effects. In this case the rapid thermal processing of Deuterated samples results in the inclusion of diffuse species within the silica matrix, thereby imparting non-diffusion dependent photosensitivity enhancement through inducing additional GODCs prior to UV exposure. Preliminary results from this work were presented in [Riziotis *et al*, 2001] and showed that the degree of photosensitivity for a thermally locked and subsequently UV exposed sample is less than for a freshly loaded and exposed sample. However, the enhancement of photosensitivity for a thermally locked sample remains for considerable lengths of time if not indefinitely when compared to a non-locked sample.

It has be shown in this chapter that planar structures produced using FHD and subsequent UV definition of waveguiding channels is a suitable technique for the production of PLC devices. However, the data presented by no means represents the absolute minimum achievable loss or maximum achievable UV induced Δn. The relevance of the work presented with respect to future directions resulting in enhancement of waveguiding properties is discussed in chapter 9. It has also been seen that the techniques used in this chapter are far from ideal for determining absolute UV induced refractive index change or the degree of layer birefringence, further determination of these properties using Bragg gratings is described in Chapter 8.

8 Simultaneously Written Planar Bragg Gratings

The use of Bragg gratings as wavelength selective elements within optical systems have found widespread application. This chapter treats the physical behaviour of periodic refractive index structures, and how optical characteristics can be used to determine properties of UV written waveguides. A review of Bragg grating application in both fibre and planar waveguides is included, particularly focusing on the definition techniques used for producing periodic refractive index within guiding structures. The specific applications of Bragg gratings within the planar geometry are discussed, followed by the proposal of a novel simultaneous waveguide and Bragg grating definition technique. This novel technique is applied to FHD fabricated three layer structures and the information gained regarding materials and UV writing parameters upon Bragg grating characterisation is presented.

8.1 Bragg Gratings

The periodic modulation of guiding characteristic in the direction of propagation, such as a variation in guide cross-sectional dimension or magnitude of refractive index, results in the formation of a Bragg grating. When light propagates through a material with a periodic structure, a narrow band of the incident optical field is reflected by successive, coherent scattering from the index variations. The reflected wavelength is known as the Bragg wavelength (λ_B), and is inherently dependent upon the structure of the grating from which it has been reflected, a schematic of this mechanism is shown in figure 8.1.

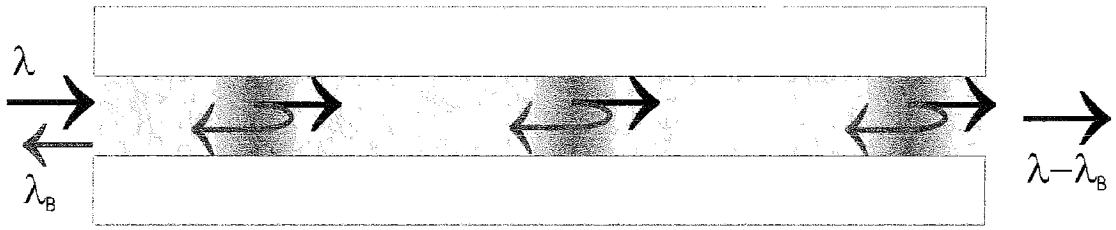

Figure 8.1, formation of Bragg reflection from periodic refractive index modulation

A periodic perturbation experienced by a propagating signal results in periodic coupling of the signal power between two modes that satisfy the Bragg condition. If the propagation constants for the two modes are β_1 and β_2, then a periodic perturbation with period Λ will induce coupling between the modes. If the modes are counter propagating, such that β_1 represents the propagation constant in the original direction and β_2 the propagation constant in the reverse direction. Substitution of the periodic index variation

into Maxwell's equations leads to the following standard coupled mode equations [Ghatak and Thyagarjan, 1998 (Chapter 21)];

$$\frac{dA}{dz} = \kappa B e^{i\Gamma z}$$
$$\frac{dB}{dz} = \kappa A e^{-i\Gamma z}$$

where $A(z)$ and $B(z)$ are the z-dependent amplitudes for the two modes, κ is the coupling coefficient, and Γ is given by;

$$\Gamma = \beta_1 + \beta_2 - \left(\frac{2\pi}{\Lambda}\right)$$

Phase matching requires $\Gamma = 0$, therefore;

$$\beta_1 + \beta_2 = \frac{2\pi}{\Lambda}$$

Thus, the coupling between two identical modes propagating in opposite directions occurs if;

$$\beta_1 = \beta_2 = \left(\frac{2\pi}{\lambda_0}\right) n_{eff}$$

where n_{eff} is the effective index experienced by the mode. The above represents the satisfaction of the Bragg condition, in which the difference in the propagation constants for the coupled forward and backward propagating modes must equal the spatial frequency of the grating.

If it is assumed that a Bragg grating is purely formed by the modulation of refractive index experienced by a propagating mode within a guide of uniform dimensions, then the Bragg wavelength can be used to attain the effective index for the mode via;

$$\lambda_B = 2\Lambda n_{eff}$$

Thus giving a measurable indication of the guide index if the period of the grating is known and the degree of modal overlap with the core is taken into account. The Bragg wavelength indicates the period and refractive index of a grating which gives strong reflection. The increase of grating length through the addition of grating planes and the associated build-up of coupling events between forward and backward propagating modes results in a proportional effect upon the degree of reflectance. The comparison between the power in the forward and backward propagating modes, in the form of reflectance (R) for a given grating, can be used to determine the magnitude of index modulation;

$$R = \tanh^2 \kappa L$$

where [Ghatak and Thyagarjan, 1998 (Appendix F)];

$$\kappa \cong \frac{\pi \Delta n I}{\lambda_B}$$

L is the grating length and I is the transverse overlap integral of the modal distribution with the region where the grating is formed. The overlap integral accounts for the grating only forming within the core of the guide (I <1), such that any modal overlap resulting in propagation outside of the core does not experience the index modulation. The bandwidth of the reflection spectrum ($\Delta\lambda$), defined as the wavelength spacing between the two reflection minima either side of the central peak, also allows information regarding index modulation to be gained and is given by;

$$\Delta\lambda \cong \frac{\lambda_B^2}{\pi n_{eff} L}\left(\kappa^2 L^2 + \pi^2\right)^{1/2}$$

It can therefore be seen that direct measurement of the wavelength selectability inherent to Bragg grating structures can be used to determine the refractive index modulation occurring within them. The use of the UV induced refractive index change to form Bragg gratings therefore allows the magnitude of the photosensitivity to be determined for a given material and the specific writing conditions used.

8.2 Review of Writing Techniques

The application of Bragg gratings induced through UV photosensitivity is widespread within the field of fibre optics. The huge amount of prior art associated with the fabrication of Fibre Bragg Gratings (FBGs) has led to the development of several UV writing processes suitable for the induction of periodic index structures. The historical progression from discovery of photosensitivity in germanosilicate fibres through to the commercially applicable production of high accuracy FBGs with tailored properties is discussed in the following section.

The formation of permanent refractive index gratings within optical fibre was first demonstrated by Hill *et al* in 1978 [Hill and Meltz, 1997]. It was found that launching Argon Ion laser radiation (488nm) down a Germanosilicate optical fibre for several minutes resulted in a steady increase in the intensity of reflected light. Upon spectral examination of the fibre, a very narrowband Bragg grating was found to have occurred within the whole length of the fibre. Later experiments showed Grating formation to be a two-photon mechanism occurring with periodic nature due to formation of a standing wave within the

fibre. Subsequent work using 244nm radiation resulted in much more effective grating formation due to the single photon nature of the process.

A more flexible technique for forming Bragg gratings within fibres was demonstrated by Meltz *et al* [Meltz *et al*, 1989] and involved the formation of a pattern with periodic intensity variation within a fibre through side illumination using two interfering laser beams. Two coherent beams at 244nm were intersected within the fibre core, forming a focal spot of approximately 4mm long by 125μm wide. The interference pattern within the spot and hence the period of the refractive index modulation produced within the fibre core, was shown to be dependent upon the angle of beam intersection. Thus, a flexible method of producing FBGs of variable period had been demonstrated. However, the length of the gratings was inherently limited by the size of the spot used.

An alternative technique involving the production of periodic intensity patterns through illumination of a phase mask has become widespread. The flexibility of the phase mask technique was greatly enhanced through the introduction of fibre translation and beam scanning relative to a stationary phase mask [Cole *et al*, 1995]. It was demonstrated that the period and UV induced Δn could be modified thus allowing chirp; variation of grating period along fibre axis, and apodisation; variation in UV induced Δn along fibre axis, to be applied within single gratings. The ability to actively chirp and apodise gratings without the need for specific phase masks greatly increased the functionality and easy of production for FBGs. A related technique employing fibre translation and pulsed illumination of a phase mask has been widely demonstrated to form highly flexible FBGs with variable chirp and apodisation [Durkin, 1999]. The strobing of UV intensity during fibre translation results in the multiple exposure build up of grating planes, the modification of pulse duration relative to fibre position allows accurate control of grating period and UV induced Δn to be achieved.

The strobing of UV intensity patterns produced by phase masks, within photosensitive fibre cores, thus producing FBGs has been widely proven academically and commercially. The applications of tailored FBGs encompass dispersion compensation, reflectors within distributed feedback laser, sensor applications, and the obvious relevance to WDM system afforded by inherent wavelength selectability. The application of Bragg gratings within integrated optics would therefore be of great relevance through imparting a huge amount of functionality to possible devices.

8.3 Planar Bragg Gratings

The implementation of Bragg gratings within the planar geometry is limited in comparison to the large-scale adoption seen within fibre waveguides. The majority of the work that has been undertaken, particularly in silicates, has focused on UV induction of Bragg grating structures using similar techniques to FBG fabrication. However, Bragg gratings in the planar geometry have been fabricated through photolithographic definition of relief structures, but have not seen widespread application. The production of Bragg gratings through the modification of waveguide refractive index is not practical using photolithograph and associated etch processes. The required grating periods for operation around 1550nm is ~520nm if the effective index of the mode is assumed to be 1.5. The definition of features half a micron in size and the subsequent deposition of an alternative material in order to produce an index modulation is likely to be exceedingly difficult. The possibilities of imperfect interfaces in-between regions of different index would also led to excessive loss for a Bragg reflector produced using etch processes.

8.3.1 UV exposed Planar Bragg Gratings

The writing of UV induced Bragg gratings into previously defined waveguide channels, analogous to the writing of FBGs into fibre cores, has been demonstrated. This technique has been widely applied in the production of integrated optical devices, [Okamoto, 1998] [Tanaka *et al*, 1996] [Maxwell *et al*, 1994] [Ibsen *et al*, 1996], in which channels defined using photolithographic processes are subsequently written into devices using a phase mask.

The information regarding UV induced index that can be gained from writing a Bragg grating has been applied to photosensitive silicate planar waveguides produced using a number of techniques, including FHD, PECVD and Sol-gel [Maxwell *et al*, 1992] [Poulsen *et al*, 1995] [Razafimahatratra, *et al*, 2000]. Of particular interest is the discussion of UV induced planar waveguides with Bragg gratings [Hill and Meltz, 1997], in which a waveguide is written using a static elongated spot and subsequent 2-beam interference in the pre-exposed region results in a UV written Bragg grating. Alternative work on UV direct written waveguides using focused spot translation and with subsequent definition of Bragg grating through phase mask illumination is of interest [Svalgaard, 1997]. A number of the pieces of work mentioned particularly highlight the relevance of UV inducing gratings for the measurement of waveguide properties. The accurate determination of effective index, birefringence and photosensitivity have all been demonstrated through

measurement of Bragg grating properties, both in photolithography/RIE and direct writing defined waveguiding structures.

8.3.2 Novel Technique for the UV Induction of Bragg Gratings

The UV definition of both waveguide and grating structures within the FHD samples produced, has taken place using a novel technique facilitating the simultaneous writing of channels with gratings, a schematic of which is shown in figure 8.2. A beam splitter was

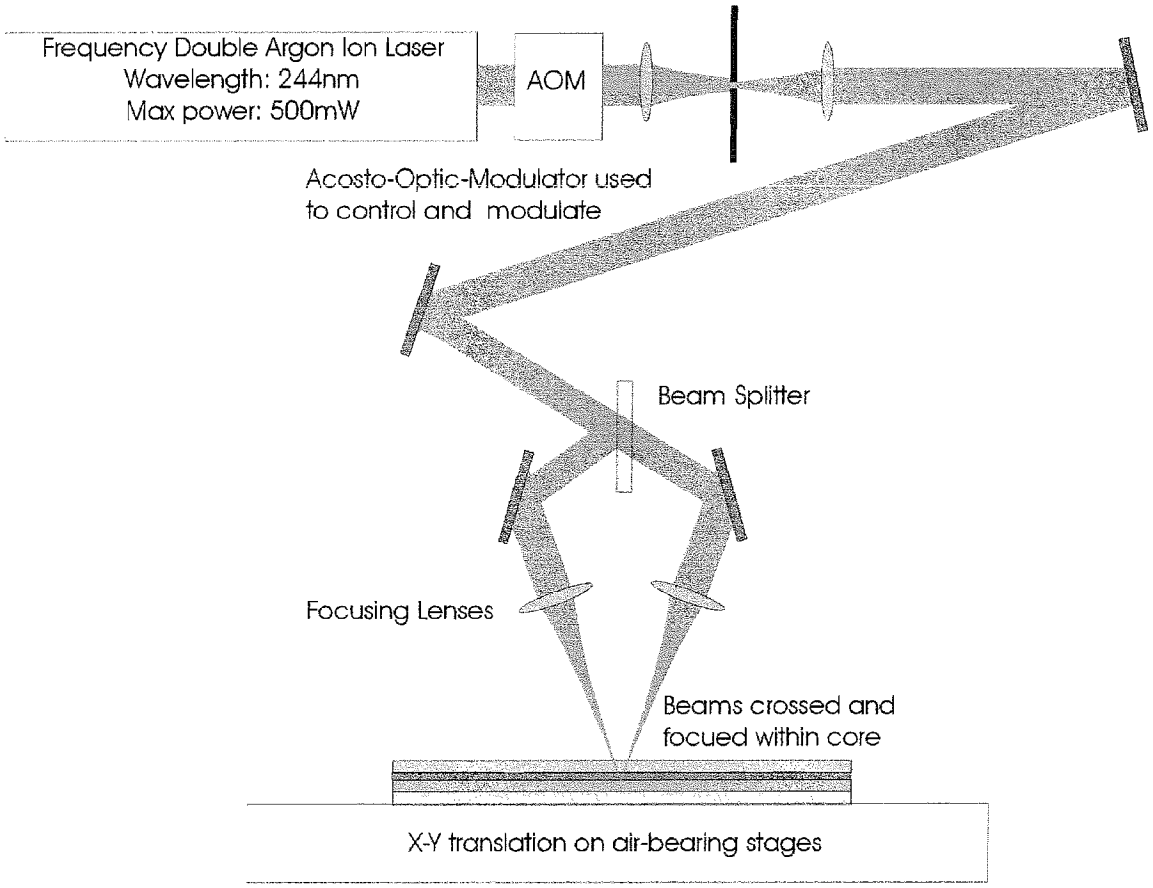

Figure 8.2, equipment used for two-beam UV writing experiments

used to create two separate beam paths at an intersection angle of 27° and each beam was individually focused to a $1/e^2$ spot size of 6μm. When crossed, the superimposition of the two focused beams within the core of the sample results in a single spot with a 522.6nm period interference pattern. This pattern is reproduced as a periodic refractive index modulation within the sample. Stepping of the fringe pattern along the sample results in the formation of additional refractive index planes. This is achieved through constant translation of the sample in the x-direction and periodic modulation of the UV beams via an AOM. The formation of Bragg gratings within the core can be directly modified by

changing the spatial superposition of the interference pattern and the AOM operating parameters. Simultaneous writing of a channel waveguide during beam modulation is performed by insuring that the minima of the intensity pattern is always non-zero. The translation of the sample at constant velocity and without beam modulation results in a uniform channel waveguide structure, as described in Chapter 6 and 7. The combination of constant intensity and pulsed intensity allows the simultaneous writing of complex channel waveguide structures with integral Bragg gratings.

The ability to simultaneously define waveguiding channels and Bragg gratings through direct UV writing presents a highly flexibly technique for characterising the photosensitive nature of materials. Gratings of widely variable length can be produced within a single sample through modifying the length of channels preceding and following the grating structures. A wide range of grating periods can be written without the need to alter the optical alignment of the system, and the magnitude of index modulation as well as period can be varied during grating writing. The simultaneous nature of the process also raises the possibilities of simplified integrated optical device fabrication by introducing the ability to "drop" gratings into any UV induced waveguiding structure. Although the possible applications of simultaneous channel and grating definition are wide ranging, the remainder of this chapter focuses on the determination of UV photosensitivity through Bragg grating definition and subsequent characterisation, within the previously described FHD samples.

8.4 Characterisation of Simultaneously UV Written Waveguides with Bragg Gratings

The characterisation of Bragg grating structures involving the determination of the Bragg wavelength can take place through either observing the transmission or reflection properties for gratings that are simultaneously excited over a broadband of wavelengths. The following section describes the equipment used during Bragg grating characterisation, as well as the samples, grating structures and writing conditions that have been investigated.

8.4.1 Measurement Technique

The broadband excitation of UV written structures was possible through use of an Amplified Stimulated Emission (ASE) source, emitting radiation in the range ~1520-1580nm. The output from the ASE source was launched into a 3dB coupler, allowing

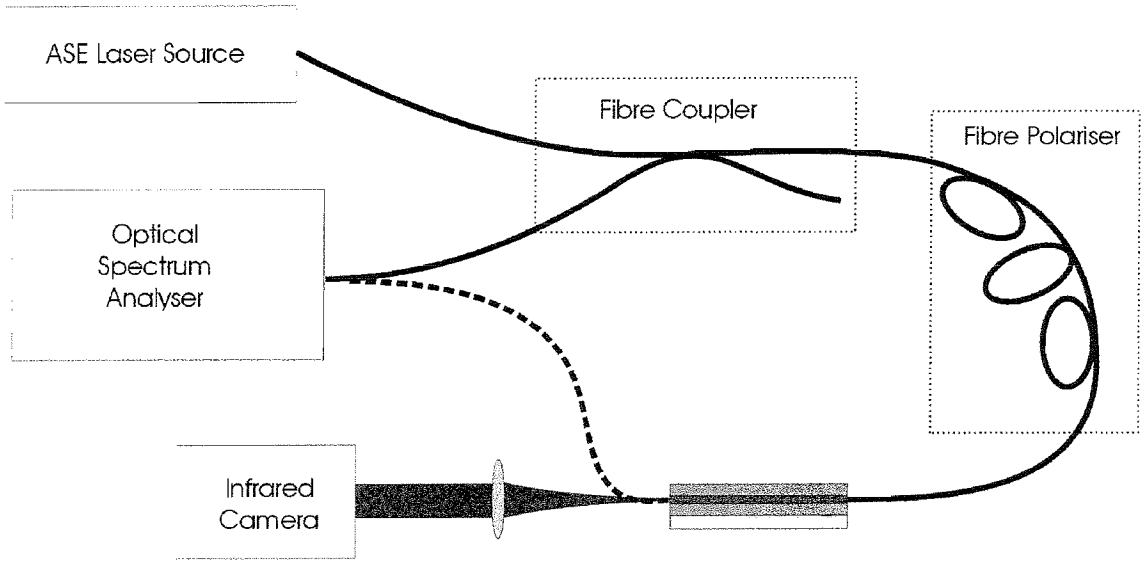

Figure 8.3, equipment used to characterise Bragg gratings

excitation of the waveguide and measurement of reflected signal propagating back from the sample. The use of a fibre polariser allows TE or TM modes to be excited within the UV written channel, therefore giving information regarding the birefringent nature of the waveguide. A schematic of the Bragg grating measurement equipment is shown if figure 8.3. The signal is fibre launched into the sample, and any Bragg reflection is coupled in the reverse direction out of the sample into the fibre. Light transmitted through the sample and out of the output facet is imaged using an infrared sensitive camera, allowing optimisation of launch conditions resulting in efficient waveguide excitation. Alternatively, the imaging set-up can be replaced by a fibre output arrangement allowing easy spectral analysis of the transmitted signal. The reflected signal originating from the Bragg grating or the transmitted signal originating from the output fibre, is spectrally analysed using an Optical Spectrum Analyser (OSA) with a resolution of ~0.05nm. It is therefore possible to measure the spectral response for a given Bragg grating through either reflection or transmission, assuming the response is in the wavelength range output by the ASE and is significant enough to be detected by the OSA.

8.4.2 Results and Discussion

The simultaneous definition of waveguiding and Bragg grating structures through the application of UV direct writing took place within the low Germanium (~2 mole %) core three layer FHD samples, previously described in chapters 6 and 7. The medium and high Germanium (4 and 6 mole %) core samples have been seen to exhibit high propagation losses and deformed mode profiles, assumed to be due to the presence of crystalline

germania at some stage during the fabrication process, and therefore are not suitable for Bragg grating writing.

Initial writing took place using conditions mimicking those used to produce waveguides with the single beam writing equipment as discussed in Chapter 6, with the aim of gaining further induced index information and reinforcing the trends observed using measurement of NA discussed in Chapter 7. Samples were therefore freshly D_2 loaded in order to achieve maximum UV induced Δn, and writing time was kept to a minimum thereby minimising the degree of outdiffusion. A variety of channels were written encompassing waveguides with and without grating structures, those with gratings included a variation in both grating pitch and length.

Upon post writing inspection and reflection/transmission spectrum analysis it was found that the channel sections written under steady-state exposure resulted in high induced index channels as found for the single beam writing experiments. However, the sections exposed to strobed intensity did not appear to have been altered to the same degree. Visual inspection revealed that channels with gratings inserted appear discontinous, with channels clearly observable where steady-state exposure has occurred, but nothing could be seen where strobed exposure had taken place. Spectral interrogations of the channels with gratings suggested that Bragg gratings were either not present, formed from very weak index modulation, or not operating within the wavelength range supplied by the ASE. It was therefore concluded that the writing regime employed during the writing of continuous high index channels may not be applicable to the definition of the fine period index structures required to produce Bragg gratings. There could be a number of explanations for this occurrence, the most likely being that high index channels as produced by a thermal process which builds up during translation of the writing spot through the photosensitive core. Upon modulation of UV intensity the temperature experienced by the core does not undergo the same steady increase thereby does not initiate the same index modification mechanism as for continuous illumination.

In order to ensure that index modification occurred purely within the regime associated with the modification of GODCs a subsequent sample was exposed to the same writing conditions but without deuterium loading thus reducing adsorption at 244nm. Post writing observation showed that channels had been written, however induced index was considerably lower and channels could not be observed by the naked eye. Upon spectral interrogation, the channels with gratings showed the reflection characteristics expected for weak Bragg gratings, a typical grating spectrum is shown in figure 8.4 and shows a

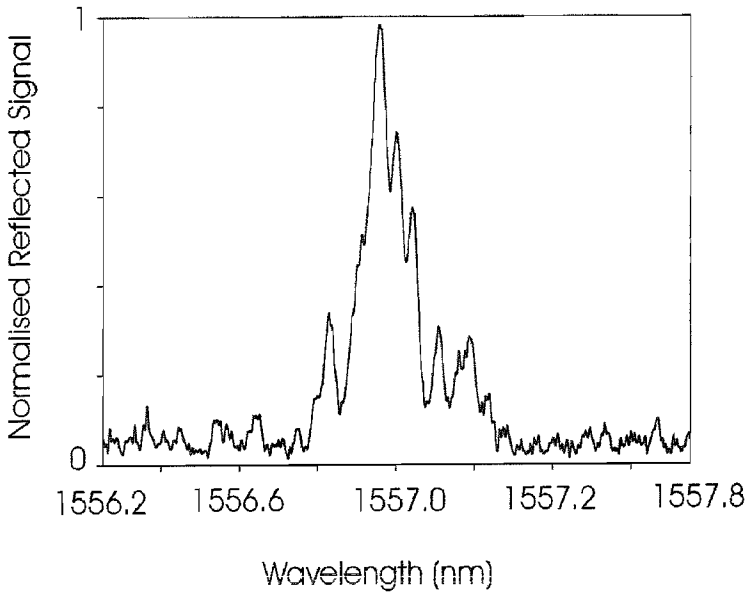

Figure 8.4, reflection spectrum for 14mm long simultaneously written Bragg grating

reflectance of approximately 25% and a FWHM of ~20GHz. Some of the noise seen in the spectrum arises from incomplete suppression of Fabry-Perot resonances between the end facets of the sample. It was therefore possible to determine the approximate wavelengths associated with peak reflectance for a number of Bragg grating writing conditions.

The measurement of peak reflectance wavelength allowed the calibration of the strobe period used during grating definition to the actual reflectance for the written Bragg grating. Figure 8.5 shows that a linear variation in the distance translated between strobes, and therefore grating plane definition, results in a linear variation in peak reflectance for the Bragg grating produced. This suggests that the dephasing of the inherent intensity pattern within the writing spot results in a Bragg grating with a period consistent with the degree of dephasing.

It is expected that the strobe period will directly define the period of the Bragg grating that is written, thus it is possible to calculate the effective index for the mode, and gain an indication of UV induced refractive index, as explained in section 8.1. It has therefore been possible to gain an indication of the dependence of induced index upon writing fluence, and the degree of birefringence experienced by a UV written waveguide in an FHD fabricated structure, shown in Figure 8.6. It is difficult to fully determine the absolute value of UV induced refractive index for this sample, the core index of 1.48 at 633nm previously defined in Chapter 5 using prism coupling equates to 1.467 at 1550 nm after dispersion correction. Thus, suggesting that the measured n_{eff} is on the low side, however this is to be expected since the refractive index is for the mode and any significant

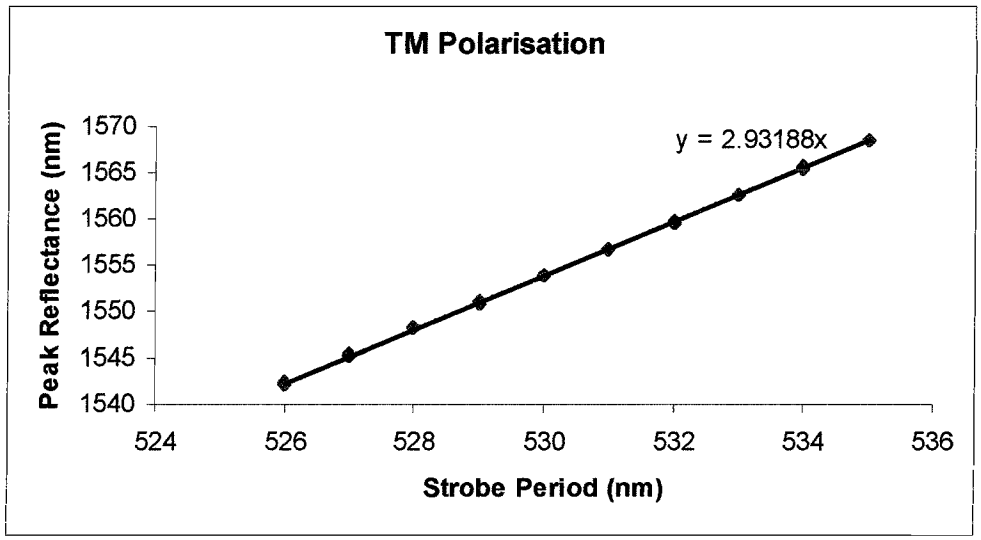

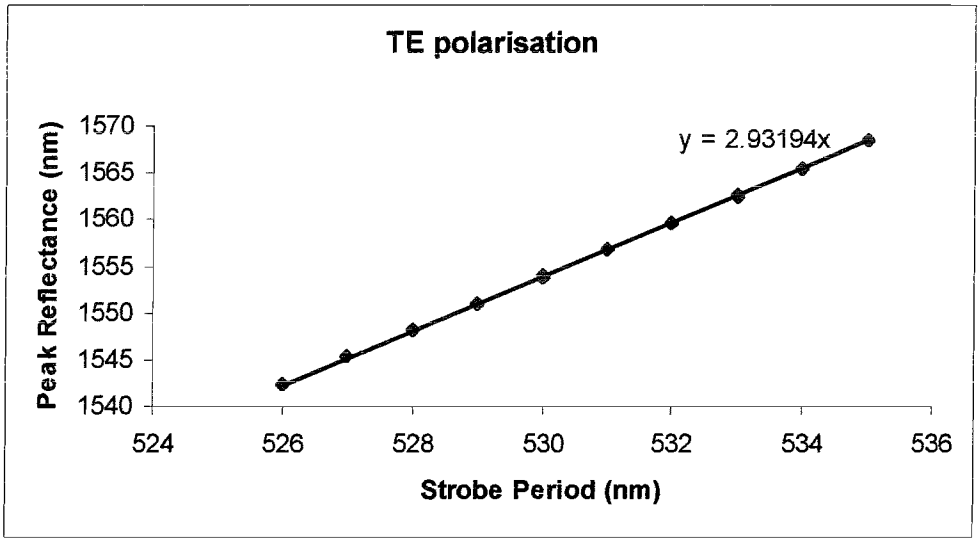

Figure 8.5, plots showing variation of Bragg wavelength against strobe period for TE and TM polarised guided modes

overlap with the clad will result in a reduced value of n_{eff}. Any dopant diffusion during the construction of the three layer samples is also likely to result in a decrease in core index and therefore a low value for measured n_{eff}. However, if the apparent offset is ignored then the trends observed for varying writing fluence are likely to be valid. It would appear that a saturation of UV inducible index occurs for fluences greater than ~2kJ/cm^2, and prior to that a rapid increase in induce index with increasing fluence is observed. The difference in UV induced refractive index is approximately 2×10^{-4} between low fluence and saturation. Assuming that low fluence typifies original core index then it appear that UV induce refractive indices of the order 1×10^{-4} to 3×10^{-4} are achievable within the low Germanium, zero deuterium sample used.

The difference in effective index for TE and TM polarised light gives an indication of the birefringence inherent to the FHD layers. It appears that a birefringence of the order 5

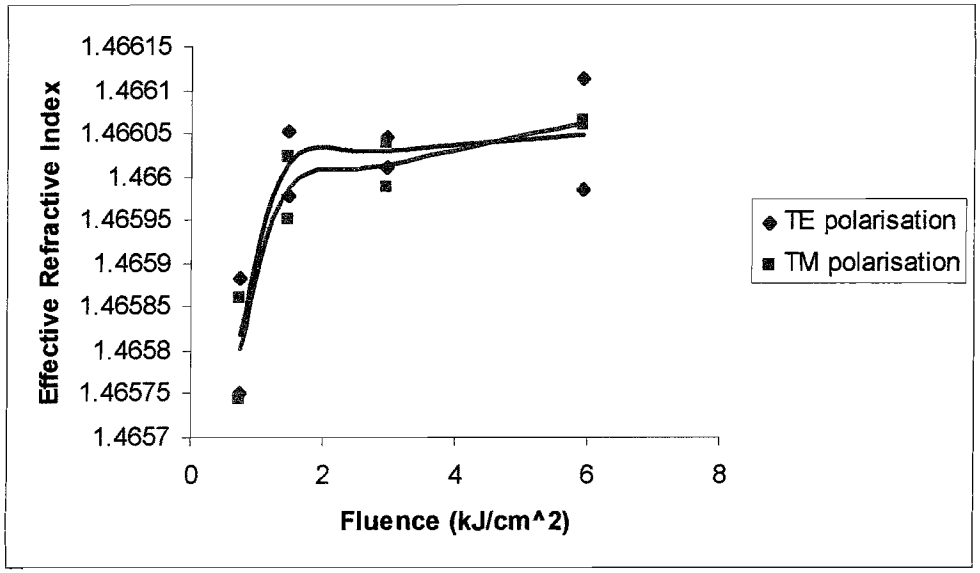

Figure 8.6, plot showing effective refractive index against writing fluence for TE and TM polarised guided modes

$\times 10^{-5}$ is present within the waveguides that have been produced with varying fluence. The comparison of the n_{eff} attained from the "strobe vs Bragg wavelength" given in figure 8.4, indicates a birefringence of 3×10^{-5}. Literature suggests that birefringence of approximately $2.5\text{-}5 \times 10^{-4}$ is common in PECVD and FHD layers [Jouanna *et al*, 1996] [Poulsen *et al*, 1995] [Kilian *et al*, 2000], however FHD layers with birefringence as low as 1.2×10^{-5} have been reported. Therefore the measured value is within the ranges reported for FHD, albeit at the low end.

8.5 Conclusion

It has been shown that a number of techniques exist which are suitable for the fabrication of refractive index modulation within photosensitive materials resulting in the formation of Bragg gratings. The two primary examples for producing periodic intensity patterns are the interference of two beams and the illumination of a phase mask with a single beam. The further development of the phase mask technique through illumination with modulated intensity during fibre translation resulting in the plane-by-plane construction of Bragg grating structure presents additional functionality. Dephasing of the inherent intensity pattern has introduced a high degree of flexibility with regards to grating length, period, and the dynamic variation of period and magnitude of induced refractive index change during grating writing.

The application of UV written Bragg gratings within planar structures for materials characterisation and as functional elements within integrated optical devices has been shown to be an active field of research. However, the definition of UV written channels and Bragg gratings has be limited to sequential definition of guiding structure and periodic elements.

The work presented has proposed a novel technique combining direct writing of UV induced channels through focused spot translation, intensity pattern production through two beam interference, and plane-by-plane construction of a periodic refractive index structure through superposition and dephasing of the inherent focused spot intensity pattern during translation. Thus, it has been possible to realise the simultaneous "one pass" direct writing of UV induced waveguiding channels with "drop in" periodic refractive index structures, allowing the fabrication of waveguides with integral Bragg gratings. The simultaneous defintion of waveguide and Bragg grating is expected to be highly applicable to the development of novel integrated optical devices. Some examples of why it is significantly advantageous are mentioned below;

- Maximum UV induced refractive index contrast that cannot be achieved via sequential channel and post Bragg grating definition.
- Small size of interference pattern allows tilting of grating planes and thus construction of tilted grating devices through translation of spot in direction not perpendicular to grating planes.
- Definition of gratings around waveguide bends through rotation of sample during writing, therefore maintaining relative grating plane alignment with respect to channel axis.
- Definition of grating structures with variable tilt through the variation of the relative alignment between grating planes and the direction of writing.
- Simultaneous nature of writing implies that realignment to pre-exposed channel region in order for Bragg grating exposure is not required.
- Single pass nature of process greatly speeds the definition of complex structures.

It is therefore apparent that the novel technique proposed readily lends itself to the future development of some very exciting device geometries, and will allow the definition of numerous functional elements, which can only result in the further progression of PLCs via the integration of complex optical signal processing.

The novel simultaneous UV writing technique has been applied to FHD fabricated three layer planar structures, waveguides and Bragg gratings have been realised and characterised. The process of Bragg grating definition has indicated that the previously observed high induced index channels are potentially produced by a mechanism that is not conducive to the fabrication of periodic structures through strobed intensity. However, non-deuterium loaded samples have allowed the realisation of periodic refractive index structures, which have allowed the determination of UV induced Δn and birefringence for the specific samples used. The results gained are consistent with historical literature and suggest that the simultaneous technique is suitable for the characterisation of UV photosensitive materials.

The work presented is merely proof of principle and by no means indicates the full analysis of the FHD samples using characterisation of UV induced Bragg gratings. It is expected that a degree of optimisation will be required before the technique can fully characterise the FHD samples used, and it is believed that the method outlined will give a plethora of information regarding material and UV writing parameters in the future.

9: Conclusion and Future Work

The work presented within this thesis represents a complete progression of the route required for optimisation of planar Germanosilicate layers suitable for direct UV definition of waveguiding structures. The stages that have taken place leading to the realisation of compositions and structures produced by Flame Hydrolysis Deposition suitable for UV writing via use of the photosensitive mechanisms can be summarised by:

- Optimisation of fabrication processes and the associated development of deposition equipment.
- Adequate compositional control during fabrication resulting in production of index matched layers of different composition.
- Construction of multiple layer samples with tolerances suitable for use as waveguiding structures.
- Characterisation of the physical effects of the direct UV writing process upon planar structures.
- Fabrication of waveguiding channels within FHD planar structures and characterisation of optical properties with respect to layer and channel fabrication parameters.
- Application of novel Bragg grating definition technique to FHD samples and subsequent characterisation of waveguide properties.

The progression through the route outlined has seen the realisation and regular reliable use of a specifically designed deposition system, allowing wide-ranging control of composition whilst maintaining the tolerances imposed by optical waveguiding.

A number of problems associated with dopant incorporation within FHD layers have been identified and solutions found. In particular, the Phosphorus-Boron coupling discussed in Chapter 5 is an effect that, to the authors knowledge, has not be previously observed but has a considerable effect during the production of index matched layers using FHD.

The application of the direct UV writing technique to Germanosilicate FHD samples has resulted in a number of effects, varying from the destructive phenomena highlighted in Chapter 6, through to the presumed photoactivation of defect centres associated with Germanium doping, discussed in Chapters 7 and 8. Additionally a mechanism assumed to be due to stress induction, has been seen to induce large positive refractive index channels with low loss (UV induced Δn of $\sim 1 \times 10^{-2}$ and losses at 1550nm of ~0.2dB/cm). It is

hypothesised that the high indices occur through inhibition of thermal expansion due to the confined nature of the core layer, and subsequent "freezing in" of associated stress.

The role of Deuterium loading within Germanosilicates and the associated enhancement of photosensitivity through increased Germanium defect centres and resultant absorption at the UV writing wavelength has been demonstrated. It has however also been shown that the high levels of photosensitivity associated with Deuterium loading does not always result in a steady-state UV induced refractive index change, it has therefore been noted that a degree of stability is required and may possibly be provided by thermal locking of Deuterium loaded samples.

The demonstration of low loss channels in Deuterium loaded samples and Bragg gratings in Deuterium free samples has demonstrated the suitability of combining FHD and direct UV writing for the fabrication of waveguiding structures. The act of defining Bragg gratings has allowed the accurate indication of the inherent birefringence present within the FHD layers, seen to be relatively low ($\sim 3\times10^{-5}$) when compared to historically observed values. The novel Bragg grating definition technique greatly enhances the flexibility of the FHD fabrication route, and makes it of particular interest for the development of future novel devices. It is envisioned that the work presented forms the basis of a feed-back system that will allow the characterisation of photosensitivity to drive materials development, and resulting in the feed-forward of developed materials allowing the future invention of novel devices which are reliant upon the photosensitive nature of the host material.

The very nature of the project outlined places it at the centre of numerous concurrently running areas of research including:

- Solution doping of FHD layers with the aim of increasing the number of novel dopants that can be included.
- Application of layer fabrication and direct UV writing techniques to novel hybrid waveguiding geometries.
- Development of novel UV written optically integrated devices.

In particular, the projects of four PhD students, including myself, have all played a significant role in allowing the results presented to take place. Greg Emmerson has largely been responsible for the implementation of the novel grating writing set-up and the characterisation of the Bragg gratings produced. Denis Guilhot has been involved with the installation of various systems within the FHD rig, and is currently actively investigating the solution doping of FHD layers. Ian Sparrow is currently undertaking further FHD system development tasks, and investigating the possible mutual advantages that can be

gained from combining FHD and PECVD fabrication routes. The work presented in this thesis has therefore been heavily reliant upon, but also fundamental to, a number of associated research projects that have not been explicitly discussed within the previous Chapters.

Possible future work within this field is vast due to the nature of the project and the number of associated directions that are currently under investigation. A few of the short-term realisable direction include:

- Further investigation of Germanium doping and Deuterium loading mechanism with respect to direct UV writing.
- Investigation of alternative and novel dopants for controlling processing properties, optical properties and photosensitivity.
- Deposition of novel layer geometries and complimentary combination of different fabrication techniques.
- Realisation of novel planar grating based devices and application of direct UV writing to trimming/connecting predefined waveguiding structures.

Of particular interest is the further investigation of Germanium doping and Deuterium loading, and the subsequent incorporation of novel dopants. The UV writing of the samples used within this work has given a glimpse of what can possibly be achieved, modification of the deposition process to allow production of low loss, high Germanium samples will no doubt lead to an associated increase in usable photosensitivity. The stabilisation of photosensitivity enhancement via Deuterium loading is also an area likely to liberate a larger range of usable photosensitivity. However, even with the current UV induced refractive index mechanisms highlighted in this work it would appear to be potentially possible to use one mechanism to produce high index channels and another to produce grating structures.

The incorporation of additional dopants to further enhance photosensitivity such as Tin, Titanium, Antimony and Nitrogen, which are all thought to enhance the magnitude of UV induced refractive index, is easily achievable using the current deposition system.

The modification of layer composition in order to result in minimisation of birefringence, either through tailoring current compositions or through the introduction of additional dopants is also possible. The incorporation of active dopants using solution doping can easily allow the production of gain media or more likely loss less devices. There is a multitude of possibilities regarding the fabrication of many layered samples in the

production of multiple cores allowing vertical integration or the application of optical structures within cladding layers as demonstrated in the fibre geometry.

The possibilities that arise due to combining different fabrication processes, and the further application of direct UV writing for the production of novel devices and trimming or connecting previously defined structure are too numerous to discuss. However, the vast range of possibilities mentioned in this Chapter go some way towards highlighting the relevance of directly UV written waveguiding structures within Germanosilicate FHD layers.

Appendix 1 Flame Hydrolysis Deposition (FHD) System Information and Operating Procedure.

What does the FHD do?

The system consists of two main parts, the gas delivery system (bubbler system and BCl_3 system) and the FHD system. The bubbler system passes a carrier gas through liquid halides where the gas becomes saturated with the vapour of the halide. The FHD system uses a hydrogen / oxygen flame to oxidise the halide vapour to produce particles of the oxide. This stream of particles in the flame is directed at a substrate to which the particles adhere. The flame is translated across the substrate to produce a uniform layer of oxide particles.

Schematic diagrams.

NB. Numbers in circles show pipe links between diagrams.

1. Gas input panel (supplies gas to bubbler glove box)

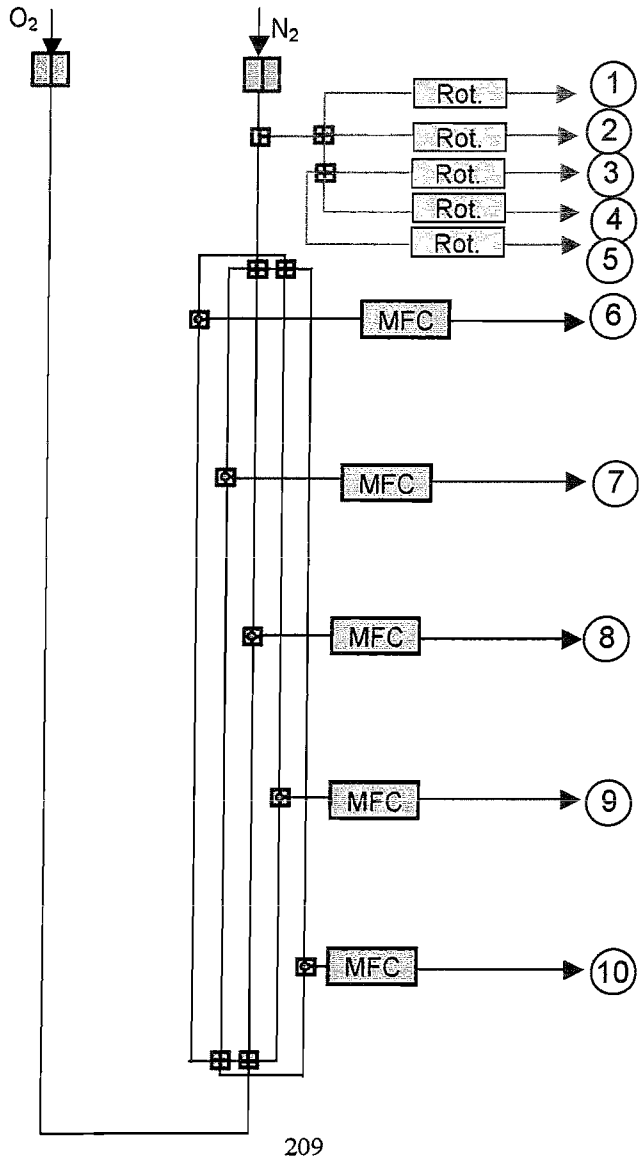

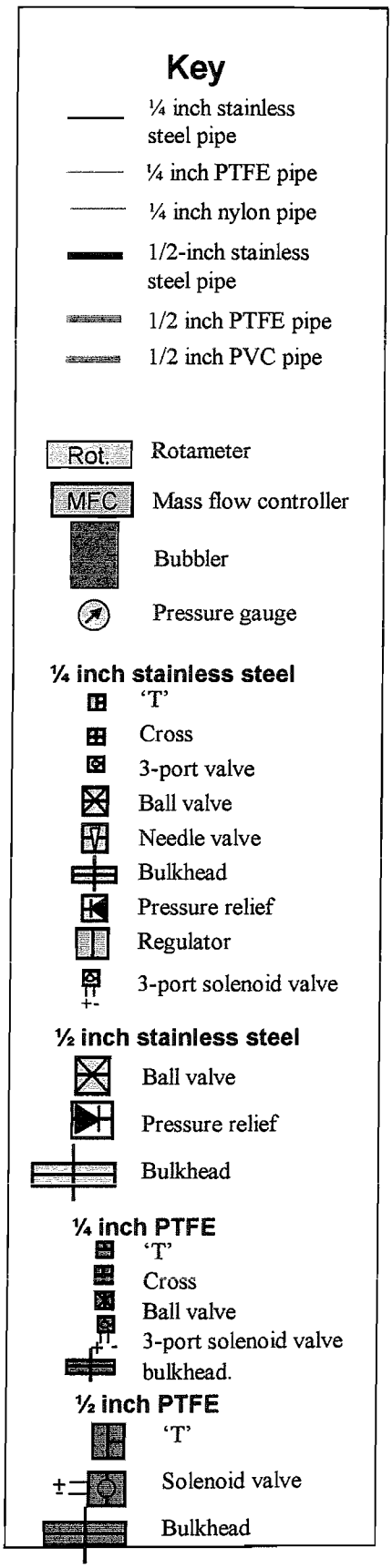

2. BCl_3 System

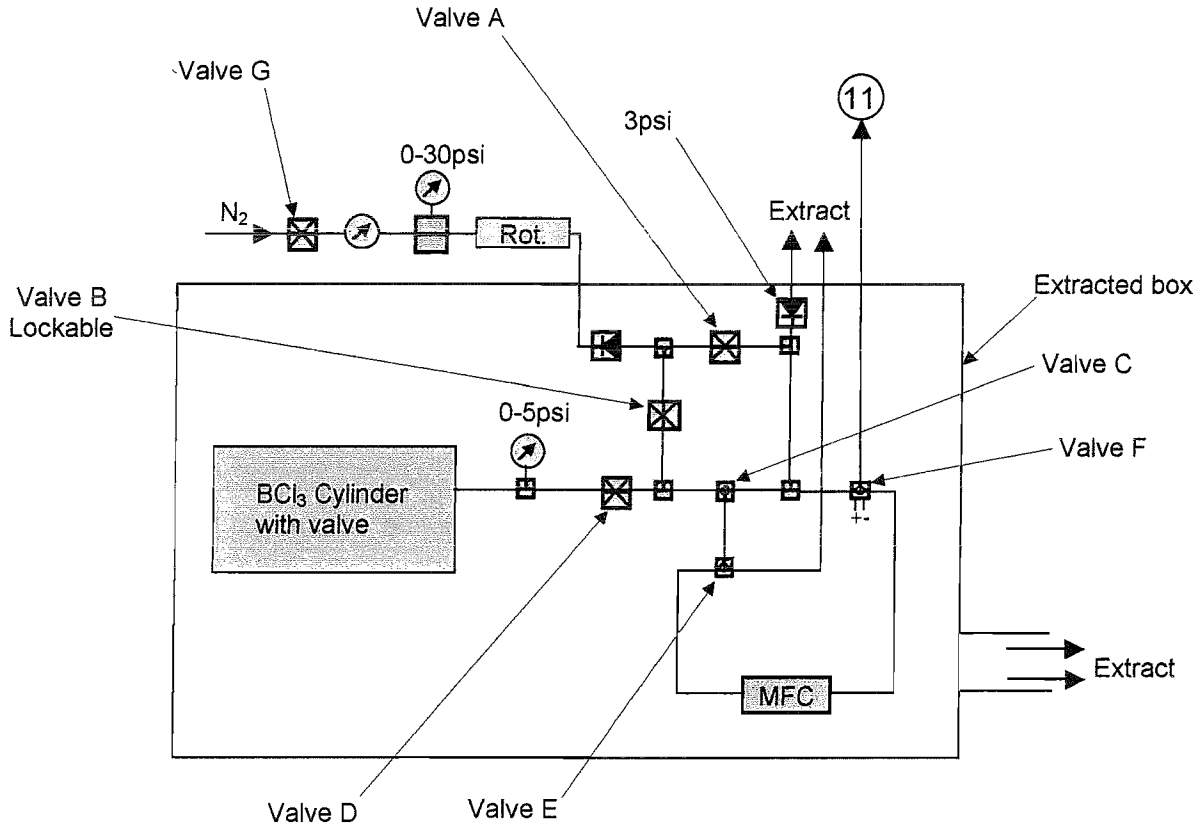

3. Gas system in and around bubbler glove box

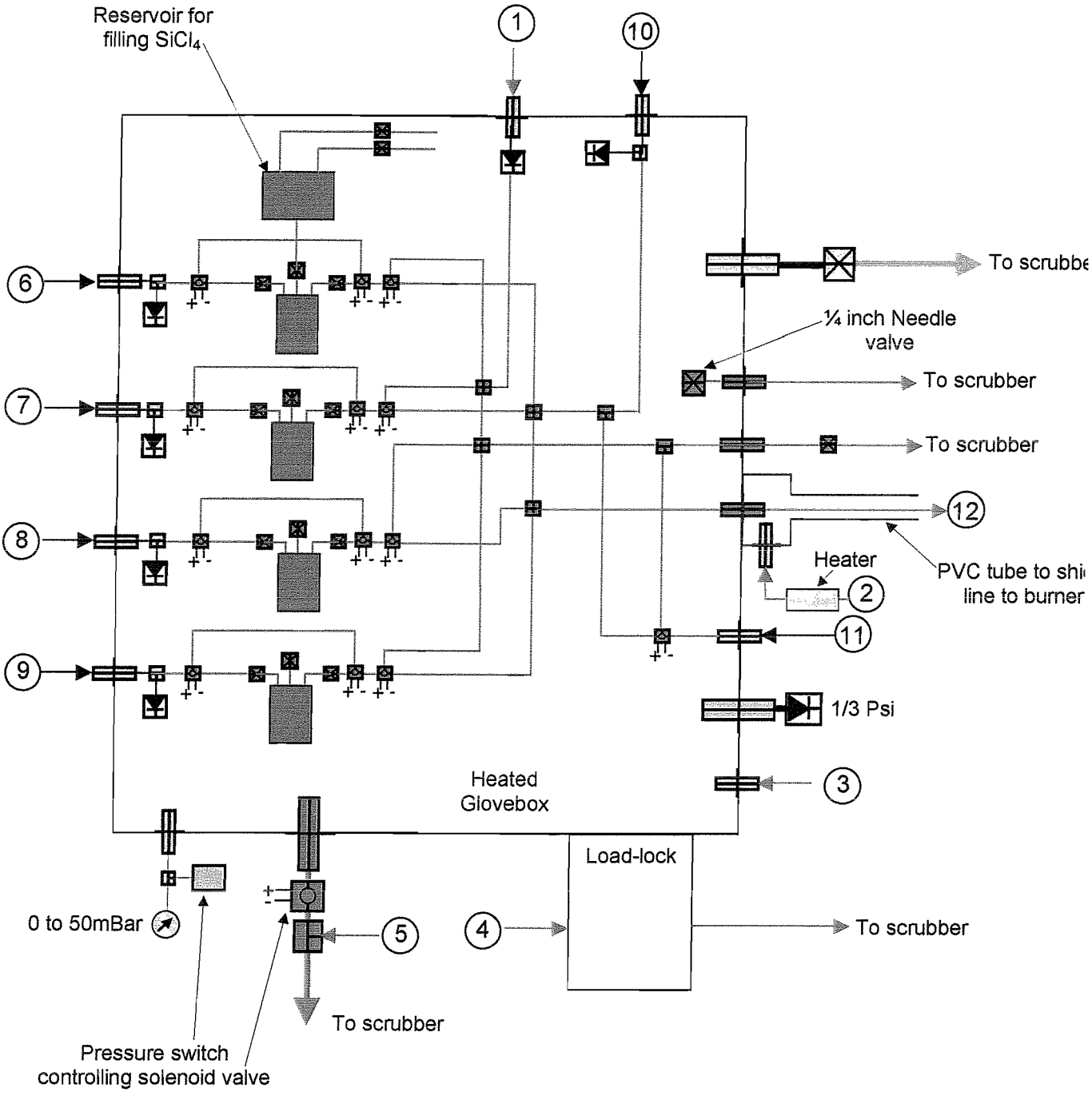

4. FHD system

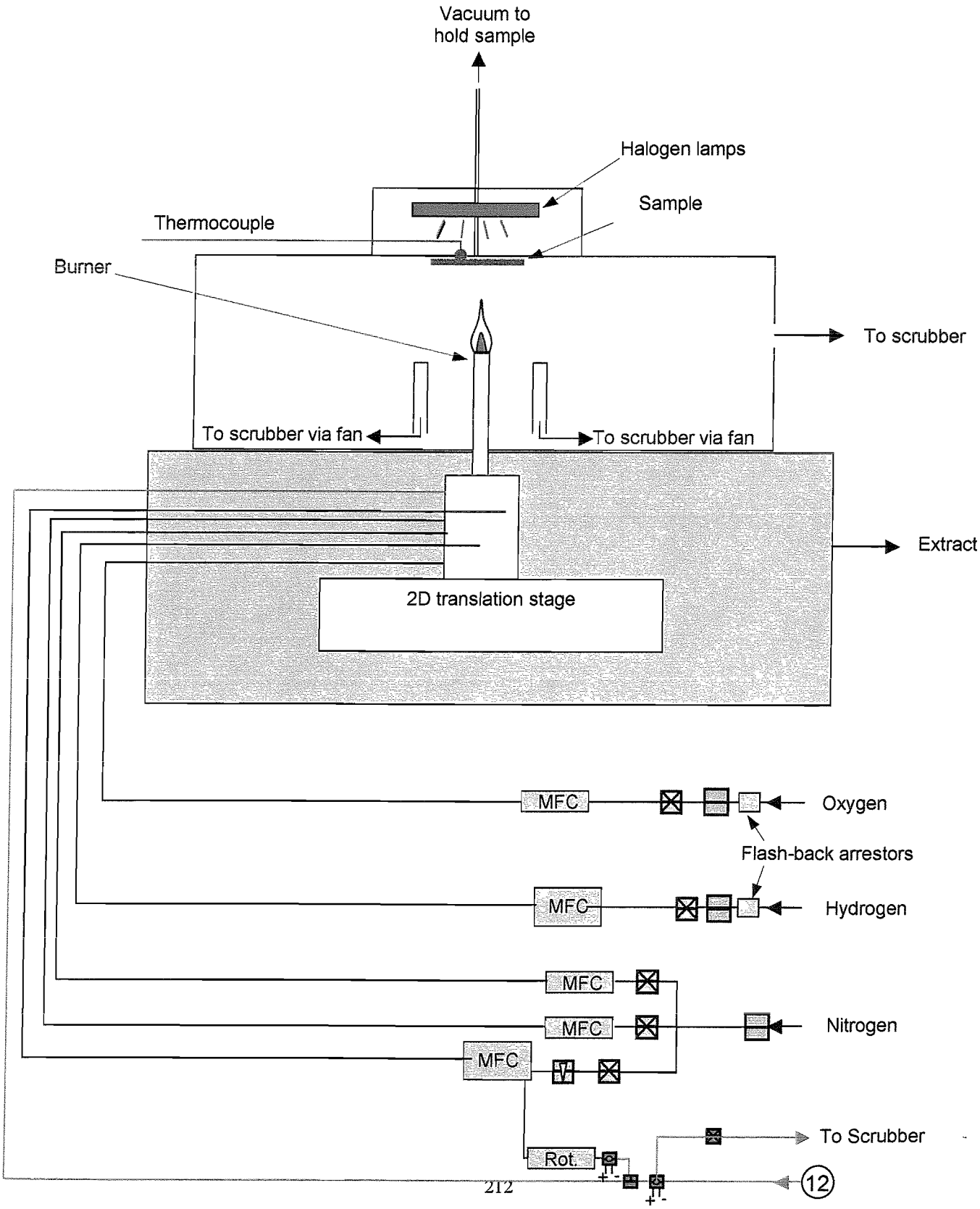
Vacuum to hold sample
Halogen lamps
Sample
Thermocouple
Burner
To scrubber
To scrubber via fan
To scrubber via fan
Extract
2D translation stage
MFC
Oxygen
Flash-back arrestors
MFC
Hydrogen
MFC
MFC
Nitrogen
MFC
To Scrubber
Rot.
12

5.Bubbler temperature control

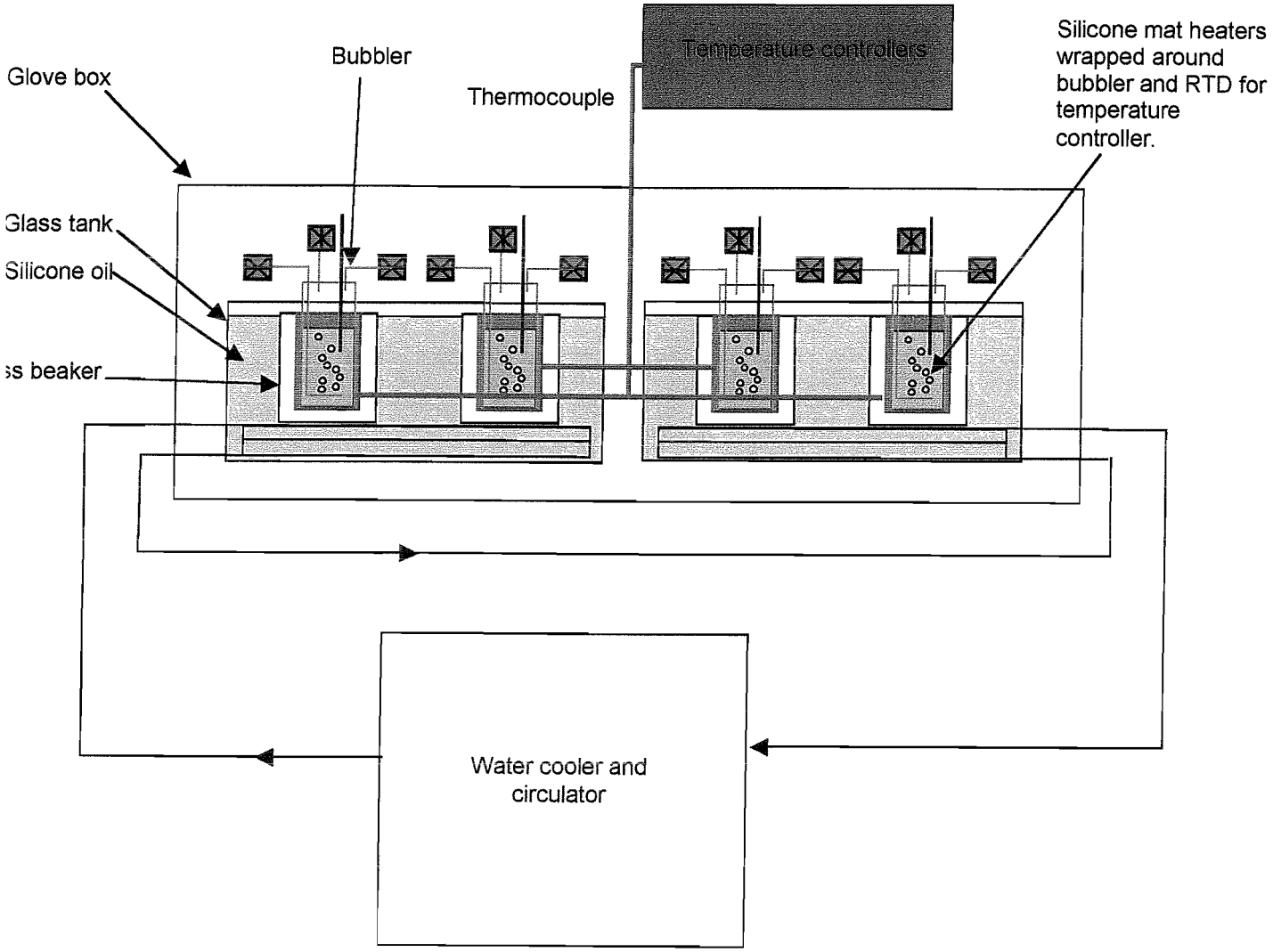

6 Block diagram of electronics

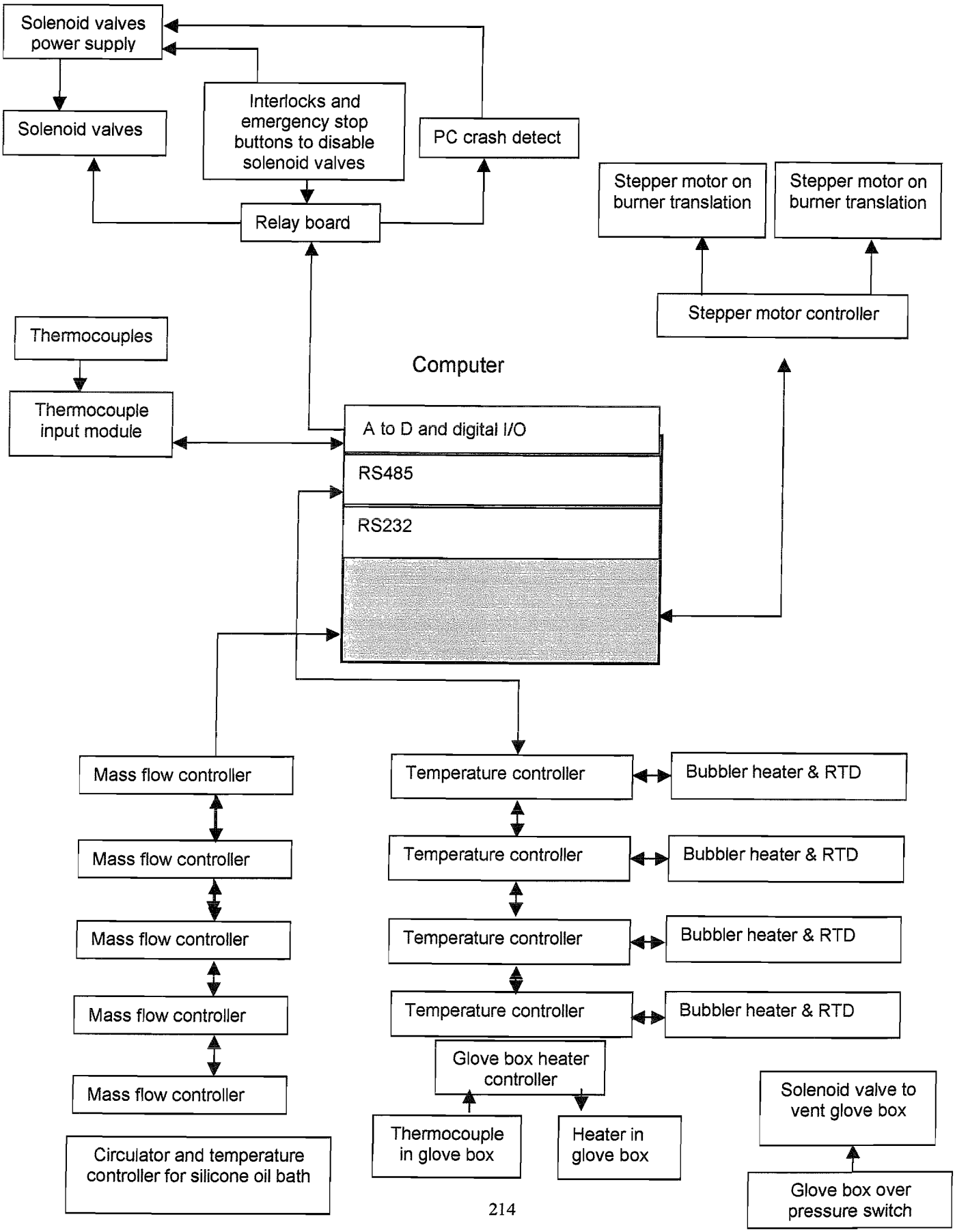

Operating procedure.

A. Filling bubblers

Before filling of the bubblers can take place the glove box and posting port must be purged for at least 12 hours. All of the pipe work used in the filling process must also have been purged for 1 hour using dry nitrogen.

i. Filling $SiCl_4$ and $POCl_3$ (using the bulk fill system).

Replace the outside posting port bung with the filling bung. The filling pipes should be coiled up into the posting port, they pipes can then be passed into the glove box from the posting port using the same procedure as any item being pass through the posting port (this is out lined in "Using the glove box").

1. Filling the $SiCl_4$ reservoir.

- Connect the tee piece at the end of the bulk fill pipes to one of the valves connected to the top of the $SiCl_4$ reservoir, but leave the valve closed.
- Purge the bulk fill pipe work to the valve connected to the top of the $SiCl_4$ reservoir, as per the instructions for the bulk fill system.
- Open both valves on the top of the $SiCl_4$ reservoir and leave the valve at the base of thee reservoir close.
- Fill the reservoir as per the instructions for the bulk fill system.

2. Filling the $SiCl_4$ bubbler from the reservoir.

- Set the $SiCl_4$ bubbler to bubbler to vent at 10sccm.
- Open one of the valves on the top of the $SiCl_4$ reservoir.
- Fill the bubbler by opening the valve between the $SiCl_4$ reservoir and the bubbler. Close this valve when the bubbler is full.

3. Filling the $POCl_3$ bubbler.

- Connect the tee piece at the end of the bulk fill pipes to the fill valve on the top of the $POCl_3$ bubbler, but leave the valve closed.
- Purge the bulk fill pipe work to the fill valve on the top of the $POCl_3$ bubbler; as per the instructions for the bulk fill system.
- Set the $POCl_3$ bubbler to bubble to vent at 10sccm and open the fill valve.
- Fill the reservoir as per the instructions for the bulk fill system.

ii. Filling GeCl4, BBr3 or SnCl4 from ampoules.

- Have 2 persons present, both wearing gloves resistant to the chemicals, eye protection, cleanroom coats and 3M 4277 respirators.
- Remover the ampoule from its packaging under a fume hood and transport to the glove box in a bucket to prevent it being dropped.
- Remove the front from the glove box, as described in the "Maintenance to bubbler system" section, place the ampoule in the glove box and replace the front.
- Leave the glove box to purge at a high flow rate (off the rotameter scale) for at least 24 hours and reduce the glove box temperature to 5°C.
- Open the fill valve on the bubbler to be filled and bubbler to vent at 10sccm.
- Use a glass knife to score the neck of the ampoule and break the neck off.
- Pour the chemical into the bubbler through the funnel.
- Once part empty the ampoule can be stood upside down in the top of the funnels, and left like this until all liquid has drained.
- Close the fill valve.
- The ampoule should then be stood up right and left until no liquid or vapour is present and soot is no longer produced.
- The glove box should be purged for a further 24 hours at 5°C, after which the ampoules maybe removed from the glove box using the reverse of the procedure for getting ampoule into the glove box.

B. Using The Glove Box

When using the glove ports the glove box purge gas must be increased to ~10lpm (full scale on rotameter is 5lpm, therefore actual flow is only approximate) from 2lpm. The ½ inch solenoid valve must be open, and it is important to observe the glove box pressure at any point when gloves are being pushed in to or out of the glove box. Pressure must not be allowed to rise above 10mbar or below 1mbar, this can be achieved by holding gloves still until pressure drops/rises to an acceptable level. When sealing the glove ports it maybe necessary to reduce purge flow to stop gloves inflating. Once the glove ports have been sealed the ½ solenoid valve can be closed and the purge flow reduced to 2lpm.

When using the posting port to pass items into or out of the glove box, the posting port and the glove box should have been purged for at least 12 hours since the presence of vapour in the atmosphere. The item can then be transferred to the posting port, which should be further purged for 30 minutes before the item can be removed.

C. BCl_3 System

The nitrogen pressure regulator should always be set to 2.5psi unless otherwise indicated. The nitrogen purge rotameter should be set to 0.5 l/min unless otherwise indicated.

i. Stand by mode:

- Valve A open.
- Valve B closed.
- Valve C position 2
- Valve D open.
- Valve E position 2.
- Valve F position 1.
- Cylinder valve closed.
- Valve G open
- 3-port valve in FHD glove box set to "vent"

ii. Run mode:

- Valve A open.
- Valve B closed.
- Valve C position 2
- Valve D open.
- Valve E position 2.
- Valve F position 2.
- Cylinder valve open.
- Valve G open
- 3-port valve in FHD glove box set to "run"

iii. Procedure to purge BCl_3 from system:

Firstly set the valves as follows

- Valve A open.
- Valve B closed.
- Valve C position 1.
- Valve D open.
- Valve E position 2.
- Valve G open.
- Cylinder valve closed.
- Valve F position 2
- 3-port valve in FHD glove box set to "vent"

Set the MFC to maximum flow rate and allow this section of the pipe work to purge for 2 hours. Then set the valves as follows:

- Valve A closed.
- Valve B open.
- Valve C position 2.
- Valve D open.
- Valve E position 1.
- Valve G open.
- Cylinder valve closed.
- Valve F position 2.

- 3-port valve in FHD glove box set to "vent"

Set the nitrogen rotameter to 2l/min and leave for 2 hours. Then adjust the nitrogen regulator pressure to 1 bar and repeatedly set valve E to the centre "off" position and then back to position 1 – This gradually dilutes the gas in the pipe directly above the cylinder. Reset the regulator and rotameter.

iv. Changing the BCl_3 cylinder:

Follow the procedure to purge the BCl_3 system, then set the valves as follows,

- Valve A open.
- Valve B open.
- Valve C position 2.
- Valve D open.
- Valve E position 1.
- Valve G open.
- Cylinder valve closed.
- Valve F position 1
- 3-port valve in FHD glove box set to "vent"

Then disconnect the cylinder and reconnect the new cylinder. Then repeat the purge procedure to ensure any water vapour has been removed from the pipework before flowing BCl_3.

D. Deposition

i. Loading substrate

Firstly verify that the extracts are working. Switch on the sample holder vacuum pump and hold the sample in plate. This is either done by hand with the lid of the FHD system open or using the sample loading tool through the small window in the front of the FHD system with the lid closed. When working in the FHD system with the lid open wear breathing mask, gloves and eye protection with the large, flexible extract positioned close to where you are working. Adjust the silica tube, which connects the vacuum pump to the sample through the large silica place so that a seal is made and the sample is sucked into place.

ii Burner start and shut down

To light the burner first check that the Nitrogen, Hydrogen and Oxygen main valves are open and the regulators are all set to ~2bar (this should always be the case). Check that no vapour is being supplied from the bubbler to the FHD system. Independently set flow rates for the rings for the various gases and check they are stable. If the system has been vapour free for 20 minutes, and has not had hydrogen or oxygen flowing for 5 minutes then it is safe to open the lid. Always wear a 3M 4277 breathing mask when the lid is open. The burner is always left purging with nitrogen through rings 2 and 6; this must be shut off 1minute prior to lighting, thus allowing air to reach the burner. Wearing a safety glove, hold the piezo-lighter to the burner. Turn the hydrogen on and **immediately** spark the lighter, continue until flame lights. Once alight flow oxygen, and introduce nitrogen through rings 2, 4 and 6 respectively. Check at all times that the flame remains stable and does not go out. The lid can then be closed. If unsure of flame condition at anytime abort the start procedure by shutting down the burner as explained below. The system should never be left unattended while the flame is alight or the lid is open.

To shut down the burner first insure that no vapour is being supplied to the burner. Then shut off the oxygen followed by the hydrogen. Reflow the oxygen for 5 seconds and shut off. This operation should take place with rings 2, 4 and 6 flowing nitrogen and with the lid shut unless a start up is being aborted. In which case shut down can take place regardless of lid position and nitrogen flow. *Step by step technical instructions for Burner Start and Shut down are included in the appendix and displayed by the FHD rig.* When the FHD system has been shut down the lid must be latched and the burner left purged with nitrogen through rings 2 and 6.

iii. Substrate heater lamps

The halogen lamp system used for heating the substrate is controlled from the box of electronics below the FHD system. To use the heater, switch this box of electronics on then set the key switch to 'heater always on'. The power supplied to the lamps is set using the 'digital' potentiometer next to the key switch. The temperature is read from the display of the temperature controller. Note that in this mode the temperature controller does not control the temperature – is just used as a temperature read-out.

iv. Computer software.

The software which controls the bubbler system, vapour supply and translation of the burner has been designed to be as intuitive as possible. The main window displayed on start up mirrors the front of the bubbler control box. There are four distinct sections, MFC control (Flow rate),

Bubbler Temperature control, Valve position, and Automatic process control (this does not appear on the front panel).

The MFC control section is used to monitor and set the flow rate of gas through the various channels (Bubbler 1, Bubbler 2, Bubbler 3, Bubbler 4, Bubbler 5 and Dilution). The "actual" box always displays the current flow rate through the given MFC. The "set" box in combination with the "set" button allows new flow rates to be set. All values are given in ccm (standard cubic centimetres), bubblers 1-4 MFC's have a maximum flow of 250ccm, bubbler 5 MFC has a maximum flow of 10ccm and the dilution MFC has a maximum flow of 500ccm.

The bubbler temperature control section displays the temperature of the heater (H) and the temperature within the bubbler (B) for each bubbler separately. The "set" boxes show current set point and can be used in combination with the "set" buttons to instigate new set points.

The valve position section allows the switching of the various valves used for routing gas flow around the system. The buttons switch the valve to the position indicated by the label and the option toggles display the current valve position (mirrored by the LEDs on the front panel).

The automatic process control section consists of a several sub sections, vapour supply control, translation control and data logging. The vapour supply section consists of a parameters window through which flow rates and valve positions can be set with respect to process time, which can be saved and loaded from text files. The "Start Process" button on the main window starts the process timer running and runs the process parameters set in the parameter window. The "Stop Process" button stops the process timer, resets all valves to the fail save position and resets all flow rates to default (10ccm per channel). The "Stop Process" button will reset the system to the fail-safe state even if the process timer is **not** running.

The translation control window allows manual movement of the translation stages through use of the "up", "down", "left" and "right" buttons. Step rate, phase and half/full step parameters should not need to be changed (if this is necessary refer to stepper controller manual for instruction). Scan programs can be used either negative (right to left) or positive (left to right). If the scan is process linked then the translation software will inform the vapour supply software that it has finished scanning and that vapour to the burner can be switched off. Process linking not only reduces the length of time vapour is flowing through the burner but also allows purging of the line to start as soon as the scan has finished.

Data logging allows all the parameters that are relevant to the process (temperatures, flow rates, valve positions and process time) to be logged to a text file. This can be started "Start" and left running in the background "Okay", to stop open the data logging window and press "Stop".

If at anytime vapour production needs to be halted pressing "Stop Process" will return the system to a failsafe state. If the software crashes the hardware returns to a failsafe state and informs the user of the crash by a continuos tone and flashing LED, this can be silenced by use of the "standby" button or by turning the key switch from "On" to "Off".

v. Removing sample and cleaning FHD system after use.

Wait for the thermocouple in the sample holder plate to indicate that the sample is cold enough to handle. Then use one of two methods to remove the sample. Firstly insert the sample loading tool through the window in the front of the FHD system and switch off the vacuum pump to release the sample into the sample loading tool and withdraw the tool complete with sample. Alternatively, wear a breathing mask, gloves and eye protection then open the lid of the FHD system. Hold the sample by its edges and switch off the vacuum to release the sample or use a scalpel to lift the edge of the sample and then pull the sample free. After the sample is removed the FHD system should be cleaned. Do this wearing breathing mask, gloves and eye protection with the large, flexible extract positioned close to where you are working. Scrape the 'soot' off the sample plate and glass extract tubes as much as possible and remove the waste using the vacuum cleaner designated for hazardous materials. Use the compressed nitrogen 'gun' to clear the FHD extract of soot. The compressed nitrogen gun should not be directed at the skin and always so that the debris travels in a safe direction.

E. Maintenance to bubbler system

Stop all processes; purge all lines (except via bubbler) for 1 hour per valve combination using dry nitrogen. Set bubbler MFC flow rates to 0ccm (dilution MFC remains set to default 10ccm) and switch valves off (key switch to "off"). Close valves on bubbler inputs and outputs (fill line valves should always be closed). Turn off glove box atmosphere heaters, open ½ inch solenoid valve when pressure reaches

atmospheric close ½ inch solenoid valve. It is now possible to remove the front window on the glove box, once the window has been removed turn the glove box purge off. When working inside the glove box have 2 people present both wearing appropriate gloves, eye protection and 3M 4277 respirator. The glove box front should not be removed if temperature is below ambient in order to minimise formation of condensation.

F. Maintenance to BCl3 System

- Make sure that the pipe work has been purged with N_2 prior to any work on the system.
- Pressure test the system to a pressure of 2 bar every 6 months.
- Confirm the operation of the pressure relief valve every 6 months

G. Maintenance to FHD system

Stop all processes; purge supply line with dry nitrogen for 1 hour. Isolate hydrogen and oxygen supplies at main valves, then depressurise lines through burner (if FHD is to be unplugged from extract then also depressurise nitrogen line). Leave system extracting for 15 minutes after depressurisation. Insure substrate heater is switched off and unplugged, that translation stage controller is off, and that translation power supply is off. Switch off valve power by turning key switch to "off" position. Close ball valve at base of burner and shut off shield line purge before any internal maintenance takes place.

H. Maintenance to gas, extract or electricity supplies.

Stop all processes and switch off the computer and solenoid valves. Leave all MFC's flowing with 10ccm of nitrogen to prevent moisture entering the system. If this is not possible seal off the bubbler system as described in emergency procedure for failure of purge gas supply.

Regular maintenance procedures

Record regular maintenance on the sheet provided.

A. Bubbler system

- Inspect the gloves before use, looking for holes especially around the fingers.
- Test the glove box pressure relief every six months. Do this by inserted your hand in one of the glove quickly so that the glove box pressure rises above 7mbar. You should hear the solenoid valve open.
- The bubblers and associated vapour supply pipe work should be pressure tested once a month using the following procedure:

i. Pressure test unit (pressure gauge and flow meter) should be fitted into vent line at exit point from the glove box, this most be done after system has been purged as per the general maintenance procedure mentioned previously.

ii. Each bubbler line should be independently switched to vent with the vent line sealed. A flow of 50ccm should be supplied until the relevant pressure relief valve is tripped. A note of the blow pressure for the pressure for each bubbler channel should be made on the pressure test sheet.

iii. The pressure relief valves should then be capped using the female ¼" swaglock blanks found in the glove box.

iv. Each channel should again be individually set to vent with flow rates of 50, 100 and 200ccm with the vent line open. Measured flow rates and associated pressures should be noted on the pressure test sheet.

v. The vent line should then be sealed and each channel pressurised to 5, 10 and 15psi using a flow rate of 50ccm. The MFC should then be set to zero, and the channel left sealed for 5 minutes. The pressure after this time should be noted on the pressure test sheet.

vi. Remove caps from the pressure relief valves and pressure test unit, and return valves and MFC to default positions.

vii. Finally any abnormalities during the tests or indication of further required maintenance should be noted in the relevant section on the pressure test sheet.

B. BCl3 System

i. Pressure testing the system to check if there are any leaks:

Carry out this procedure every six months.

Set the valves as follows

- Valve A closed.
- Valve B open.
- Valve C position 2.
- Valve D closed.
- Valve E position 2.
- Valve G open.
- Cylinder valve closed.
- Valve F position 1
- 3-port valve in FHD glove box set to "vent"

Then set the MFC to maximum flow rate and adjust the regulator pressure to read approximately 2 bar. Close valve G and record the exact reading on the regulator output pressure gauge. Leave the system in this state for 16 hours (ie. overnight) and record the pressure again. There should be no change in the pressure reading.

This procedure doesn't test a small section of pipework adjacent to the pressure gauge close to the BCl_3 cylinder. This is because the limit for this pressure gauge is 0.35 bar. To test this section of pipework, close valve D, open the cylinder valve, then close the cylinder valve. Record the reading on the pressure gauge then leave the system for 24hours then read the pressure again. There should be no change in pressure.

ii. Checking the operation of the pressure relief valve:

Carry out this procedure every six months.

Set the valve as follows

- Valve A open.
- Valve B closed.
- Valve C position 2.
- Valve G open.
- Valve F position 2
- The rotameter needle valve wide open

With the regulator set to 2.5psi (as usual) the rotameter should register zero flow. Slowly increase the pressure using the regulator until the rotameter just starts to show a flow. This pressure is the pressure at which the pressure relief valve opens. It should be 3psi, if this pressure becomes greater than 4psi then replace the pressure relief valve.

C. FHD system

- Test the interlock on the FHD lid every month by setting the solenoid valve at the base of the burner to burner with no chemicals in the gas stream. Open the FHD lid and check that the valve switches to vent.
- The vapour supply line from the bubbler to the FHD and associated valve work should be pressure test once a month (at the same time as the bubblers set is pressure tested). The following procedure should be followed:
  - i. Insure vapour supply line has been purged as per the general maintenance procedure mentioned previously.
  - ii. Set dilution MFC to zero flow, insure all bubbler channels are set to vent and insert pressure test unit into the burner vent line, up stream from the shut off valve.
  - iii. Seal the burner vent line and pressurize the supply line, with the dilution MFC set to 100ccm, until the pressure relief valve blows. Note the trip pressure on the pressure test sheet.
  - iv. Cap the dilution pressure relief valve in the glove box using one of the female ¼" swaglock blanks found in the glove box.

v. Open the burner vent line and set the dilution MFC to 125, 250 and 500ccm and note the resultant flow rate and associated pressure.
vi. Seal the burner vent line and pressurize the supply line to 5, 10 and 15psi, by flow 100ccm through the dilution MFC. Once pressurized set MFC to zero and leave sealed for 5 minutes. Note the resulting pressure on the pressure test sheet.
vii. Remove cap from pressure relief valve and pressure test unit, and return valves and MFC to default position.
viii. Finally any abnormalities during the tests or indication of further required maintenance should be noted in the relevant section on the pressure test sheet.

- The extract and associated systems must be cleaned monthly, the following procedure outlines this process:

i. Insure FHD system has been purged for maintenance as outlined in a previous section.
ii. Move circulator unit out of the access space between the glove box and FHD rig.
iii. Detach vapour supply line from mounting and insure that it can move freely.
iv. Raise FHD rig legs and unlock wheels.
v. Carefully manoeuvre the FHD rig into the access space in front of the glove box, insuring that the vapour supply line does not become trapped, bent or kinked.
vi. Once sufficient space has been made, to gain access to the extract system and gas/electrical inputs on the rear of the FHD rig, lock the wheels.
vii. Disconnect the supply line from the extract tee-piece, within the body of the FHD rig. (nb. Whenever supply line or extract is open to atmosphere operator must use 3M 4277 mask and appropriate protective eyewear and gloves).
viii. Disassembly of extract tee-piece within the body of the FHD rig is now possible. The components should be cleaned using the toxic vacuum and provided cleaning implements.
ix. Next shut off the extract booster (fan or venturi) and disassemble extract pipe work and clean as afore mentioned.
x. Reassemble all extract components, restart extract booster and, reattach and open supply line.
xi. Finally move FHD rig and associated pipe work back into normal operating position and secure.

- Before a deposition takes place measure the flow rates for the burner extract at North, South, East and West positions using the digital anemometer. Measurements should be time averaged over 10seconds and should be approximately in the range of 0.4-0.5m/s. (Note; all four measurement positions will not give the same reading, and flow fluctuations on the scale of 1-2 seconds are to be expected). If extract rate is significantly deviated from the expected range, the degree of extract boost should be modified. Continued deviation from expected flow rates may indicate that the extract requires cleaning.
- After post-deposition cleaning the burner extract flow rate should again be measured using the same procedure as outlined above. Any significant deviation from pre-deposition measurements may indicate that the burner extract and immediate pipe work requires further cleaning.

Emergency procedures.

A. Spillage of halide in glove box or breakage of bubbler containing halide

Turn off all solenoid valves and the bubbler heaters. Open wide the needle valve on the glove box purge outlet. Allow the spilt liquid to evaporate and be carried out of the glove box by the purge gas. Whilst this is in progress monitor the pressure in the glove box, a rise in pressure will indicate that the outlet is becoming blocked. Attempt to prevent blockage of the outlet by adjusting the purge gas flow

rate into the glove box and adjusting the needle valve to dislodge any oxide blocking it. If the outlet does block then ensure that the larger diameter PTFE glove box vent line has been purged and is therefore dry. Use the switch on the emergency solenoid valve to open the larger diameter PTFE vent for the glove box. There is an additional manual vent line for the glove box if necessary. Leave the glove box purging for at least two days after all signs of the halide have disappeared before removing the window to repair any damage and test all components in the glove box.

B. Any problem during deposition.

Press the emergency stop button for the bubbler system. Evacuate the area and activate the cleanroom emergency gas extract if a gas escape is suspected. Shut down the burner as described in the operating procedure. Turn off the heater lamps. Turn off the translation stage power supply. Only investigate the fault if you are sure it is safe to do so.

C. Failure of purge gas supply

If deposition is under way follow the above procedure. Turn off the solenoid valves. Set all gas flow controllers to zero flow rate and shut the gas supply valves on the wall. Shut the ball valve in the glove box outlet pipe and shut the glove box purge supply. Shut the ball valve in the halide delivery line at the base of the burner in the FHD system.

Appendix 2 Papers submitted

a) Electronics Letter submitted September 2002
b) Paper submitted September 2002 for OFC 2003

a) Fabrication of directly UV-written channel waveguides with simultaneously defined integral Bragg gratings

G. D. Emmerson, S.P. Watts, C. B. E. Gawith, V. Albanis, M. Ibsen,
R. B. Williams and P. G. R. Smith

A new technique for UV direct writing of Bragg gratings in planar silica is presented. In this method the Bragg gratings and the channels are defined simultaneously, conferring advantages in flexibility of design and grating performance. Photosensitive Germanium doped silica-on-silicon produced by Flame Hydrolysis Deposition was used.

Introduction: Direct UV-writing is a fabrication process for planar waveguides based on the permanent photoinduced refractive index change used in the fabrication of fibre Bragg gratings [1]. This UV induced refractive index change has recently been applied to the field of integrated optics, showing that an intense UV beam focused to form a writing spot and translated within the photosensitive core of a planar sample can form a low loss channel waveguide [2]. Subsequent progress has demonstrated the suitability of direct writing to produce integrated optical components, including power splitters and directional couplers [3]. The integration of directly UV written waveguides and Bragg gratings within a planar geometry is of great significance, but to date directly written channels with Bragg gratings have been produced using a two-step process. In such cases, a primary exposure is often used to create a channel waveguide while a secondary exposure superimposes the grating structure. As the

channel writing process often saturates the photosensitive response of the material a sequential process cannot be used to optimise both the grating strength and waveguide geometry in a single process. To this end we present a new method of directly writing a Bragg grating structure whilst simultaneously defining the channel waveguide, thus allowing the optimal use of the photosensitivity of the material.

Experimental: For these initial experiments three-layer Germanium doped Silica-on-Silicon samples developed at the Optoelectronics Research Centre using Flame Hydrolysis Deposition (FHD) were used as the writing media. Germanium doping of the middle layer introduces inherent photosensitivity to UV radiation [1], while all three layers were co-doped with Phosphorus and Boron facilitating independent control of refractive index and processing parameters.

Figure 1 shows a schematic of our approach. Direct UV writing into the buried Gemanosilicate layer was preformed using a CW frequency doubled Argon-Ion laser operating at 244nm. A beam splitter was used to create two separate beam paths at an intersection angle of 27° and each beam was individually focused to a spot size of 6μm. The two focused beams are crossed within the photosensitive layer resulting in a writing spot with an inherent interference pattern. During writing this interference allows a channel waveguide containing a periodic refractive index modulation within the photosensitive layer to be written.

When the sample is translated under a constant writing spot the intra-spot intensity pattern is averaged out, resulting in a channel waveguide. However, if the laser beam intensity is strobed with a period close to that of the intra-spot pattern as the sample is

translated, then a channel waveguide is induced that has a periodic index modulation thus forming a Bragg grating. In our system the laser beam is strobed using an acoustic optic modulator triggered by an interferometer monitoring the position of the sample. The formation of Bragg gratings within the core can be directly controlled by changing the spatial superposition of the interference pattern, as is utilized in the fabrication of continuous fibre Bragg gratings [4]. This technique allows different grating periods to be defined without the need to change the beam intersection angle. The period of the Bragg grating is defined by the laser modulation as the sample is translated, and not solely by the period of the interference pattern. The range of detuning allowed depends inversely upon the number of planes in the writing spot and so a small spot is advantageous in writing widely detuned gratings. In this paper we are presenting preliminary results on Bragg gratings of varying period, length, and strength.

Results: The gratings were analysis using an EDFA based ASE source, the output of which was transmitted and selectively orientated through a fibre polarizer. Connected to the polarizer was a 3dB coupler to allow the back-reflected signal to be analysed using an OSA. Fabry-Perot resonances were partially suppressed through use of index matching fluid at the point of fibre launch.

An example of the back-reflected signal from a 14mm long grating is shown in Figure 2 and exhibits a reflectivity of approximately 28% with a FWHM of 0.132nm. As can be seen, the spectral response is not optimised and exhibits Fabry-Perot fringes from the sample facets. Future devices are planned, that will incorporate chirped and

apodised grating structures with optimised UV induced index, thereby allowing higher reflectivity and tailored spectral response.

Figure 3 shows the effect of the period of the grating written against the peak reflected wavelength. As expected from the Bragg condition the response is linear, allowing for n_{eff} of the channel and grating to be measured to a high degree of accuracy. Precise control of the polarisation state launched into the sample allowed the birefringence of the structure to be obtained, n_{eff} for TE and TM polarisation states were 1.46597 and 1.46594 respectively, implying a of birefringence of 3×10^{-5}.

Figure 4 shows n_{eff} for a range of different waveguides written at different fluences by varying the translation speed of the sample.

Discussion: In conclusion, we have demonstrated the first simultaneously written channels with integral Bragg gratings in a photosensitive planar media. We have shown that it is possible to write Bragg gratings over a large range of wavelengths through strobing of the writing spot intensity during translation entirely under software control. Based on these initial results, future FHD samples will be optimised for UV writing and photosensitivity will be enhanced through the investigation of Deuterium loading, selective dopant concentrations and other associated processes. The future development and optimisation of photosensitive materials and UV direct writing techniques will ultimately allow the realisation of high quality integrated Bragg grating and channel waveguiding structures suitable for application within telecomms devices.

References

1. K. O. Hill and G. Meltz, "Fiber Bragg Grating Technology Fundamentals and Overview," J. Lightwave. Technol. 15, 1263-1276 (1997)

2. M. Svalgaard and M. Kristensen, "Directly UV written silica-on-silicon planar waveguides with low loss," Electron. Lett. 33(10) 861-863 (1997)

3. K. Faerch and M. Svalgaard, "Symmetrical Waveguide Devices Fabricated by Direct UV Writing," IEEE Photonic. Tech. L. 14(2), 173-175 (2002)

4. UK Patent Application: GB2316760A

Author Affliation:

G. D. Emmerson, S.P. Watts, C. B. E. Gawith, V. Albanis, M. Ibsen, R. B. Williams and P. G. R. Smith (Optoelectronics Research Centre, University of Southampton, SO12 1BJ, United Kingdom) (gde@orc.soton.ac.uk)

Figure Captions:

Fig. 1 Simultaneous direct UV writing of channel and subsequent grating sections using focused beam interference within the core of a photosensitive planar FHD sample.

Fig. 2 Typical reflection spectra for simultaneously defined planar Bragg grating.

Fig.3 Range of Grating periods and associated measured peak reflection wavelengths, allowing determination of n_{eff} for TE and TM polarisation.

Fig.4 Variation of n_{eff} with writing fluence, varied by altering sample translation speed.

Figure 1

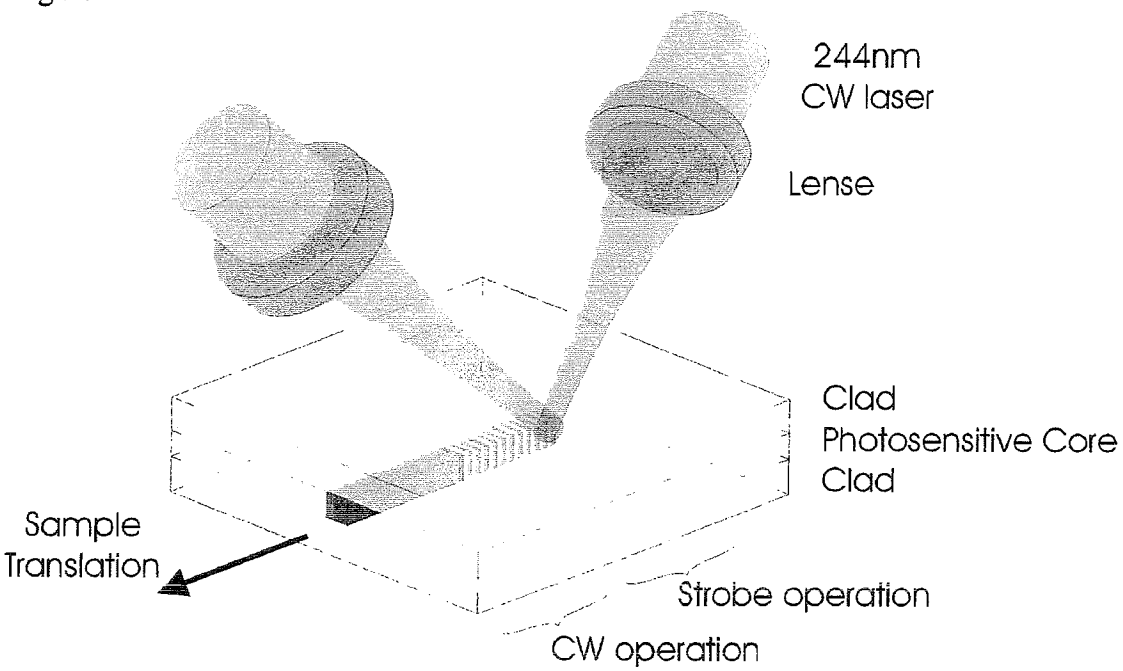
244nm
CW laser
Lense
Clad
Photosensitive Core
Clad
Sample
Translation
Strobe operation
CW operation

Figure 4

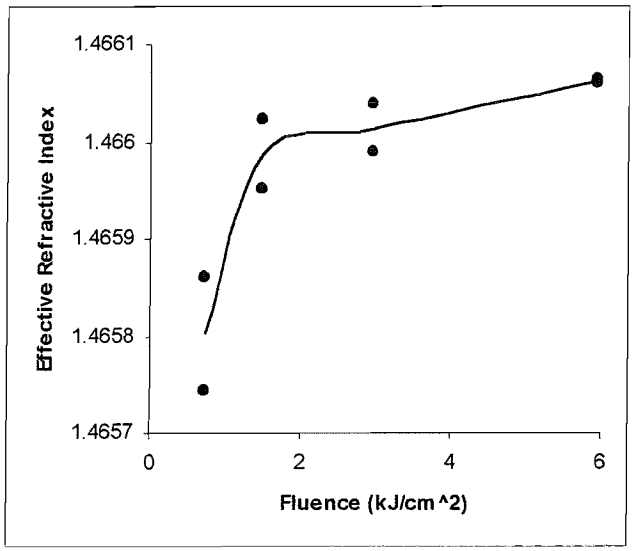
1.4661
1.466
1.4659
1.4658
1.4657
Effective Refractive Index
0
2
4
6
Fluence (kJ/cm^2)

b) Directly UV-written planar channel waveguides containing simultaneously defined Bragg gratings

G. D. Emmerson, S. P. Watts, C. B. E. Gawith, V. Albanis, C. Riziotis, A. Fu, M. Ibsen,

R. B. Williams and P. G. R. Smith

Optoelectronics Research Center, University of Southampton, SO17 1BJ, United Kingdom

gde@orc.soton.ac.uk

Abstract: We demonstrate a new technique for the simultaneous writing of channels and Bragg gratings in planar silica. By interfering focused UV beams in a photosensitive planar layer with suitable sample translation and laser strobing we were able to fabricate near-ideal Bragg gratings, with 60% reflectivity.

OCIS Codes: (###.###)

Direct UV-writing offers a low cost, rapid fabrication process for planar lightwave circuits (PLC's) in photosensitive materials. In the past it has been demonstrated that the UV induced refractive index increase, which has been so successfully implemented in fibers to produce high quality gratings [1], can be utilized in a planar geometry to produce low loss channel waveguides [2]. Subsequent development of this technique has demonstrated the suitability of direct writing to produce integrated optical components without the need for mask manufacture, lithography, etching or subsequent deposition steps [3]. In previous work directly written channels with Bragg gratings have been produced in a two-step process, using a primary exposure to create a channel waveguide and a secondary exposure to superimpose a grating structure. This sequential process cannot optimize both the grating strength and waveguide strength, as the channel writing step will tend to saturate the photosensitive response.

In this paper we present the first demonstration of a simultaneously direct UV-written channel waveguide containing a Bragg grating structure. The UV writing was performed on three layer silica-on-silicon samples fabricated using flame hydrolysis deposition (FHD). Where the core layer was

germanium doped to produce an intrinsic photosensitivity, which was further enhanced through deuterium loading and thermal locking [4]. Thermal locking is a process whereby, after removing the sample from the high pressure deuterium loading cell, it is rapidly heated to 1400°C for 5s and quenched to room temperature. This locking process results in samples with significantly enhanced photosensitivity compared to non-loaded samples without the out-diffusion time limitations of deuterium loaded samples. The resulting photosensitivity persists for many months compared with out-diffusion times of minutes for simple deuterium loading, which is less than the typical UV writing times.

The UV writing was performed using a frequency doubled Ar-ion (244nm CW output) laser. Unlike prior implementations of direct UV writing the beam was split into two paths, both of which were individually focused and crossed at the focal point with a half angle of 13.5° (Fig. 1). The resulting 6μm writing spot has an intrinsic intensity modulation in one dimension created by the interference of the two beam paths. When the sample is translated under a constant writing spot the intra-spot intensity pattern is averaged out, resulting in a channel waveguide. However, if the laser beam intensity is strobed with a period close to that of the intra-spot pattern as the sample is translated, then a channel waveguide is induced that has a periodic index modulation thus forming a Bragg grating. In our system the laser beam is strobed using an acoustic optic modulator triggered by an interferometer monitoring the position of the sample.

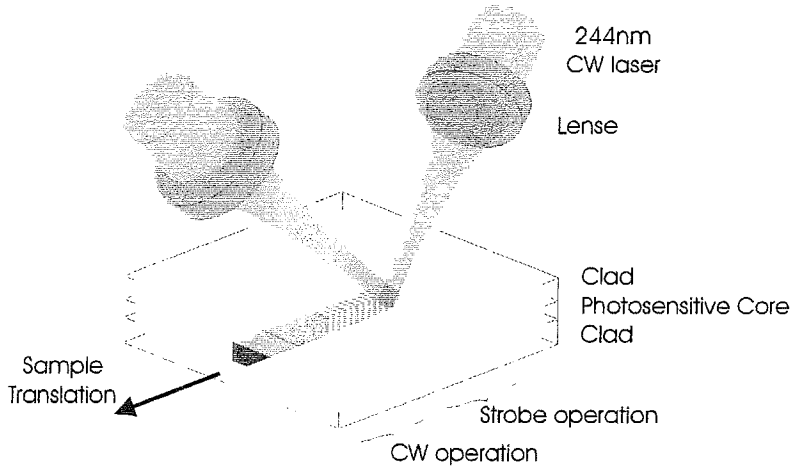

Fig. 1. Simultaneous direct UV writing of planar channels and Bragg gratings. In CW operation any grating structure is averaged out. If the laser is strobed with a period close to the interference pattern of the intersecting beams a channel waveguide with integral Bragg grating is written.

This novel technique has many potential advantages over previous processes including: flexibility of grating design, optimal use of photosensitivity, avoidance of etching processes, ability to control taper, control of waveguide properties, ability to create complex devices, etc. A key advantage of the technique, demonstrated here, is the potential for center-wavelength detuning to allow the creation of Bragg gratings with center-wavelengths not matching the period of the underlying light intensity pattern used in the writing process [5]. Centre-wavelength detuning is used in fiber grating fabrication and has many applications, the most basic of which allows uniform gratings of varying period to be fabricated from one phase mask. The same advantages apply to the planar grating fabrication technique presented here, but with greater flexibility. This is because to a first approximation, the amount a grating can be detuned is inversely proportional to the writing beam size. As the 6μm diameter writing spot currently implemented for planar work is 10 to 50 times smaller than that used in fiber grating fabrication [5], this means that Bragg gratings with peaks over the entire EDFA spectral range can be written without any change to the experimental setup.

To demonstrate this effect we have fabricated a range of planar gratings in a single sample with center wavelength that span the entire bandwidth of the ASE source currently used for analysis of our planar Bragg grating devices, the results of which are given in Figure 2. The centre-wavelength, of the Bragg grating channels were defined completely under computer control with no changes being made to the optical set-up. The ASE source used for this grating evaluation is based on an EDFA with a maximum output of 0dBm, the output of which was passed through a Micro-Optics fiber polariser and a 3dB coupler, one output is terminated in index matching fluid and the other is put through the fiber polarization controller. The output fibre from the polariser was cleaved and butt-coupled to the sample, with index matching fluid used to partially suppress Fabry-Perot resonances. The remaining output from the coupler is monitored with an OSA.

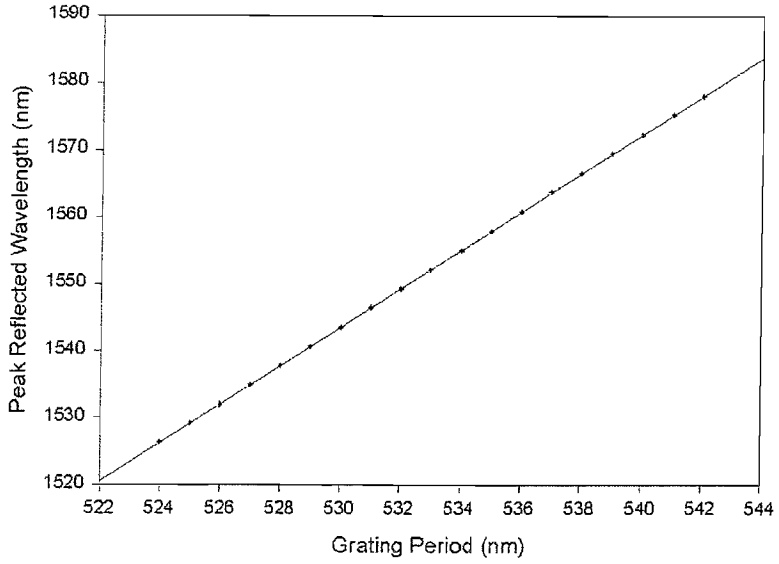

Fig. 2. Range of Bragg gratings formed, all with the same intersection angle of the writing beams spanning the EDFA spectrum under software control.

In our first demonstration we have realized single mode planar channels containing gratings with various periods, lengths and numerical apertures. A typical spectral response is shown in figure 3, where the investigated grating was written with an effective fluence of $0.5KJcm^{-2}$. The spectrum shows a peak reflection intensity of 60% with a corresponding bandwidth of 0.14nm from a 10mm long Bragg grating. From the gradient of the graph an effective grating index modulation of $\sim 5x10^{-5}$ can be inferred via the Bragg condition. By characterizing the grating with both TE and TM polarized light the effective refractive index of the directly written waveguide can be rapidly determined in both cases. Using this technique the structure in figure 3 was determined to have a birefringence of $4x10^{-5}$ with a n_{eff} (TE) of 1.45645.

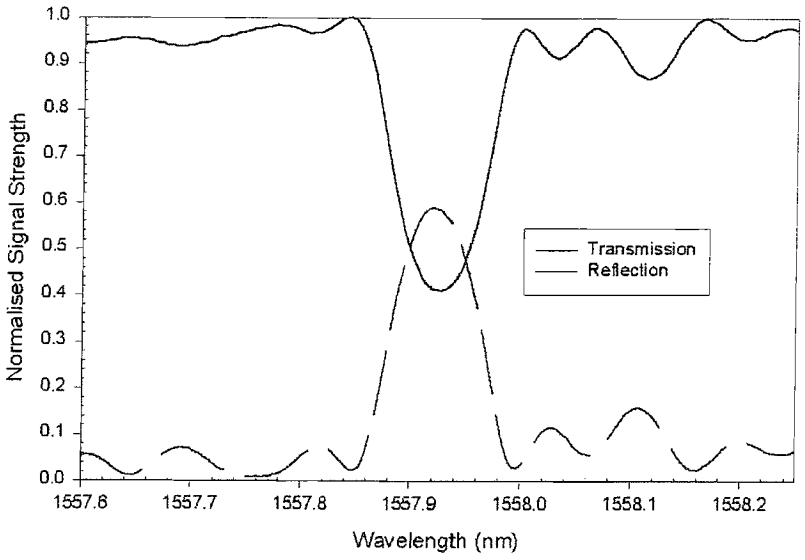

Fig. 3. Typical spectral response for a 10mm long simultaneously UV written channel waveguide with integral Bragg grating

These initial results demonstrate the potential of the direct UV writing process to simultaneously produce channel and grating structures with no need for a phase mask or subsequent processing steps. Offering a rapid, accurate and versatile method for characterizing the suitability of various photosensitive materials, this technique provides a simple route towards the fabrication and application of integrated optics. The further optimization of channel and grating writing parameters and resultant enhancement of the simultaneous definition of channels with integral Bragg gratings shows great promise for the future.

References

[1] K. O. Hill and G. Meltz, "Fiber Bragg Grating Technology Fundamentals and Overview," J. Lightwave. Technol. **15**, 1263-1276 (1997)

[2] M. Svalgaard and M. Kristensen, "Directly UV written silica-on-silicon planar waveguides with low loss," Electron. Lett. **33**(10) 861-863 (1997)

[3] K. Faerch and M. Svalgaard, "Symmetrical Waveguide Devices Fabricated by Direct UV Writing," IEEE Photonic. Tech. L. 14(2), 173-175 (2002)

[4] C. Riziotis, A. Fu, S. P. Watts, R. Williams and P. G. R. Smith, "Rapid heat treatment for photosensitivity locking in deuterium-loaded planar optical waveguide," Optical Society Amer. Technical Dig.: Bragg Gratings, Photosensitivity, and Poling in Glass Waveguides, Stresa, Italy, 2001, BThC31

[5] UK Patent Application GB2316760A

References:

[Atkins *et al*, 1993] Atkins, R.M., Lemaire, P.J., Erdogan, T. and Mizrahi, V., "Mechanisms of Enhanced UV photosensitivity via hydrogen loading in germanosilicate glasses", Elec. Lett, Vol. 29, No. 14, 1993, 1234-1235.

[Atkins, 1992] Atkins, P.W., "The elements of physical chemistry", Oxford University Press, 1992, ISBN: 0-19-855723-x

[Bardos *et al*, 1997] Bardos, L., Barankova, S. and Berg, S., "Thin film processing by radio frequency hollow cathodes", Surf. Coat. Technol., Vol. 97, 1997, 723-728.

[Bautista and Atkins, 1991] Bautista, J.R. and Atkins, R.M., "The formation and deposition of SiO_2 aerosols in optical fiber manufacturing torches", J. Aerosol Sci., Vol. 22, No. 5, 1991, 667-675.

[Bendell *et al*, 1990] Bendell, T., Miller, R.M.G. and Wilson, G., "Taguchi methodology within total quality", Bedford, 1990, ISBN: 1-854-23069-7.

[Bonar, 1995] Bonar, J.R., "Waveguide lasers in rare earth doped planar silica", PhD thesis, Glasgow University, 1995.

[Brinker and Scherer, 1990] Brinker, C.J and Scherer, G.W., "Sol-gel Science", Academic Press Inc., 1990, ISBN: 0-121-34970-5.

[Brodie and Muray, 1982] Brodie, I., and Muray, J.J., "The physics of microfabrication", Plenum Press, 1982, ISBN: 0-306-40863-5.

[Cho *et al*, 1998] Cho, J., Kim, J. and Choi, M., "An experimental study of heat transfer and particle deposition during the outside vapor deposition process", J. Heat Mass Transfer, Vol. 41, No. 2, 1998, 435-445.

[Cole *et al*, 1995] Cole, M.J., Loh, W.H., Laming, R.I., Zervas, M.N. and Barcelos, S., "Moving fibre/phase mask-scanning beam technique for enhanced flexibility in producing fibre gratings with uniform phase mask", Elec. Lett., Vol. 31, No. 17, 1995, 1488-1490.

[Cordier *et al*, 1997] Cordier, P. *et al*, "Evidence by transmission electron microscopy of densification associated to Bragg grating photoimprinting in germanosilicate optical fibres", Appl. Phys. Lett., Vol. 70, No. 10, 1997, 1204-1206.

[Coudray *et* al, 1996] Coudray, P., Chisham, J., Malek-Tabrizi, A., Li, C.-Y., Andrews, M.P., Peyghambarian, N. and Najafi, S.I., "Ultraviolet light imprinted sol-gel glass waveguide devices on silicon", Optics Communications, Vol. 128, 1996, 19-22.

[Douay *et al*, 1997] Douay, M. *et al*, "Densification involved in the UV-based photosensitivity of silica glasses and optical fibers", J. Lightwave Technol., Vol. 15, 1997, 1329-1342.

[Durkin, 1999] Durkin, M.K., "Advanced fibre Bragg gratings: Application to dispersion compensation", PhD thesis, University of Southampton, 1999.

[Edahiro *et al*, 1980] Edahiro, T., Kawachi, M., Sudo, S. and Tomaru, S., "Deposition properties of high-silica particles in the flame hydrolysis reaction for optical fiber fabrication", Jpn. J. App. Phys., Vol. 19, No. 11, 1980, 2047-2054

[Faerch and Svalgaard, 2002] Faerch, K. and Svalgaard, M., "Symmetrical waveguide devices fabricated by direct UV writing", IEEE Photon. Technol. Lett., Vol. 14, No. 2, 2002, 173-175.

[Gaydon and Wolfhard, 1970] Gaydon, A.G. and Wolfhard, H.G., "Flames", Chapman and Hall Ltd., 1970, ISBN: 0-412-09330-8.

[Ghatak and Thyagarjan, 1998] Ghatak, A. and Thyagarajan, K., "Introduction to Fiber Optics", Cambridge University Press, 1998, ISBN: 0-521-57785-3.

[Haiyan *et al*, 1999] Haiyan, O., Qinqing, Y., Hongbing, L., Hogjie, W., Qiming, W. and Xiongwei, H., "Thick SiO_2 layers produced by anodisation", Elec. Lett., Vol. 35, No. 22, 1999, 1950-1951.

[Hill and Meltz, 1997] Hill, K.O. and Meltz, G., "Fiber Bragg grating technology fundamentals and overview", IEEE J. Lightwave Technol., Vol. 15, No. 8, 1997, 1263-1276.

[Hoffmann *et al*, 1997] Hoffmann, M., Kopka, P. and Voges, E., "Low-loss fibre-matched low-temperature PECVD waveguides with small-core dimensions for optical communication systems", IEEE Photon. Tech. Lett., Vol. 9, No. 9, 1997, 1238-1240.

[Hsin-Chuan *et al*, 1996] Hsin-Chuan, T., Greif, R. and Wu, C.K., "A study of thermophoretic transport and flame hydrolysis deposition with application to the manufacture of optical waveguides", J. Materials Processing and Manufacturing Science, Vol. 4, 1996, 299-321.

[Hubner *et al*, 1996] Hubner, J., Poulsen, C.V., Pedersen, J.E., Poulsen, M.R., Feuchter, T. and Kristensen, M., "UV-written Y-splitter in Ge-doped silica", Lasers and integrated optics, SPIE, Vol. 2695A-11, 1996, 98-105.

[Ibsen *et al*, 1996] Ibsen, M., Hubner, J., Pedersen, J.E., Kromann, R., Andersen, L.-U.A. and Kristensen, M., "30dB sampled gratings in germanosilicate planar waveguides", Elec. Lett., Vol. 32, No. 24, 1996, 2233-2235.

[Iino *et al*, 1990] Iino, A., Kuwabara, M. and Kokura, K., "Mechanism of Hydrogen-induced losses in silica-based optical fibers", IEEE J. Lightwave Technol., Vol. 8, No. 11, 1990, 1675-1679.

[Jaeger, 1989] Jaeger, R.C., "Introduction to microfabrication", Modular series on solid state devices, Addison-Wesley publishing company, 1989, ISBN: 0-201-14695-9.

[Jouanna *et al*, 1996] Jouanno, J.-M., Hubner, J., Pedersen, J.E., Kromann, R., Feuchter, T. and Kristensen, M., "Strong Bragg gratings for WDM devices in non-sensitised low-loss Ge-doped waveguides", Elec. Lett., Vol. 32, No. 23, 1996, 22-23.

[Kawachi *et al*, 1980] Kawachi, M., Sudo, S., Shibata, N. and Edahiro, T., "Deposition properties of SiO_2-GeO_2 particles in the flame hydrolysis reaction for optical fiber fabrication", Jpn. J. App. Phys., Vol, 19, No 2, 1980, L69-L71.

[Kawachi, 1990] Kawachi, M., "Silica waveguides on silicon and their application to integrated-optic components", Optical and Quantum Electronics, Vol. 22, 1990, 391-416.

[Kilian *et al*, 2000] Kilian, A., Kirchhof, J., Kuhlow, B. Przyrembel, G. and Wischwann, W., "Birefringence free planar optical waveguides made by flame hydrolysis deposition through tailoring of the overclad", J. Lightwave Technol., Vol. 18, No. 2, 2000, 193-198.

[Lee, 1986] Lee, D.L., "Electromagnetic Principles of Integrated Optics", John Wiley and Sons, 1986, ISBN: 0-471-87978-9.

[Lemaire, 1991] Lemaire, P.J., "Reliability of optical fibers exposed to hydrogen: prediction of long-term loss increases", Opt. Eng., Vol. 30, No. 6, 1991, 780-788.

[Maxwell and Ainslie, 1995] Maxwell, G.D. and Ainslie, B.J., "Demonstration of a directly written directional coupler using UV-induced photosensitivity in a planar silica waveguide", Elec. Lett., Vol. 31, No. 2, 95-96.

[Maxwell *et al*, 1992] Maxwell, G.D., Kashyap, R., Ainslie, B.J., Williams, D.L. and Armitage, J.R., "UV written 1.5μm reflection filters in single mode planar silica guides", Elec. Lett., Vol. 28, No. 22, 1992, 2106-2107.

[Maxwell *et al*, 1994] Maxwell, G.D., Kashyap, R., Sherlock, G., Collins, J.V. and Ainslie, B.J., "Demonstration of a semiconductor external cavity laser using a UV written grating in a planar silica waveguide", Elec. Lett., Vol. 30, No. 18, 1994, 1486-1487.

[Meltz *et al*, 1989] Meltz, G., Morey, W.W. and Glenn, W.H., "Formation of Bragg gratings in optical fibers by a transverse holographic method", Opt. Lett., Vol. 14, No. 15, 1989, 823-825.

[Miller and Chynoweth, 1979] Miller and Chynoweth, "Optical Fiber Telecommunications", Academic Press, 1979, ISBN: 0-124-97350-7.

[Mizrahi *et al*, 1993] Mizrahi, V., Lemaire, P.J., Erdogan, T., Reed, W.A., DiGiovanni, D.J. and Atkins, R.M., "Ultraviolet laser fabrication of ultrastring optical fiber gratings and of germania-doped channel waveguides", Appl. Phys. Lett., Vol. 63, No. 13, 1993, 1727-1729.

[Ohring, 1992] Ohring, M., "The materials science of thin films", Academic Press Inc., 1992, ISBN: 0-125-24990-x.

[Okamoto, 1998] Okamoto, K., "Recent progress of integrated optics planar lightwave circuits", Optical and Quantum Electronics, Vol. 31, 1999, 107-129.

[Poulsen *et al*, 1995] Poulsen, C.V., Hubner, J., Rasmussen, T., Andersen, L.-U.A. and Kristensen, M., "Characterisation of dispersion properties in planar waveguides using UV-induced Bragg gratings", Elec. Lett., Vol. 31, No. 17, 1995, 1437-1438.

[Rabinovich, 1985] Rabinovich, E.M., "Review: Preperation of glass by sintering", J. Mat. Sci, Vol. 20, 1985, 4259-4297.

[Razafimahatratra, *et al*, 2000] Razafimahatratra, A.D., Benatsou, M., Bouazaoui, M., Xie, W.X., Mathieu, C., Dacosta, A. and Douay, M., "UV-induced permanent gratings in sol-gel germanosilicate thin films", Opt. Mat., Vol. 13, 2000, 439-448.

[Reimer, 1985] Reimer, L., "Scanning Electron Microscopy", Springer-Verlag, 1985, ISBN: 0-387-13530-8

[Riziotis *et al*, 2001] Rizotis, C., Fu, A., Watts, S., Williams, R. and Smith, P.G.R., "Rapid heat treatment for photosensitivity locking in deuterium-loaded planar optical waveguides", OSA Technical Digest 2001, paper presentation, BThC31-1.

[Sakaguchi, 1994a] Sakaguchi, S., "Consolidation of silica glass soot body prepared by flame hydrolysis reaction", J. Non-Cryst. Sol. Vol. 171, 1994, 249-258.

[Sakaguchi, 1994b] Sakaguchi, S., "Consolidation of GeO_2 soot body prepared by flame hydrolysis depostion", J. Non-Cryst. Sol. Vol. 171, 1994, 228-235.

[Scherer, 1977a] Scherer, G.W., "Sintering of low-density glasses: I, Theory", J. Am. Ceram. Soc., Vol. 60, No. 5-6, 236-239.

[Scherer, 1977b] Scherer, G.W., "Sintering of low-density glasses: II, Experimental study", J. Am. Ceram. Soc., Vol. 60, No. 5-6, 239-243

[Scherer, 1977c] Scherer, G.W., "Sintering of low-density glasses: III, Effect of a distribution of pore sizes", J. Am. Ceram. Soc., Vol. 60, No. 5-6, 243-245

[Shackelford *et al*, 1972] Shackelford, J.F., Studt, P.L. and Fulrath, R.M., "Solubility of gases in glass II. He, Ne, and H_2 in fused silica", J. Appl. Phys., Vol. 43, No. 4, 1972, 1619-1626.

[Sherman, 1987] Sherman, A., "Chemical Vapour Deposition for microelectronics", Materials science and processing technology series, Noyles Publications, 1987, ISBN: 0-815-51136-1.

[Stone, 1987] Stone, J., "Interactions of hydrogen and deuterium with silica optical fibers: A review", IEEE J. Lightwave Technol., Vol. LT-5, No. 5, 1987, 713-733.

[Strehlow, 1984] Strehlow, R.A., "Combustion fundamentals", McGraw-Hill, 1984, ISBN: 0-070-62221-3.

[Sulimov *et al*, 1996] Sulimov, V.B., Sokolov, V.O. and Poumellec, B., "Cluster modelling of the oxygen vacancy in SiO_2-GeO_2 system", phys. Stat. Sol. (b), Vol. 196, No. 175, 1996, 175-192.

[Sun and Schmidt, 1999] Sun, C.J. and Schmidt, K.M., "Building passive components with silica waveguides", SPIE, Vol. 3795, 1999, 313-319.

[Svalgaard *et al*, 1994] Svalgaard, M., Poulsen, C.V., Bjarklev, A. and Poulsen, O., "Direct UV writing of buried single mode channel waveguides in Ge-doped silica films", Elec. Lett., Vol. 30, No. 17, 1994, 1401-1403.

[Svalgaard, 1997] Svalgaard, M., "Ultraviolet induced refractive index structures in germanosilica", PhD thesis, Technical University of Denmark, 1997.

[Svalgaard, 1999] Svalgaard, M., "Effect of D_2 outdiffusion on direct UV writing of optical waveguides", Elec. Lett., Vol. 35, No. 21, 1999, 1840-1842.

[Svalgard and Kistensen, 1997] Svalgaard, M. and Kristensen, M., "Directly UV written silica-on-silicon planar waveguides with low loss", Elec. Lett., Vol. 33, No. 10, 1997, 861-863.

[Sze, 1988] Sze, S.M, "VLSI technology", McGraw-Hill series in electrical engineering electronics and electronic circuits, McGraw-Hill, 1988, ISBN: 0-071-00347-9.

[Tanaka *et al*, 1996] Tanaka, T., Takahashi, H., Oguma, M., Hashimoto, T., Hibino, Y., Yamada, Y., Itaya, Y., Albert, J. and Hill, K.O., "Integrated external cavity laser composed of spot-size converted LD and UV written grating in silica waveguide on Si", Elec. Lett., Vol. 32, No. 13, 1996, 1202-1203.

[Tien and Hummel, 1962] Tien, T.-Y. and Hummel, F.A., "The system SiO_2-P_2O_5", J. Am. Cerm. Soc., Vol. 45, No. 9, 1962, 422-424.

[Tosello *et al*, 2001] Tosello, C. *et al*, "Erbium-activated silica-titania planar waveguides on silica-on-silicon substrates prepared by rf sputtering", J. Non-Cryst. Sol., Vol. 284, 2001, 230-236.

[Ulrich and Riehl, 1982] Ulrich, G.D. and Riehl, J.W., "Aggregation and growth of submicron oxide particles in flames", J. Colloid. Sci, Vol. 87, No. 1, 1982, 257-265.

[Varshneya, 1994] Varshneya, A.K., "Fundamentals of inorganic glasses", Academic Press Inc., 1994, ISBN: 0-12-714970-8.

[Waldron and Daniell, 1978] Waldron, M.B. and Daniell, B.L., "Sintering", Heyden and Sons Ltd., 1978, ISBN: 0-85501-178-5.

[Ward, 1988] Ward, L., "The optical constants of bulk materials and films", The Adam Hilger series on optics and optoelectronics, Adam Hilger : IOP publishing Ltd, 1988, ISBN: 0-85274-168-5.

[Yoshida and Prasad, 1996] Yoshida, M. and Prasad, N., "Sol-gel processed SiO_2/TiO_2/Poly(vinylpyrrolidone) composite materials for optical waveguides", Chem. Mater. Vol. 8, 1996, 235-241.

[Zauner *et al*, 1998] Zauner, D., Kulstad, K., Rathje, J. and Svalgaard, M., "Directly written silica-on-silicon planar waveguides with low insertion loss", Elec. Lett., Vol. 34, No. 16, 1998, 1582-1584.

Bibliography:

Optical Integrated Circuits:	Nishihara, H., Haruna, M. and Suhara, T., McGraw-Hill, 1989, ISBN: 0-07-046092-2.
Optical Fiber Communications, Principles and Practice:	Senior, J.M., Prentice Hall, 1992, ISBN: 0-13-635426-2.